Effect of Transpiration Cooling on Boundary Layer Transition for Hypersonic Flight



Philipp Kerth

Balliol College

University of Oxford

A thesis submitted for the degree of

Doctor of Philosophy

Michaelmas 2022/2023

Acknowledgements

I started this DPhil in late 2018 and at this point I had no experience or prior knowledge in hypersonics at all. Having studied Physics before, I was also widely unfamiliar with much of the engineering design tasks that I was eventually confronted with. To say that I jumped right into cold water is an understatement. I owe much of the success during my time at the Oxford Thermofluids Institute to the exceptional support and patience of many people!

First and foremost to my supervisor Matthew McGilvray. Your guidance has helped the at the most critical moments of the project and I thank you for all the productive meetings and calls as well as super fast feedback and comments on my written work.

I am also very much indebted to Sebastien Wylie. Your work on boundary layer transition and cones in HDT has paved the way for my research. But much more importantly, your mentoring during my PhD has been incredibly valuable and all the social events you have organized shaped life in the research group well beyond our work.

Thank you to the senior researchers of the group! Particularly to Luke Dohetry, Tobias Hermann, Chris Hambidge and Laurent Le Page. You have all helped me with magnificent practical tips along the way.

During the course of the DPhil I was very lucky to work with excellent technical staff. Foremost David O'Dell, who has done a terrific job machining most of the cone model. The design was exceptionally challenging to machine, and I think we created a very capable test model that will surely serve future generations of hypersonic cone researchers very well. Thank you to Duncan Blake, Leon Blake and Harry Kachika! You have all done an equally amazing job at machining various parts of the cone model and other equipment. Thank you to Andrea Dabija, Liam Boland and Gregory King for your outstanding work on sensors, gauges and cabling and for letting me solder, glue and assemble components in the instrumentation workshop.

Tristan Crumpton, thanks for the energy that you brought into the control room every single day. Without you, I could never have done this many shots! The same is true for Maxime Dahmani Moussa. Thanks for your tireless efforts during my first test campaign. I would also like to thank Kalin Dragnewski for all your help with the Alicona Focus microscope. Thanks to Craig Parsons and Noelia Martin

for repairing my computer several times!
Thank you to my fellow PhD students! Research in hypersonics is a true team effort and I could not have succeeded without you. In particular, thanks to Eric Hembling for helping me assembly the cone model at ungodly hours, re-align schlieren many times, trial a new camera and laser, discuss code and the best aircraft to fly. Thanks to Raghul Ravichandran for all your work on the traverse system and the for the cooperation during the second test campaign. Thanks to: Andy for beating me at squash every now and then, Hassan and Marc for your work on transpiration cooling which proved hugely beneficial to me as well as countless conversations, lunches and events. Thanks to: William Ivison for your help with the calibration oven, Suria for many good conversation about boundary layer experiments, Alex and Joe for being so considerate when you had to regularly interrupt your work on T6 due to my test campaign, Jack Hillyer for all your great efforts with the DAQ system, Nathan Donaldson for your help with Blender. Thanks to all my friends who have made my time in Oxford very special. In particular, Tina Christmann! I am incredibly thankful for all the good vegetarian food and the friendship we built during those four years.
Also thanks to the people form Oxford University Gliding, Oxford Gliding Club and the Bicester Gliding Centre. My time in the UK was unbelievably enriched because I was able to continue my hobby in such an open and welcoming gliding community. Lastly, my DPhil would not have been possible without the support of the Rhodes Trust. I would also like to express my personal thanks to Elizabeth Kiss and Mary Eaton. Your effort for the trust and the scholars is exceptional and your support has meant the world to me at the most critical times.
Lastly, thanks to my parents and my brother. I would not be where I am without you!

"Des is wia bei jeda Wissenschaft, am Schluss stellt sich dann heraus, dass alles ganz anders war."

"It's like with any science, in the end it turns out that everything was entirely different."

— *Karl Valentin, Bavarian Comedian*

Abstract

Superseding ablative cooling techniques with active thermal protection could benefit the development of hypersonic flight technology by improving resistance of vehicles to thermal loads, re-usability and shape stability. Transpiration cooling could ensure protection of areas that are most affected by aerothermodynamic heating by injecting a coolant gas through a porous surface and thus shield the vehicle from hot surrounding gas. Problematically, gas effusion can advance boundary layer transition and resulting turbulence would cause excess heating and sabotage the local upstream cooling effect. In addition, turbulence reduces aerodynamic efficiency and influences critical variables of flight system dynamics. Transpiration cooling can only be applied if sufficient boundary layer transition control is achieved simultaneously or its influence on stability can be predicted accurately.

This thesis investigates the effect of transpiration cooling on hypersonic boundary layer transition experimentally by conducting tests in a low enthalpy hypersonic Ludwieg tube at Mach 7 using a 7° half-angle cone model. Coolant gas injection is performed at two locations on the model. Firstly, fully porous nose tips with 1 mm nose radius and 58.5 mm axial length are used. Secondly, helium, nitrogen, argon and carbon dioxide are injected through a small segment in the frustum, while a sharp impervious nose tip is employed. The porous frustum injector is 25 mm long and spans 60° azimuth in the axial centre of the cone. Outflow profiles of all porous injectors were characterized using a hot wire, whereby three-dimensional maps at high resolution could be obtained. All model parts were optimized for smoothness. This work utilizes high frequency schlieren imaging, focusing laser differential interferometry and surface instruments to conduct instability measurements.

At a unit Reynolds number of $17.9 \cdot 10^6/m$ using a 1 mm porous nose tip helium injection was applied from said permeable nose cone segment. Thin film gauges show a delayed rise of the surface heat flux above laminar level, surface pressure measurements indicate a delay in growth and decay of the second mode instability and schlieren imaging shows a delayed onset of turbulence. Stabilization was stronger with 0.04% helium injection than with 0.02%. Nitrogen injection at a comparable rate was found to advance instability growth and transition. Helium injection at a blowing ratio of 0.1% caused early transition, potentially due to boundary layer blow off at the stagnation point.

Employing a sharp, impervious aluminium nose tip, the cone was tested at a unit Reynolds number of $12.2 \cdot 10^6/m$ with injection from the frustum. At this freestream condition, strongly amplified second mode instabilities are present near the frustum injector segment. It was observed to experience a stronger reduction in second mode frequency with increasing blowing ratio and coolant molecular mass. In contrast, the thickening of the boundary layer increased with decreasing coolant molecular mass. Due to the waveguide nature of the second mode, it was inferred that a change in local speed of sound and boundary layer temperature profile must play a role.

Schlieren images and spectral analysis showed how turbulence and instability mechanisms are displaced from the surface by helium injection. FLDI confirmed how second mode instability oscillations are pushed away from the cone. Reduction in heat flux and attenuation of surface pressure disturbances were thus ascribed to a cooling and displacement effect instead of a true transition delay. Fluid turbulence moves upstream for all coolants as seen with schlieren. Heavier injection gases caused less cooling and less displacement of the boundary layer.

This thesis provides the first experimental demonstration of efficient hypersonic stagnation point cooling combined with a boundary layer transition delay. It furthermore makes experimental contributions to the fundamental understanding of the influence of different gas injections on the transition mechanisms on a hypersonic slender cone.

Contents

List of Figures **xiii**

List of Abbreviations **xix**

1 Introduction **1**
1.1 Motivation and Historical Perspective 1
1.2 Challenges of Hypersonic Flight 2
1.3 Heating, Cooling and a Millennium Problem 3
1.4 Research Aims 8
1.5 Structure of the Thesis 10

2 Background **13**
2.1 Foreword 13
2.2 Hypersonic Boundary Layer Transition 14
2.2.1 Flow Stability 14
2.2.2 Transition Mechanisms in Hypersonic Boundary Layers . . . 15
2.2.3 Ground Testing for Boundary Layer Transition 20
2.2.4 Effect of Nose Bluntness on Transition 22
2.3 Active Cooling at Hypersonic Speeds 23
2.3.1 Transpiration Cooling 23
2.3.2 Application of Porous Materials 27
2.4 Mass Addition and Boundary Layer Stability 30
2.4.1 Destabilization by Injection 30
2.4.2 Injection from Nose Cone Segments 32
2.4.3 Stabilization by Injection 33
2.4.4 Injection and Instability Mechanisms 36
2.5 Outlook 38

3 Experimental Infrastructure **39**
3.1 Cone Model 39
3.1.1 Design and Assembly 39
3.1.2 Surface Instrumentation 43
3.2 Schlieren Imaging 44

3.2.1 Working Principle of Schlieren Techniques 44
3.2.2 Use of z-type Schlieren in Hypersonic Wind Tunnel Testing . 46
3.3 The Oxford High Density Tunnel 48
3.3.1 General Information 48
3.3.2 Ludwieg Tube Mode 49
3.3.3 Calculation of Flow Conditions and Uncertainty Analysis . . 50
3.3.4 Free Stream Characterization of the HDT Mach 7 Nozzle . . 50
3.3.5 Gas Injector System and Operating Procedure 52
3.4 Instability Measurements 54

4 Gas Injection into Second Mode Instability at Mach 7 59
4.1 Foreword 59
4.2 Introduction 60
4.3 Experimental Setup 61
4.3.1 Cone Model and Instrumentation 61
4.3.2 Injector System 62
4.3.3 Oxford High Density Tunnel and Test Conditions 66
4.4 Influence of Injection on Second Mode Frequencies 67
4.4.1 Data Analysis Procedure 67
4.4.2 Experimental Results 70
4.4.3 Helium Injection 73
4.4.4 Frequency Drop and Flow Characteristics 75
4.5 Schlieren Measurements - Boundary Layer Thickness 77
4.6 Discussion 81
4.7 Conclusion 85

5 Hypersonic Boundary Layer Stabilization by Helium Injection 89
5.1 Foreword 90
5.2 Introduction 90
5.2.1 Hypersonic Boundary Layer Transition 90
5.2.2 Transition and Injection 91
5.3 Test Model and Environment 93
5.4 Instability Measurements 94
5.5 Heat Flux and Transition 96
5.6 High Speed Schlieren Measurements 98
5.7 Discussion 99
5.8 Conclusion 101
5.9 Methods 102
5.9.1 Oxford High Density Tunnel 102
5.9.2 Coolant Injection 103

5.9.3 PCB Piezoelectric Sensors . . . 104
5.9.4 Kulite Piezoresistive Sensors . . . 104
5.9.5 Thin Film Gauges . . . 104
5.9.6 Z-type Schlieren . . . 106
5.9.7 Uncertainty Analysis . . . 108
5.10 Extended Data . . . 109
5.10.1 Experiment at low Reynolds Number . . . 109
5.10.2 Experiments with different Injector Material . . . 109
5.10.3 Nosetip Outflow Profiles . . . 110
5.10.4 Continuous Wavelet Transforms . . . 112
5.10.5 Average Schlieren Image . . . 112

6 Decoupling Boundary Layer Transition and Heat Flux Reduction for Hypersonic Transpiration Cooling 119
6.1 Foreword . . . 120
6.2 Introduction . . . 120
6.3 Experimental Setup . . . 123
6.3.1 Test Model with Gas Injection . . . 123
6.3.2 Surface Instrumentation . . . 126
6.3.3 Z-type Schlieren . . . 126
6.3.4 Focused Laser Differential Interferometry (FLDI) . . . 127
6.3.5 Flow Conditions . . . 132
6.4 Experimental Results . . . 133
6.4.1 Surface Heat Flux . . . 133
6.4.2 Surface Pressure Fluctuations . . . 133
6.4.3 Schlieren Images . . . 136
6.4.4 Schlieren Power Spectra . . . 137
6.4.5 Frequency Shift within Boundary Layer . . . 141
6.4.6 Second Mode Power Distribution across the Boundary Layer Thickness . . . 141
6.4.7 Experimental Definition of Transition . . . 147
6.5 Discussion . . . 152
6.6 Conclusions . . . 153

7 Summary and Conclusion 157
7.1 Summary of Presented Work . . . 157
7.2 Conclusion . . . 158
7.3 Recommendations for Future Work . . . 161

References 163

Appendices

A Appendix **189**
A.1 Technical Drawings for Cone Model 190
A.2 Surface Quality of Cone Model 220

List of Figures

1.1 Free flight temperature data from the relatively slender NASA X-43 vehicle [29]. 5
1.2 Summary of cooling methods by Kelly and Blosser. Taken from [45]. 7

2.1 Overview of physical mechanisms leading to transition of a boundary layer. Figure taken from Fedorov et al. [83] and Saric [69] who both adapted it from Morkovin [94]. 17
2.2 Schematic of the second mode instability as a trapped acoustic waveguide mode. Figure taken from [83], permission obtained via Copyright Clearance Center. 18
2.3 Mach number dependency of temporal amplification rate of different modes, replotted from [90]. The modes 1 and 2 are commonly referred to as the first and second mode, whereas the latter may also be called the (second) Mack mode. 19
2.4 Tranpiration cooling in a laminar boundary layer. 1: Unhindered heat flux to the surface due to friction and radiation. 2: Convective cooling of porous material and substructure. 3: Coolant film protects surface. Inspiration for the figure loosely from Ifti etl al. [51] and Langener [71]. 25

3.1 Exploded view of cone model. Part descriptions are given in Table 3.1. Part 6 and 7 can be replace through 6b. 41
3.2 Coordinate system of the cone model. The x = 0 plane always refers to the apex of the nose tip in use. Correspondingly, the injector starts at x = 300 mm (sharp) or x = 293 mm ($R_N = 1\,\mathrm{mm}$) and ends 25 mm further downstream. 42
3.3 Cone model on sting mount in the tunnel test section. Nose is a porous CE170 $R_N = 1\,\mathrm{mm}$ tip. The cone is rotated with the frustum injector side towards the test section window in the photo. 43
3.4 Alignment of 7° cone model using second mode instability. The shaded region was computed by considering the maxima and minima in every sensor spectrum recorded in the time ($\sim 100\,\mathrm{ms}$) before the model is surrounded by tunnel flow. 45

3.5 Pitot-probe spectral analysis of HDT Mach 7 condition at $Re_u = 12.1 \cdot 10^6/m$. Figure taken from [68]. The shaded-gray area outlines conventional facilities such as the Hypersonic Ludwieg Tube Braunschweig (Mach 6) [247], the BAM6QT (Mach 6) [253], the Sandia Mach 8 hypersonic wind tunnel (see e.g. [102]) and the AEDC Hypervelocity tunnel 9 ([254] as cited in [255]) and was re-plotted by Wylie from Duan [120]. r refers to the radial coordinate from the nozzle centre-line of the respective probe. 51
3.6 Schematic of mass flow controller setup with coolant gas supply. Firing valve and filling valve are remotely controlled solenoid valves. 53
3.7 Snippets of surface differential pressure signals for a sharp cone without coolant injection at $M = 7$ and $Re_u = 12.8 \cdot 10^6/m$. 56
3.8 Z-type schlieren images of second mode wave packets on a sharp 7° half-angle cone at $M = 7$ and $Re_u = 12.8 \cdot 10^6/m$. 57

4.1 Geometry of the cone model. Green: PCB, Blue: Kulites. The given coordinate system (x, y, z, φ) will be used in all further representations. 62
4.2 Hot-wire outflow measurement at atmospheric pressure. 65
4.3 PSD of two conditions used during the testing. 67
4.4 Exemplary fits to PSD data. The injector spans from $x = 300\,\text{mm}$ to $x = 325\,\text{mm}$. The signal in row three of the Figure was not deemed sufficient to perform a fit and use it for further analysis. Accordingly, the respective point in Figure 4.6 (red crosses for $F(\text{CO}_2) = 0.66\%$) is missing. 69
4.5 Condition 1 and 2 second mode development without injection. . . 71
4.6 Condition 1 second mode properties for various gases and blowing ratios. 72
4.7 Condition 2 second mode properties for various gases and blowing ratios. 72
4.8 PSDs for helium injection at condition 1. 74
4.9 Comparison of relative frequency drop for several conditions, gases and blowing ratios. 76
4.10 Comparison of relative frequency drop for supplementary conditions. 77
4.11 Schlieren analysis procedure for an exemplary image. 79
4.12 Boundary layer edge thickness for carbon dioxide injection, Condition 2. 80
4.13 Boundary layer edge thickness for carbon dioxide injection, Condition 1. 81
4.14 Averaged schlieren images corresponding to Figure 4.12. Location of the injector is indicated with dashed lines. 82

4.15 Averaged schlieren images corresponding to Figure 4.13. Location of the injector is indicated with dashed lines. 83
4.16 Model for the coolant wall concentration above and downstream of a porous injector. Adapted from [49, 285] with permission. 85

5.1 Seven-degree cone model with measurement infrastructure. Coloured dots represent the surface instrumentation and the rectangular schlieren field of view is indicated in the bottom side view. Gas injection only happens at the nose tip and the coolant is delivered via a pipe in the centre of the cone. 95
5.2 Results from surface instrumentation. On the left-hand column, individual power spectral estimates are shown for several differential pressure sensors along the $\varphi = 0°$ plane on the model. The top right corner shows the integrated bandpower belonging to said power spectra. The bottom right plot indicates the heat flux measured by thin film gauges along the $\varphi = 15°$ plane on the cone. The discrete points are compared to Eckert correlations [267]. Colours represent different injection rates and gases and are kept consistent across all plots. Error bars indicate 68% confidence intervals. 97
5.3 z-type Schlieren images for natural transition and gas injection. $\bar{y}$ is the model wall-normal direction. Schlieren signal intensity is represented by a colormap. Tunnel freestream flows from left to right. All images are taken at the same time relative to the start of the flow with accuracy $\pm 1\,\mu$s. An average of 1000 schlieren images has been subtracted from the shown frames. This leaves only temporal fluctuations, such as instabilities and turbulence. The purely laminar boundary layer for the helium injection case is hence nearly invisible. 99
5.4 Oxford University High Density Tunnel schematic. 103
5.5 z-type schlieren system at HDT test section. 108
5.6 Results from surface instrumentation for lower unit Reynolds number. On the left-hand column, individual power spectral estimates are shown for several differential pressure sensors. The top right corner shows the integrated bandpower belonging to the power spectra. The bottom right plot indicates the heat flux measured by thin film gauges along the cone. The discrete points are compared to Eckert correlation [267]. Colours represent different injection rates and gases and are kept consistent across all plots within the figure. Error bars indicated 68% confidence intervals. 110
5.7 Results for surface instrumentation. The nose tip in use was made from BF100Al. All error bars indicated 68% confidence intervals. . . 111

5.8 2D projection of Outflow profile, BF100Al nose tip. The uncertainty color map represents 68% confidence intervals. 113
5.9 Continuous Wavelet Transform for natural transition case. All individual plots are shown with the same color scale. The CWT relate to the experimental cases shown in Figure 5.2 113
5.10 Continuous Wavelet Transform for low helium injection case. All individual plots are shown with the same color scale. The CWT relate to the experimental cases shown in Figure 5.2 114
5.11 Continuous Wavelet Transform for moderate helium injection case. All individual plots are shown with the same color scale. The CWT relate to the experimental cases shown in Figure 5.2 114
5.12 Continuous Wavelet Transform for moderate nitrogen injection case. All individual plots are shown with the same color scale. The CWT relate to the experimental cases shown in Figure 5.2 115
5.13 Continuous Wavelet Transform for high helium injection case. All individual plots are shown with the same color scale. The CWT relate to the experimental cases shown in Figure 5.2 115
5.14 Average of 1000 schlieren frames around point of interest. Those images were subtracted from the single frames shown in Figure 5.3. 116

6.1 Test model geometry. Blue points represent absolute pressure gauges, red are thin film gauges and green PCB high frequency pressure transducers. The porous injector patch is marked in yellow, which spans a 60° azimuth. $\bar{y}$ is the wall normal coordinate. 124
6.2 Injector effusion map. 125
6.3 FLDI setup. The components can be found in Table 6.1. 129
6.4 a) Depth of field of the FLDI setup. z is the coordinate parallel to the beam centred at the focal point of the system. Measured data for a single frequency near the expected instability is compared to the fitted transfer function and the extrapolated transfer function at the expected second mode frequency. Error bars indicate the diameter of the sound transceiver. b) Replots Fig. 4 from Ceruzzi and Cadou [320] and shows the full transfer function of the FLDI. $d_b = 2r_b$ is the beam diameter. 132
6.5 Results from surface instrumentation. (left) High frequency pressure. Only the cumulative bandpower is shown in the figure. Second mode frequency peaks lie in the 280 kHz region and hence the first and second harmonic are included in the integrated power. (right) Heat flux distribution across the cone. Colours represent gases and injection ratios and are kept coherent across figures. 134

6.6 All power spectra used to calculate the bandpower shown in Figure 6.5. Color convention is the same as in Figure 6.5. 135
6.7 Single schlieren frames of shots with and without injection. The injector is marked in the images. Images are not to scale in width and height. 138
6.8 Power spectra maps of schlieren images. The PSD is calculated for every pixel along the shown paths. Power is represented in the colorscale. Both power spectra along the paths are calculated with the same procedure across the same images. The schlieren images correspond to the case $F = 0.06\%$ in Figure 6.7. 140
6.9 Power spectra maps of schlieren images. PSDs are calculated for each pixel along a path with the given distance from the detected cone edge. The error bars given for the central frequency of the second mode as measured by PCB at the surface represent the full width at half maximum of the fitted gaussian distribution. The injector location is marked as a white dashed in the colour maps. 142
6.10 Wall-normal power spectra through boundary layer thickness without injection. The power spectra are plotted for four locations along the transition process. Because the schlieren system was not always aligned to the exact same position, $\bar{y}$ ranges change across the test cases. The same PSD calculations as for Figure 6.8 and 6.9 were used to generate the plots. The number of data points in $\bar{y}$-direction is limited by the schlieren optics and camera sensor. A resolution of approximately 6 pixels per mm. 143
6.11 Wall-normal power spectra through boundary layer thickness with nitrogen injection. The power spectra are plotted for four locations along the transition process. Because the schlieren system was not always aligned to the exact same position, $\bar{y}$ ranges change across the test cases. The same PSD calculations as for Figure 6.8 and 6.9 were used to generate the plots. The number of data points in $\bar{y}$-direction is limited by the schlieren optics and camera sensor. A resolution of approximately 6 pixels per mm. 144
6.12 Wall-normal power spectra through boundary layer thickness with helium injection. The power spectra are plotted for four locations along the transition process. Because the schlieren system was not always aligned to the exact same position, $\bar{y}$ ranges change across the test cases. The same PSD calculations as for Figure 6.8 and 6.9 were used to generate the plots. The number of data points in $\bar{y}$-direction is limited by the schlieren optics and camera sensor. A resolution of approximately 6 pixels per mm. 145

6.13 Wall-normal power spectra through boundary layer thickness with helium injection. The power spectra are plotted for four locations along the transition process. Because the schlieren system was not always aligned to the exact same position, $\bar{y}$ ranges change across the test cases. The same PSD calculations as for Figure 6.8 and 6.9 were used to generate the plots. The number of data points in $\bar{y}$-direction is limited by the schlieren optics and camera sensor. A resolution of approximately 6 pixels per mm. 146
6.14 Both locations above the injector, where FLDI was applied are marked in a schlieren image. The errorbars do not indicate the size of the FLDI laser point but rather the goodness of reproducible realignment. 147
6.15 Summary of different transition location metrology for a case without injection. 149
6.16 Comparison of transition locations. Figure plotted similar to [187, 190] with correlation from Marvin and Akin [187] included. In those calculations we followed Marvin and Akin [187] and used F in percent. 151

A.1 Cone model with porous nose tip $R_N = 5\,\text{mm}$ configuration. The examined locations for surface roughness are indicated. 220

List of Abbreviations

Variables

A	Amplitude of oscillation
a	Local speed of sound
b	Boundary layer height
B_h	Blowing parameter
c	Disturbance phase speed
C_p	Specific heat capacity under isobaric conditions
d	Distance or Diameter
F	Blowing ratio
f	Frequency
h	Enthalpy
i	Imaginary unit
k	Gladstone-Dale Coefficient
K_D	Darcy coefficient
K_F	Forchheimer coefficient
M	Mach Number
m	Molecular mass
$\dot{m}$	Mass flow
N	N-factor
n	Refractive Index
Pr	Prandtl number
px	Pixel
R	Gas constant
R_N	Nose radius
r	Recovery factor

Re	Reynolds number
s	Injector length
St	Stanton number
T	Temperature
t	Time
U	Free stream velocity
v	Velocity
x, y, z	Spatial coordinates
$\widetilde{x}$, $\widetilde{y}$	Arbitrary image coordinates
Δb	Change in boundary layer height
ϵ	Emissivity
γ	Ratio of specific heats
φ	Azimuth angle on cone surface
λ	Wavelength
μ	Kinematic viscosity
σ	Standard Deviation
τ	Proportionality constant
ω	Angular frequency

Subscripts

$_{tr}$	Transition property
$_{\infty}$	Free stream property
$_{b}$	Laser beam
$_{c}$	Injection gas properties
$_{CO}$	Circular orbit
$_{e}$	Boundary layer edge properties
$_{ent}$	Entrainment properties
$_{i}$	imaginary
$_{0}$	Uncooled properties
$_{N}$	Nose tip
$_{p}$	Pressure/Isobaric

$_r$ . . . . . real, recovery

$_{SL}$ . . . . . Sea Level

$_u$ . . . . . (per) unit

$_w$ . . . . . Model wall properties

Abbreviations

AIAA . . . . . American Institute of Aeronautics and Astronautics

ABS . . . . . Acrylonitrile Butadiene Styrene

AEDC . . . . . Arnold Engineering Development Centre

AKTiV . . . . Aktive Kühlung im Versuch (DLR transpiration cooling flight experiment)

ALTP . . . . . Atomic Layer Thermopile

AoA . . . . . Angle of Attack

AoY . . . . . Angle of Yaw

CAV . . . . . Cruise and Acceleration Vehicle

CUBRC . . . . Calspan-University of Buffalo Research Center

CFD . . . . . Computational Fluid Dynamics

CMC . . . . . Ceramic Matrix Composite

C/C . . . . . Carbon/Carbon

DLR . . . . . Deutsches Zentrum für Luft- und Raumfahrt (German Aerospace Center)

FLDI . . . . . Focused Laser Differential Interferometer

HDT . . . . . (Oxford) High Density Tunnel

LaRC . . . . . (NASA) Langley Research Centre

LED . . . . . Light-Emitting Diode

FWHM . . . Full width at half maximum of a peak

MFC . . . . . Mass Flow Controller

NASA . . . . . National Aeronautics and Space Administration

NI . . . . . National Instruments

PEEK . . . . . Polyether Ether Ketone

PSD . . . . . Power spectral density

RV . . . . . Re-Entry Vehicle

RV-W . . . . . Winged Re-Entry Vehicle

TFG . . . . . Thin Film Gauge

TRL . . . . . Technology Readiness Level

UHTC . . . . . Ultra High Temperature Ceramics

VKI . . . . . Von-Karman Institute

1 Introduction

Contents

1.1 Motivation and Historical Perspective 1
1.2 Challenges of Hypersonic Flight 2
1.3 Heating, Cooling and a Millennium Problem 3
1.4 Research Aims 8
1.5 Structure of the Thesis 10

1.1 Motivation and Historical Perspective

More than 200 years of aerospace development lie behind us [1] and it is safe to say that humanity has developed outstanding flying machines. And in return, those machines contributed to humanity's development. Nowadays, gliders, powered planes, jets, rockets, satellites and drones populate earth's atmosphere and the space beyond, shaping our lives in various ways. Technology has been developed to overcome bad weather, to fly slow, fast, low and high, transport things and humans, fight wars, dust crops, research earth, space and bring joy to recreational pilots. Human perception of distance has changed as a result, oceans that took weeks to sail through can now be crossed within hours, whilst mountains and deserts can be overflown.

Although becoming more common and routine - 1809 objects were launched into orbit in 2021 alone [2] - access to space remains complicated and costly, putting a firm limit to human ingenuity and exploration spirit. What if there was a plane that could take off from a runway, cross the entire atmosphere and range of flying speeds and bring satellites or people into orbit [3]? Afterwards it will return to its point of departure and be ready for another flight after re-fuelling.
Groundbreaking pioneering work in this field of aeronautical design dates back to the 1930s [4], when Eugen Sänger presented his Silbervogel (silverbird) idea, a spaceplane that should be capable of reaching orbits cost effectively [3, 5]. Within his works, Sänger already outlined thoughts about heat loads, a boost glide phase and characteristics of different speed regimes. Not long after, the first theoretical and experimental work in this speed regime was carried out. Incipient high speed flow research, supersonic and hypersonic, was initially conducted by Ludwig Prandtl and in multiple institutes and facilities in Göttingen, Aachen, Pennemünde and Kochel, paving the way for the very first steps of developing such a spaceplane [4, 6–8]. Only a few decades later the X-15 finally reached true hypersonic speeds [4, 9] on multiple test flights without going into orbit and without disintegrating. A proper spaceplane, as conceived by Sänger and then elaborated by the National Aerospace Plane (NASP) project until its cancellation [10], has however never flown. At least, not yet!

1.2 Challenges of Hypersonic Flight

Some exposed parts of the X-15 vehicle were simply melted when it reached Mach 6.7 in 1967 [11–13] delivering an impressive demonstration of how unforgiving this environment is. Despite leaving the hypersonic speed regime as quickly as possible, re-entry vehicles such as the Space Shuttle [14] or the Apollo capsule [15, 16] had to be fitted with heat shields and protect themselves via ablation. Maintaining longer duration controlled flight at such speeds is posing unprecedented challenges to aerospace technology. Due to the importance of hypersonic flow regime understanding for atmospheric glide-entry vehicles [17, 18], transport planes [19] and missiles [20] great research effort has been spent at detecting “unknown unknowns”

[11, 13] and solving technical challenges, which has evidently revealed itself to be an arduous task and path.

Depending on the mission type, vehicles can have a wide variety of shapes and fly substantially different trajectories [18, 19]. A cruise and acceleration vehicle (CAV) may have a significantly dissimilar shape and flight path than a blunt winged re-entry vehicle (RV-W) and thus be exposed to a divergent spectrum of flow phenomena [18, 21, 22]. In addition, each vehicle may encounter a large range of speeds, angles of attack and atmospheric densities. The common characteristic is however the high Mach number [18, 23]. Satellites in low earth orbit fly high enough to avoid earths atmosphere, and commercial airliners or fighter jets are slow enough to avoid excessive heating. For both of those cases a manifold of successful missions and high Technology Readiness Level (TRL) solutions have existed for a long time. In hypersonics, one however tries to combine the worst of those two worlds. Passing through earth's (or other planet's) atmospheres at extremely high speeds yet at low enough altitudes and high enough Knudsen numbers so that surrounding gases are of concern. In 1970, when many of the "unknown unknowns" [11, 13] were yet to be discovered, it has already been called "the ultimate achievement of aeronautics" [24].

Aerospace engineers designing vehicles for this regime are yet to answer questions about thermochemical effects, propulsion systems and their integration, plasma effects and most importantly heat loads and thermal management [18, 23].

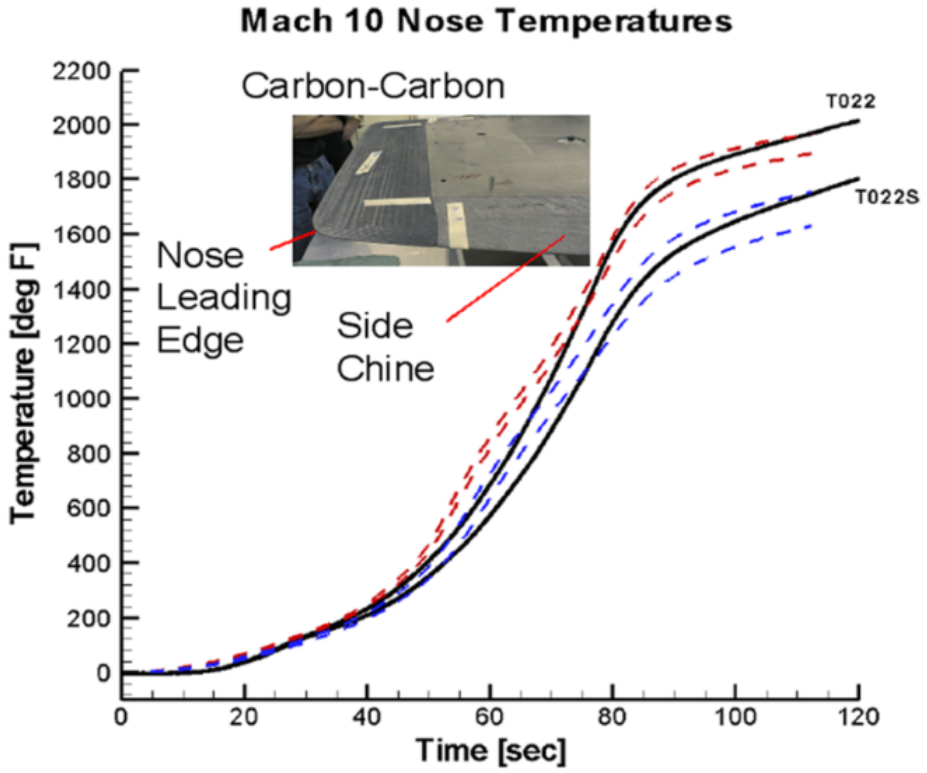
1.3 Heating, Cooling and a Millennium Problem

Solutions have been trialled in the past for mitigating the mentioned heat fluxes. Ablation has been used [25], albeit it limits the re-usability of any vehicle [24], its payload, speed and most importantly shape [11, 26, 27]. Sharp leading edges will be an integral part of future hypersonic design as they enable a broad spectrum of mission types well beyond RVs [28].Those small curvature radii shall self-evidently remain constant throughout the trajectory, requiring them to withstand and repel harsh environmental forces.

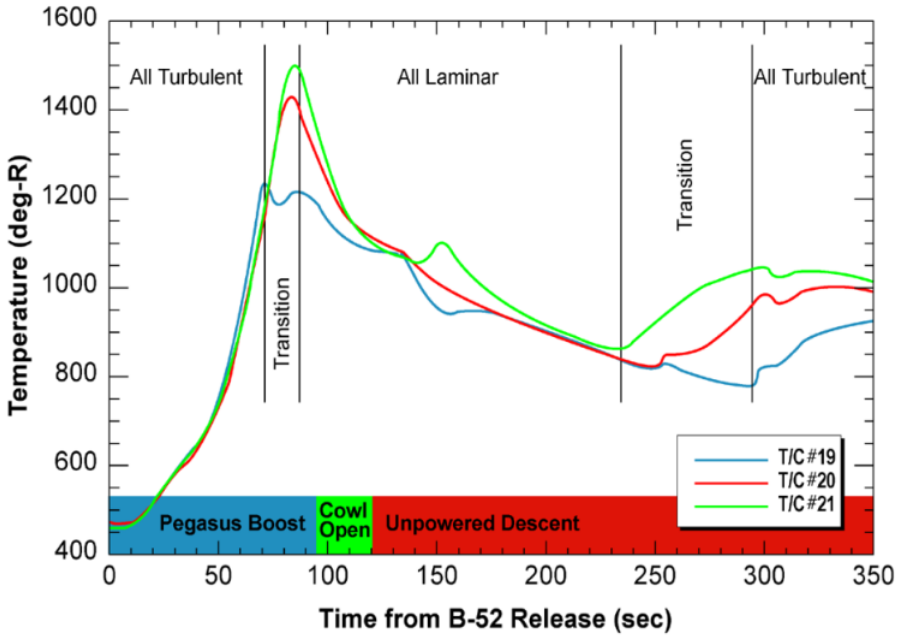
An example for the heat loads encountered at those locations is given in Figure 1.1. In only 120 s, the C/C leading edge of the slender NASA X-43 vehicle heated up to more than 1100°C during the boost phase and subsequent unpowered flight at speeds of around Mach 10 [29]. For this test, the leading edge had a radius of 1.27 mm [30]. Leonard et al. [30] also state how this was larger than for the previous Mach 7 flight and several material choices had to be adapted when increasing the Mach number to 10. A relation of density, flight velocity and spherical leading edge radius for the heat flux to those exposed locations is given in Equation 1.1 [18, 32] and similar estimations or correlations were developed by Sutton and Graves [33] as well as Fay and Riddell [34]. $\dot{q}$ is the heat flux, R_N the nose radius, ρ the density and U the velocity. Following Bertin [18], the subscript SL stands for sea level and CO is the circular orbit.

$$\dot{q} = \frac{11,030}{(R_N)^{0.5}} \left(\frac{\rho_\infty}{\rho_{SL}}\right)^{0.5} \left(\frac{U_\infty}{U_{CO}}\right)^{3.15} \tag{1.1}$$

Using said formula, Reimer et al. [32] calculated how the surface heat flux can exceed $10\,\mathrm{MW/m^2}$ with realistic flight velocities U_∞, if curvature radii below 100 mm are considered. Kasen [35] obtains very similar results with a slightly different formula and scenario. Extending those examples, the stagnation point surface temperature shall be estimated for some notional trajectory cases: Simplifying the physics of heat transfer such that the convective heat flux is only in equilibrium with re-radiation, namely a radiation-adiabatic wall condition [23], is certainly incomplete but nevertheless deemed sufficient for a simple introductory example [36], taking $U = 2\,\mathrm{km/s}$, $\rho = 3.85\,\mathrm{g/m^3}$ (at 40 km altitude), $\epsilon = 0.9$ and a spherical nose radius of 10 mm, the temperature would establish at around 2030 K. Considering the X-43 vehicle, all those estimates were rather conservative, particularly the speed, only equating to around Mach 4.3 in the example and, similarly, the nose radius selected nearly an order of magnitude larger. Doubling the velocity to $4\,\mathrm{km/s}$ raises the temperature to roughly 3400 K. Even if, and the exemplary values were particularly selected for this purpose, the calculation is a dramatic overestimate, then low estimates for trajectory parameters likely compensate. The X-43 flew



(a) C/C leading edge temperature of the X-43 flight test Mach 10. Taken from [31] Fig. 14 with permission from AIAA. Those plots are also found in [29, 30]. The maximum measured temperatures equate to around 980°C and 1120°C. Temperature measurements were taken 25.4 mm and 31.1 mm downstream of the edge, respectively.



(b) Thermocouple data from X-43 top surface, flight test two. Taken from [31] Fig. 13 with permission from AIAA. Those plots are also found in [29]. The maximum measured temperature of thermocouple 21 equates to roughly 560°C

Figure 1.1: Free flight temperature data from the relatively slender NASA X-43 vehicle [29].

faster than Mach 6 or Mach 9, depending on which flight test, at altitudes around 30 km [29, 37, 38] and the temperature traces in Figure 1.1 show no sign of reaching an inflection point, despite the measurement location significantly downstream of the edge. Nonetheless, far more extreme examples exist. Johnson et al. [39] report a flight test of a 5° half-angle cone-shaped object, principally carried out to study transition and boundary layer properties, which had a nose radius of 2.54 mm and flew at Mach 20 descending from about 36 km.

Kasen [35] makes similar temperature estimates and infers that such geometries and their resulting heat loads generally go beyond capabilities of available materials. Herein, it is added that should long-duration flight or re-usability be required, also general passive thermal protection is insufficient [32, 36, 40]. Current material developments for ablative leading edges are aiming to achieve resistance up to $2000 - 2400°C$ [35, 41] and C/C materials have been praised for their "extremely high temperature limit" [42], while Haidn et al. [43] work with a threshold of only 2500 K for said ceramic. Moreover, sustained hypersonic flight may mean that temperatures of the underlying vehicle structure partly equilibrate with the stagnation gas. Capabilities of usual aerospace structural materials would be exceeded by far [35]. Without significant advances in cooling concepts, hypersonic vehicles cannot evolve past certain flight trajectories and geometries. Considering work by Modlin [44], one has to add that even 'internal' active cooling techniques are deficient to protect leading edges. It is not only desirable but plainly requisite to experimentally explore cooling techniques that hinder heat from penetrating the vehicle surface in the first place.

Kelly and Blosser [45] divide heat mitigation strategies into three different categories as shown in Figure 1.2. It has already been found in the 1950s that transpiration cooling is the most promising in terms of reducing heat flux efficiently [46]. Active cooling is defined as employing independent infrastructure within the vehicle that applies a specific coolant to mitigate heating of critically endangered vehicle parts [45, 47]. Especially sharp leading edge components as described above are candidates for its application (see e.g. [45] Fig. 27). To achieve cooling, a gas or liquid [48] is

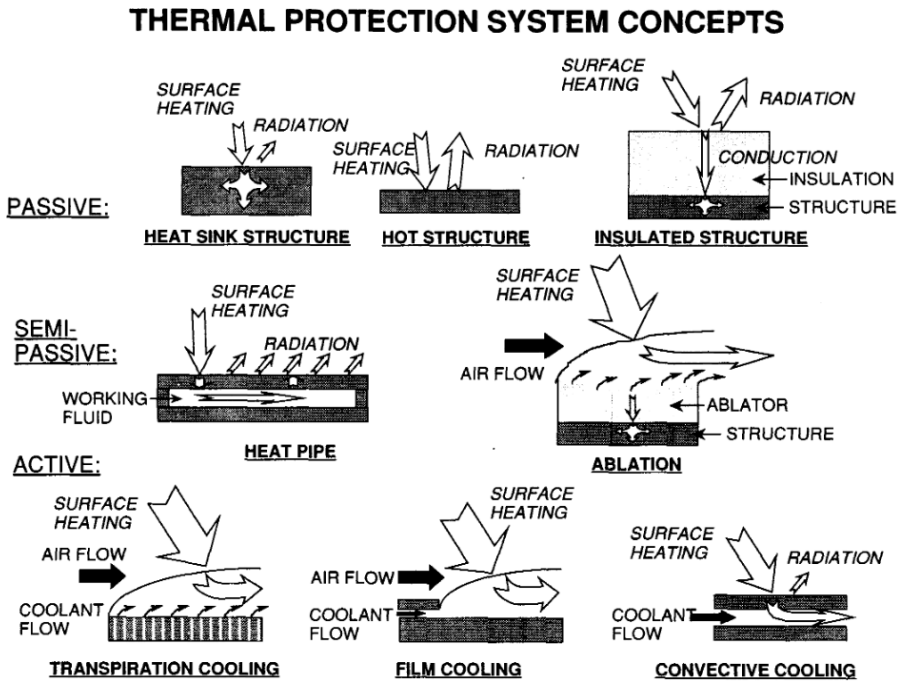


Figure 1.2: Summary of cooling methods by Kelly and Blosser. Taken from [45].

transpired through a permeable segment in the vehicle surface. Inert or combusting gases [36, 45], water [48] and even electrons [40] have been scrutinized as coolants. Transpiration cooling has been found to be effective at reducing heat transfer to the surface [36, 49–51] and the stagnation point [52–54] as well as preventing material oxidation [53, 55]. One of the major remaining questions for this technique is its unfortunate entanglement with laminar-turbulent transition [56].

The state of the boundary layer, whether it is laminar or turbulent is a vital parameter for vehicle design [57–59]. Drag, skin friction and heat transfer, control surface effectiveness and many other parameters depend on the stability of the boundary layer [57, 60–64]. Predicting and understanding turbulent fluid behaviour is in its broadest sense currently set out as a millennium problem by the Clay Mathematics Institute in the form of proving the “existence and smoothness of Navier-Stokes solutions” [65]. Hence, only simulation and experiments can provide estimates about transition for real flight conditions for now. Considerations by Whitehead for NASP [66] yield how turbulence can halve the attainable payload on a mission, highlighting how devastating its early onset is for a flight vehicle

[59]. A further example is the temperature increase found in Figure 1.1. Heating loads throughout transitioning and turbulent periods for the X-43 flight test two are substantially higher than during laminar conditions. The major setback for active cooling technologies is the boundary layers' sensitivity to the smallest disturbances [56, 57].

Coolant injection is such a disturbance and can cause earlier transition onset [56]. While providing efficient cooling in the near vicinity of the transpiration location, overall net heat flux to the vehicle could still increase further downstream [47]. Application of such cooling will thus only be possible if its effect on laminar-turbulent transition is researched, understood and then minimized or possibly eliminated. McClinton [31] summarizes the TRL of necessary components of future hypersonic flight vehicles. It is evident how actively cooled components, whether surface elements or propulsion infrastructure, are consistently ranked lowest on the TRL scale [31]. Regarding the potential of active cooling techniques and the urgent prerequisite to address the hypersonic heating problem, this work shall aim to make a step forward in the research of transpiration cooling and its effect on hypersonic boundary layer transition.

1.4 Research Aims

This research work contributes to the fundamental understanding of foreign gas injection on hypersonic boundary layer transition. Wind tunnel tests were conducted on a 7° half-angle cone in a low enthalpy hypersonic facility. Experiments and subsequent analysis were directed at the following overarching research questions:

1. **Does light gas injection always decrease the transition Reynolds number on a hypersonic cone?**

   Transpiration cooling with a light gas, which may be the most effective way of achieving heat mitigation on a vehicle surface, is usually found to have a devastating impact on boundary layer stability. To research whether those effects - light gas cooling and transition advance - are unavoidably

interconnected, helium injection into hypersonic flow is thoroughly studied. Experiments are carried out with different injection locations, flow rates and porous materials. Direct comparisons with nitrogen as a coolant shall highlight the role of the chemical properties of helium with respect to boundary layer stability mechanisms.

2. **How does the second mode instability respond to gas injection of different coolants?**

   Understanding transition-driving mechanisms has shifted into the spotlight of hypersonic boundary layer research. For gas injection, provided that the second mode is the dominant instability, an insight into the interaction of coolant gas and oscillation parameters may increase fundamental understanding of (de)stabilizing effects. At different stages of the growth and decay process, this thesis aims to precisely measure any influence of coolant effusion on second mode waves, employing non-intrusive techniques and surface instruments. To enable future engineering predictions, it attempts to correlate coolant gas properties, injection and flow parameters with affected second mode attributes.

3. **Does gas injection at different locations of a model and different stages of the instability growth process cause the same physical effect on transition?**

   Active cooling could be applied anywhere on a flight vehicle. Given this flexibility of choice for innovative designs, research shall deliver recommendations about the most advantageous (or least disadvantageous) locations for transpiration cooling. With respect to transition, this would likely mean balancing effective cooling with a minimization of disruptions to any flight system dynamics. Consequently, it must be understood whether injection from different locations, for example the leading edge in contrast to the body of a vehicle, subjects the boundary layer to the same alterations. The used test body is fitted with two independent injector systems, namely one at the nosetip and one at the frustum, and thus provides the unique ability to study

injection at the stagnation point and downstream, while ensuring constancy of other variables. Gas injection into developed second modes can be compared to gas effusion into a forming boundary layer on a slender geometry.

4. **Can transition be unequivocally identified in an experiment with coolant gas injection?**
   Considering surface heat flux, the contrastive nature of transition and transpiration cooling may corrupt surface measurements or make them susceptible to misinterpretation. Dominance of effective heat mitigation could suppress turbulent heating and make a recognition of turbulence based on heat flux data ambiguous. By carefully comparing different measurement techniques, assessing their capabilities and shortcomings as well as demarcating various experimental definitions of transition onset, this work aims to provide unambiguous conclusions about heat flux reduction and boundary layer transition. Statements about the state of the boundary layer are aimed to be made independently from findings about cooling efficiency.

1.5 Structure of the Thesis

The thesis presented does not follow those four research questions in a linear way, and is more practically structured around the separate experimental cases which avoids repetition of results and analysis steps. Some of the aforementioned aims, which were intentionally written in a more abstract way, are hence addressed and covered at multiple points in the document, respectively.

Chapter 2: Despite the high cost and effort of experiments in this research field, similar aims have been studied extensively. After summarizing the main theoretical background about transpiration cooling and boundary layer transition, the literature is reviewed in detail. Experimentalists have been concerned with researching stability and injection since the 1950s. Nonetheless, the often mentioned near infinite complexity of transition phenomena leaves fundamental gaps and great uncertainties in the field. Limitless possibilities

of flight geometries and flow conditions make comparability arduous, and many phenomena have only been investigated for a short time due to recent developments in indispensable experimental methods. Successively, the review approaches contemporary findings and outlines the need for more investigation into hypersonic transpiration cooling, to answer the research aims outlined in Section 1.4.

Chapter 3: The experimental infrastructure and data acquisition is described. Test model, sensors, optical methods and the wind tunnel with its coolant injection procedure are briefly outlined. Each application of those methods is then specified in the results chapters.

Chapter 4: This chapter is mainly dedicated to researching second mode frequency behaviour under the influence of foreign gas transpiration. The model configuration entails a sharp, impervious nosetip, while gas is injected into developed instabilities in the axial middle section of the cone. Mainly surface pressure measurements are used to analyse power spectra of second mode oscillations and infer correlations with gas properties.

Chapter 5: This chapter revolves around injection in the stagnation point segment of the cone. Herein, helium and nitrogen are injected into the boundary layer far upstream of the natural onset of transition. Independent analysis of surface heat flux, pressure and schlieren images - all techniques sampled at sufficiently high frequencies - shows a congruent transition delay for helium injection. Addressing aspects 1 and 3 from Section 1.4 a discussion is added and, due to the seemingly unsuspected findings, attention is paid to duly contextualise work and past literature.

Chapter 6: A comparison is made between different measurement techniques for downstream gas injection and its influence of boundary layer stability. The simultaneous effect of cooling and boundary layer transition is discussed with respect to surface instrumentation and non-intrusive optical techniques.

With helium injection, particular emphasis is paid to point 4 in Section 1.4. Differentiations in between cooling and transition effects are achieved by comparing different measurement techniques, which lead to a recommendation for future applications of metrology in the field.

Chapter 7: Lastly, the combined results are discussed, summarized and a conclusion is reached. The author gives his personal views how the presented results could be used and what questions could be targeted in the future ranging from theoretical to free flight experiments.

Appendix: Technical drawings of the cone model and further machined parts are provided.

2 Background

Contents

2.1 Foreword 13
2.2 Hypersonic Boundary Layer Transition 14
2.2.1 Flow Stability 14
2.2.2 Transition Mechanisms in Hypersonic Boundary Layers 15
2.2.3 Ground Testing for Boundary Layer Transition 20
2.2.4 Effect of Nose Bluntness on Transition 22
2.3 Active Cooling at Hypersonic Speeds 23
2.3.1 Transpiration Cooling 23
2.3.2 Application of Porous Materials 27
2.4 Mass Addition and Boundary Layer Stability 30
2.4.1 Destabilization by Injection 30
2.4.2 Injection from Nose Cone Segments 32
2.4.3 Stabilization by Injection 33
2.4.4 Injection and Instability Mechanisms 36
2.5 Outlook 38

2.1 Foreword

Much of the presented work is interdisciplinary and combines different aspects of previously researched fields. Boundary layer transition in high speed wind tunnels is paired with coolant gas injection through a porous medium and small nose bluntness. Experimental methods span from commercially available surface pressure sensors

to interferometry. Reviewing all those aspects in detail is beyond the scope of this thesis. While all of them will be touched in varying amounts of depth, a list is given here pointing to more detailed reviews:

- Information about transition research in hypersonics in the last fifty years and even beyond is provided by S.P Schneider for cones in general [57], for experiments with gas injection [56] and also about roughness effects [67]. Recently published theses by Grossir [8] and Wylie [68] about the topic give summaries on the work done on boundary layer transition for lifting and non-lifting conical geometries in wind tunnels.

- The receptivity stage in the transition process is reviewed by Reed and Saric [69].

- Much detail about focusing laser differential interferometry and its history can be found in Parziales work [70].

- A summary of transpiration cooling methods, materials and relevant heat transfer correlations is presented by Langener [71].

- The effect of nose bluntness on boundary layer transition on slender cones is reviewed in detail in the papers of Paredes et al. [72, 73]

As all the work was carried out at zero AoA, review of boundary layer transition and transition with injection will foremost focus on slender, non-lifting cones.

2.2 Hypersonic Boundary Layer Transition

2.2.1 Flow Stability

It is generally understood that viscous flow along any boundary such as a wall or inside a pipe cannot remain stable infinitely [74–76]. Empirical observations yield the existence of a “critical Reynolds number” [74], past which any instabilities will grow and result in transition to turbulence [74, 76], an observation that may date back well more than a century to Osborne Reynolds [76, 77]. Understanding

and predicting said phenomenon has been called “a riddle” [76], “a near total mystery” [76], “baffling” [78] and “poorly understood” [79–81] by highly regarded academics in the field. All in all, those statements sound encouraging - there is surely much left to learn - but also slightly intimidating to the ears of a young researcher. Summing up the *status quo* in the first sentences of a thorough review from 1969 about transition research, Tani [82] states:

> “The problem of the transition from laminar to turbulent flow in the boundary layer is unparalleled in having attracted the interest of investigators for so many years. Despite the enormous amount of research effort devoted to it, our understanding of the problem is still far from complete. Most of the difficulty in understanding lies in the large number of factors which affect transition, but which are not independent of each other.” [82]

From the perspective of theoretical physicists, Landau and Lifshitz issue a similar statement by writing: “[...] a mathematical investigation of stability is extremely complicated, however. The theoretical problem of the stability of steady flow past bodies with finite dimensions has not yet been solved.” [74] Although progress has evidently been made in many areas since Tani issued his statement in the 1960s (see e.g. Schneider [57] or Fedorov [83]) science is still far away from accurately predicting and deciphering the mechanisms of transition.

2.2.2 Transition Mechanisms in Hypersonic Boundary Layers

This aforementioned stability problem also applies to the hypersonic flow regime [78]. A boundary layer is generally an effect due to viscosity and defined as a thin layer of fluid covering a surface exposed to flow [84], with a velocity profile increasing from zero (“no-slip condition” [84]) to free stream speed with increasing wall normal coordinate, an idea conceived and mathematically formulated by Ludwig Prandtl ([85] as cited in [86]) at the start of the 20th century [87]. The large Reynolds number flow in this work causes the boundary layer to be thin compared to the dimensions of the body and the surrounding inviscid free stream flow [84]. Transition of such a thin layer from laminar to turbulent depends on a large set of variables [57, 88]

and anything that could have a destabilizing effect is summarized as a disturbance in Figure 2.1. Examples may be surface roughness, steps, gaps or noise in the free stream of a wind tunnel [57, 60, 69, 79]. In later chapters, due to their importance, an effort is made to thoroughly characterize as many of those aspects as possible. Receiving [89] those disturbances from the environment into the boundary layer marks the first step of any transition mechanism [69]. It is understood from the previous section 2.2.1 that downstream of a certain Reynolds number any arbitrarily small disruption will be amplified, irreversibly initiating any one of the procedures of transition [74] outlined in Figure 2.1. Those paths range from one extreme to the other: If the noise environment - in whatever form it may occur - is small enough, the boundary layer will transition naturally via its eigenmodes [69, 83, 90], whose growth and decay will determine the final transition location [69, 78, 83, 91]. With growing disruption level, which may well be introduced through foreign gas injection, the transition becomes increasingly transient [83, 92, 93] defined by Saric et al. [69] as a situation "when two, nonorthogonal, stable modes interact" [69] and Reshotko describes his early suspicions that said process is "inherently nonlinear" [93]. On the other extreme side, once a certain level of disruption is exceeded, laminar conditions can turn into turbulence without exciting any linear or modal growth [83, 92]. All those mechanisms are bypassed [89], and breakdown to turbulence ensues instantly [78, 83, 92, 94]. A more detailed description of all paths is for example provided by Grossir [8] or Reshotko [92].

Eigenmodes in High Speed Boundary Layers

Prandtl [95] discovered growing waves in a transitioning boundary layer [96]. The description in his publication suggest this was in strong contrast to the current state of research at the time. According to Prandtl [95], mathematical analysis had apparently shown how small oscillations in a laminar flow, which originates from viscous effects in between two walls, are always damped [95]. His calculations however yielded consistently how laminar flow is unstable against small perturbations, leading Prandtl to voice his scepticism about the result multiple times in the paper [95].

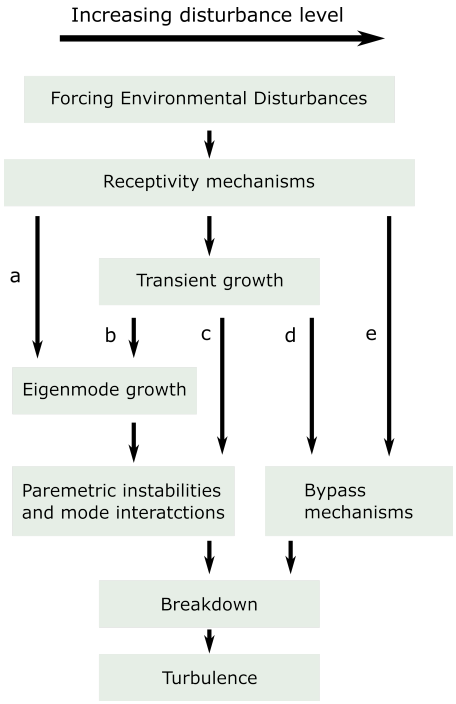


Figure 2.1: Overview of physical mechanisms leading to transition of a boundary layer. Figure taken from Fedorov et al. [83] and Saric [69] who both adapted it from Morkovin [94].

However, more than 60 years later Mack [96] credited Prandtl with paving the way for modern instability research thanks to the aforementioned finding.

The paths described in Section 2.2.2 generally hold for any speed regime [83], nonetheless, the characteristics of the eigenmode instabilities strongly depend on the Mach number [78, 91]. Stability theory for the boundary layer is formulated based on "linearized parallel-flow [Navier-Stokes] stability equations" [90, 96]. The first experimental proof of the applicability of linear stability theory [96] was delivered by Schubauer and Skramstad [97], justifying such theories by reporting hot-wire measurements of "laminar boundary-layer oscillations" [97] and relating them to subsequent turbulence [96, 97]. Depending on the Mach number and whether the flow is assumed as viscous or inviscid, a spectrum of modes coexists in high speed boundary layers but they vary with respect to their stability and amplification [90] (see Figure 2.3). For Mach numbers exceeding 4 on 2D axisymmetric geometries, the second mode (Mack mode) has been found to be decisive [83, 90, 91, 96]. This instability is a trapped "waveguide normal mode[...]" [83] and it oscillates in

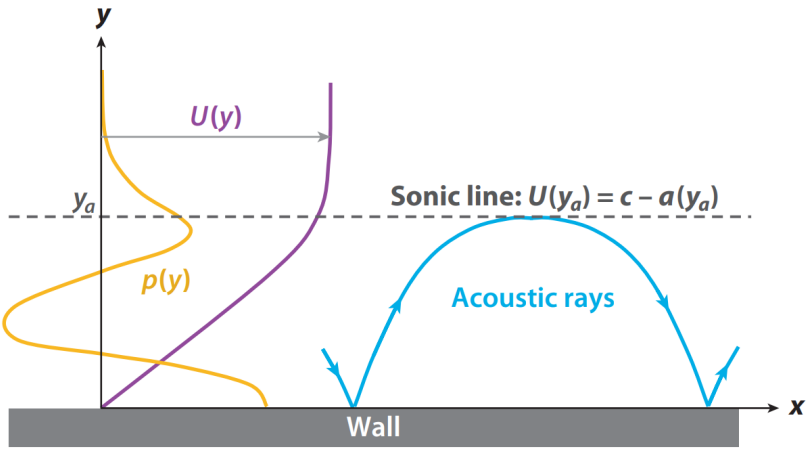


Figure 2.2: Schematic of the second mode instability as a trapped acoustic waveguide mode. Figure taken from [83], permission obtained via Copyright Clearance Center.

between the sonic line and the model or vehicle surface (see Figure 2.2). Hereby, the sonic line is defined as y_a with [83]

$$U(y_a) = c - a(y_a) \tag{2.1}$$

Such trapped modes can thus only exist due to a "region of supersonic mean flow relative to the disturbance phase velocity" [83] which commonly appears on slender bodies at hypersonic speeds. Under those conditions, the compressible inviscid parallel flow stability equations yield a wave equation for the momentum in wall normal direction [90], revealing "an infinite sequence of wavenumbers that will satisfy the boundary conditions" [90]. The second of those forms the dominant Mack mode. Those waveguide modes have been observed in multiple ground testing experiments with a variety of experimental instrumentation and in several different facilities [8, 68, 98–102]. Detailed analysis has been conducted with schlieren (e.g. [99, 102]), high frequency piezoelectric surface sensors (e.g. [8, 68, 100]), hot wires (e.g. [103]) or ALTP (e.g. [104]).

Mathematically, the normal modes can be derived as a wave function [90]. The form from [105, 106] is used here:

$$\Psi(x) = \Phi(x) e^{-\alpha_i x} e^{i(\alpha_r x - \omega t)} \tag{2.2}$$

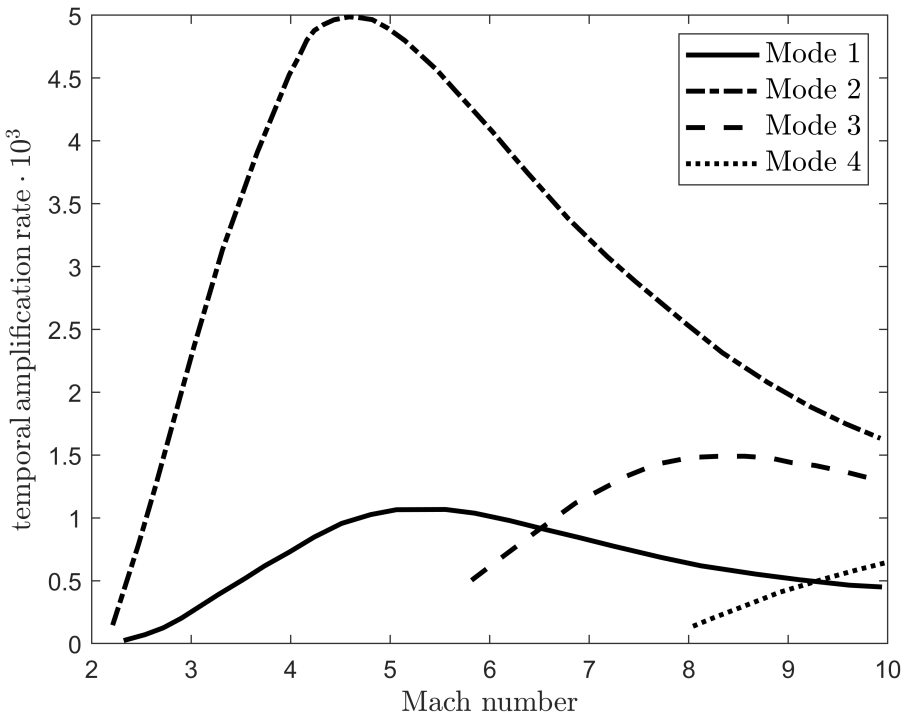


Figure 2.3: Mach number dependency of temporal amplification rate of different modes, replotted from [90]. The modes 1 and 2 are commonly referred to as the first and second mode, whereas the latter may also be called the (second) Mack mode.

where the imaginary part of $\alpha = \alpha_i + \alpha_r$ determines the spatial development of the oscillation in the given example. A possible method for transition prediction is the e^N method [105, 107]. Considering spatial growth of said eigenmodes along x in Equation 2.2 an integration along the stream-wise direction yields the following form [105]:

$$N = ln(a/a_0) = \int_{x_0}^{x} -\alpha_i \mathrm{d}x \tag{2.3}$$

As an input, amplification rates α and an initial amplitude a_0 are required. Similar geometries and flow conditions can then be expected to transition at the same N-factor [8], making the technique rather an extrapolation method than a full prediction of transition onset and Saric et al. [69] for example note how determining initial amplitudes poses difficulties. The critical N-factor of HDT on a similar conical geometry has been determined to be around 9.4 [68]. Other examples are the VKI-H3 tunnel, where the N-factor for a smooth cone was determined to be 5.9 [108] or the Langley 31-inch tunnel where the boundary layer transitioned at

$N \approx 5$ [101].

Due to the waveguide nature of this oscillation the frequency of the second mode has been successfully estimated with the following, simplistic mathematical expression [8, 58, 109, 110]:

$$f = \beta \frac{u_e}{2b} \tag{2.4}$$

A variety of values for β has been used to empirically improve the correlation with experiments. For example, Demetriades [110] used 1, Stetson or Wagnild used $\beta = 0.8$ [58, 111] and Jewell modified it to $\beta = 0.7$ [109], citing an improved match with simulation. The boundary layer thickness b is usually defined via the velocity profile or at high total temperature flow conditions via the total enthalpy (e.g. [109–111]), by relating the edge to the coordinate where either parameter has recovered to 99% of the free stream value [84].

Early findings from Demetriades et al. [110, 112] revealed how the second mode power is concentrated near the boundary layer edge [8]. During the same hotwire measurements the fluctuations could be observed extending above b. Both findings have been repeatedly confirmed by schlieren measurements [8, 99, 102, 113, 114]. The second modes have been described as "rope-like" [99, 115] when visualized with said imaging technique. Those structures occur in wavepackets, which travel downstream and dissolve into a turbulent spot [102].

2.2.3 Ground Testing for Boundary Layer Transition

One major setback for ground testing is briefly summarized in this quote:

> "Conventional hypersonic wind tunnels and shock tunnels suffer from high levels of freestream fluctuations, which are typically 1 to 2 orders of magnitude above flight levels." [60]

Many sources from the 1960s and even before identified this noise to mainly be of acoustic nature [116] and originate from "turbulent boundary layers on the nozzle wall" [60] [116–119], a feature nearly inevitable when constructing a wind tunnel. To improve analysis of said noise levels, Duan et al. [120] have proposed a

"decomposition" [120] of fluctuation measurements into "vorticity mode, entropy mode and sound-wave mode" [121]. An influence of those disturbances, or more generally external fluctuations, was already discussed as early as 1947 by Schubauer and Skramstad [97]. Mack [96] highlights how in such early attempts for example from Bennet [122] or from Spangler and Wells [123] free stream noise was understood as a driving factor for turbulent onset and observed mechanisms when comparing data across facilities and experiments.

Ground testing cannot replicate the boundary layer transition mechanisms and Reynolds number of real flight trajectories [124] due to the disproportionate influence of free stream disturbances on transition [79, 125]. Correspondingly, wind tunnel measurements can only provide a conservative estimate for transition Reynolds numbers [57]. Qualitative discrepancies also exist, meaning the transition mechanism may differ due to high noise environments and some physical effects may not be observable due to prohibitive noise levels [126, 127]. In Schneiders work [79], who summarizes noise driven influences on causative variables for transition, it is described how in wind tunnels one can only measure a distorted version of reality with respect to nearly every transition-driving variable [79]. This may be supported by comparisons of instability observations in quiet tunnels versus similar measurements in conventional facilities. While second mode spectra in the former usually include multiple higher harmonics of the second mode (see e.g. Lachowicz et al. [128] or [129]) experiments in conventional tunnels on similar geometries and measurement techniques usually cannot reveal such detail (see e.g. Grossir [8], Wylie [68] or Casper et al. [102]).

Specialized low noise facilities have existed for a few decades [60, 126] but those available can, due to technological complexity and simply number of available machinery, not provide a sufficiently large range in flow variables for thorough and meaningful pre- or post-flight investigations [120]. Current research efforts thus aim to characterize the disturbance spectra of hypersonic wind tunnels for example via pitot pressure measurements [68, 120, 130] and this subject will be touched in Section 3.3.4 for the facility used in this work.

Despite those shortcomings, wind tunnel measurements are still a frequent choice for research [57] and a recent flight test (HIFiRE 5) [127] has shown how successful case of a partly meaningful symbiosis of flight and ground testing. Another impressive example is the design and testing process of the X-33 vehicle, where "[o]ver 1100 tunnel runs" [131] were carried out as the geometry advanced along various designs [131]. Similarly, also the NASA X-43 development has been centred around extensive wind tunnel testing in multiple facilities at LaRC to research heating and transition on the geometry [132].

2.2.4 Effect of Nose Bluntness on Transition

Boundary layer transition Reynolds numbers on a slender cone can be increased by increasing the nose bluntness to a certain extent [133–137]. At some point a tipping point is reached and transition advances [72, 133, 137]. The phenomenon is thus divided into two domains [73, 138]: The 'small bluntness' and 'large bluntness' regime [62, 72, 73].

Marineau et al. [136] concluded that with increasing bluntness, the second mode alone cannot drive transition and similarly, Reshotko [93] theorizes how small scale roughness may comprise a critical factor in the reversal. Recent experimental-numerical research has partly confirmed said suspicion and shown how the reversal phenomenon may be due to "linear, non-modal optimal growth of oblique travelling disturbances" [73] originating near the blunt tip [72], which could cause transition without presence or growth of second modes [72, 73]. Amplification of Mack modes is not strong enough to be a relevant factor under those conditions [72, 73, 139].

The reason for this damping is to be sought in the entropy layer, a discovery where Rushton [137] in an early experimental investigation credits Ferri and Libby ([140] as cited in [137]) and Zakkay and Krause [141] with its discovery. Owing to energy conservation, the curved shock around the blunt tip creates a layer of high entropy gas, an effect that influences many boundary layer parameters and gradually subsides downstream, which is characterized by the so-called swallowing distance [137]. The presence of the entropy layer stabilizes second modes [142] until

said layer has subsided and first modes initially amplify [143]. Further downstream, second modes and their harmonics are present [57, 133, 144] and grow faster than for a sharp cone as soon as the influence of the entropy layer wanes [145].
The cone model in this work is either sharp $R_N \approx 0.05\,\text{mm}$ or has a small bluntness $R_N = 1\,\text{mm}$. Research by Wylie [68] has shown how similar or larger nose radii at comparable Reynolds numbers in HDT lead to a transition delay on 7° half-angle cone. The geometry is thus assumed to adhere to the 'small bluntness' regime.
Transition and instability characteristics furthermore depend on several other variables such as Mach number (see e.g. Softley et al. [146]), AoA and AoY (see e.g. Wylie [68], Kocian et al. [147] or Gronvall et al. [148]), wall-to-total temperature ratio (see e.g. Paquin [149]) and unit Reynolds number (see e.g. Schneider [57] or Softley et al. [146]). Except for the unit Reynolds number, none of those parameters are specifically varied during the presented investigations. Instead of a deeper review of each individual parameter, the reader is referred to the references given in the sentences above.

2.3 Active Cooling at Hypersonic Speeds

2.3.1 Transpiration Cooling

Transpiration Cooling Quantities

The concept of this active cooling technique is usually summarized as follows: A coolant is delivered directly to the outside vehicle skin by being released through a porous surface segment, hence separating boundary layer from wall and consequentially almost insulating the vehicle surface by creating a thermodynamic barrier [45, 47]. Interestingly, some early studies do not differentiate between film cooling and transpiration cooling as depicted in Figure 1.2 and described by Kelly and Blosser [45]. Scott et al. [150] for example only use the term 'film cooling', which they present as injection realized from "a porous strip or a slot" [150]. Specifically for porous injection, the amount of surface coverable is constricted by the weight of the coolant gas and additional equipment having to be carried along [45]. Active gas effusion can - in addition to cooling - offer chemical protection of the wall

material at those selected locations and specifically, if a stable, non-reacting coolant is selected inhibit oxidation [53, 55, 151]. During the transpiration process, the porous material cools itself through convection [47, 152], whereby the slow transport of the coolant passing between pores can yield high efficiencies [47]. All effects are summarized in Figure 2.4.

Similarly to Ifti [49] some essential variables shall be introduced now. Two of those are common practice for comparison of transpiration cooling in experiments as follows [36]: The cooling efficiency, η is the ratio of Stanton numbers (Equation 2.5).

$$\eta = 1 - \frac{St_c}{St_0} \tag{2.5}$$

and the blowing ratio F describes the ratio of mass fluxes in between coolant and hot boundary layer gas [153].

$$F = \frac{\rho_c u_c}{\rho_e u_e} \tag{2.6}$$

Hereby, the subscripts $_e$ denote conditions at the boundary layer edge and $_c$ is the coolant. Once the Stanton number is introduced as:

$$St = \frac{h}{\rho_e u_e c_p} \tag{2.7}$$

one can define the blowing parameter B_h [154–156] as

$$B_h = \frac{F}{St_0} \tag{2.8}$$

using the uncooled Stanton number St_0. B_h has originally been used to characterize ablation and resulting gas effusion at a stagnation point [154] but will be applied beyond this geometric point in the following experimental work. Those parameters allow drawing comparisons in between different coolant gases and flow conditions. Especially B_h eliminates dependencies on "Mach number and Reynolds number" [157]. Experimentally, cooling efficiencies η of up to 58% have been reported for Shefex II [158] in the close downstream vicinity of the injector using nitrogen as a coolant. A blowing ratio is unfortunately not provided for this case, however the injection mass flow was reported as 0.4 g/s. In wind tunnel tests, efficiencies of 80%

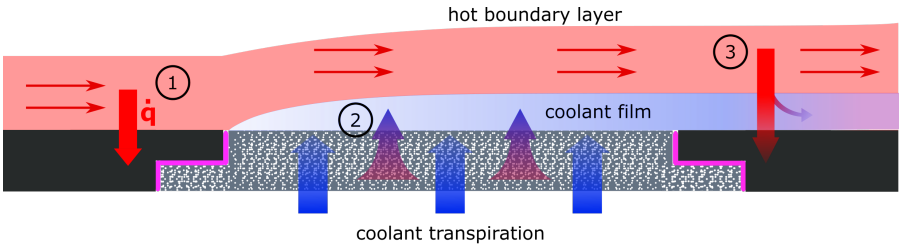


Figure 2.4: Tranpiration cooling in a laminar boundary layer. 1: Unhindered heat flux to the surface due to friction and radiation. 2: Convective cooling of porous material and substructure. 3: Coolant film protects surface. Inspiration for the figure loosely from Ifti etl al. [51] and Langener [71].

[36] and more [159] could be observed for helium and nitrogen as coolants.

Multiple studies such as from Gülhahn et al. [36], Langener [160] and many others (see e.g. [50, 151, 159, 161, 162]) determined multiple parametric dependencies of transpiration effectiveness. Depending on Reynolds number and required blowing ratio, different categories are found by Hermann et al. [163] to evaluate the effectivity of transpiration cooled heat shields, based on a variety of summarized research results [161, 163–167]. When attempting to find the ideal application of said technique, the first parameter considered may be the state of the boundary layer. In the categorization from Hermann et al. [163] injecting into turbulent flow is shown to yields a low cooling effectiveness, yet has however no further consequences for the boundary layer: Turbulent stays turbulent. In contrast, causing turbulence because of too much injection at moderate to high Re_x at the effusion location yields low cooling effectiveness and may even increase heating to the entry-vehicle [47, 56, 163]. It was thus found to be most beneficial if one could inject moderately below laminar flow [36, 163]. Herein, Otsu et al. [151] deliver a further aspect for this evaluation. Exceeding minimal blowing rates in laminar conditions does seemingly not induce comparative improvements in cooling [151, 163].

Coolants for Transpiration Cooling

In contrast to ablator studies which require complex mutli-species models to be accurately simulated (see e.g. [168]), transpiration cooling experiments or computations have mostly been performed with air, nitrogen and other common

gases [56, 104, 108, 109, 169–171]. Effectiveness to reduce the Stanton number depends on the heat capacity of the coolant as well as injection rate [36, 47, 50, 157, 159, 160] and can be approximately correlated with the parameter $B_h \cdot C_{p_c}/C_{p_e}$ for turbulent boundary layer conditions [157]. Another empirical correlation of Stanton numbers and transpiration cooling is from Naved et al. [159]. For laminar flow

$$\frac{St}{St_0} = 3 \cdot B_h \cdot \left(\frac{x - x_i}{x}\right)^{0.5} \cdot \left(\frac{m_e}{m_c}\right)^{0.4} \tag{2.9}$$

and for turbulent flow

$$\frac{St}{St_0} = 3 \cdot B_h \cdot \left(\frac{x - x_i}{x}\right)^{0.8} \cdot \left(\frac{m_e}{m_c}\right)^{1.4} \tag{2.10}$$

predicted the cooling efficiency profile [159] downstream of the injector surface. Those equations were ascertained for a flat plate and although Naved et al. [159] note how those correlations may not be transferable to other geometries or flow environments, the overarching trend inferred from those three relations - two from Naved et al. [159] and one from Woodruff and Lorenz [157] above - is that lighter gases are better coolants [44]. Helium was found to be most effective at reducing surface heat flux by many studies [36, 50, 51, 159, 160, 172] at hypersonic speeds. The same investigations found how air, argon and nitrogen all had similar success at mitigating heating but could not compete with helium [36, 160]. Especially in a turbulent boundary layer, helium proved to be superior by resisting mixing with hot boundary layer gas longer, leading to an "effectiveness 16 times greater than nitrogen" [159].

Research has not been restricted to gases. Water was found to have excellent cooling performance but directly lead to icing which may complicate coolant release and aerodynamics in real applications [32, 48]. Electrons are also considered for heat mitigation. Materials releasing high energy electrons as a reaction to heat were proposed as a form of cooling [40, 173]. This is however beyond the experimental scope of this thesis and also resembles a material characteristic more than performing active injection.

2.3.2 Application of Porous Materials

The Darcy-Forchheimer Equation

In the present work, coolant gases are assumed to be perfect gases and relating density, temperature and pressure is achieved via the ideal gas equation. A robust mathematical expression relating the mass flow through a porous medium to the pressure differential for a large range of flow speeds is given by the Darcy-Forchheimer equation (see e.g. [174]). It is shown in its integrated form in Equation 2.11 where K_D and K_F denote the viscous and inertial permeability coefficients and terms, respectively [49].

$$\frac{p_{in}^2 - p_{out}^2}{2p_{in}L} = \frac{\mu(T_{in})}{K_D} v_{in} + \frac{\rho(p_{in}, T_{in})}{K_F} v_{in}^2 \tag{2.11}$$

Outflow experiments have shown the relevance of the additional, quadratic 'Forchheimer' term in this work and related experiments [175].

Porous Materials in Hypersonic Transpiration Cooling

Coolant injection through machined slots would rather be classified as film cooling (see Figure 1.2), and thus microporous materials are an integral component of ejecting coolant into hot free stream [47]. A wide variety of solutions is available and has been trialled:

A material which has been used to investigate the concept in a free flight experiment is porous Carbon/Carbon CMC [158, 176, 177]. With AKTiV, DLR delivered data by transpiring nitrogen into the free stream from a tile in the sharp, octagonal test body SHEFEX II, flying at more than Mach 9 [158, 176, 177]. This family of materials has been previously investigated for transpiration cooling of rocket engine combustion chambers [42, 152] and a similar material sample from this category has been used by DLR in wind tunnel tests as an injector for mass transpiration on a hypersonic cone [104]. Beneficial characteristics of C/C CMCs are a temperature high enough to be applied in high enthalpy environments paired with favourable mechanical strength [160, 175, 178] and due to the variety of already investigated cases they have been branded “ideal candidates” [71] for future innovative cooling

concepts.

Ifti et al. [175] investigated the outflow properties of porous ZrB_2 UHTC according to ISO 4022. Opeka et al. [41] state, how this group of materials extends the suitable characteristics of C/C with its oxidation resistance. Should gas effusion not be able to prevent said thermochemical process, they could still be applied beyond 1600°C [41]. Ewenz et al. [53] and Ifti et al. [50, 179] later used said UHTC samples to investigate transpiration cooling effectiveness against oxidation and to research laminar coolant mixing in hypersonic flow.

Naved et al. [159] compared cooling efficiencies of Zirconia and METAPOR CE170 using infrared thermography. Both materials enable IR measurements due to their low thermal effusivity, compared to ZrB_2 [159]. While sintered ZrO_2 manufactured by Imperial College London roughly matched the $1-2\,\mu$m pore size and homogeneous permeability profile of UHTC, CE170 did not [159]. For the latter material, the majority of the outflow was found to be unevenly distributed and patchy across the surface, with the majority of the coolant released through irregularly distributed open pores [159]. By comparing those materials, Naved et al. [159] conclude that more homogeneous transpiration distributions allows for spatially consistent protection against heat.

A porous material used by at least four independent experimental studies across half a century for conical and cylindrical injection sections is sintered stainless steel [109, 150, 180, 181]. Placing a segment of this material within the model seems to have no influence on boundary layer stability, which probably means the surface is maintained smooth enough despite some limited porosity [109, 182]. Two of those studies characterized their porous cone section with respect to permeability by relating mass flow rate to pressure drop [109, 180]. Results follow the usual Darcy-Forchheimer behaviour for microporous materials. A characterization of the uniformity and spatial distribution is not given in both cases.

Other concepts found in literature are moulding [170, 171], “selective laser melting” [108] or drilling to generate pores. Experiments with a transpiration cooled segment in a cone at VKI used the latter two of those techniques to generate porosity of 37%

with pores of 0.8 mm size [108]. Compared to the μm range in other approaches this almost resembles film cooling. Avoiding direct interference of the tunnel flow with the coolant reservoir is achieved by installing a "finer interior porous layer" [108] of unknown material below the outer perforated skin.

Porous Transpiration Homogeneity and Comparability

Considering that small disturbances can be amplified exponentially in transition mechanisms (see Figure 2.1 and Section 2.2.2) disruption due to injection should be kept to a minimum [36]. As seen for example by Naved et al. [159], porous media can exhibit significant inhomogeneities with respect to their outflow velocity distribution. Furthermore, few loosely comparable examples yield an impact of said outflow homogeneity on the cooling performance. Specifically Naved et al. [159] highlight how IR measurements showed small locations of less effective heat mitigation on the porous material itself, which seemed to correlate with the respective non-uniform outflow profile. Similarly, Basore et al. [183] stressed how a microporous CMC surface had superior cooling effectiveness compared to a slot injector. The latter concept, film cooling [45], is self-evidently an extreme case of 'non-uniformity' but may provide a valuable hint about the connection of coolant film stability and effusion quality [183]. Considering influences of roughness on boundary layer transition [67], it is very likely blowing uniformity plays a role in destabilizing boundary layers [175]. To the knowledge of the author no correlation, systematic research or review of this topic exits to date. This may partly be because different levels of uniformity are intricate to quantify, reproduce and compare.

Details about outflow profiles from gas injectors are scarce, especially in older publications explicitly addressing active cooling and boundary layer stability. While some studies neglected possible inhomogeneities across the porous surface [104], others characterize the profile using pitot-probes [71, 108, 184, 185] or hot-wires [159, 175]([186] as cited in [187]).

Miró Miró et al. [108] observed a significant outflow jet at the rear end in one of their conical injector profiles. Nevertheless, they reported "minor" [108] or "negligibl[e]"

[108] influences of the nonuniformity on transition location. Given how different the pore size is from most other applied transpiration materials it is impossible to determine whether this statement may hold for all practical cases. Likewise, Langener [71] measured differences in outflow speed by a factor 30 within two flat C/C specimen but nevertheless concluded that the distribution of those outflow hotspots was even enough to not be of concern.

2.4 Mass Addition and Boundary Layer Stability

2.4.1 Destabilization by Injection

A summary about most of the mentioned literature in this paragraph can be found in Schneider [56] and in multiple other thesis that dealt with similar experimental studies (e.g. [109],[180]). A detailed review of the most important trends and cases concerning hypersonic effusion cooling and its influence on boundary layer stability is given in the Sections below.

Coolant injection generally has a destabilizing effect on the boundary layer [56], which was acknowledged as early as the 1950s. In one of the first transpiration cooling experimental studies Rubesin et al. [47] describe their scepticism. While stating that this technique "shows promise" [47] they warn how gas injection can destroy a laminar boundary layer and thus increase overall heat flux instead of reducing it [36, 47]. Gülhahn et al. [36] note how therefore laminar cooling was ignored in early studies (see e.g. [47, 153, 157]).

Some experiments replicated ablation with low temperature ablator materials such as paradichlorobenzene [188] or camphor [189, 190] also delivering results on transition and outgassing in a broader context. Due to the focus of this work on active cooling, those will not be discussed.

Potentially the earliest published investigation on an porous cone at hypersonic speeds is from 1960, when Scott et al. [150] tested a cone with gas effusion at Mach 5 by blowing nitrogen and helium from the large injector section covering most of the cone frustum. An optical technique, namely shadowgraphs, revealed a core result of many similar studies that should follow: Gas transpiration destabilizes

laminar flow and causes transition, helium more so than nitrogen [56].
Stalmach et al. [190] investigated a similar 12° half-angle conical geometry in a modified arc-heating wind tunnel. For the experiment, injection was achieved through a porous sintered nickel frustum, manufactured by rolling a sheet of said material into the desired shape [190]. By injecting monochlorodiflouromethane, nitrogen and methane at various blowing rates they reached - among other results - the following conclusions that are in agreement with and summarize the literature from the 20th century [18, 56]:

- Gas injection usually has a destabilizing effect on the boundary layer [47, 56, 108, 150, 187, 190–192].
- For the same coolant gas, the advance of the transition location is somewhat proportional to the mass flow rate [47, 56, 108, 150, 187, 190–192].
- At the same mass injection rate, upstream movement of transition is vaguely inversely proportional to the coolant molecular mass [56, 150, 187, 190].
- Lighter gases are more effective coolants in a laminar boundary layer at the same mass flow rate [36, 50, 51, 159, 179, 190].
- Uniform coolant release distributed across the entire test object causes less destabilization than spatially concentrated outgassing near the leading edge [56, 190].

For almost 40 years after publication of this study, no other research found anything that substantially deviated from those remarks [56]. Most of those core statements, or at least a subset would largely be confirmed by Marvin and Akin [187], Laganelli [192], Boudreau [193] or Miró Miró et al. [108] and any historical studies deviating from said conclusions (e.g. Dunavant and Everhart [181, 194] or Martellucci [195]) are viewed with scepticism [56].

2.4.2 Injection from Nose Cone Segments

For the studies presented in Section 2.4.1, the cones mostly consisted of a large porous body and an impermeable nose tip [150, 190], a geometric feature Camillo et al. [104] recently identified as a potential driver of transition advance. The opposite is the case for Cresci et al.'s research [172]. A 20° half-angle cone with a 0.5 in. radius spherical porous nose section was exposed to Mach 8.0 flow while helium or nitrogen were injected. Despite those significant differences in the test object, experimental findings aligned qualitatively with the core outcomes of 20th century research. Due to the blunt nature of the cone, those experiments may not be directly comparable to the slender geometry used in this work. Laganelli's [191] results on a more slender geometry with nosetip injection followed the same destabilizing trend. Further work by Laganelli focuses on coupled effects of foreign gas injection and angle of attack [192], which will not be included here.

More generally, stagnation point cooling has been studied separately on hemispherical geometries for instance [196] and yielded - amongst other valuable results - guidelines for boundary layer blow-off [196–199]. Ewenz [196] determined a threshold of $B_h = 0.59$ for helium injection leading to blow-off using a correlation given by Yoshikawa [200]. Herein, blow-off is defined as destroying the boundary layer by blowing so thoroughly it is promptly "lifted away from the wall" [199]. Correspondingly, the critical value for nitrogen injection is $B_h \approx 1.5$ [196] and both values - for nitrogen and helium - are confirmed within reasonable range by Holden et al. [170, 171] in experiments on a variety of conical geometries.

A disputed result from the late 1960s may hold relevance for the experiments presented in this work. Dunavant and Everhart [181] tested a slender cone at Mach 10. An impervious sharp nosetip and frustum enclosed a conical porous injector which covered only about 5% of the 1.76 m axial length and started 96.5 mm from the tip coordinate. Schneider [56] notes how this is in contrast to other studies from the 1960s and 1970s, where large porous injectors covered most of the cone surfaces downstream of solid tips to more accurately replicate evenly distributed ablation. Surprisingly, Dunavant and Everhart [181] found the

transition Reynolds number to be “unaffected by helium transpiration” [181] but not by air, where transition seemingly followed the well documented tendency. Those findings lead them to conclude that helium is overall beneficial while air feeds the usual ’transpiration cooling paradox’ by originating more heating than cooling [181]. Yet another contradiction to other studies (e.g. [135, 190]) is the reported surface pressure increase across the transpiration inset. Both, the apparent independence of transition front and helium blowing ratio as well as the pressure behaviour have been viewed sceptically by Schneider [56]. He notes that owing to the lack of complementary measurement techniques other than thermocouples, the cooling and destabilizing contributions of gas injection cannot be accurately decoupled [56].

Furthermore, extensive work on conical geometries with injection has been carried out in CUBRC facilities by a research group around Holden [171]. Many of their investigation included parameters irrelevant to the given discussion, such as patterned roughness, hemispherical models and mostly a focus on turbulent flow [27, 170, 171, 201]. Two studies [27, 201] with perforated hemispheres however replicated the usual trends of transpiration cooling with respect to the relationships of efficiency and molecular weight as well as a tripping the boundary layer. Those trends held true even when the model was exposed to a helium/hydrogen mixture-flow in their shock tunnel [201].

It can herein already be concluded how modern stability data for slender conical geometries with injection from the nose tip is particularly rare. Due to the heightened relevance of leading edge cooling this seems rather surprising and motivates new studies for those configurations.

2.4.3 Stabilization by Injection

Mateer and Larson published findings on cone boundary layer transition, which they titled “unusual” [189] [79]. In the Ames 3.5 ft hypersonic blowdown facility [189] at Mach 7.4 ± 0.25 helium or air were injected into the tunnel flow upstream of the nozzle throat. Their work has received attention from multiple other studies [57, 79,

134, 135] for the fact that helium in the nozzle boundary layer largely eliminated the free stream Reynolds number dependency of the transition location on a cone in the test section. Schneider calls this result "more important" [79] than another core finding which has, to the knowledge of the author, not been discussed in as much detail: Helium transpiration into the nozzle, compared to air, caused a transition delay on a 5° nickel cone [189], which can most likely, just like the other result, be linked to the "[reduction of] noise radiated from the tunnel nozzle boundary layer" [134]. Schneider [79] justifies this inference with a similar effect observed on supersonic jets by Papamoschou [202]. It is remarkable how in Mateer and Larson's [189] example a light gas - helium - must have been more effective at shielding, preventing or stabilizing turbulence in a boundary layer than a heavier gas, namely air [189]. Said investigation is self-evidently not an example of gas being transpired from a test model or flight vehicle. Nonetheless, it may be an early finding of how light gas injection into a boundary layer can possibly reduce noise and fluctuations. A recently described effect to delay boundary layer transition is based on "vibrational relaxation of [carbon dioxide] molecules" [109] and Leyva et al. [203] briefly reconstruct the chronological sequence of its core result's discovery: At sufficiently high total temperatures, molecular vibration of carbon dioxide absorbs oscillation energy from second mode disturbances [109, 203–205]. The first hint may have been an investigation by Johnson et al. [205] who found that chemical compositions, which reduce the average dissociation energy of the boundary layer gas mixture could irreversibly extract energy from oscillations, which are driving transition in the hypersonic speed regime [90, 205]. Prior to Johnson et al.'s [205] study, experimental findings were obtained using carbon dioxide/nitrogen, carbon dioxide/air mixtures or pure CO_2 as the tunnel gas in the T5 facility [203, 204, 206–208], whereby transition onset and completion moved rearwards on a 5° half-angle cone of 1 m length with increasing carbon dioxide concentration in the free stream. As a logical next step, CO_2 was then injected from within the model. Following a thorough investigation by Leyva et al. [182] about injector types, a short microporous conical segment was selected, as it outperformed slot injectors with respect to smoothness.

For early qualitative attempts with injection from the cone model, schlieren images indicate destabilization due to high outflow velocities [203]. Following simulation work from Wagnild et al. [209] experiments in T5 - hereby filled with air - then finally found stabilization generated by CO_2 effusion from a 10 μm pore size [182] porous sintered stainless steel injector segment of 41.3 mm length [104, 109, 210]. Herein, transition data was inferred from 80 thermocouples, providing adequate response time and, due to the instrumentation layout, sufficient spatial resolution. Comparison to argon, which has a similar molecular weight ($m_{CO_2} = 44$g/mol and $m_{Ar} = 39.5$g/mol) but is inert and mono-atomic, were made and ensured successful identification of carbon dioxides molecular geometry and consequently vibrational relaxation as assignable cause of stabilization [109, 210].

Another discovered effect is independent from molecular vibrations and thermochemistry. Camillo et al. [104, 211] found "a transition delay of approximately 17%" [104] by injecting nitrogen through a small porous injector close to natural transition onset on a 7° half-angle cone. Their motivation for the respective experiment design originated from a meticulous analysis of studies in the field, many of which were mentioned in Section 2.4.1. Camillo et al. [104] and Wartemann et al. [211] spotted an overarching tendency in older studies to use injectors that cover most of the total model surface. Citing a study from Fedorov [212], Camillo et al. [104] theorize that long outgassing sections may induce their destabilization by inevitably increasing the "cumulative N-factor" [104], while "localized mass addition might be able to detune the boundary layer with respect to the most amplified second mode frequencies such that transition delay is achieved" [104]. In their experiments, transition onset location was inferred by comparing thermocouples to an uncooled laminar CFD calculation [104]. When injection was performed close to the transition onset, second mode instabilities were damped in intensity as seen by schlieren imaging [104]. Heat flux remained below the laminar baseline for an extended distance and thus Camillo et al. [104] concluded to have found a transition onset delay with respect to heat transfer and instability mechanism [104].

Those two independent experimental-numerical studies have successfully demonstrated the possibility to interfere with the transition mechanism in different physical ways to achieve stabilization. While one is based on high temperature molecular effects, the other utilizes a "detuning" [104] of the second mode frequency spectra. Especially Camillo et al.'s [104, 211] discovery leaves many open questions. Could such and effect also be exploited elsewhere on a conical geometry? The study was furthermore limited to a single coolant and hence the gas type dependency is entirely unclear. Moreover, their wind tunnel produced a high enthalpy flow [104] and more understanding could be gained by repeating said study in a low temperature environment.

2.4.4 Injection and Instability Mechanisms

Sections 2.4.1, 2.4.2 and 2.4.3 were predominantly focused on studies measuring the transition coordinate and its behaviour with gas injection. Modern optical imaging techniques or surface instrumentation with sufficiently high sampling frequencies however allow measuring the influence of injection on the hypersonic instability mechanism.

Using planar laser induced florescence, schlieren imaging or ALTP it has been found by multiple studies how gas injection reduces the instability oscillation frequency [104, 108, 180]. Hereby, higher blowing ratios and higher molecular weights of coolants caused stronger reductions [108, 180].

Schmidt et al. [180, 213–215] conducted a series of experiments on a 5° half-angle cone that was directly aimed at investigating interactions of active cooling gas effusion and flow instability mechanisms. Their test object comprised either a conical or a cylindrical porous middle section an was placed in a Mach 4 Ludwieg tube, causing Schmidt et al. [215] to speculate for a while but eventually identify the first mode to prevail over the second in driving the transition mechanism [180]. With injection, instability characteristics changed substantially and Schmidt [180] writes how an independence of oscillation characteristics from the boundary layer thickness could only be explained by the presence of a "shear layer instability"

[180] and they thus concluded that in the cases of nitrogen and helium injection "the Kelvin-Helmholtz mode is likely the transition mechanism" [180]. Results on transition locations furthermore agreed with the general destabilizing trends described in Section 2.4.1.

In a recent publication from 2020, Miró Miró et al. [169] addressed the need for a modern re-investigation of experimental work from Marvin and Akin, conducted 50 years ago [135], who performed analysis of gas injection on a 5° cone. For any given nose bluntness the transition location was found to correlate with $1 - 0.25F(m_{air}/m_c)^{0.25}$ which agrees well qualitatively with results found in similar studies (see Section 2.4.1) [56, 135]. In their computations, Miró Miró et al. [169] have however shown that the presence of helium - the lightest coolant gas of the study - in the boundary layer alone does not cause a destabilizing effect. They clearly deviate from the previous dogma that light gases cause transition advance [56, 135, 150, 190], and conclude in their work that Helium actually stabilizes a boundary layer on the given geometry in Mach 7.4 flow [135, 169]. Consistent experimental observations of destabilization through gas effusion are explained by "a weak shocklet" [169] - an effect exacerbated for lighter gases - forming at the upstream interface of any porous injector. Considering proportionalities given in other publications it is likely that $\Delta b \sim 1/M_c$ [49], the relative change in boundary layer thickness may present a driving factor behind observed correlations of coolant mass and destabilization.

Numerical research work from Li et al. [216, 217] was foremost focused on blunt geometries to replicate ablative outgassing, but nevertheless also included a slender cone and correspondingly to Miró Miró et al. [169] gas effusion was found to minimally shift transition downstream [217], a discovery that Li et al. called "surprising" [217]. Albeit their outgassing section is a large frustum attached to an impervious tip, similarly to Marvin and Akin [135] and Miró Miró et al. [169] and thus not suitable for conclusions about active cooling [45] those findings are still promising and demonstrate how stabilization and injection may not be mutually exclusive.

Lastly, it is also acknowledged that work on transpiration cooling on cones exists for the supersonic regime [218, 219] and even for subsonic flow [220] yielding overall similar tendencies as studies at hypersonic speeds. Research has furthermore been carried out investigating the stability problem with injection at supersonic speeds [221]. Said work however deals with different fluid physical phenomena at Mach 2 compared to the work presented in the chapters below and was furthermore limited to flat plates [221].

2.5 Outlook

More than 60 years of stability and outgassing research have yielded some progress, but many fundamental questions are still unsolved. The generally accepted trend that helium is by far the most superior gaseous coolant, but unfortunately $Re_{tr} \sim 1 - 0.25F(m_e/m_c)^{0.25}$ [187] provides a rather unfavourable starting position for transpiration cooling applications. Particularly the understanding of foreign gas injection on instability mechanisms is in its very initial stages, but promisingly, some studies had outcomes to show stabilization instead of transition advance. Especially the numerical results from Li et al. [217] and Miró Miró et al. [169] motivate scrupulous experimental work to figure out any possible ways to reveal those effects in experiment and then exploit them on flight geometries. The focus on ablation in many older studies [56] also means little data is specifically tailored towards active cooling methods and this lack demands more research for small injector surfaces at critical geometric locations.

3

Experimental Infrastructure

Contents

3.1 Cone Model 39
3.1.1 Design and Assembly 39
3.1.2 Surface Instrumentation 43
3.2 Schlieren Imaging 44
3.2.1 Working Principle of Schlieren Techniques 44
3.2.2 Use of z-type Schlieren in Hypersonic Wind Tunnel Testing 46
3.3 The Oxford High Density Tunnel 48
3.3.1 General Information 48
3.3.2 Ludwieg Tube Mode 49
3.3.3 Calculation of Flow Conditions and Uncertainty Analysis 50
3.3.4 Free Stream Characterization of the HDT Mach 7 Nozzle 50
3.3.5 Gas Injector System and Operating Procedure 52
3.4 Instability Measurements 54

3.1 Cone Model

3.1.1 Design and Assembly

A 7° half-angle cone has been selected as a test body for various reasons. Firstly, cones are very common in boundary layer transition research in wind tunnels [57] and free flight (e.g. [39, 222]). Therefore, numerous possible experimental comparison cases may improve an integration of the shown results into the literature.

Heppenheimer [4] summarizes how the interest in nose cone geometries rose relatively quickly owing to its relevance for missile design in the 1950s and 1960s. Very early examples of considerations for cones as re-entry bodies are found at the beginning of the 1950s (e.g. Allen and Eggers [223]). Compared to other transpiration cooling studies that were conducted using flat plates [36, 50, 159] the rotational symmetry of a cone eliminates edges and increases the suitability for stability measurements [8]. Moreover, said round and edgeless geometry attributes benefit the applied optical techniques (see Section 3.2). Lastly, the shape and dimensions were selected to be equivalent to the model tested by Wylie [68, 224, 225] in the same wind tunnel. This provided confidence in the presence of a second mode dominated transition process in HDT when $M = 7$ [68, 225] as well as preliminary data for the design of the injector locations and characteristics.

The cone is subdivided into several segments to facilitate machining, assembly and instrumentation. An exploded view of the design is shown in Figure 3.1, all shown components are specified in Table 3.1 and detailed drawings of the individual designs are provided in Appendix A.1. Nose tips (Part 6 or 6b) are threaded onto the front segment and can be exchanged whenever necessary. Part No. 3 (Mid Segment North Half) has a 360° section at the front end, which contains an internal thread for the central pipe (Part 9) and an external thread to connect to the front segment and nose tips (Part 8 and Part 7, 6 or 6b). This allows to assemble the porous nose section and its associated pipework before closing the model mid-segment halves (Part 2 and 3), whereby the experimenter greatly benefits from being able to organize internal cabling while having full access to the open interior. Part 7 seals to part 8 via an O-ring and its respective groove. Part 5 and 2 use the same technique. Threads in the pipework were sealed using Loctite 577® and all interfaces and connections were thoroughly checked with leak detector spray while maintaining injectors and respective pipework under reasonably constant pressure. Just downstream of the 360° segment of Part 3, two M2 bolts ensure tight fastening of said part with its opposite, Part 2. The counterbore holes of said bolts therefore penetrate the cone surface and a different method was applied for each of

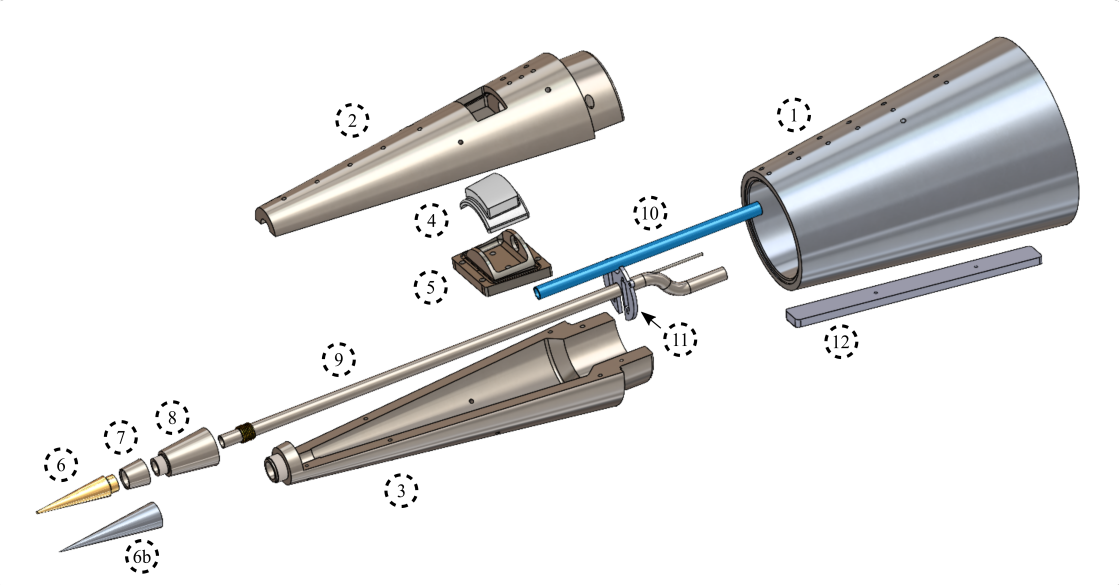


Figure 3.1: Exploded view of cone model. Part descriptions are given in Table 3.1. Part 6 and 7 can be replace through 6b.

Table 3.1: Description of model parts. Part numbers shown in Figure 3.1.

Part No.	Description	Material
1	Rear segment	Aluminium 7075 T6
2	Mid segment south half	304 stainless steel
3	Mid segment north half	304 stainless steel
4	Porous frustum insert	BF100 Al
5	Frustum lid	304 stainless steel
6	Porous or solid nose tip	BF100 Al or CE170
6b	Solid nose tip (sharp)	Al 7075 T6
7	Porous nose tip adapter piece	304 Stainless steel or PEEK
8	Front segment	304 stainless steel
9	Central pipe	Steel
10	Frustum injector pipe	Steel
11	DSUB holder plate	3D print
12	Insert into frustum	PEEK

the two tunnel entries to ensure a smooth surface finish. For the model assembly presented in Chapter 4, those holes were filled with RTV silicone which was cut to the right shape after hardening using a razor blade. In all other results, ABS cover cylinders were 3D printed, glued into the respective hole and then sanded with P3000 sandpaper until a satisfactory surface finish was achieved.

The precise configuration of the model changed throughout the campaigns and tunnel entries where data was collected. Nosetip, instrumentation and injector

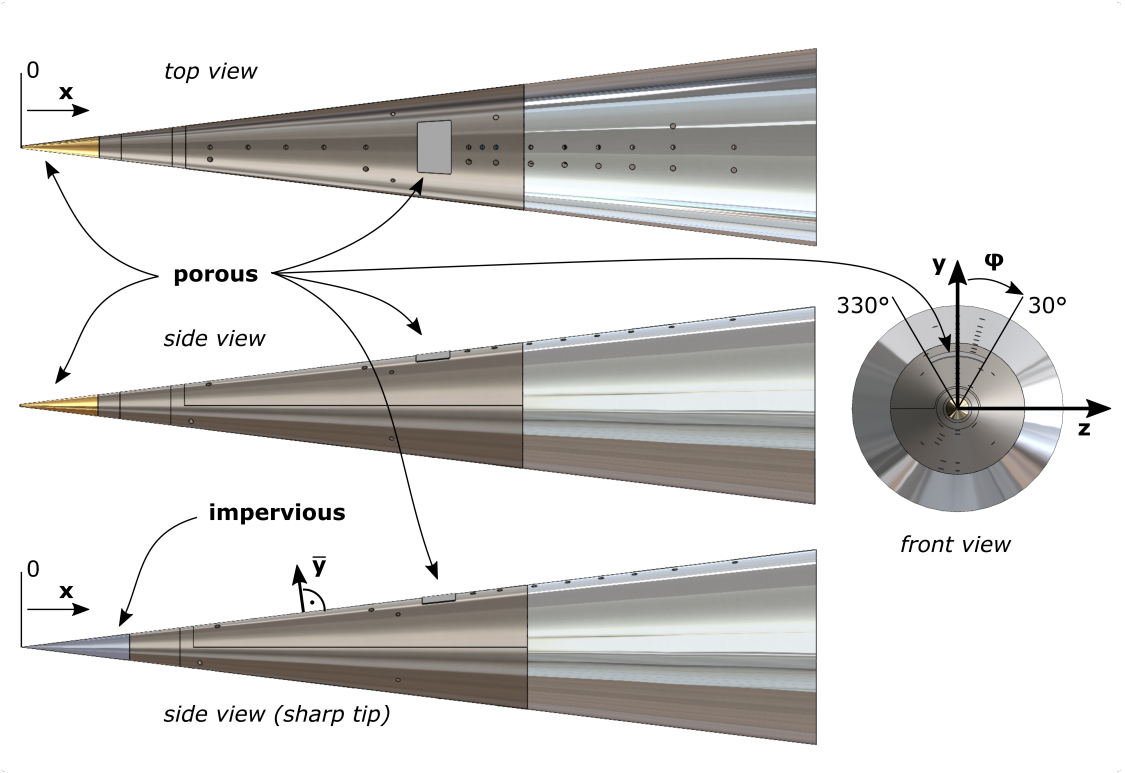


Figure 3.2: Coordinate system of the cone model. The x = 0 plane always refers to the apex of the nose tip in use. Correspondingly, the injector starts at x = 300 mm (sharp) or x = 293 mm ($R_N = 1\,\text{mm}$) and ends 25 mm further downstream.

status are reported in each chapter. Technical drawings and information about the surface quality are provided in the Appendix A.2 and A.1.

Model-Flow Alignment

The model is mounted on a Micromech 2-axis traverse. Detailed depictions of this system can be found in References [68, 226] and it is also visible in Figure 3.3 beneath the cone. In the sensor layout, four PCB 132B38 piezoelectric differential pressure transducers are included at the same axial distance ($x = 282$ mm) and at four different azimuthal positions ($\varphi = 45°$, $\varphi = 135°$, $\varphi = 225°$ and $\varphi = 315°$). Using a solid, sharp ($R_n = 0.05\,\text{mm}$) aluminium nosetip, AoA and AoY are adjusted until the mean second mode frequency during the steady state test time matches at all azimuthal positions. This procedure is repeated, whenever the model has to be re-aligned due to a change in experimental setup. Around three to four test runs and traverse re-adjustments were usually necessary to achieve satisfactory alignment.

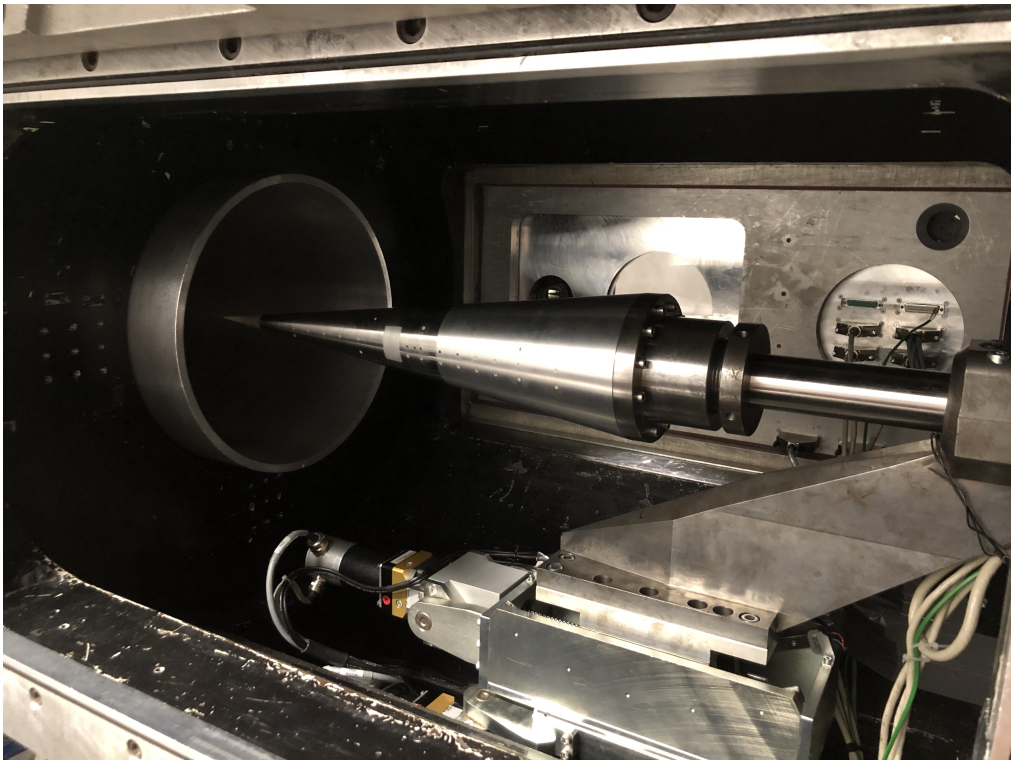


Figure 3.3: Cone model on sting mount in the tunnel test section. Nose is a porous CE170 $R_N = 1\,\text{mm}$ tip. The cone is rotated with the frustum injector side towards the test section window in the photo.

Hereby, the maximum and the minimum mean second mode peak frequency had to be within 5% of the mean frequency value. Achieving such precision usually required alignment steps in the order of 0.05° on the traverse mechanism and the uncertainty for the angular alignment to the mean flowfield of the nozzle is hence conservatively reported as ±0.1°. An example for a completed procedure can be seen in Figure 3.4, where the limit for agreement was ±7 kHz.

3.1.2 Surface Instrumentation

In order to measure heat flux, static pressure and high frequency pressure disturbances, different sensor types were flush mounted with the conical surface. All cabling was soldered into DSub connectors and then connected to amplifiers outside of the tunnel test section using jacketed, shielded twisted pair cabling. For an overview of each sensors functioning principle, the specific application to each experiment as well as data recording procedures, the reader is referred

Table 3.2: Full capability of sensor locations on cone model. Not all sensor holes were instrumented and active during all experiments. ($\varphi = 0°$) corresponds to the central plane of the frustum injector as indicated in Figure 3.2. Locations are given relative to a perfectly sharp nose tip. Sensor x coordinates relate to the centre of the surface-normal hole.

$x\,[mm]$	Sensor Type					
	PCB No.	φ_{PCB} [°]	TFG No.	φ_{TFG} [°]	Kulite No.	$\varphi_{\mathrm{Kulite}}$ [°]
107.0	1	0	-	-	-	-
127.0	2	0	2	30	-	-
145.0	-	-	-	-	1	180
147.0	3	0	-	-	-	-
175.0	4	0	3	210	-	-
203.0	5	0	4	210	-	-
231.0	6	0	5	210	-	-
262.0	7	0	6	30	-	-
282.0	11,12	45, 135	-	-	-	-
282.0	13,14	225, 315	-	-	-	-
338.0	8	0	7	15	-	-
348.0	9	0	-	-	-	-
358.0	10	0	-	-	-	-
312.5	15	180	-	-	2	180
358.0	16	180	8-10	195, 220, 15	-	-
383.7	17	0	11	15	-	-
408.7	18	0	12	15	-	-
433.7	19	0	13	15	-	-
458.7	20	0	14	15	-	-
488.7	21	0	15	15	3	330
533.7	22	0	16	15	-	-

to the Chapters 4, 5 and 6.

3.2 Schlieren Imaging

3.2.1 Working Principle of Schlieren Techniques

Visualization of optically transparent flow phenomena has proven beneficial for many experimental studies. Providing an overview for the experimenter can contribute to the understanding of complex phenomena or help with spotting errors in an experiment. High sampling rates of modern camera systems have hereby proven particularly expedient as they allow sophisticated mathematical data analysis of underlying flow physical phenomena (see e.g. [99, 227]).

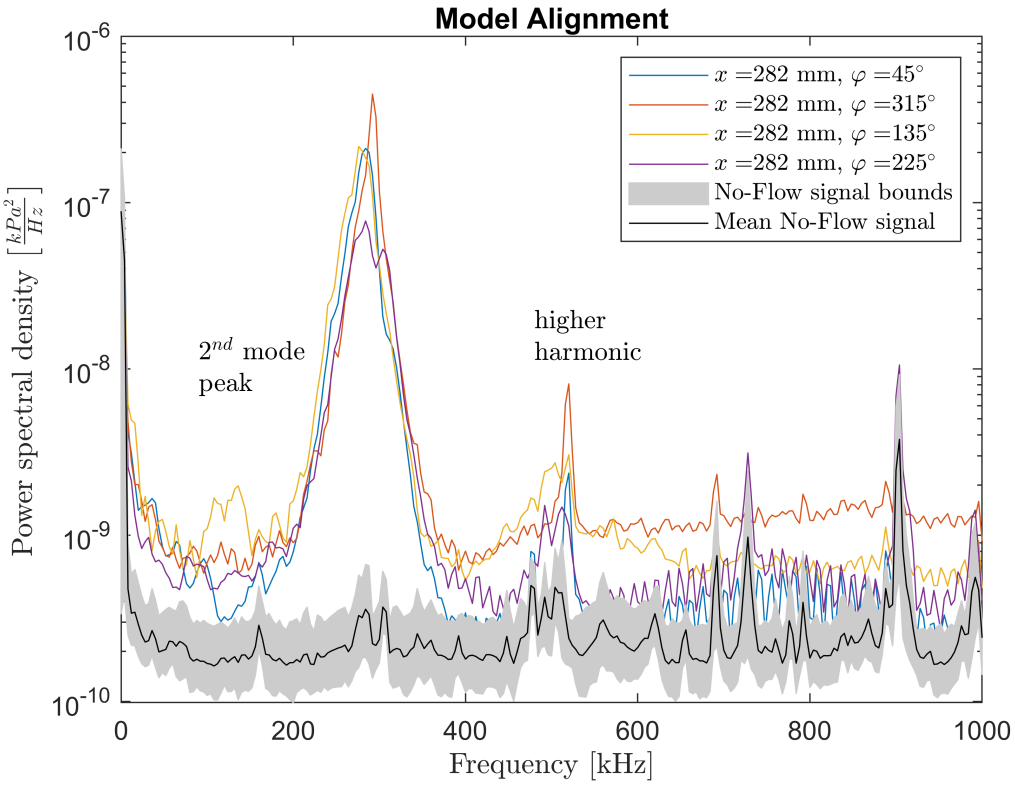


Figure 3.4: Alignment of 7° cone model using second mode instability. The shaded region was computed by considering the maxima and minima in every sensor spectrum recorded in the time ($\sim 100\,\text{ms}$) before the model is surrounded by tunnel flow.

Schlieren techniques are a category of optical systems capable of imaging density gradients as intensity changes in a photograph or video [228]. They hence "allow us to see the invisible" [228]. Their origin dates back to the 16th century, when Robert Hooke [229] used a concave lens and his bare eye to observe density fluctuations in rising air from a flame [228, 230]. Important milestones in the history of those instruments are the introduction of the knife-edge into the setup by Focault [231, 232] and developments from Toepler [233], who established the invention for scientific applicability to flow phenomena [228]. A variety of schlieren methods has originated from those starting points and more detail about them can be found in the book by Settles [228].

Their principle is however always the same. The refractive index of a gas depends on its density, which Hooke already interpreted correctly nearly 400 years ago [229, 230].

The Gladstone-Dale equation describes said dependency in a linear relationship [234]:

$$n = k\rho + 1 \tag{3.1}$$

A density gradient hence translates into a refractive index gradient, which in turn dictates the speed of light in a gas. Consequently, a bend in a light ray will result from any non-zero gradient $\partial n/\partial y$ orthogonal to its direction of travel (see e.g. Fig. A.1 in Appendix 6 of Reference [228]). The resulting deflection can be mathematically expressed as shown in Equation 3.2 [228], whereby the coordinate system was chosen as defined for the cone, with the schlieren beam pointing in z-direction and β is the deflection angle in the xz-plane.

$$\frac{\partial \beta}{\partial z} \approx \frac{\partial^2 x}{\partial z^2} = \frac{1}{n}\frac{\partial n}{\partial y} \tag{3.2}$$

According to Schardin [235, 236], any schlieren system works by translating such deflections into a change in intensity via a variable cut-off, which can then be optically recorded.

Light rays coming from the LED have an angle relative to the optical axis of the parabolic mirror, which leads to a coma [237]. The reason for a z-like layout (see e.g. Figure 5.5) is that the second parabolic mirror compensates the coma of the first [228], consequently eliminating this spherical aberration from the images and ensuring blur free visualization of objects in the image path.

The setup used in this work largely follows the z-type layout described by Schardin [236], which dates back to Toepler [235]. A setup schematic can be found in Figure 5.5, Section 5.9.6 together with Table 5.2, which describes all parts of the setup. Further details, such as the applied camera and recording settings are subject to changes and therefore described in the individual chapters.

3.2.2 Use of z-type Schlieren in Hypersonic Wind Tunnel Testing

Schlieren, particularly the z-type setup, is very common in its application to high speed wind tunnel research and thus only few, prominent key publications can be

summarized below. An influential and recent example of schlieren experiments and data analysis is the work of Laurence et al. [99, 238], wherein schlieren was proven to be very effective at studying second mode instability spectra and their development along a 7° cone. Oscillation characteristics could be obtained from high speed schlieren images [238] via spectral analysis, which could for example provide insight into the attributes of wave packets at different flow enthalpies [99]. Similar work was conducted by Schmidt et al. [180, 215], which was already reviewed in Section 2.4.4. Frame rates of 290 kHz enabled suitably high frequency analysis of instability structures and thus the measurement of their convective speed and frequency [215]. In consequence, interpretation of flow visualization delivered an essential contribution to identifying a Kelvin-Helmholtz instability above the injector [180]. Applying a wavelet transform to a series of schlieren images allowed Camillo et al. [104] to observe damping of second mode wave packets in combination with a frequency drop as they were travelling across a porous injector with nitrogen transpiration [104]. Image post-processing was hereby essential to reveal more details than just raw schlieren images.

Moreover, Subiah [226] developed sophisticated ultra-high speed schlieren analysis methods at the Oxford Thermofluids Institute independently from the presented work, whereby she compared second mode instability data from the Oxford HDT to its neighbouring facility, the T6 Stalker tunnel [239]. Herein, a 7° half-angle smooth cone without injection served as a test object in both tunnels and similar schlieren setups as described above were used, albeit with minimal differences in the beam path and mirror arrangement. Among other results, Subiah's [226] research complements the facility commissioning work done by Wylie et al. [225], by providing confidence in the detection and spectral analysis of boundary layer instability using schlieren data. In addition, the work increases reliance on HDT as a suitable facility for boundary layer transition research [226].

Schlieren as Line Integration Technique

Light rays in between the two parabolic mirrors of a z-type schlieren setup are largely parallel [240]. Therefore, such schlieren systems have a large depth-of-field [237], meaning that objects moving away from the middle of the optical path only move out of focus very slowly. Consequently, density fluctuations across the entire light path are imaged with comparable sensitivity and focus [240], including free stream disturbances beyond the core flow and even air fluctuations beyond the HDT test section. However, for the analysis presented in the following chapters, none of those disadvantageous features are of relevance. Firstly, any air fluctuation outside of the test section will be of speeds orders of magnitude below the effects encountered inside the tunnel. At sufficiently high frame rates those stand still, compared to boundary layer flow. In addition, they are kept to a minimum in the experimental setup by for example shielding the light beam from the cooling fan of the camera. Secondly, post-shock free stream disturbances are visible in the recorded field of views and could thus be examined with respect to signal strength and spectral content. In addition to exhibiting orders of magnitude lower schlieren signals than the boundary layer itself, the frequency spectra can be calculated and subtracted from those of the measured instabilities. Furthermore, results in the chapters below offer comparisons of oscillation data obtained by schlieren to surface sensors and FLDI. Both of those techniques show good agreement with schlieren measurements.

3.3 The Oxford High Density Tunnel

3.3.1 General Information

The Oxford High Density Tunnel (HDT) is a wind tunnel facility located at the Oxford Thermofluids Institute. Since its initial installation and commissioning starting in 2012, the tunnel has been used for a variety of hypersonic flow experiments ranging from boundary layer transition research [225] to free flight testing [241] and fluidic thrust vectoring [242]. A capability for light isentropic compression

heating mode was also implemented [243, 244], but most of the roughly 2700 shots conducted in the facility so far were run in Ludwieg tube mode [245].

3.3.2 Ludwieg Tube Mode

This concept for a super- and hypersonic wind tunnel was invented by Hubert Ludwieg in 1955 [245–247]. The 'upstream' side of HDT consists of the Ludwieg or "storage tube" [247] which can be pressurized up to 275 bar and heated up to 573 K [243]. The 'downstream' region consists of the converging-diverging nozzle, test section and 28 m^3 dump tank [243]. To reduce operation cost and time, the latter component is kept under vacuum and is separated from the test section by a pendulum valve. Test section and nozzle are evacuated to around 60 - 80 Pa before a shot and the Ludwieg tube is kept permanently heated along its entire 17 m length by four electrical heaters. In contrast, other Ludwieg tubes only sustain the first few meters upstream of the nozzle at high temperatures [246, 247]. As a result, no internal geometric changes needed to be made and HDT has a constant diameter straight Ludwieg tube as opposed to other facilities, where for example an internal step is applied or more complex geometrical designs for the tube were chosen [243, 246, 247]. Heating ensures the test gas - dry air or pure nitrogen - does not partially liquefy upon expansion into the test section throughout a test run [243, 246, 247]. After filling the Ludwieg tube to the desired pressure before a shot, a 150 second wait time is applied to ensure the test gas has equilibrated. A signal from the programmable logic computer opens the plug valve ([248] as cited in [243]), which subsequently initiates an expansion wave as gas rushes from the tube towards the evacuated test section [246, 247]. Until its reflection from the tube end reaches valve and nozzle again, steady state test conditions are achieved [243, 246, 247]. For a detailed schematic of the operating principle, the reader is either referred to Reference [243] or to Section 5.9.1, where a simplified drawing can be found.

3.3.3 Calculation of Flow Conditions and Uncertainty Analysis

The total temperature and Pitot pressure of the facility have been measured for a variety of Mach and Reynolds numbers [249]. Depending on the chosen conditions, the most similar configuration is used.

The nozzle supply pressure is measured by a Kulite XCQ-080-70BARA located at the nozzle throat. Using an iterative procedure, the free stream Mach number is obtained by solving the Rayleigh-Pitot formula (see e.g. NACA-1135) employing the ratio of measured Pitot to stagnation pressure. Utilizing the total temperature profile for the condition and previously obtained Mach number, the free stream static temperature T_∞ is computed. Due to the cold flow temperatures of the HDT, Keyes viscosity model [250, 251] is assumed to provide the best approximation for μ. All other flow quantities are deduced from those parameters using the ideal gas relation.

The uncertainty of the Mach number is obtained via a Monte-Carlo method: A normal distribution is generated using the statistical standard error estimate of the Pitot-to-stagnation pressure ratio as one standard deviation. The iterative calculation is carried out for 10,000 values randomly drawn from the generated distribution. One standard deviation of the resulting set of Mach numbers is subsequently used as ΔM. The uncertainty for the total temperature profile is assumed to be $\pm 15\,\mathrm{K}$. All other uncertainties are calculated by propagating those initial statistical errors through the analytical expressions [252].

3.3.4 Free Stream Characterization of the HDT Mach 7 Nozzle

Wylie [68] has conducted experiments investigating the free stream in the HDT by employing up to ten linearly, horizontally arranged Pitot probes with different radii instrumented with Kulites and PCB sensors. In combination, those gauges allow coverage of the full frequency range up to 1 MHz.

All in all, HDT has been found to exhibit relatively low noise levels compared

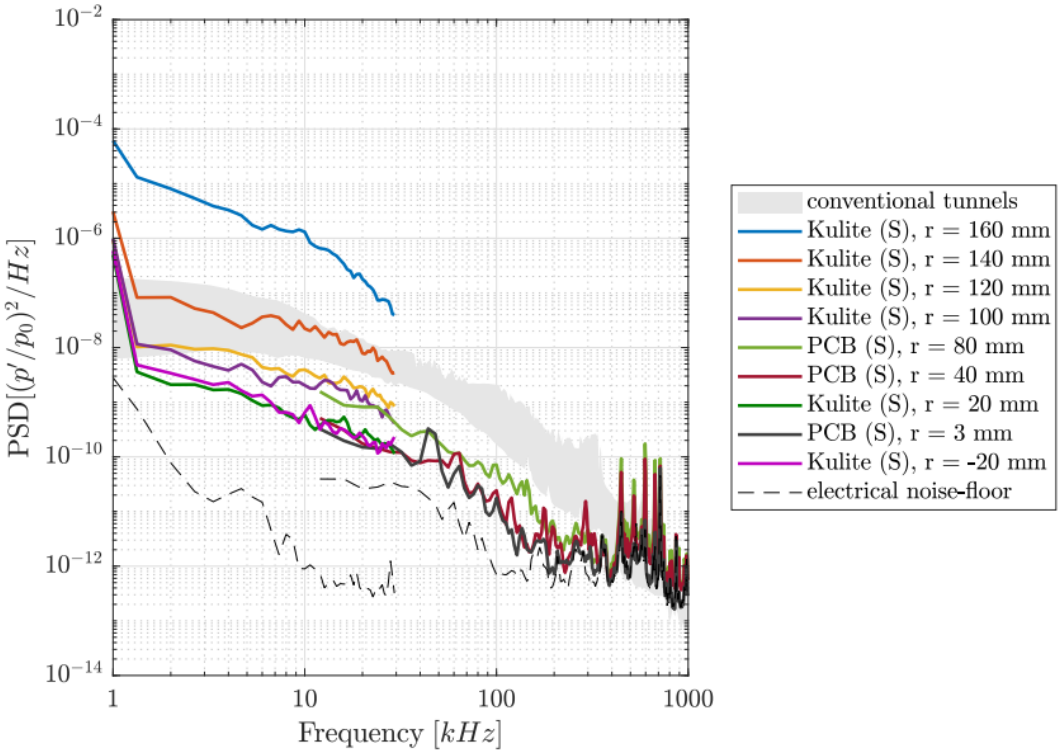


Figure 3.5: Pitot-probe spectral analysis of HDT Mach 7 condition at $Re_u = 12.1 \cdot 10^6/m$. Figure taken from [68]. The shaded-gray area outlines conventional facilities such as the Hypersonic Ludwieg Tube Braunschweig (Mach 6) [247], the BAM6QT (Mach 6) [253], the Sandia Mach 8 hypersonic wind tunnel (see e.g. [102]) and the AEDC Hypervelocity tunnel 9 ([254] as cited in [255]) and was re-plotted by Wylie from Duan [120]. r refers to the radial coordinate from the nozzle centre-line of the respective probe.

to other conventional tunnels across a large spectrum of frequencies (see Figure 3.5). Pitot measurements with Kulite and PCB sensors revealed approximately 0.44 - 0.5% noise fluctuation percentage from $1\,\text{kHz} - 1\,\text{MHz}$ within relevant test conditions [68]. Any fluctuations are only read by the sensors once they have penetrated the shock around the probe, meaning the shown spectra do not truly represent the tunnel flow itself [68, 256]. Nevertheless, other studies followed the same procedure [130] allowing retrospective comparability of obtained fluctuation quantities. Hereby, Wylie [68] normalized the rms of Kulite and PCB data by the nearest absolute (Kulite) Pitot pressure to form such a percentage value. Compared to expected values around $0.5\% - 3\%$ for comparable facilities [126], the obtained noise levels are indeed modest. Moreover, the Mach 7 nozzle also showed good

radial flow homogeneity across its diameter up to $r = 130\,\text{mm}$ from the centreline [68]. Only beyond this threshold, the rms noise percentage increases above 2%, which spatially coincides with a drop in absolute Pitot pressure (see Fig. 4.4 in [68]). 418 mm downstream of the nozzle exit, a narrowing of the core flow diameter could be observed [68], albeit only constricting the useable radius by 10-20 mm. The cone model has a base radius of 73 mm at a length of 594.5 mm, whereby the most upstream 100 mm were inside the nozzle exit, and it is thus assumed to have been fully covered by the low-noise core flow.

Albeit the main dilemma, that all tunnel data is neither representative of free flight [124, 125] nor easily comparable to other facilities [57, 60], remains, one can confidently assume the Oxford HDT to be a reliable source of hypersonic flow conditions not significantly deviating from other established facilities in the field.

3.3.5 Gas Injector System and Operating Procedure

Before a tunnel test run, a gas reservoir is filled with the coolant to $5 - 8.5\,\text{bar}$, depending on what amount of gas is needed during the test. Reservoir and pipework are evacuated to ensure purity of the injected gas, in case of a change in coolant. A relief valve is included into the setup to protect porous injectors, their plenum cavities, hoses, connectors and mass flow controllers from overpressure and mechanical failure. Gas is supplied to the model injectors via Omega mass flow controllers FMA2611A and FMA2609A which have a range of 250 and 50 slpm, respectively. Their accuracy is $(0.8\%\,\text{of reading} + 0.2\%\,\text{of full scale})$ as given by the calibration certificate. Both controllers are connected to the experimenter's computer via and RS232 port and controlled remotely using a serial terminal. Before every shot, the connected mass flow controller is set to the correct injection gas. The firing valve (see Figure 3.6) is opened five seconds before the HDT plug valve opens (see Figure 5.4). During this time, the mass flow controller is activated manually via a command in the serial terminal. This allows for around four seconds for the desired flow rate to establish. Only little variation was found in the flow rate and injection plenum pressure during HDT test time. The mass flow controller delivers

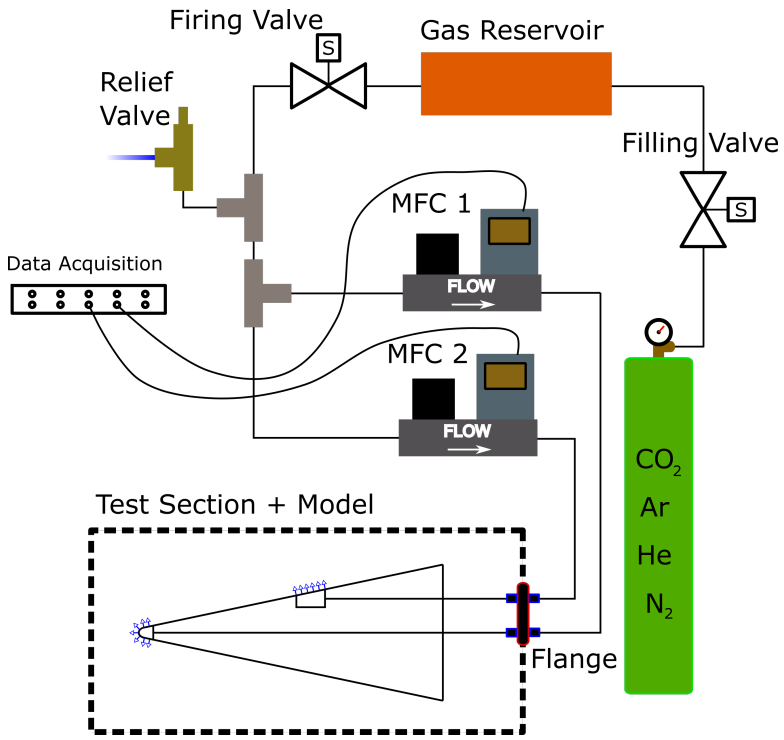


Figure 3.6: Schematic of mass flow controller setup with coolant gas supply. Firing valve and filling valve are remotely controlled solenoid valves.

a $0-5\,\mathrm{V}$ signal which represents the mass flow rate relative to the full scale [257]. It is recorded with a NI PXIe-6368 Multifunction I/O Module data acquisition system at $2\,\mathrm{MHz}$ sampling rate during the tunnel test time.

For this study, two different injector materials were chosen. For the frustum injection patch aluminium BF100Al was selected. For the nose tips BF100Al and CE170 were used [258]. Both are products from Portec [258]. The good machinability of BF100 made it possible to produce the complex conic section geometry necessary for the frustum injector patch, a design inspired from Camillo et al. [104], who managed to produce a similar geometry with C/C. Both materials were known to exhibit some outflow non-uniformity (see e.g. [159] for CE170) and thus an outflow characterization method was applied that is outlined in Chapter 4. While the 20 % porosity and $20\,\mu\mathrm{m}$ pore size [258] compares to other examples in the literature, it is unknown whether the uniformity does as well. Measurements from Langener [71] demonstrate how gas effusion from C/C pieces is far from evenly distributed,

however too little data is available from other studies to conduct a systematic and thorough comparison.

Any temperature gradient within the thickness of the porous medium is neglected, because the experiments are conducted in short duration, low enthalpy wind tunnel facilities. The initial wall temperature of an HDT test run is the measured room and test section temperature. As seen by thermocouple and thin film gauge data, the temperature normally increases by only $2 - 3\,\mathrm{K}$ on the outer model surface during a test run. Herein, much of this increase happens after the nozzle has unstarted. During the utilized test time, heat transfer into the profile of the porous media is therefore neglected. Consequently, the Darcy-Forchheimer equation as presented in Section 2.3.2 is utilized without modification to compute the blowing ratio for the constant thickness frustum injector piece.

3.4 Instability Measurements

Many arguments in this work are based on spectral analysis of instability oscillations found in the boundary layer. Presented spectra from schlieren or surface instrumentation will only provide a time averaged analysis of recorded signals. Before moving on to those types of analysis in the results chapters below, this section will give an insight into the underlying raw signals of the boundary layer oscillations obtained with the given techniques. Figure 3.7 presents differential surface pressure traces and Figure 3.8 shows every tenth image from a schlieren video. The data stems from a tunnel run with a sharp cone without any gas injection. The pressure samples were recorded with 2 MHz sampling rate and show distinct wave packets travelling downstream. Their amplitude mostly grows and eventually they dissolve into more chaotic signals. Following the cross-correlation approach from Kegerise and Rufer [259] the packet's group velocity was determined to be around $850\,\mathrm{m/s}$, which lies slightly below the freestream speed of $\sim 900\,\mathrm{m/s}$ for the given condition. Schlieren images of second mode instability wave packets have been observed by numerous other authors. The waves shown in Figure 3.8 exhibit similarity with optical samples presented by Grossir [8], Kennedy et al. [227], Oddo et al. [260] or

Laurence et al. [99]. In contrast, those observed wave structures differ distinctively in their shape and number of wave crests per packet from the images presented by Schmidt [180], which were first mode instabilities.

The schlieren system employed in this work is evidently sufficiently sensitive to resolve the relevant boundary layer features (see Figure 3.8). The exposure time of the camera does however limit the sharpness of the schlieren objects in the frames. In order to capture longer durations of the tunnel test, a continuous LED light source was employed for most of the schlieren recordings. Therefore, the whole $1.161\,\mu s$ exposure time of each frame was illuminated. The optical features travel approximately 1 mm during the exposure, which does in fact result in some motion blur (see zoomed area of Figure 3.8). Subiah [226] collected schlieren data with the same optical setup, same facility and Mach number, similar frame rates and a similar cone model. However, Subiah [226] employed a pulsed laser with 10 ns pulse width as a light source, resulting in overall sharper and clearer second mode schlieren signals. Nevertheless, the smear in this work was deemed tolerable because the sought-after features could be adequately resolved and all frequency analysis could be conducted successfully. The choice of the continuous light source hence allowed for significantly longer recording times without prohibiting any analysis steps due to a moderate loss in focus.

The test model in use is slender, either sharp or only possesses a small bluntness, axisymmetric and a 2D geometry. It thus fulfils the conditions outlined by Mack [90] to potentially exhibit inviscid second mode instabilities in the boundary layer. Considering the propagation speed of wave-like surface pressure fluctuations, their frequency, the similarity of wave like structures in schlieren images to other studies with confirmed second mode activity (e.g. [8, 99, 227, 260]) and the distinct difference to Schmidt's [180] first mode schlieren photographs, it is concluded that the observed effects stem from second modes as per Mack's [90] terminology.

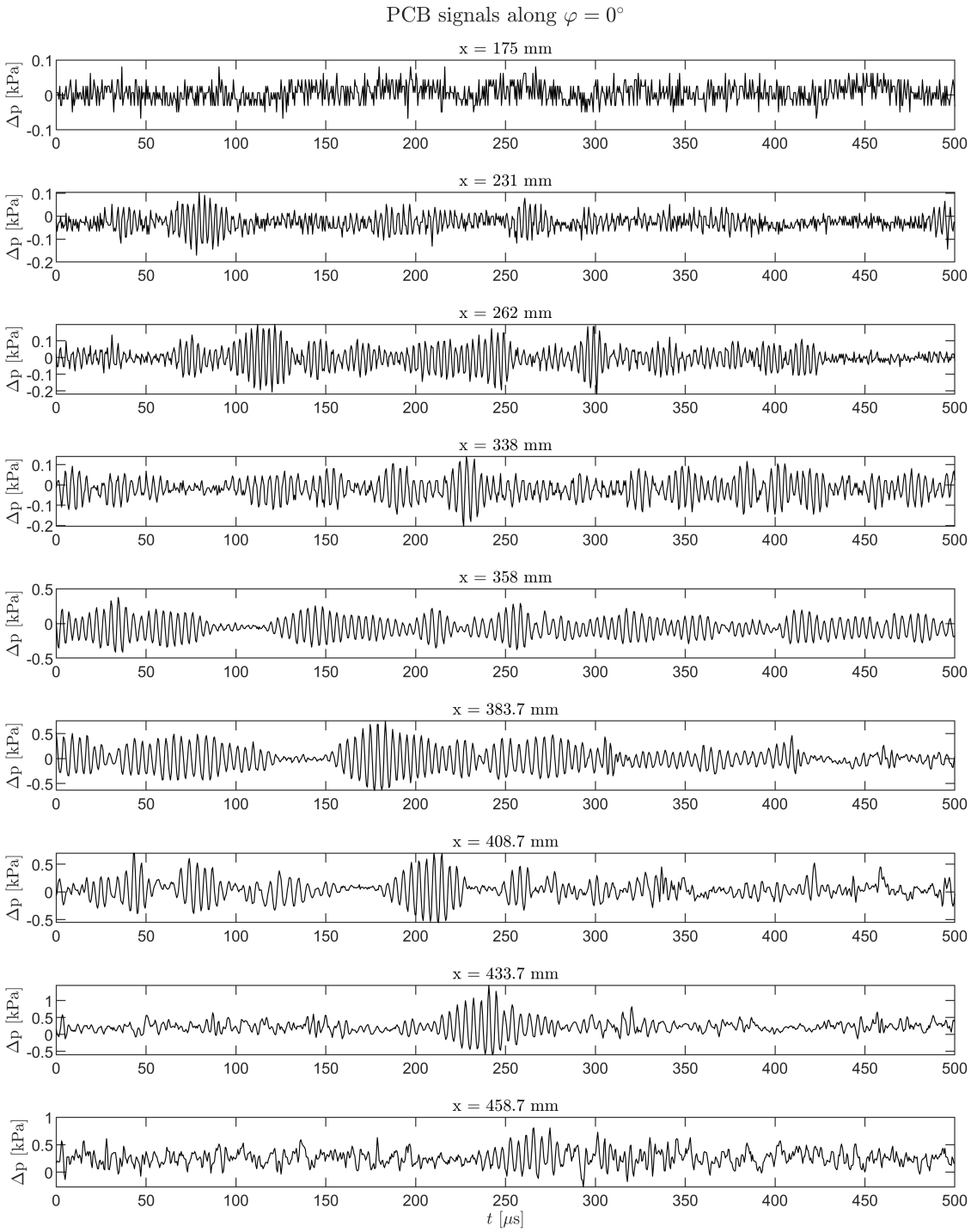


Figure 3.7: Snippets of surface differential pressure signals for a sharp cone without coolant injection at $M = 7$ and $Re_u = 12.8 \cdot 10^6/m$.

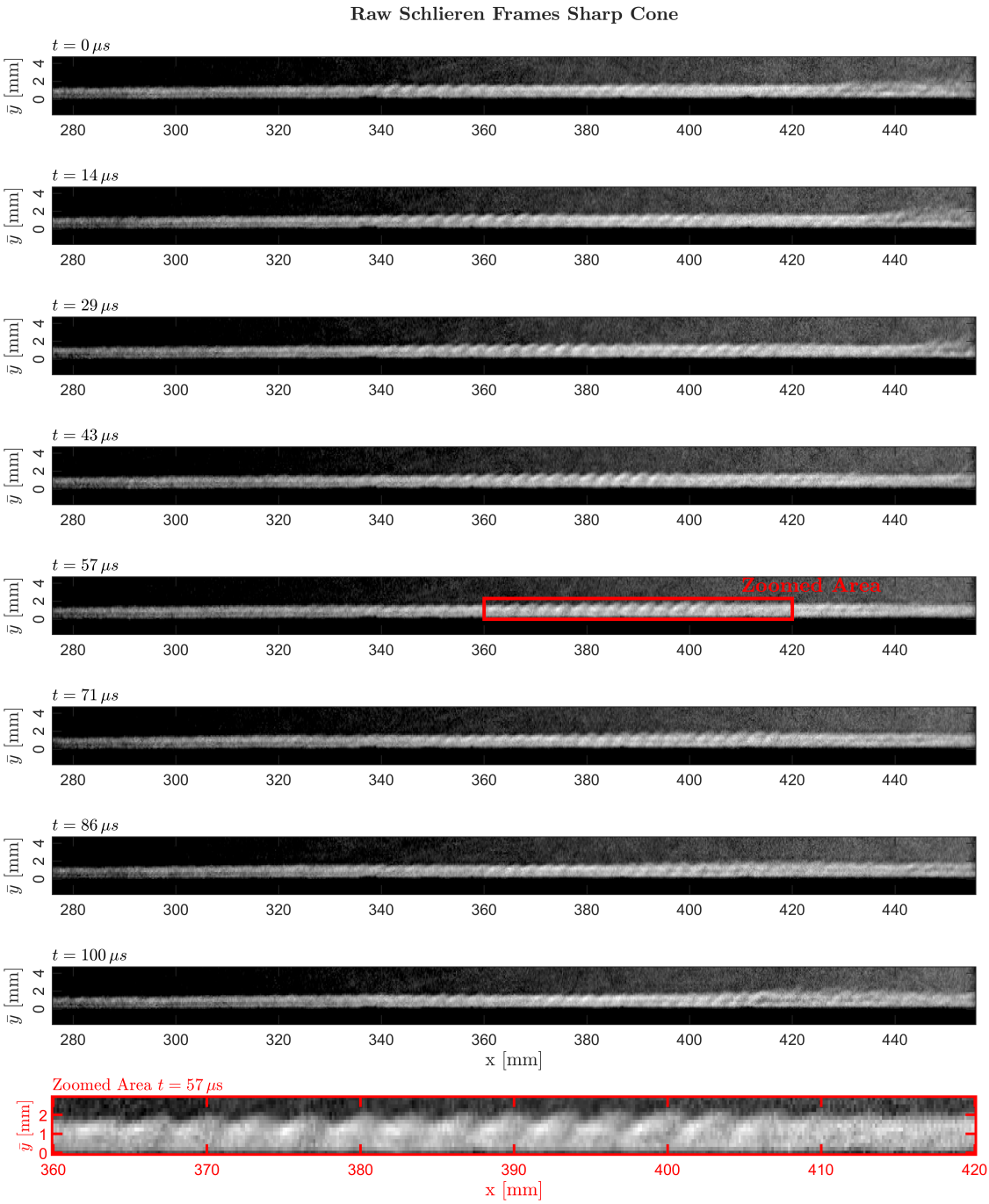


Figure 3.8: Z-type schlieren images of second mode wave packets on a sharp 7° half-angle cone at $M = 7$ and $Re_u = 12.8 \cdot 10^6/m$.

4

Gas Injection into Second Mode Instability at Mach 7

Contents

4.1 Foreword 59
4.2 Introduction 60
4.3 Experimental Setup 61
4.3.1 Cone Model and Instrumentation 61
4.3.2 Injector System 62
4.3.3 Oxford High Density Tunnel and Test Conditions 66
4.4 Influence of Injection on Second Mode Frequencies . . 67
4.4.1 Data Analysis Procedure 67
4.4.2 Experimental Results 70
4.4.3 Helium Injection 73
4.4.4 Frequency Drop and Flow Characteristics 75
4.5 Schlieren Measurements - Boundary Layer Thickness 77
4.6 Discussion 81
4.7 Conclusion 85

4.1 Foreword

The next chapter is dedicated to investigating the influence of injection on developed second mode instability oscillations and to derive initial engineering correlations between coolant and transition mechanisms properties. It is based on a conference paper [261] which was presented to AIAA Aviation 2022. The manuscript was

then converted into a journal paper which is not yet under review. It is presented in unchanged form in the chapter below. The statement of authorship can be found at the end of the chapter.

4.2 Introduction

Minimizing the heat load on spaceplanes or re-entry vehicles is a critical issue for hypersonic flight [262]. Boundary layer transition research has been of interest due to its overarching role in this problem for a long time [263]. Increased heat loads of turbulent boundary layers [64, 88] and subsequent design requirements necessitate rigorous experimental and theoretical investigations into cooling techniques and their intrinsic influence on transition. Older research in the area only provides transition location data, mostly inferred from heat transfer measurements (e.g. [56, 187]). It is nowadays however well established that the so called second mode or Mack mode [90] is the decisive mechanism that causes transition in hypersonic boundary layers on slender, axisymmetric 2D geometries. Owing to the high relevance of those shapes, contemporary research is additionally focused on capturing frequency data (see e.g. [8, 100, 104]). It used to be a broad agreement, for example described by Schneider [56], how gas injection (as an active cooling method) into a boundary layer has a purely destabilizing effect. Nevertheless, during the last 20 years this has been challenged [104]: Leyva, Fuji, Hornung and Jewell et al. [109, 203, 204, 209, 210] have published research on the stabilizing effect of CO_2 injection into high enthalpy boundary layers. Furthermore, work from DLR suggested a strong influence of the position of injection with respect to Reynolds number on its repercussions for stability. Camillo et al. [104, 211] observed that all publications which found a destabilizing effect had something in common: “mass addition in those studies was performed along a large portion of the body” [104]. In their experimental case however, gas effusion confined near the transition Reynolds number resulted in “a transition delay of approximately 17%” [104] using nitrogen as a coolant and hence excluding the thermochemical effects discovered by Fuji et al. [104, 204].

Their tests were conducted in HEG, a reflected shock tunnel at Mach 7.3 [104,

211] and a total flow enthalpy from 3.08 MJ/kg to 3.24 MJ/kg. In contrast, an experiment in the VKI-H3 Mach 6 noisy blowdown tunnel with a cone including a porous section provides similar unit Reynolds number and total temperature as found in the University of Oxford's HDT facility [108]. Miró Miró et al. [108] found no transition delay and rather confirmed the historical consensus of destabilization by gas transpiration. Camillo et al. [104] explain the difference in observations with the discrepancies in model and injector geometries.

In numerical investigation Miró Miró et al. [169] recently challenged the belief that light gases automatically destabilize more, by finding helium to dampen instability oscillations. Similarly to Camillo et al. [104], they highlight the role of the injector geometry. In contrast, they found not the location, but the "discontinous" [169] geometry of effusion to be driving the historically observed advance in transition. Furthermore, Schmidt et al. [180, 213, 214] provide extensive data for three different coolants - Nitrogen, Helium and RC318 - and their influence on a conical boundary layer as well as instability oscillations. This study is limited to Mach 4 and therefore rather assigned to the supersonic speed regime [180].

Because an entirely continuous injection area is not realistic for a transpiration cooling application [45], more effort is necessary to investigate small porous sections. For this work, a variation of freestream unit Reynolds numbers allows different levels of instability at the injection location on a cone. A variety of different gases were injected, whilst keeping the blowing ratios comparable. In order to create a realistic case for transpiration cooling, the injection location is confined to a small area relative to the whole model comparable to Camillo et al. [104].

4.3 Experimental Setup

4.3.1 Cone Model and Instrumentation

The model for wind tunnel testing is a 7° half-angle cone with a sharp nosetip ($R_N \approx 0.05\,\text{mm}$) and a total length of 594.5 mm. The porous injector is a 60° frustum insert at 300 mm from the sharp tip as shown in Figure 4.1 and it was machined from porous aluminium Metapor BF100 Al, produced by Portec [258].

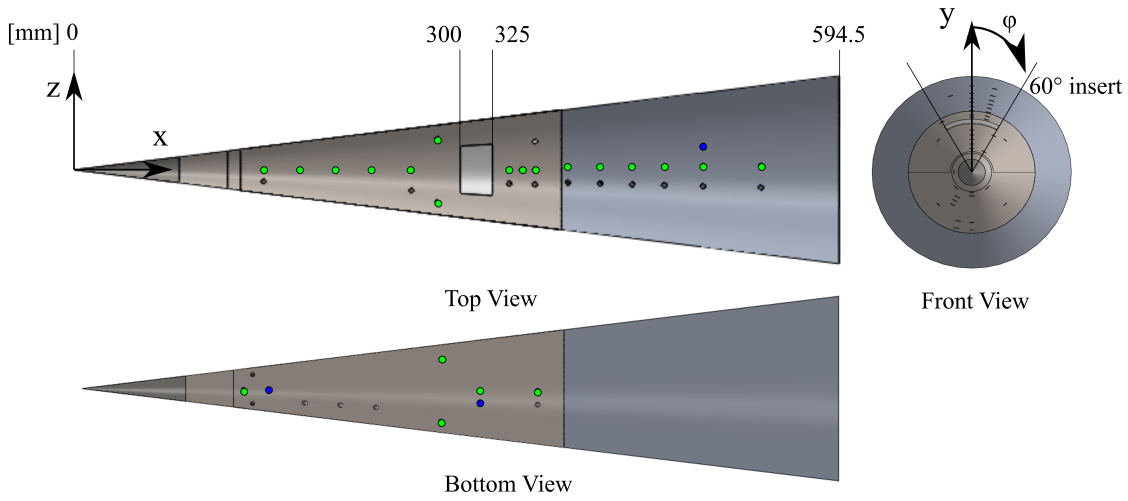


Figure 4.1: Geometry of the cone model. Green: PCB, Blue: Kulites. The given coordinate system (x, y, z, φ) will be used in all further representations.

Remaining components are manufactured from stainless steel except for the rear segment and sharp nosetip which are made from 7075 T6 aluminium. Albeit not aerodynamically matched, the model has similar proportionalities to the cone used by Camillo et al. [104], which may allow reasonable qualitative comparisons at similar Mach numbers. 19 PCB ultra high speed piezoelectric differential pressure transducers are flush mounted on the model surface to provide high frequency pressure data. This sensor model has been used by multiple research groups for boundary layer instability investigation such as Wylie et al. [224], Grossir [8], Casper et al. [102, 264] and Estorf et al. [100]. Types PCB132A31 and PCB132B38 are used and no noticeable difference in their frequency response was found. In addition, three Kulite XCEL-152 provide absolute pressure data for the model surface and the inside of the injection gas plenum, respectively. The instrumentation types and location are shown in Figure 4.1.

4.3.2 Injector System

A reservoir tank and a mass flow controller supply the porous injector with coolant gas. For this application, an Omega FMA2611A 250 slpm range model is chosen. The repeatability is ±0.2 % of the full scale and the accuracy of the mass flow is

Table 4.1: Sensor locations on cone model. ($\varphi = 0°$) corresponds to the central plane of the injector.

Hole Number	Sensor Type	x [mm]	φ [°]
PCB 1	Differential Pressure - Surface	107.0	0
PCB 2	Differential Pressure - Surface	127.0	0
PCB 3	Differential Pressure - Surface	147.0	0
PCB 4	Differential Pressure - Surface	175.0	0
PCB 5	Differential Pressure - Surface	203.0	0
PCB 6	Differential Pressure - Surface	231.0	0
PCB 7	Differential Pressure - Surface	262.0	0
PCB 8	Differential Pressure - Surface	338.0	0
PCB 9	Differential Pressure - Surface	348.0	0
PCB 10	Differential Pressure - Surface	358.0	0
PCB 11	Differential Pressure - Surface	282.0	45
PCB 12	Differential Pressure - Surface	282.0	315
PCB 13	Differential Pressure - Surface	282.0	135
PCB 14	Differential Pressure - Surface	282.0	225
PCB 15	Differential Pressure- Surface	312.5	180
PCB 16	Differential Pressure - Surface	358.0	180
PCB 17	Differential Pressure - Surface	383.7	0
PCB 18	Differential Pressure - Surface	408.7	0
PCB 19	Differential Pressure - Surface	433.7	0
PCB 20	Differential Pressure - Surface	458.7	0
PCB 21	Differential Pressure - Surface	488.7	0
PCB 22	Differential Pressure - Surface	533.7	0
Ku 1	Absolute Pressure - Surface	145.0	180
Ku 2	Absolute Pressure - Surface	312.5	180
Ku 3	Absolute Pressure - Surface	388.7	330
Ku 4	Absolute Pressure - Plenum	N/A	N/A

$\pm(0.8\%\,\text{reading} + 0.2\%\,\text{fullscale})$ [257]. Two main reasons motivated the choice of those devices for the application: firstly, the mass flow rate can be directly read from the MFC. Secondly, precisely setting the mass flow rate for different gases shall enable a high level of repeatability in between experiments while keeping the operational procedure simple. The mass flow rate $\dot{m}$ is directly used for the calculation of the blowing ratio F.

$$F = \frac{\rho_c u_c}{\rho_e u_e} \tag{4.1}$$

Where the index e represents the boundary layer edge and c the properties of the injected gas. This normalization is a standard practice in the literature (e.g.

[53, 104, 153]). Boundary layer edge properties are hereby calculated using the Taylor-Macoll solution [265] via Ishimatsu's approximation [266].
Another quantitative comparable value for the amount of blowing can also be defined via St and is for example shown in [154, 156]:

$$B_h = \frac{F}{St_0} \tag{4.2}$$

Hereby, the uncooled Stanton number St_0 is obtained via a laminar Eckert reference enthalpy calculation [267] using the Chilton Colburn analogy factor [268] and the viscosity models from Keyes [251] and Sutherland [269]. The given St_0 is then adapted for a cone by multiplication with $\sqrt{3}$ according to the Mangler transformation [64, 270] for laminar flow and a factor of 1.15 for turbulent flow as given by Crabtree [271]. The injector outflow characteristics are determined using the method described in Ref. [175]. It is based on a Nelder-Mead algorithm [272] and carried out using Matlab's inbuilt FMINSEARCH function [273]. Herein, the Darcy-Forchheimer coefficients were found to be $K_D = (4.2 \pm 0.1) \times 10^{-12}\,\mathrm{m}^2$ and $K_F = (2.28 \pm 0.01) \times 10^{-8}\,\mathrm{m}$ within 95 % confidence. The porous material in use might have a macroscopically inhomogeneous distribution of porosity, or leaks could be present at the interfaces with surrounding stainless steel. The outflow is hence characterized by employing a Dantec Dynamic 55P11 straight hot-wire probe. Due to the curved shape of the injector, the probe tip is guided using a five-axis traverse system. It keeps the probe arm at a constant distance of $(1.5 \pm 0.5)\,\mathrm{mm}$ to the porous material, while the mounting arm maintains a surface normal orientation to minimize flow interactions. Velocity values are recorded as an average over three seconds at every location. Buffer time between measurements minimizes likely disturbances from traverse readjustment motions. During the entire test time the dry air flow rate is kept constant by a mass flow controller Omega FMA2609A at 3.0 slpm. Figure 4.2 depicts a total of 500 points measured along the surface, with 20 columns along the 25 mm axial length of the injector and 25 rows spanning $-35° \leq \varphi \leq 35°$ in azimuth. The spatial step width of the sampling procedure as well as the wire length of the probe ($\approx 1.25\,\mathrm{mm}$) do not allow to resolve single

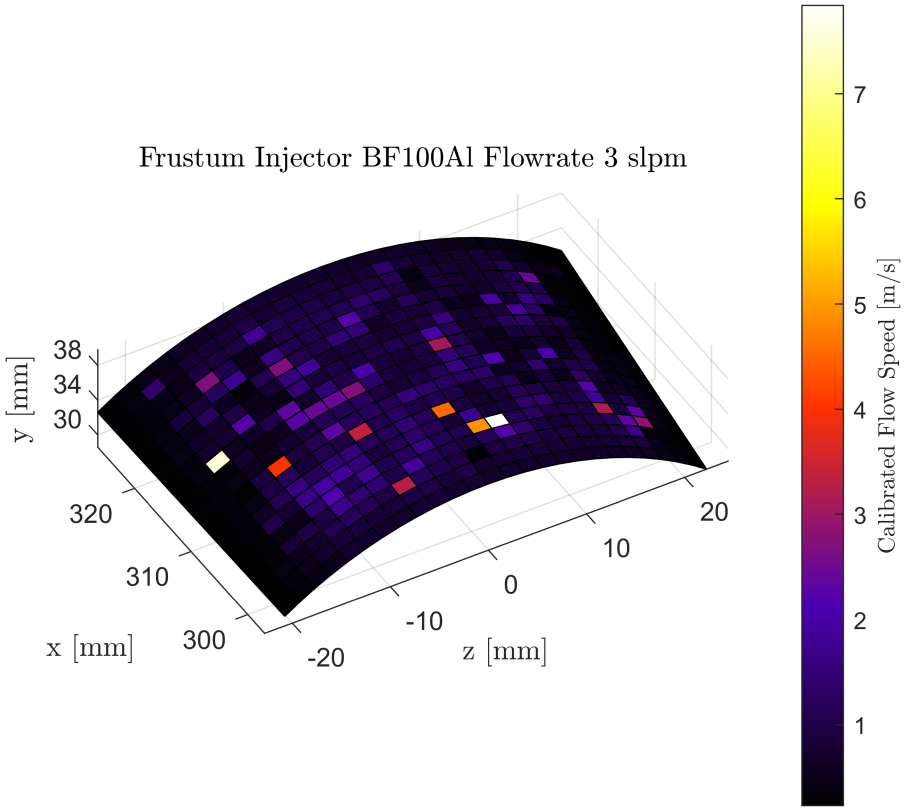


Figure 4.2: Hot-wire outflow measurement at atmospheric pressure.

pores and their respective outflow jets. Instead, the setup only aims to measure macroscopic non-uniformities or leaks on the scale of the model. Interfaces of porous aluminium and impervious steel seal sufficiently. No leaks can be seen in Figure 4.2 around the circumference of the porous segment. In contrast, outflow hotspots on the millimetre scale are revealed across the injector. Miró Miró et al. [108] characterized their injectors using a pitot tube. They found mass transpiration to be inhomogeneously distributed in general, but one of two samples had a substantially uneven effusion profile. While acknowledging such features become visible with IR thermography, they report almost no influence on the stability measurements [108]. As those tests were conducted in a noisy blowdown tunnel and had pore sizes an order of magnitude higher than BF100Al, more research is necessary to explore the effect of blowing inhomogeneities in HDT on boundary layer transition experiments.

Table 4.2: Flow properties for the HDT Conditions.

Cond.	T_0 [K]	M_∞	T_∞ [K]	Re_u [10^6/m]	p_∞ [Pa]	p_0 [kPa]
1	450 ± 15	7.0 ± 0.06	42 ± 1.5	12.2 ± 0.7	490 ± 15	2000 ± 10
1a	460 ± 15	7.0 ± 0.06	42 ± 1.5	12.9 ± 0.7	520 ± 15	2200 ± 10
1b	470 ± 15	7.0 ± 0.06	43 ± 1.5	13.4 ± 0.8	560 ± 16	2340 ± 10
2	450 ± 15	7.0 ± 0.06	42 ± 1.5	7.1 ± 0.4	283 ± 8	1140 ± 10
2a	450 ± 15	7.0 ± 0.06	43 ± 1.5	7.5 ± 0.4	306 ± 9	1220 ± 10
2b	460 ± 15	7.0 ± 0.06	43 ± 1.5	7.9 ± 0.5	330 ± 10	1320 ± 10

4.3.3 Oxford High Density Tunnel and Test Conditions

Measurements are conducted in the Oxford High Density Tunnel (HDT) at Mach 7, while operating the facility as a Ludwieg Tube [245]. The barrel is 17.4 m long and is attached to a fast acting plug-valve and a converging/diverging nozzle [243]. It has been commissioned by Wylie et al. [225] for boundary layer experiments at Mach 7, by comparing its characteristics to the DLR H2K facility. Additional information about the HDT's design can be found in Refs. [225, 243].

Two levels of stability are investigated by varying Re_u: Firstly, a transitioning boundary layer at the location of the injector (Condition 1) and secondly, a status of slowly growing second modes (Condition 2). HDT produces several steady state 'plateaus' of flow conditions downstream of the nozzle during a single test run, which enable a narrow sweep in flow variables. Details about total temperature profiles and how those 'plateaus' have been previously utilized in hypersonic transition testing can be found in Refs. [68, 249]. Table 4.2 summarizes the flow properties of the main 'plateau' (1 or 2) and of the supplementary steady state conditions (a and b) with slightly higher Re_u, respectively. Data is recorded at 2 MHz using a NI PXIe-6368 Multifunction I/O Module data acquisition system and suitable amplifiers for each sensor type. The Kulite signals are processed by a FYLDE transducer amplifier and the PCB sensors by a PCB Piezotronic 483C15 series signal conditioner.

All experiments are conducted at zero degrees angle of attack, with the cone model mounted on an automated traverse mechanism to allow alignment of the model with $\pm 0.1°$ accuracy. The positioning procedure is carried out using frequency

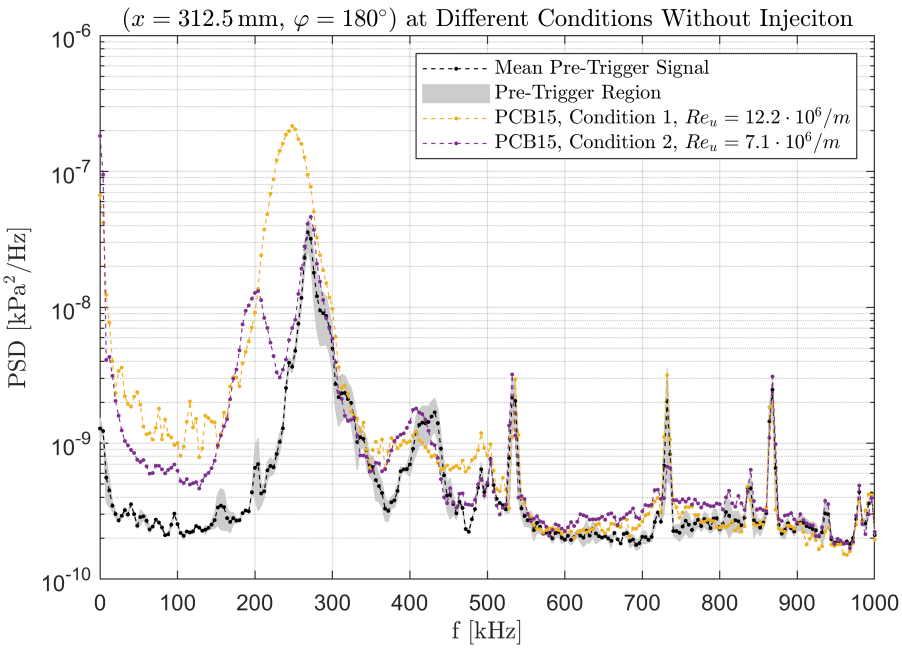


Figure 4.3: PSD of two conditions used during the testing.

measurements at four different azimuthal positions and the same axial location. The model is considered aligned upon acquisition of sufficiently congruent second mode frequency spectra at all azimuthal measurement points.

4.4 Influence of Injection on Second Mode Frequencies

4.4.1 Data Analysis Procedure

Characteristics of the second mode are investigated using frequency data obtained from PCB sensors. Herein, a power spectral density is calculated using Welchs PSD estimate [274, 275] with a Hann window of 50% overlap [276, 277]. An example is pictured in Figure 4.3. The investigated tunnel conditions show either strongly amplified second modes at the injection location (Condition 1, $Re_u = 12.2 \cdot 10^6/\mathrm{m}$) or initial growth of instabilities (Condition 2, $Re_u = 7.1 \cdot 10^6/\mathrm{m}$). PCB15 is located at $x = 312.5\,\mathrm{mm}, \varphi = 180°$ and hence at the opposite side of the porous injector location. During those shots, no coolant injection was present. A resonance frequency and electrical noise peak that is also found in the pre-trigger signal, where no flow is present over the sensor, unfortunately lies closely to the expected value

of the second mode. In the presented examples (Figure 4.3), the signal during the flow is either about an order of magnitude stronger than the noise signal or the frequency peaks are at different locations. This is however not true for all sensors and conditions. In order to investigate the development of the second mode characteristic frequency peak via its centre, FWHM and amplitude it is necessary to remove this artefact. The applied procedure was loosely inspired by approaches from Morris [278] or Lindner et al. [279] and aims to iteratively remove noise peaks. In agreement with Ref. [104], we herein assume that all fitted peaks follow a Gaussian distribution. Fitting is carried out through a least square method [280] from Pythons *scipy* package [281]. An example of the fitting results can be seen in Figure 4.4. The central frequency and the power carried in the spectrum are selected to characterize changes in instability behaviour and infer relations across injection gases and flow conditions. The frequency f is the centre of the fitted Gaussian distribution. f/f_0 will be plotted to reveal effects of gas effusion, wherein f_0 is the frequency at the same sensor location without any coolant injection. For the shown amplitudes of the second mode, Matlabs *bandpower* function is applied to the PSDs from 100 kHz to 400 kHz. The bandpower from the same interval in the pre-trigger signal is subtracted. Said integration boundaries are held constant to provide comparability between conditions, even if the second mode peak shifts. Regular occurrence of turbulence at a sensor location is depicted in surface pressure spectra by a broad, evenly spread out rise in signal at lower frequencies (see e.g. Figure 4.4 $x = 383.7\,\mathrm{mm}$ compared to $x = 282\,\mathrm{mm}$ in between ($0 < f < 150\,\mathrm{kHz}$) or [8, 68]). This may influence the signal to background level of the second mode peak to a prohibitive extent and distort the aforementioned fitting procedure. A fit is only performed to the signal, and second mode characteristics are likewise only deduced, if the spectral peak can be unambiguously identified.

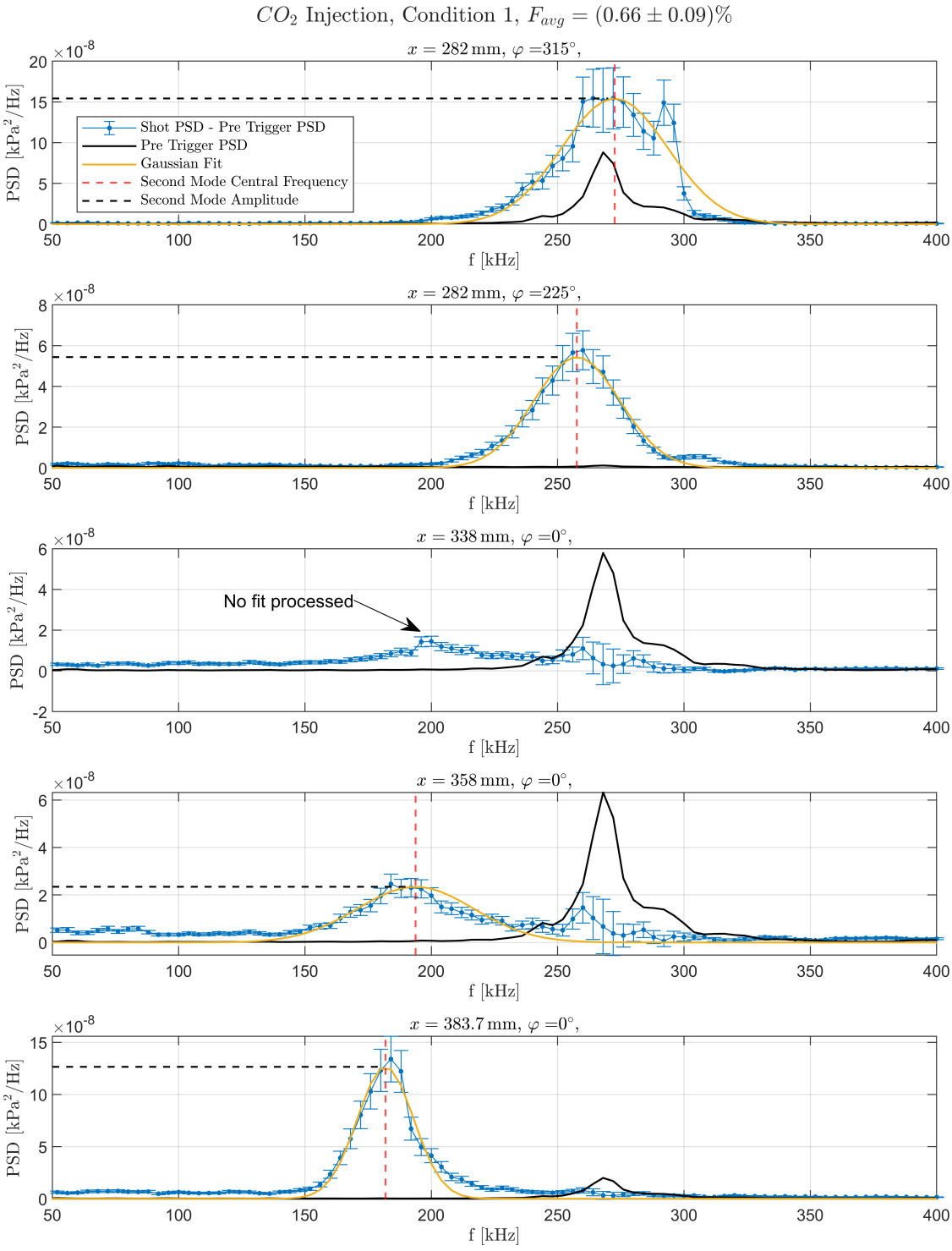


Figure 4.4: Exemplary fits to PSD data. The injector spans from $x = 300\,\text{mm}$ to $x = 325\,\text{mm}$. The signal in row three of the Figure was not deemed sufficient to perform a fit and use it for further analysis. Accordingly, the respective point in Figure 4.6 (red crosses for $F(\text{CO}_2) = 0.66\%$) is missing.

4.4.2 Experimental Results

Frequency Development without Injection

Tracking the central frequency of the second mode gives insight into behaviour of the mechanism leading to transition. Schlieren images, frequency measurements, comparisons to previous work using similar geometries in the same facility [68] and variables like geometry and Mach number (see Section 3.4) are ground for supposing that the frequency peak around 280 kHz stems from second mode instability waves. As shown in Figure 4.5 their frequency decreases steadily downstream when no coolant was injected. For Condition 1, the sensors with $x > 470$ mm already showed an increase in low frequency content, making the fitting procedure less reliable. The points with $x > 470$ mm are therefore excluded. The decrease can be explained due to the increase in boundary layer thickness downstream, as for example also observed and described by Grossir [8]. The frequency of the second mode is therefore expected to be lower for $Re_u = 7.1 \cdot 10^6/m$ than for $Re_u = 12.2 \cdot 10^6/m$. Those baseline frequency parameters will hereafter be used as f_0 in all further plots. Symbols represent the conditions or blowing ratios, colours the coolant gases and the values of F are given in the figure legends.

Moderate Reynolds Number - $Re_u \approx 12.2 \cdot 10^6/m$

Figure 4.6 displays mean second mode frequencies which were obtained from surface pressure measurements downstream of a porous injector. When gases are injected into the boundary layer, the power and frequency of the second mode are reduced. For carbon dioxide, argon and nitrogen, we report a larger reduction in those parameters with increasing blowing ratio. Those results are in qualitatively agreement with Schmidt's work [180], Camillo et al. [104] and also Miró Miró et al. [108]. For $F \approx 0.6\,\%$ the effects of CO_2 and Ar are comparable. A clear dependency on gas type cannot be inferred, yet. In contrast to all other gases and aforementioned studies, helium appears to cause a frequency increase further downstream for one blowing ratio. Increasing F(He) further, the frequency peaks in the second mode spectra were damped significantly and the fitting procedure could thus only be

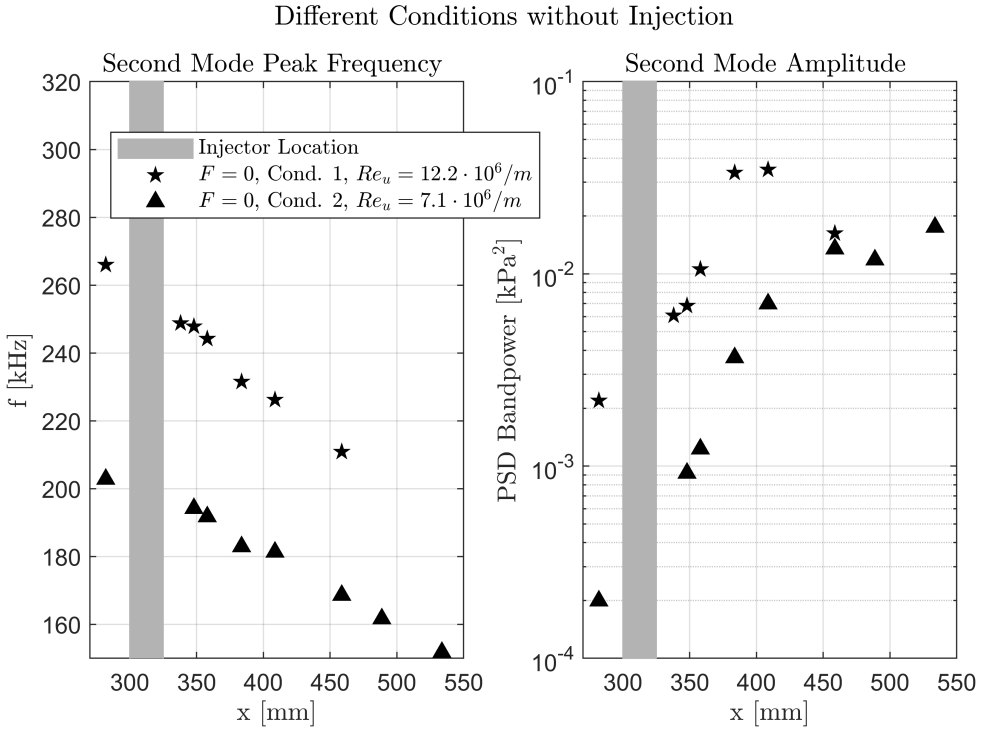


Figure 4.5: Condition 1 and 2 second mode development without injection.

performed reliably for a single sensor at $x = 383.7\,\text{mm}$, $\varphi = 0°$. Correspondingly, helium also shows a unique effect among the gases on the spectral power. Especially downstream of 400 mm, Figure 4.6 (left) shows substantial reductions in bandpower with helium effusion. The values only approach the shot without injection at the most downstream sensor. Section 4.4.3 offers further insights and details.

Low Reynolds Number - $Re_u \approx 7.1 \cdot 10^6/m$

At the condition shown in Figure 4.7 (Condition 2), slowly amplifying second modes were present at the location of the injector (see Figure 4.3). The coolant flow from the porous material causes the frequency of the observed second mode peak to drop by up to 28% for argon. At $x = 338\,\text{mm}$, which is 13 mm downstream of the injector, the PSD profile was altered to a degree that second mode peaks could no longer be recognized and no Gaussian fit was calculated. Those points are hence not shown in the plot. Heavier gases seem to cause a slightly larger effect in terms of frequency reduction, which is visible when comparing nitrogen and argon as well as argon and carbon dioxide for their respectively comparable injection rates. In

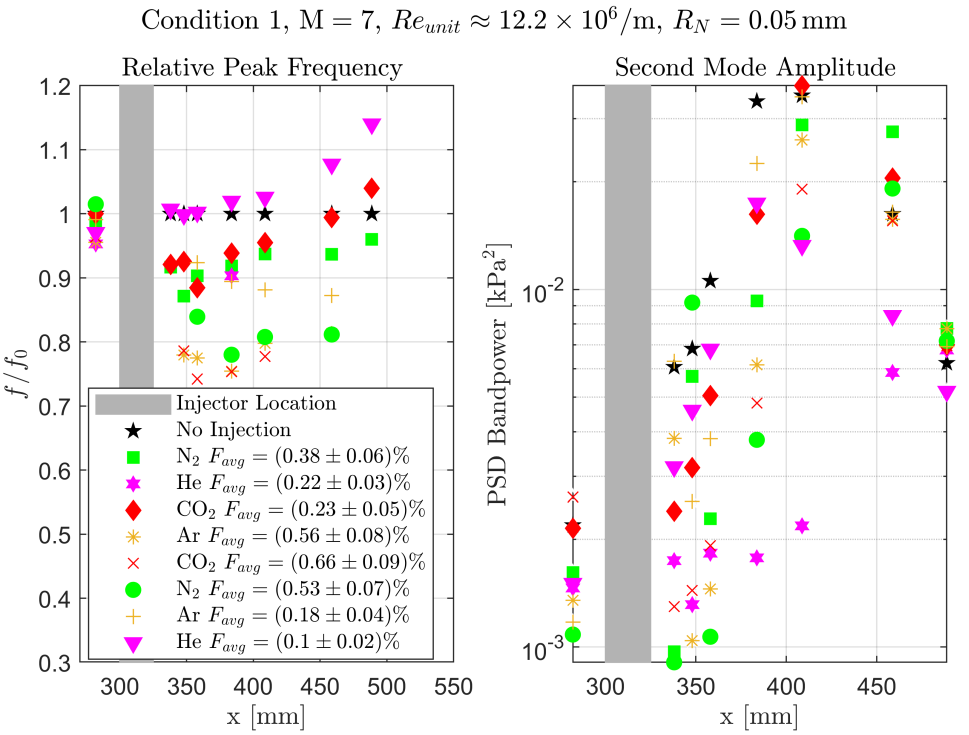


Figure 4.6: Condition 1 second mode properties for various gases and blowing ratios.

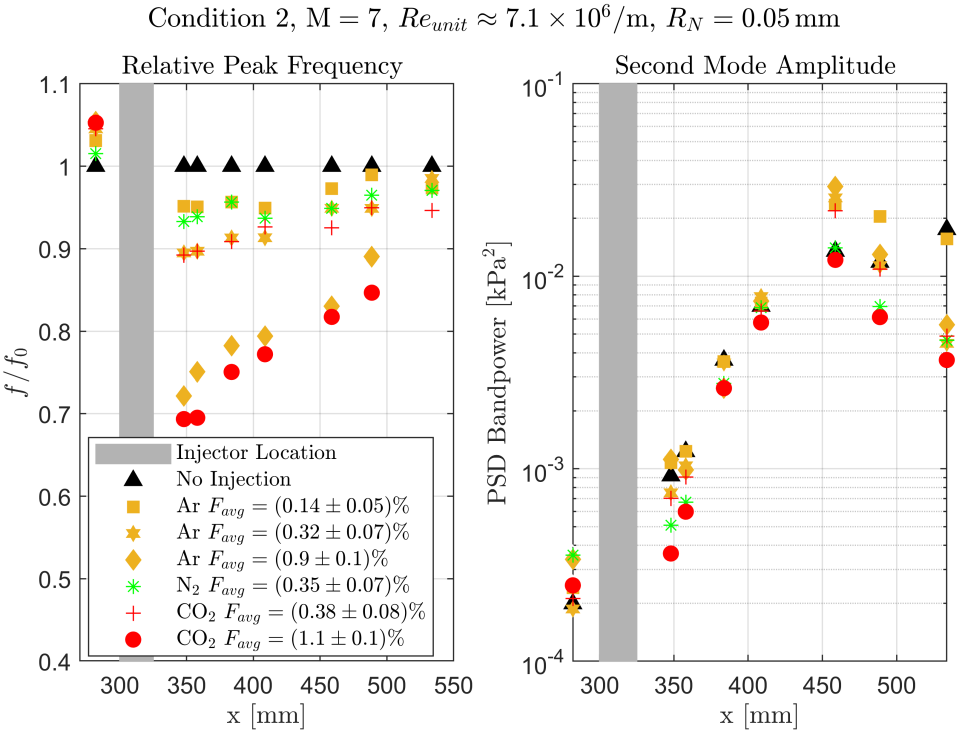


Figure 4.7: Condition 2 second mode properties for various gases and blowing ratios.

contrast, the behaviour of f/f_0 seems to be more strongly dependent on the blowing ratio itself. This is evident for all three argon and both carbon dioxide cases. The power in the frequency band surrounding the second mode shows slightly different dynamics. Just downstream of the injector, carbon dioxide and nitrogen show the strongest reduction in power despite the second mode frequency not being affected to a similar degree. However, the trend is not as permanent further downstream. For both conditions the second mode parameters slowly approach the undisturbed values when monitoring its behaviour in streamwise direction. An explanation for this could be increased mixing of the coolant gases, as simulated and measured by Ifti et al. [49–51] at alike flow conditions.

4.4.3 Helium Injection

Despite comparably low blowing ratios helium injection had a unique effect on the second mode characteristics. For Condition 1 and $F_{avg}(\mathrm{He}) = 0.22\,\%$, the PSD was changed too significantly to still recognize a second mode peak and perform the fitting procedure. It is consequently necessary to thoroughly investigate the individual PSD traces. Injection gases other than helium had a similar effect at moderate and low blowing ratios: The second mode peak was shifted to lower frequencies and also lost total height causing a reduction in bandpower. This is for example shown in Figure 4.4 for carbon dioxide. During the experiments, it was found that with heavier gases only blowing ratios exceeding 0.5 % at condition 1 disturb the boundary layer flow to such an extent that no second mode could be recognized in the power spectra. Those cases are accompanied by an instantaneous rise in low frequency content indicating a turbulent frequency spectrum. In contrast, minimal helium blowing caused the second mode peak to shrink disproportionally without causing a strong rise in low frequency content as revealed in Figure 4.8. The shot with $F_{avg}(\mathrm{He}) = 0.22\,\%$ is plotted in blue. The spectrum shows a substantial reduction of power in the frequency band around the usual second mode peaks. This effect is particularly pronounced at the sensors with locations downstream of $x = 358\,\mathrm{mm}$. It is also notable how the low frequency content $f < 170\,\mathrm{kHz}$ follows

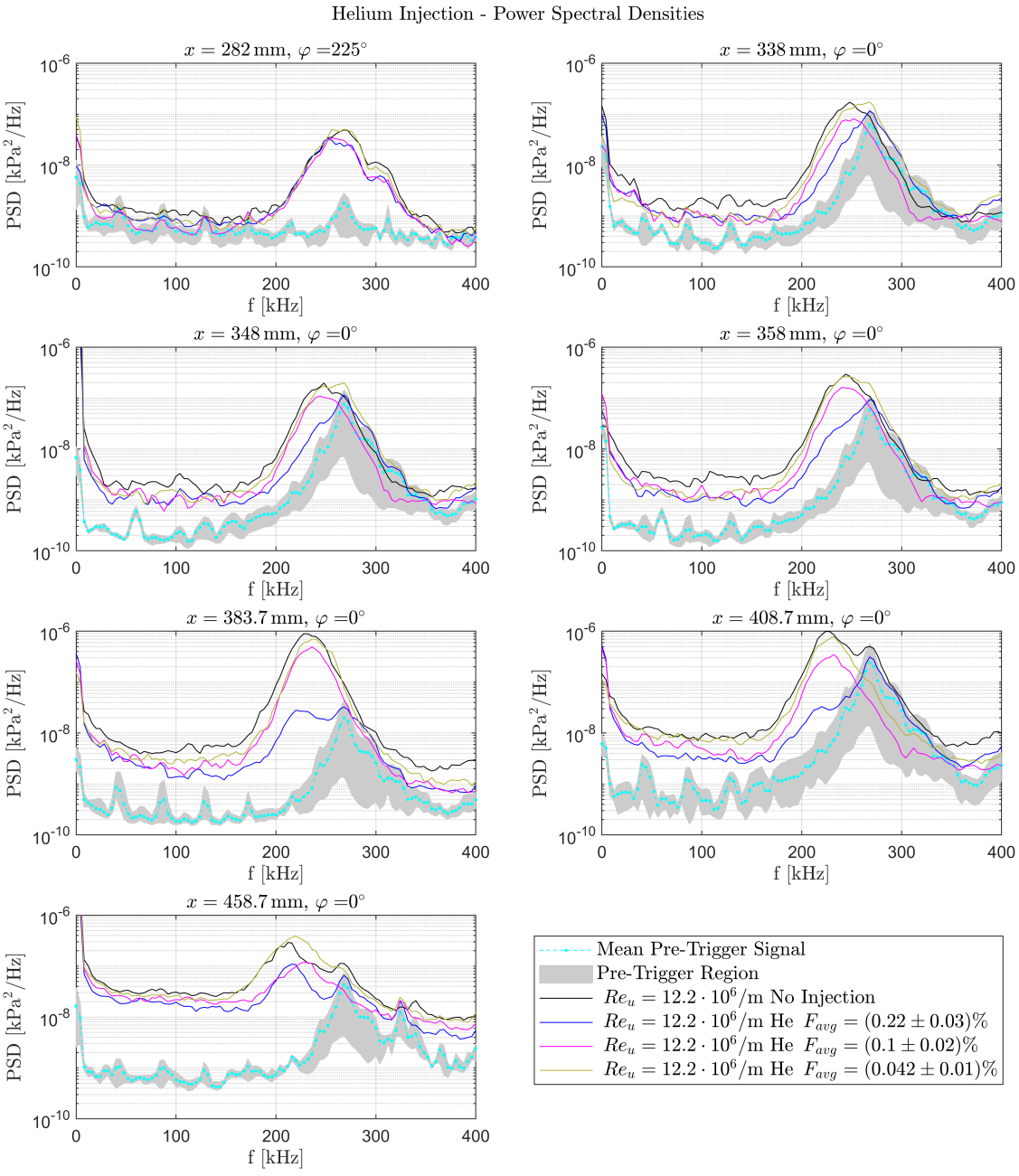


Figure 4.8: PSDs for helium injection at condition 1.

the order of the blowing ratios reciprocally for all sensors downstream of the injector once it starts rising.

In the simulation work from Miró Miró et al. [169], where gas effusion covered the entire cone except the tip, it is predicted that helium cooling would dampen second modes [169]. Miró Miró et al. [169] theorize - albeit they quickly dismiss this inference - that the effect of helium may cause a transition process entirely independent from the Mack mode.

The bandpower shown in Figures 4.6 and 4.7 is a cumulative value representing the entire range from 100 kHz to 400 kHz. In view of the values shown in Figure 4.6 for this helium experiment, there seems to be a significant deviation from the usual amplification and growth process of the instability. Up to the point of a nearly turbulent frequency spectrum there is almost an order of magnitude difference in spectral power between the uncooled case and helium injection. The shown initial PSD analysis of surface measurements might therefore be insufficient to capture a non-Mack mode instability spectrum, if such an effect is present. Ref. [169] does not provide second mode frequency spectra for discontinuous injection geometries, which makes the comparison of f/f_0 plots less feasible.

4.4.4 Frequency Drop and Flow Characteristics

All previous figures focus on the spatial development of the second mode downstream of the injector for several different gases. For each comparison, the tunnel condition and, as far as possible, the blowing ratio were kept constant and comparable. As different tunnel conditions lead to a variety of changing boundary layer characteristics, Figure 4.9 shall attempt to draw conclusions between flow environment, blowing ratios and oscillation variables simultaneously. The relative peak frequency is plotted against three different normalization parameters for one location 32 mm downstream of the injector. Self-evidently, the non-blowing cases for conditions 1 and 2 (in black) align at $F = 0$ and $f/f_0 = 1$ due to their role as reference cases. Adding further considerations about simplified flow physics, the blowing parameter B_h, which is calculated according to the procedure described in Section 4.3.2 is multiplied by

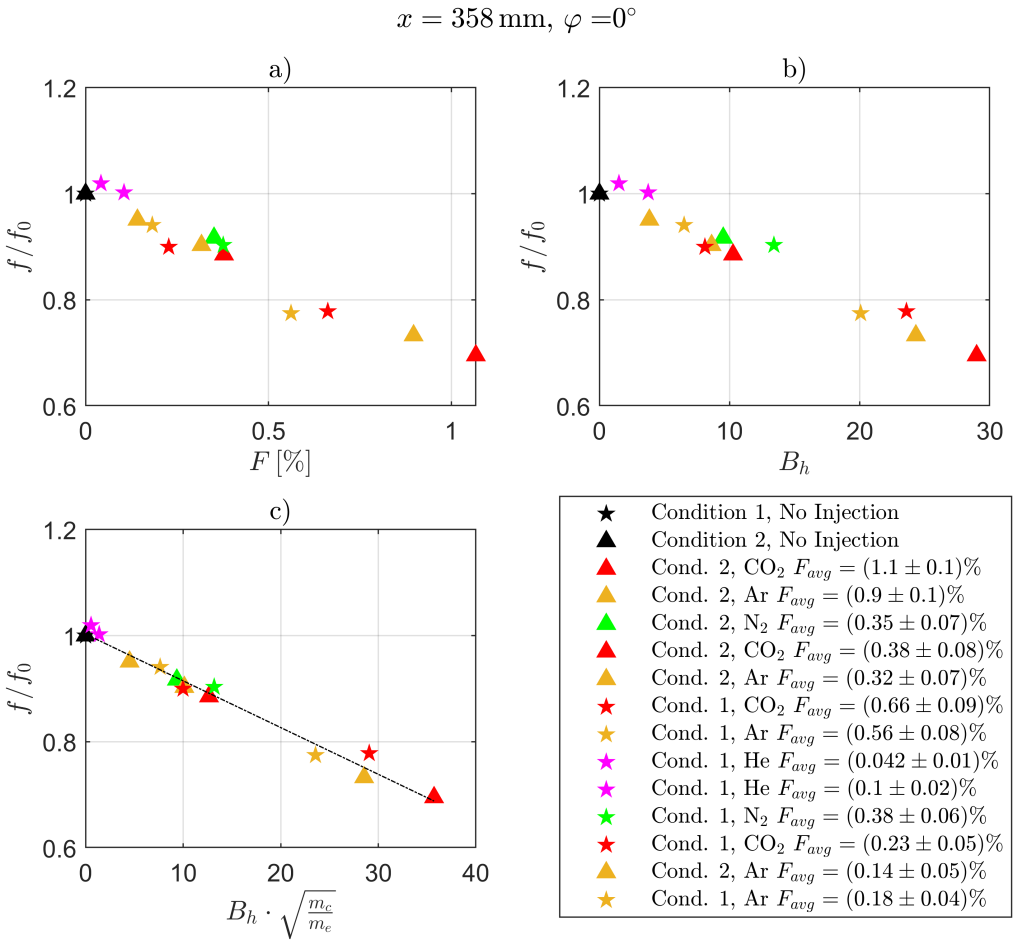


Figure 4.9: Comparison of relative frequency drop for several conditions, gases and blowing ratios.

the square root of the normalized molar mass of the coolant gas in an attempt to incorporate the molecular weight of the injection gas in part c) of Figure 4.9. Herein, we roughly follow Marvin and Akin [187] who produced a similar correlation for transition Reynolds numbers with injection. We use $M_e = 28.9583\,\mathrm{g/mol}$ as the molecular mass of dry air [282] in the freestream. The shown data underlines the trend observed for helium. Its effect on the second mode frequency is minimal, if present at all. It is also observed that a higher blowing ratio is necessary for Condition 2 to achieve the same relative frequency reduction as in Condition 1, using the same coolant gas. Due to the lower Re_u the boundary layer thickness should be larger for Condition 2 and therefore more 'robust' towards disruptions through cooling. Miró Miró et al. [108] provide the same reason for their equivalent result with air injection. The Reynolds number dependency of the Stanton number

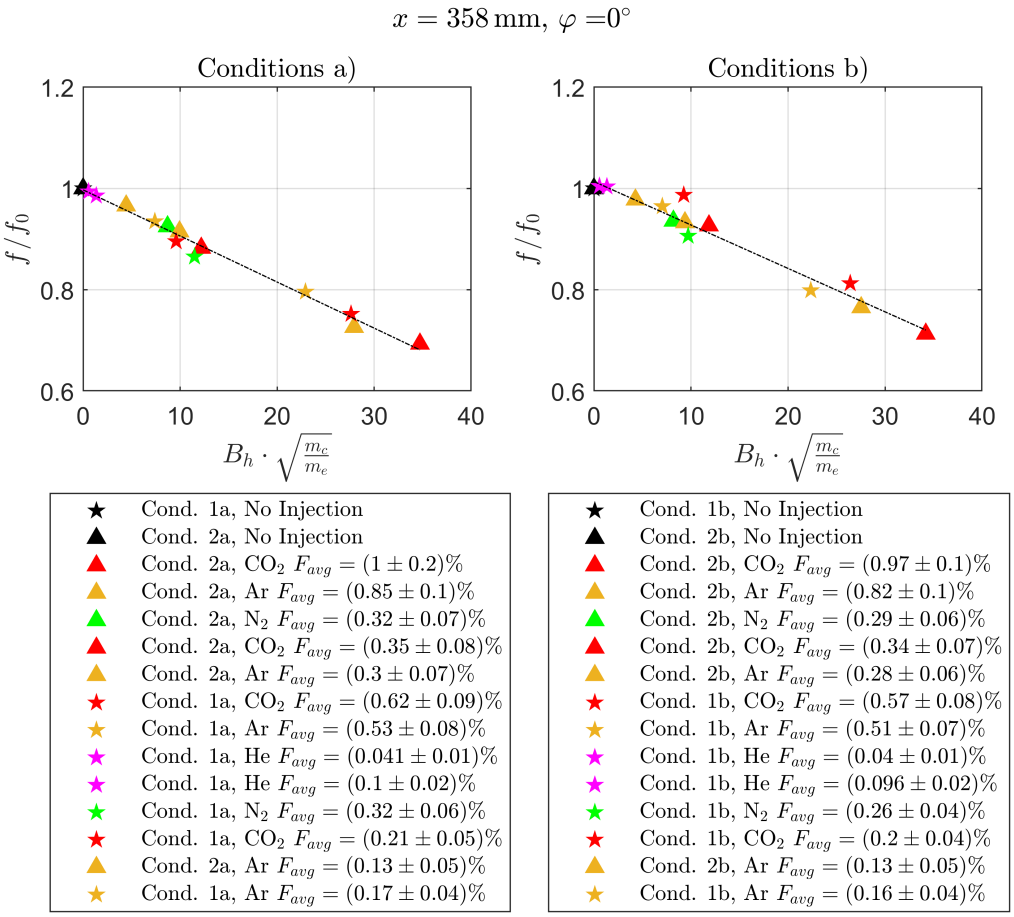


Figure 4.10: Comparison of relative frequency drop for supplementary conditions.

used in the blowing parameter B_h seems to account for said effect, as it enhances the linear relationship in Figure 4.9 c). We now repeat the procedure of said plot using the data from the supplementary steady state conditions a) and b) as outlined in Table 4.2. We obtain two more figures which are shown in 4.10. Again, the relative frequency diminution roughly follows a linear relation against $B_h\sqrt{m_c/m_e}$. Except for one outlier at condition 1b with carbon dioxide injection, the dependency appears unchanged when Re_u and tunnel noise level are slightly varied.

4.5 Schlieren Measurements - Boundary Layer Thickness

The pressure measurements on the cone surface were accompanied by z-type schlieren. Those imaging techniques have been around for centuries [228, 233, 235, 236] and

have been used by multiple experimentalists in hypersonic wind tunnel testing [8, 99]. Schlieren images were recorded with a Photron AX200 Mini at 12,500 fps and 57,600 fps. A Cavilux Smart UHS laser provides 3000 light pulses of 15 ns length, which were synchronized with the camera operation. The position of the image relative to the cone model as well as the resolution in pixel per mm is calibrated using a recognizable, rectangular metal object in the image, yielding roughly 6.5 px/mm for all images. The cone was rotated axially to $\varphi = 15°$ in order to capture the side of the injector. The image plane does thus not correspond to the central array of PCB sensors. Camera, focusing optics and the razor blade were all mounted on an optical rail, which was tilted by 7°. The field of view was hence parallel to the cone and density gradients normal to the model surface can be imaged as intensity changes. Those gradients seen in the images were found to show a very sharp separation of boundary layer and post-shock flow. Even though it might not represent the boundary layer thickness with respect to velocity, such a dimension delivers insights into the relationship of second mode frequency, injection and boundary layer edge. A data analysis procedure is hence applied to 100 consecutive frames to obtain quantitative details and the procedure is shown exemplary in Figure 4.11:

For comparability, a background image - taken while the tunnel is off - is subtracted from every individual schlieren image. To account for possible deviations in light intensity, every image is then scaled to the same cumulative value. Background as well as schlieren images of the video during the shot are then subjected to an edge detection algorithm [283, 284]. Firstly, the cone surface is determined by averaging linear fits through said detected edge points in the background and flow-on images. Secondly, a part of the detected boundary layer edge is then selected manually for one image during the shot. An additional algorithm collects as many points as possible along the boundary layer edge within each video frame, utilizing the manual selection as a starting value. All of the collected edge data points are used to calculate a boundary layer thicknesses dimension relative to the fitted cone edge. Lastly, those thicknesses are converted into millimetres and transformed into the

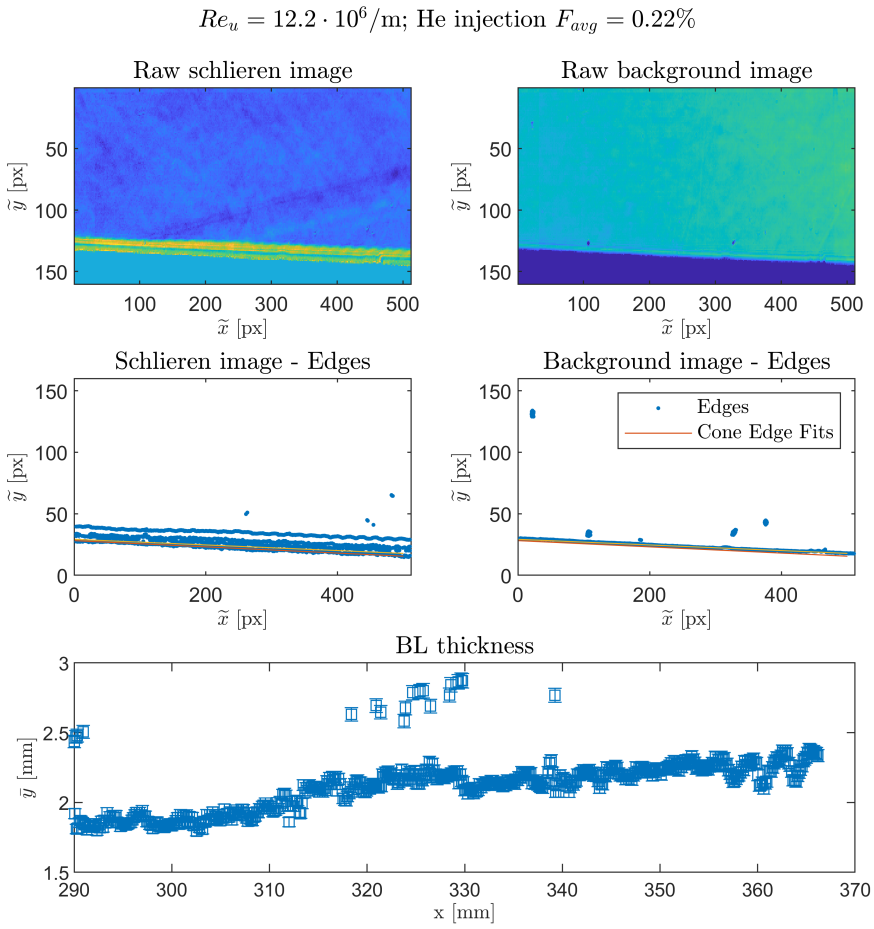


Figure 4.11: Schlieren analysis procedure for an exemplary image.

cone coordinate system. The data is binned to a resolution of 1 mm along the x coordinate which allows statistical averaging of every value across the 100 frames. The errorbars shown represent the mentioned statistical uncertainty as well as the propagated systematic error from the spatial image calibration and the precision of the cone edge detection. The spike visible in every trace just downstream of the injector at $x \approx 327\,\text{mm}$ is due to an image artefact most likely caused by the tunnel windows. Results for carbon dioxide injection during Condition 2 flow are shown in Figure 4.12. The increase in thickness only starts to be visible at around 305 mm, which can however be explained by the measured outflow profile of the injector in Section 4.3.2. Effusion predominantly takes place downstream of the porous segments's front edge. A dependency of F and boundary layer thickness

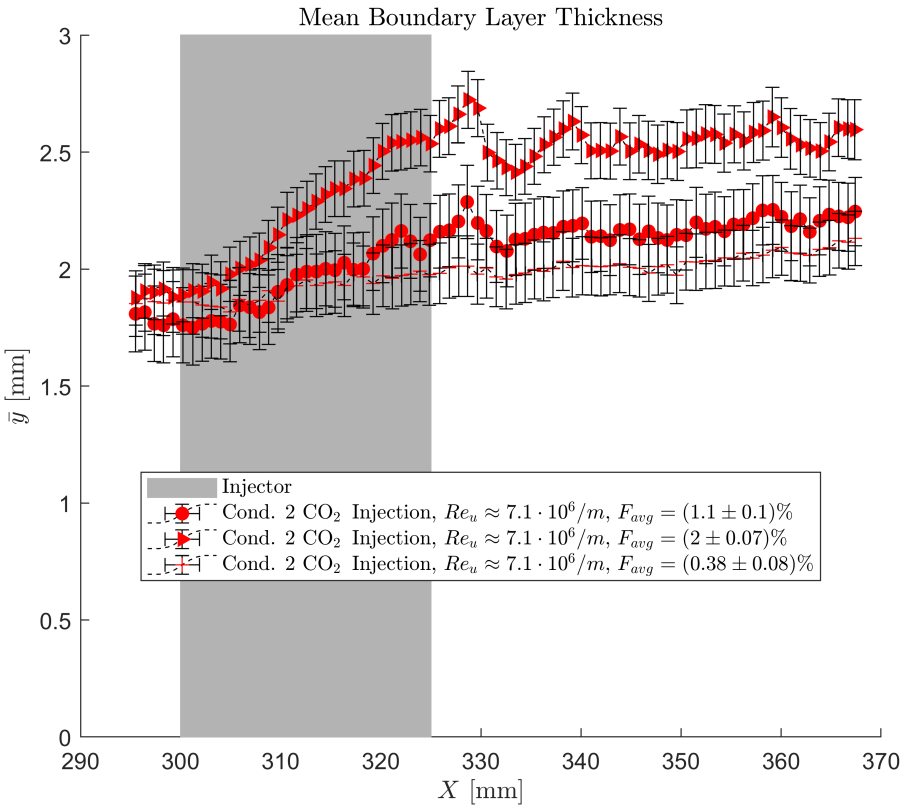


Figure 4.12: Boundary layer edge thickness for carbon dioxide injection, Condition 2.

across the injector is evident for carbon dioxide as a coolant gas (see Figure 4.12). With $F_{avg} = 2\%$, the boundary layer was already transitioning, as shown by the downstream PCB frequency content during the test. A comparison of helium and carbon dioxide can be seen in Figure 4.13. Similar blowing ratios lead to a distinct difference in the detected boundary layer edge geometry. In agreement with the simulations in Ref. [169] and also the analytical model described in Section 4.4.4 [49, 285], helium causes a disproportionally large effect on the boundary layer thickness. The plot symbols in Figure 4.13 correspond to the ones in Figure 4.6 and considering the frequency and power behaviour for the second mode of all three shots, this suggest there are other effects present than only a thickness increase. Herein, the aforementioned comparison of helium and carbon dioxide allows to decidedly rule out that the frequency drop seen in Figures 4.6, 4.7 and 4.9 is exclusively driven by changes of the boundary layer edge geometry. These preliminary results propose a likely gas dependent mechanism that accompanies the

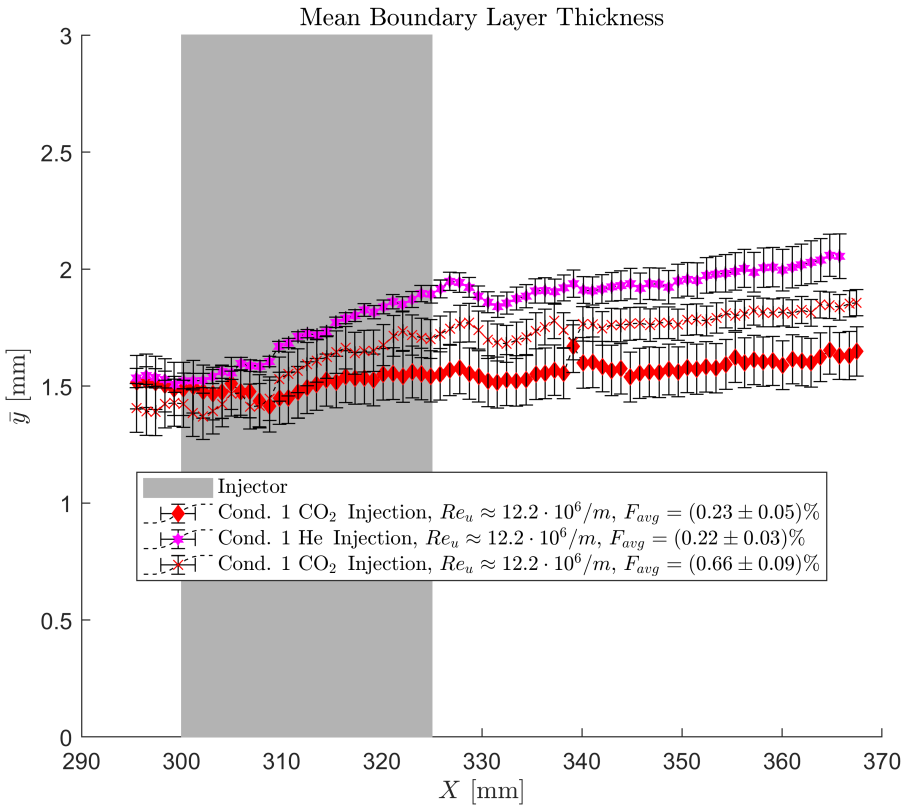


Figure 4.13: Boundary layer edge thickness for carbon dioxide injection, Condition 1.

thickness increase to explain the frequency findings in combination with the observed thickness increase. Further research is hence necessary to determine what physical properties or measurement techniques could play a role. For completeness, the raw schlieren data is shown in Figures 4.14 and 4.15. Those images are an average of the 100 frames used in the thickness calculation algorithm. The background has been subtracted and all images within one figure are normalized by the intensity of a line of pixels within the boundary layer. A change of thickness is evident in all images showing injection cases.

4.6 Discussion

Most of the shown results are consistent with Camillo et al.'s [104] and Miró Miró et al.'s [108] experiments, where nitrogen or air effusion also caused a reduction in second mode frequency downstream of the respective injectors. The presented findings are however in strong contrast to the work of Schmidt et al. [180, 214,

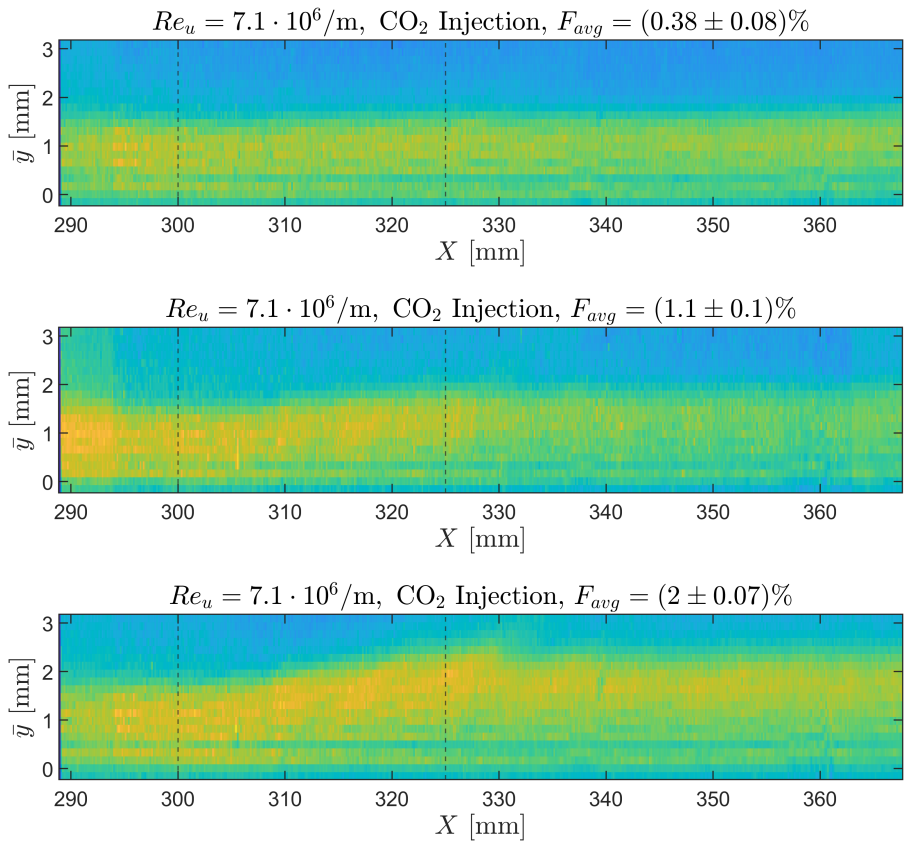


Figure 4.14: Averaged schlieren images corresponding to Figure 4.12. Location of the injector is indicated with dashed lines.

215] which might be due to the difference in speed regime. Camillo et al. [104] and Miró Miró et al. [108] measured frequency diminution of second mode waves with schlieren and planar laser induced fluorescence (PLIF), respectively. Both ascribe the effect to the dependency of the second mode frequency on the boundary layer thickness. Hereby, Camillo et al. [104] reason that gas injection drives "forced boundary layer profile changes" [104]. Similarly, Miró Miró et al. [108] refer to the Reynolds number dependency of the boundary layer thickness. As also identified in this work, they note that boundary layers forming at higher Re_u are more susceptible to changes in their geometric profile through injection and thus exhibit larger relative frequency drops [108].

Those two studies provide an initial insight into the frequency drop effect and its likely origin. However, both studies do not attempt to quantitatively correlate the drop with any other measured boundary layer parameter. It is also unclear how the

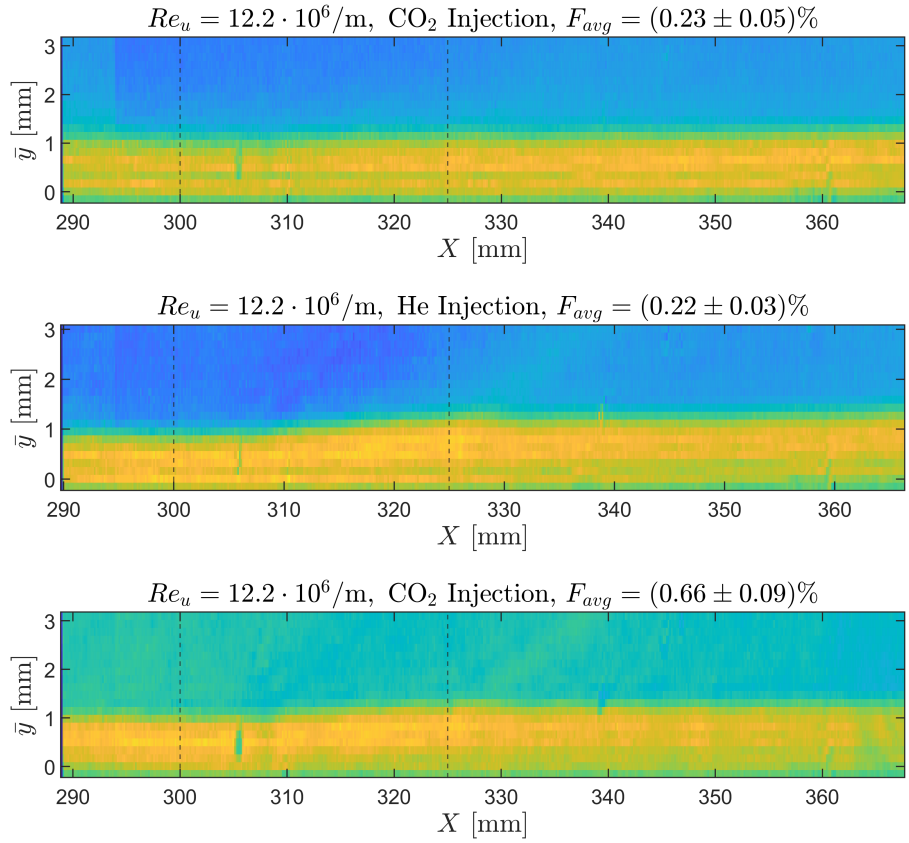


Figure 4.15: Averaged schlieren images corresponding to Figure 4.13. Location of the injector is indicated with dashed lines.

coolant type may influence the frequency reduction as for example demonstrated by Schmidt [180] for a first mode dominated environment. Furthermore, results for helium injection in Section 4.5 clearly demonstrated how a boundary layer thickness increase imaged by schlieren does not necessarily correspond to a frequency reduction.

Introducing a model for coolant concentration in the boundary layer proposed by Ifti et al. [49, 285] shall enhance insight into parametric dependencies. The boundary layer thickness increase due to the coolant outgassing shown in Figure 4.16 can be expressed as shown in Equation 4.3, which is taken from Refs. [49, 285]. Hereby, the length of the axial injector s as well as the wall-to-edge temperature ratio are constants. Little change is found in the static temperature across tunnel conditions and hence the boundary layer edge temperature (see Table 4.2) is also constant. Due to the low enthalpy in the tunnel flow, model wall temperatures changes are

negligible in HDT and $T_w = const.$ is room temperature. When only comparing data points of the same tunnel condition, the entrainment thickness δ_{ent} should not play a role in the proportionalities. The meaning of this additional thickness and other involved variables is demonstrated in Figure 4.16.

$$b = b' + \delta_{ent} = \frac{m_e T_w}{m_c T_e} F s + \delta_{ent}(Re, s) \tag{4.3}$$

A rough estimation of the second mode frequency can be made by calculating the wavelength using the waveguide thickness. It is usually expressed as $f = u_e/(2b)$ [8, 58, 109]. Using b as described by Equation 4.3, those considerations leave a dependency of f/f_0 to the blowing ratio F and the normalized coolant molecular mass. The analytical approach thus correctly predicts how higher blowing ratios yield a larger drop in frequency using the same coolant. Regarding the upper left plot in Figure 4.9 this holds true and seems relatively independent of the injection gas type. Nevertheless, when considering the molar mass of the injection gas, a lighter gas should cause a stronger frequency drop at the same blowing ratio due to the disproportionately large thickening seen in schlieren, as correctly predicted by Ifti's model [49]. Nonetheless, this is clearly not found in the surface pressure spectra (see e.g. Figure 4.9). This implies the presence of a compensating effect. The given estimation formula for the second mode frequency maximally simplifies the waveguide normal mode by assuming it has to travel twice the distance of a fixed boundary layer height. Conveying this into the slab-model for injection one could now assume that there is a layer of pure coolant below the original air boundary layer at e.g. $x = 358\,\text{mm}$. Those layers would have different speeds of sound a_c and a_e as indicated in Figure 4.16.

Simplistic calculations, wherein the coolant slab height is scaled by its effective speed of sound and therefore any thermal diffusion and mixing as well as temperature profiles or waveguide interactions are neglected, did not yield immediate success in predicting the frequency drop accurately. Specifically helium and nitrogen exhibit a smaller frequency reduction than predicted, which is most likely due to the aforementioned left-out properties. Those are plausible causes of observed

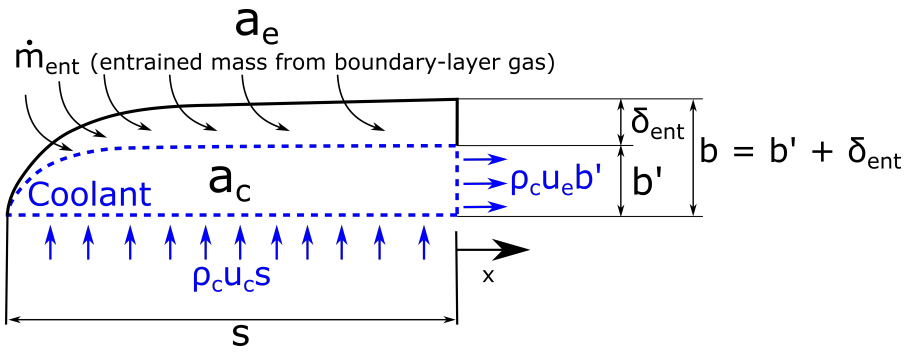


Figure 4.16: Model for the coolant wall concentration above and downstream of a porous injector. Adapted from [49, 285] with permission.

discrepancies in view of publications addressing similar issues (see Schmidt [180] and also Miró Miró et al. [169]). More sophisticated analysis may be part of future work to accurately reveal all underlying physical processes leading to the frequency attenuation and its proportionalities to effusion gas properties.

Parts b) and c) of Figure 4.9 aim to minimally improve the linear relationship by establishing different normalizations. When the molecular mass of the coolant gas is taken into consideration in Figure 4.9 c), an enhancement of the linear relation can be observed, especially at $F < 0.5\%$. Roughly following the approach from Marvin and Akin [187] albeit for the drop in second mode frequency at the surface we found the relationship

$$\frac{f}{f_0} = 1 - \tau \cdot \frac{F}{St_0}\sqrt{\frac{m_c}{m_e}} \tag{4.4}$$

to approximately correlate the behaviour of the instability frequency (see Figure 4.9) for our specific experimental setup. The proportionality constant only varied minimally across conditions and we determined $\tau = (8.8 \pm 0.2) \cdot 10^{-3}$.

4.7 Conclusion

A 7° half-angle cone with a small porous injector was tested at multiple conditions in a Ludwieg tube at M = 7 to investigate systematic dependencies of the second mode instability with coolant injection. Herein, we characterized the Mack mode by applying a fitting procedure to power spectral densities obtained from high

frequency piezoelectric PCB surface pressure sensors. In agreement with other studies, we report a reduction of the second mode frequency downstream of gas injection with a strong dependency on the blowing ratio. Higher blowing rates led to a stronger drop in frequency, except when using helium as a coolant. In this case, the frequency analysis with said methods was inconclusive for moderate blowing ratios as typical second mode spectra vanished completely. Heavier injection gases at similar blowing rates did not affect instability oscillations to such an extent. Increased injection rates led to earlier transition as inferred by low frequency PCB data, however more research is necessary to conclude how the destabilization of the boundary layer changes with coolant gas type. Further downstream of the injector, the mass addition effect on second mode characteristics weakens and the physical parameters approach the undisturbed values. This might be due to increased mixing. Comparison to a simplified boundary layer model has not yet produced coherent results for the influence of injection gas molar mass on second mode properties.
Schlieren images revealed a significantly larger boundary layer thickness increase through helium injection compared to carbon dioxide effusion. For carbon dioxide alone, the thickening was directly related to F and this reiterates the matching findings from the analytical model and the experiments of the inverse proportionality of F and f/f_0. Considering the wave guide nature of the second mode, the schlieren data, the frequency data and a simplified analytical model for a boundary layer's behaviour with transpiration cooling, it can be concluded that neither the boundary layer geometry alone nor the potential change in speed of sound are sufficient to fully interpret the observed frequency behaviour across injection gases, Reynolds numbers and blowing ratios. This supplements the work of Camillo et al. [104] and Miró Miró et al. [108] who both only mentioned boundary layer geometry as the physical reason of a reduced instability frequency downstream of coolant effusion. Macroscopic inhomogeneity in the outflow map of the injector patch has been found and may have influenced the results. Further investigations are requisite to understand this parameter's influence on transition better.

Statement of Authorship

Title: Gas Injection into Second Mode Instability at Mach 7

Status: Unpublished and unsubmitted work written in a manuscript style

Author Contributions:

- **Philipp Kerth** had the idea for the test cases, cone model and analysis performed. He designed the model, assembled it, instrumented it, ran the experiments, collected the data and analysed it. He wrote the manuscript with input from Matthew McGilvray.
- **Raghul Ravichandran** designed and commissioned the hot wire traverse system. He also ran it during the outflow testing.
- **Sebastien Wylie** acted in a supervising role during model design, test case selection, data analysis and testing.
- **Matthew McGilvray** supervised the project and organized and managed the funding.

Student Confirmation:



Date: 08/01/2023

Supervisor Confirmation:



Date: 10/01/2023

5

Hypersonic Boundary Layer Stabilization by Helium Injection

Contents

5.1 Foreword 90
5.2 Introduction 90
5.2.1 Hypersonic Boundary Layer Transition 90
5.2.2 Transition and Injection 91
5.3 Test Model and Environment 93
5.4 Instability Measurements 94
5.5 Heat Flux and Transition 96
5.6 High Speed Schlieren Measurements 98
5.7 Discussion 99
5.8 Conclusion 101
5.9 Methods 102
5.9.1 Oxford High Density Tunnel 102
5.9.2 Coolant Injection 103
5.9.3 PCB Piezoelectric Sensors 104
5.9.4 Kulite Piezoresistive Sensors 104
5.9.5 Thin Film Gauges 104
5.9.6 Z-type Schlieren 106
5.9.7 Uncertainty Analysis 108
5.10 Extended Data 109
5.10.1 Experiment at low Reynolds Number 109
5.10.2 Experiments with different Injector Material 109
5.10.3 Nosetip Outflow Profiles 110
5.10.4 Continuous Wavelet Transforms 112
5.10.5 Average Schlieren Image 112

5.1 Foreword

The following chapter is solely dedicated to presenting results and analysis about transpiration cooling effects with injection from a nose cone. Boundary layer transition delay with helium is discovered. As it was aimed at a certain journal, the structure deviates slightly from those of classical papers in the field. Following an introduction, all main results are briefly presented in the beginning, with only three display items depicting the main data analysis, whereas technical details, methods and further results that support the findings but do not significantly shape the conclusions are presented afterwards. To aid the thesis structure the drawing of the porous nosetip, originally intended for the supplementary materials of the paper, was added to the appendix together with all other technical drawings. References to other papers written by the author have been changed to references to the appropriate chapters.

5.2 Introduction

5.2.1 Hypersonic Boundary Layer Transition

Hypersonic boundary layer stability and surface heating are two interwoven challenges for the feasibility of sustained hypersonic flight [57, 62]. Laminar-turbulent transition is a natural process occurring in any flow along a boundary – including flight vehicles - which is notoriously hard to predict [11, 59, 74, 286]. Knowledge about the state of the boundary layer however is critical for vehicle design as it determines the heat load, drag, separation susceptibility, necessary propulsion forces and for example the effectiveness of control surfaces [13, 57, 61–63, 67, 88, 286]. Turbulence significantly increases the surface heat load [64] and can diminish a vehicle's efficiency by a factor of two [59, 66]. Consequently, a laminar boundary

layer would be desirable in most cases [59, 66, 263] and difficulty to ensure its existence or predict its breakdown has severely limited inventiveness of new flight vehicle concepts [287] for decades. The transition process and mechanism itself are also highly sensitive to an enormous variety of parameters [57, 58, 60, 67, 286] complicating all forms of research efforts. Transition itself has defied a fully theoretical explanation for centuries [74, 82] and hence design tools for engineers are gravely deficient. Nevertheless, it is known that hypersonic boundary layer transition is commonly caused by the second mode (or Mack mode) [90, 112, 288–290] on slender 2D geometries, if no bypass mechanism is present [94]. The second mode is an eigenmode of a waveguide [83, 94] (or trapped waveguide mode) forming in between the model surface and the sonic line at the edge of the boundary layer [83]. Only at sufficiently high Mach numbers in the hypersonic regime specifically the second mode will become the underlying cause of transition [83, 90].

5.2.2 Transition and Injection

Replacing ablation with active cooling allows to provide shape stability which ensures optimal aerodynamic profiles throughout the entire trajectory [26, 27, 32]. Specifically sharp edge vehicle designs of sustained flight concepts may benefit from active cooling as it could increase the tolerable heat loads [36, 40, 48]. Moreover, a coolant gas transpired through a porous surface of the spacecraft can mitigate aerothermal heating more efficiently than any other proposed method [46] and multiple studies have been performed experimentally and numerically for flat plates[36, 50, 51], cones [104, 211] and flight realistic geometries [176]. Many of those studies on slender, conical shapes are summarized in a review by S.P. Schneider [56], where extensive information about historical and more recent investigations can be found. As the transitioning process reacts so sensitively to disturbances such as model surface imperfections [88], historical experiments consistently found gas injection to reduce the transition Reynolds number [56], while lighter gases were thought to destabilize more [56, 135, 180, 192]. This self-contradiction – a cooling method that leads to excess heating – has sparked scepticism at least as

early as 1956 [47]. Furthermore, transpiration cooling and other active cooling methods have been criticized for adding weight and intricacy to vehicles [11], which "discourage[s] the designer from using" [11] those technologies. Antithetically, transition control [59] is indispensable for future innovation. Consequently, an inescapable coupling of efficient heat mitigation and transition advance could put active cooling developments into a stalemate. Two effects have been discovered experimentally to counteract this general trend:

At high enthalpies, carbon dioxide injection was found to stabilize the transition process. [203, 204, 209, 210]. Leyva [203] ascribes the underlying reason to findings from Johnson [205], who states how vibration and dissociation of molecules like CO_2 can interact with and attenuate macroscopic gas oscillations. Alternatively, as measured by Camillo et al. [104], if nitrogen injection is performed close to the natural onset of transition, the rise in heat transfer from the laminar baseline can be temporarily suppressed while the second mode is concomitantly damped, resulting in a transition delay [104, 211].

Those experimentally confirmed effects are invaluable for the understanding of injection and transition. Nonetheless, those findings and their respective studies suffer from significant constraints. For both previously discovered stabilization effects, injection has not been performed at the nose tip, namely the most critical location [163]. Neither carbon dioxide nor nitrogen are the most effective coolants available [36, 50]. Both cases are also strictly limited to a narrow subset of conditions which complicates their applicability to realistic trajectories. Carbon dioxide stabilization only works at sufficiently high enthalpies [204]. The other stabilization effect only occurred if injection was performed in a specific location with very little tolerance relative to the transition onset [104, 211]. While a flight vehicle travels along its trajectory or descends back into the atmosphere, a gradual evolution of the flight Reynolds number induces a similarly continuous shift in transition fronts [39]. Such a Reynolds number dependency would make any applicability of said discoveries to free flight unfeasible.

In simulations conducted by Miró Miró et al. [169], helium transpiration surprisingly

yielded a firmly attenuating effect on growing disturbances [169]. The same investigation then theorizes that the generally accepted destabilizing effect of said gases may be due to the geometrical nature of the injectors. A sudden start of light coolant flow along the model surface generates "a weak shocklet" [169] which advances transition [169]. No influence of enthalpy is mentioned and the finding thus suggests that if one manages to avoid the "shocklet" [169] phenomenon, a substantial transition delay may be achievable with helium while concurrently providing effective cooling. However, Miró Miró et al. [169] do not elaborate how this may be technically feasible and do also not consider leading edge cooling.
To our knowledge, no solution currently exists to address the interwoven hypersonic heating and transition problem. Known stabilization effects cannot provide cooling at crucial locations, and effective cooling methods trigger turbulence. Here we overcome both shortcomings at once. We demonstrate how helium injection from the nose segment of a hypersonic cone can induce a substantial transition delay in combination with effective leading-edge cooling. Three independent measurement methods - schlieren, surface pressure and surface heat flux – provide a thorough and comprehensive representation of the boundary layer ensuring unambiguous identification of either stabilization, or early transition.

5.3 Test Model and Environment

The test geometry is a 7° half-angle cone with a 1 mm nose radius. Essential geometric features are shown in Figure 5.1. The nose tip of the cone is manufactured from porous CE170 [258] with a total permeable axial length of 58 mm enabling injection of various gases. Coolant is delivered to the nose tip via a central pipe and the internal geometry of the nose tip allows for a specifically homogeneous outflow distribution with respect to the incoming freestream flow. Tests are conducted in the Oxford University High Density Tunnel [225, 243] (HDT) at a unit Reynolds number of $18 \cdot 10^6 m^{-1}$ at Mach 7 using dry air as a test gas, which hence replicates a flight relevant condition. Due to the low enthalpy in the free stream flow, thermochemical and real gas effects can be excluded. Use of a mass flow controller to regulate

the coolant injection rate ensures steady gas effusion throughout the tunnel test. The selected parameter to compare the amount of injection in between gases and conditions is the blowing ratio. Frequently used in the literature it is defined as [291]

$$F = \frac{\rho_c u_c}{\rho_e u_e} \tag{5.1}$$

Where ρ denotes the density and u the velocity of the coolant c or the boundary layer edge e, respectively. More information about the test model and wind tunnel as well as conditions can be found in the methods and supplementary materials Sections 5.9.2 and 5.10.3.

5.4 Instability Measurements

Time averaged power spectral density estimates of surface differential pressures and their integrated bandpower are shown in Figure 5.2 a) and b), respectively. Such closely spaced measurements enable to thoroughly monitor instability growth, substantially increasing comprehension of said fast-moving processes in lieu of solely deriving a transition location.

Figure 5.2 summarizes the instability and heat flux data from surface measurements. During an undisturbed transition process, the second mode grows in power, gradually shifts to lower frequencies and ultimately breaks down to turbulence, a behaviour already observed in numerous studies on hypersonic cones [8, 102, 104, 108]. The breakdown is indicated by a rise of low frequency power and disappearance of the spectral peak at roughly $f \approx 280\,\mathrm{kHz}$, seen in Figure 5.2 a) from ($x = 367.7\,\mathrm{mm}$) onwards for the uncooled case. Simultaneously, as demonstrated by Figure 5.2 b), the total power of the frequency band is falling again, which can be interpreted as instability growth having ceased. A mainly laminar boundary layer with a growing eigen-mode oscillation has now transitioned to turbulence, hence lacking a specific frequency amplified beyond chaotic behaviour.

Helium injection at moderate rates ($< 0.05\%$ of the boundary layer mass flux) causes this growth and decay process to be spatially delayed. For the most upstream measurement points, the difference is not significant. However, as soon as the second

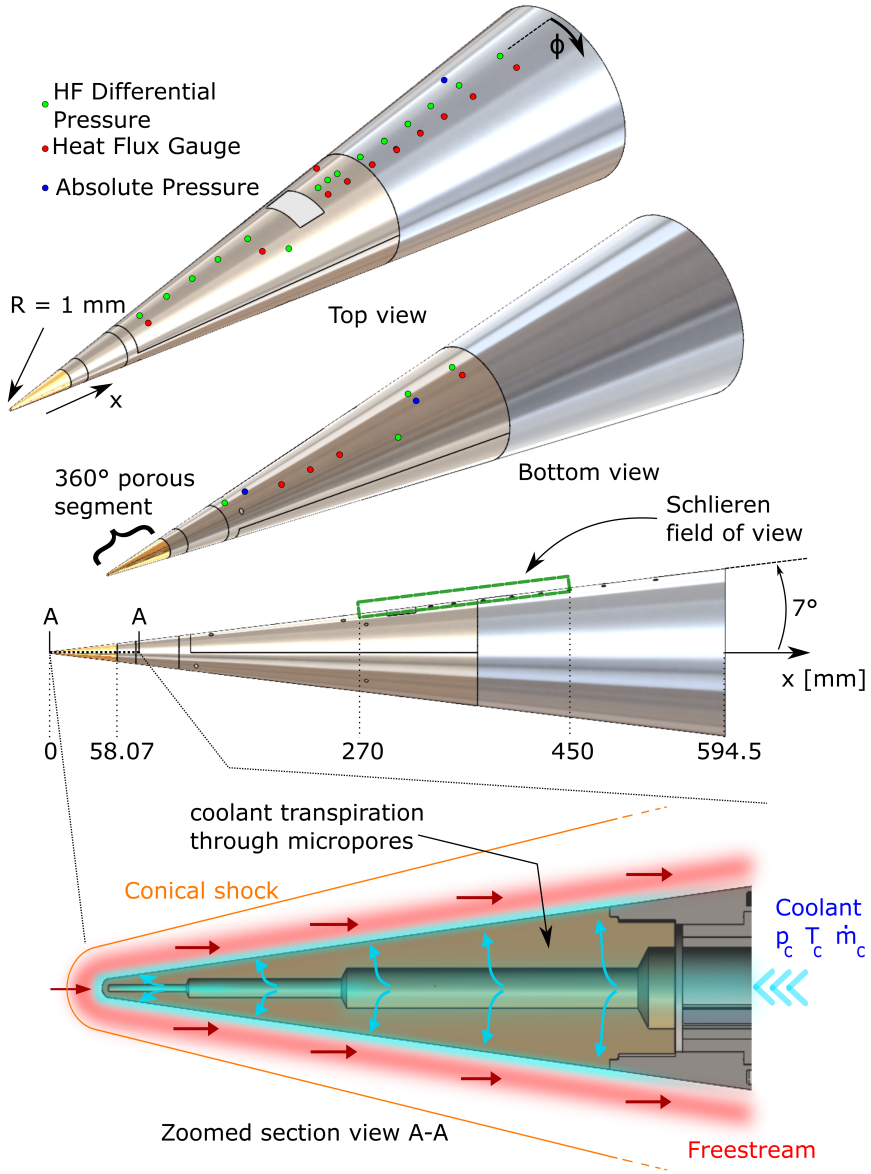


Figure 5.1: Seven-degree cone model with measurement infrastructure. Coloured dots represent the surface instrumentation and the rectangular schlieren field of view is indicated in the bottom side view. Gas injection only happens at the nose tip and the coolant is delivered via a pipe in the centre of the cone.

mode would naturally start growing ($x = 224\,\text{mm}$), an attenuation in bandpower (Figure 5.2 a)) and low frequency content (Figure 5.2 b)) is observed. The maximum bandpower for natural transition is reached at ($x = 367.7\,\text{mm}$), whereas a similar inflection point only appears at ($x = 451.7\,\text{mm}$) for $F(\text{He}) = 0.02\%$ and is potentially not reached at all for $F(\text{He}) = 0.039\%$. A further increase in helium injection ($F(\text{He}) = 0.13\%$) fully reversed the stabilization. An instantaneous rise in low frequency content indicates an entirely turbulent boundary layer far upstream on the cone. This possibly indicates a transition bypass mechanism [94].
Nitrogen injection at a comparable rate had the opposite effect to helium. An increase in spectral power demonstrates a destabilizing effect of this gas with respect to second mode pressure signals, particularly evident at ($x = 224\,\text{mm}$) and ($x = 255\,\text{mm}$). An influence of nitrogen on the receptivity phase [89] in the transition process, or on the modal growth process may be conceivable drivers of the measured enhancement in second mode growth.

5.5 Heat Flux and Transition

Heat flux to the surface increases concurrently with transition [64]. As shown in Figure 5.2 c), the laminar baseline correlation only describes the heat flux accurately close to the nose tip. Further downstream, an increase in Stanton number at ($x = 320\,\text{mm}$) corresponds to the location of an increase in band power shown in Figure 5.2 b) jointly indicating transition onset. For every measurement location, the cases with moderate helium injection ($F(\text{He}) = 0.02\%$ and $F(\text{He}) = 0.04\%$) exhibit a lower Stanton number, underlining the previous findings. Consistent with a delay in terms of eigen-mode growth, an increase in corresponding surface heating also shifts rearwards. If transition is defined as the first thin film gauge showing a heat flux significantly exceeding the laminar baseline, then a 37% transition delay could be achieved with $F(\text{He}) = 0.04\%$. Herein, the decrease in surface heating is likely a superposition of transpiration cooling and the boundary layer stabilization itself. As shown for the case of ($F(He) = 0.13\%$), care has to be taken when inferring a stabilization from thin film gauge measurements alone. Although high

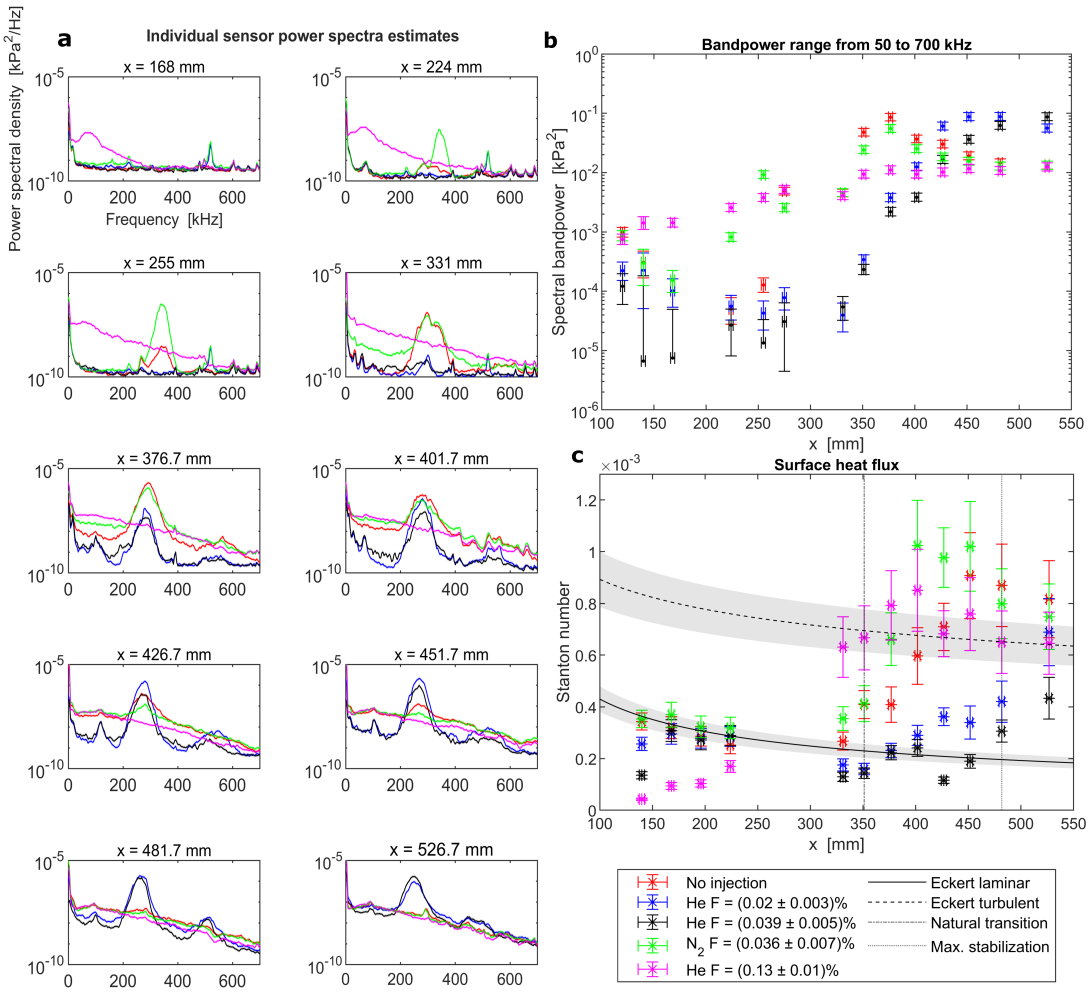


Figure 5.2: Results from surface instrumentation. On the left-hand column, individual power spectral estimates are shown for several differential pressure sensors along the $\varphi = 0°$ plane on the model. The top right corner shows the integrated bandpower belonging to said power spectra. The bottom right plot indicates the heat flux measured by thin film gauges along the $\varphi = 15°$ plane on the cone. The discrete points are compared to Eckert correlations [267]. Colours represent different injection rates and gases and are kept consistent across all plots. Error bars indicate 68% confidence intervals.

frequency pressure spectra indicate a fully turbulent flow for ($x < 250\,\mathrm{mm}$) in this regard, heat flux values lie below the laminar correlation. Nonetheless, interpreting this as a laminar boundary layer is certainly incorrect, because the strong cooling effect suppresses any heating from turbulence. Confidence in a stabilization can consequently only be achieved by simultaneously observing a delay in second mode growth for pressure spectra as e.g. for $F(\mathrm{He}) = 0.04\%$. Furthermore, said suspected early transition onset with ($F(He) = 0.13\%$) is a prime example for suboptimal

application of transpiration cooling. Downstream of ($x > 300\,\mathrm{mm}$) the heat flux evidently exceeds the uncooled case. As before, nitrogen causes earlier transition onset as represented by an advanced rise in heat transfer.
As cooling at the stagnation point is of particular interest [32, 163], the blowing parameter $B_h = F/St_0 = 0.22$ was calculated [33, 292] with the uncooled Stanton number St_0 for the case $F(\mathrm{He}) = 0.04\%$ aiding the contextualization of this work with realistic values for ablation experiments [292]. As the case with ($F(\mathrm{He}) = 0.13\%$) yields $B_h = 0.7$, the respective bypass transition could have been caused by boundary layer blowoff [196, 197].

5.6 High Speed Schlieren Measurements

Model surface measurements are accompanied by z-type schlieren. As indicated in Figure 5.1, the field of view is aligned with the middle section of the model, enabling recordings of strongly amplified and growing second modes as well as transition to turbulence for non-injection cases. The uncooled case (Figure 5.3) features a largely laminar boundary layer, although showing strongly amplified second mode packets in their typical "rope-like" [99] appearance. Frequent presence of disturbance clusters as well as full turbulence onset indicates good agreement to the x-locations for heat transfer increase in Figure 5.2. Similarly, Figure 5.2 frequency spectra expose the complete disappearance of the second mode peak for $x > 450\,\mathrm{mm}$, correlating with the visualized vanishing of any laminar features.
Without any injection, transition to turbulence can be observed in schlieren images and the given field of view. When helium is transpired into the flow at moderate rates from the nose segment, the behaviour changes substantially: schlieren now reveal a fully laminar boundary layer and no second mode packets are visible. This unambiguously underlines the consistent results from surface measurement techniques and suggests the stabilization trend does not only hold for the immediate vicinity of the model surfaces but for the entire thickness of the boundary layer. Consequently, it can also be decidedly ruled out that only a cooling effect drives the reduction in heat flux observed in Figure 5.2 c), which would not necessarily

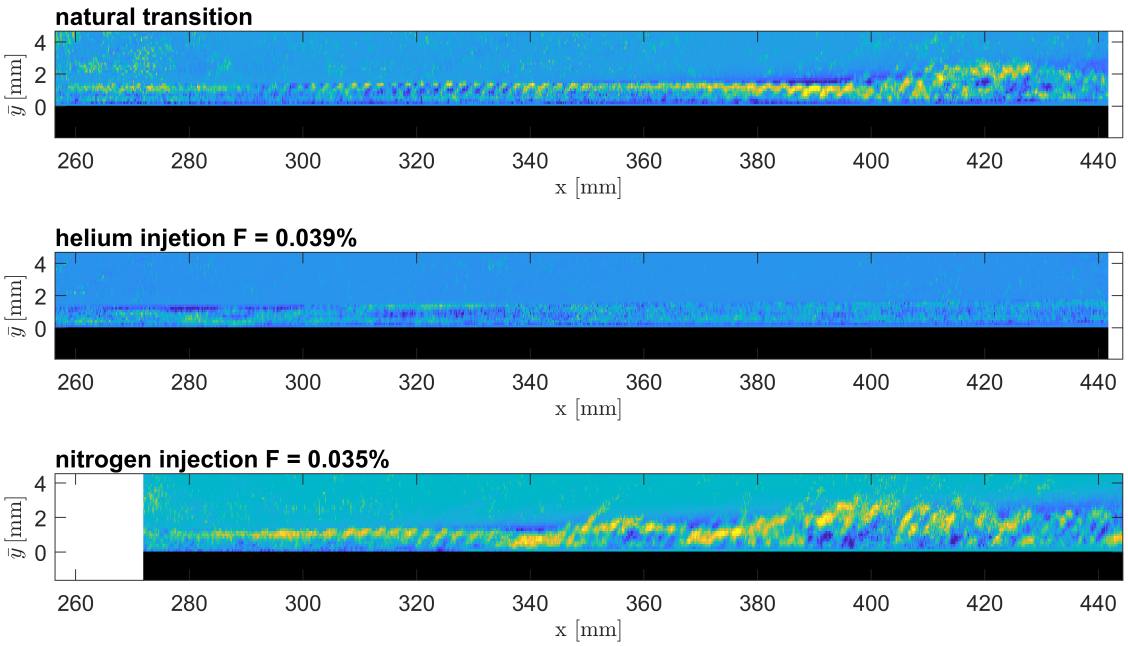


Figure 5.3: z-type Schlieren images for natural transition and gas injection. $\bar{y}$ is the model wall-normal direction. Schlieren signal intensity is represented by a colormap. Tunnel freestream flows from left to right. All images are taken at the same time relative to the start of the flow with accuracy $\pm 1\,\mu$s. An average of 1000 schlieren images has been subtracted from the shown frames. This leaves only temporal fluctuations, such as instabilities and turbulence. The purely laminar boundary layer for the helium injection case is hence nearly invisible.

influence instability growth.

It is generally understood that such single schlieren frames are a snapshot in time of a continuously fluctuating phenomenon, but in order to reveal time-dependent details like second mode packets, no other option but to arbitrarily select a certain image for depiction remains. Mean schlieren are provided in Section 5.10.5, to augment the robustness of conclusions drawn from said frames.

5.7 Discussion

All three measurement techniques consistently show a transition delay through helium injection. Heat transfer measurements indicate a downstream shift of transition onset. High frequency pressure measurements reveal significant attenuation of disturbance oscillations by helium effusion and consequently a spatially delayed instability growth process. Both findings are supported by non-intrusive schlieren

measurements. They depict a purely laminar boundary layer along parts of the cone, where transition onset would have been observed without any injection. Direct comparisons to nitrogen blowing signify crucial relevance of the coolant type.
Many studies have historically been performed researching injection and stability [56]. While most of them were aimed at slightly different objectives, one must be mentioned explicitly for comparability: Using thermocouples for transition measurements, Dunavant and Everhart [181] found helium effusion from a small injector segment far upstream, albeit not directly at the apex of the sharp geometry, to seemingly neither advance, nor delay transition. In a review from 2010, Schneider [56] comments this paper in the following way: "The helium heat-transfer data is even more difficult to interpret; although Dunavant and Everhart believe that helium blowing did not move transition forward, the data can also be used to infer that transition moved just as far forward as it did with air." [56]. In the same paragraph it is also questioned how an injection-induced pressure gradient could have influenced stability [56]. Dunavant and Everhart's [181] blowing ratios were comparably large, the lowest for helium being 0.12%, which could have caused them to miss the region where stabilization by helium exceeds transition advancement through introduction of additional disturbances due to gas effusion. An apparent independence of transition location and helium blowing ratio visible in their plots casts further doubt on the state of the boundary layer for such high injection rates. Modern numerical computations by Miró Miró et al. [169] - as already summarized in the introduction of this Chapter - strongly support the observed helium stabilization effect in this work. Evidently, the "weak shocklet" [169] could be successfully avoided by injecting at the upstream end of a slender geometry and hence preventing helium effusion from irretrievably disrupting an established boundary layer to a degree where transition is inevitably advanced. In our experiments, a small nose bluntness was chosen to enable such an outflow geometry. For a sharp cone tip, machinability and homogeneity of the coolant transpiration may not have been feasible. It is however not clear, whether the entropy layer due to the small nose bluntness [137] in combination with the effusion may have prevented such a "shocklet" [169].

Assuming Miró Miró et al.'s [169] simulations are applicable to the experiments due to similarities in flow variables, the stabilization may be based on a foreign gas reducing "the maximum amplification rate" [169] while simultaneously "increas[ing] the range of unstable frequencies" [169] for the given second mode instability. This comparison suggest that the injection specifically influences the eigen-mode growth phase on the slender geometry within the transition mechanism and not noise receptivity [94]. Taking Miró Miró et al.'s [169] observation how helium stretches the boundary layer temperature profile as an ansatz to physically interpret their findings' relevance for this work, one could theorize the presence of helium in the boundary layer to cause an ineffective waveguide [83] for the second mode, not allowing the instability to grow [169]. Once however the mechanism has gained momentum, no spectral broadening could however be observed in surface pressure signals in disagreement with Miró Miró et al. [169]. Frequency spectra mostly resemble those from a non-injection case (see Figure 5.2) and the same is true for the bandpower profile, which grows to the same critical level as for uncooled flow and then decays, though further downstream. The latter process then coincides with a rise in Stanton numbers. All those aspects coherently suggest dominance of a natural, second mode driven mechanism once the helium stabilization has abated. Either the coolant concentration has dropped far enough to no longer be effective [50] at this stage or another unknown compensating effect is present. Further work in Chapter 4 will show how helium transpiration at a downstream location had a minimal effect on second mode frequency while other gases caused a significant reduction.

5.8 Conclusion

Here we have shown a 37% delay of boundary layer transition by helium injection at the nose tip of a slender cone with small nose bluntness. Three independent measurement techniques were applied to prove that helium injection, if performed under certain constraints, can achieve a prolonged transition delay along a hypersonic conical flow, which resulted in a reduced heat transfer across all measurement points. The stabilization happened when helium was injected from a porous nose segment

with 1 mm nose radius on a 7° half-angle cone in a low enthalpy Mach seven flow, at flow rates lower than 0.05 % of the boundary layer mass flux. This investigation fills a gap within the present hypersonic transition research on injecting or ablating geometries, which usually only achieved leading edge effusion cooling at the cost of early boundary layer transition. Concluding from past studies, our experimental work managed to successfully minimize all destabilizing aspects of mass transpiration. Injection was performed far enough upstream, homogeneously enough and at a sufficiently low rate to reveal the true stabilization effect of a light gas in a second mode driven transition process. Having selected a small injector geometry does not allow to draw conclusions about ablation and hence this work aims at providing data towards active hypersonic cooling techniques. While transpiration cooling has been known for its effectiveness in cooling and preventing oxidation [53, 196], its paradox has always been causing turbulence and thus sabotaging its own upstream success. Helium injection in the right geometric constraints has now been shown to solve this issue, which could yield a substantial step forward in resolving the hypersonic heat load problem as it is the first ever demonstration of simultaneous effective leading edge cooling and stabilization. Moreover, this finding may deliver an effective tool for boundary layer transition control in the hypersonic speed regime, if proven applicable to flight vehicles. Further theoretical research is necessary to understand more of the underlying physics how helium prevents the transition mechanism from progressing. Confirming the stabilizing effect at flight realistic enthalpies could be the next experimental step. It may also be beneficial for future studies to consider systems level questions, such as availability of similar light coolants on a flight vehicle and total amounts needed for realistic flight trajectories.

5.9 Methods

5.9.1 Oxford High Density Tunnel

This wind tunnel is a Ludwieg tube [243, 245]. Its capabilities are outlined by McGilvray et al. [243]. Tunnel as well as Mach 7 nozzle have been determined to provide suitably quiet flow for hypersonic boundary layer transition research by

Table 5.1: Free stream flow conditions.

	Nominal	'Low Re_u'
Total Temperature [K]	450 ± 15	460 ± 15
Freestream Mach number	7.1 ± 0.1	7.0 ± 0.03
Freestream Static Temperature [K]	42 ± 1.5	42 ± 1.4
Freestream Re_u [10^6 m^{-1}]	18 ± 1	12.8 ± 0.7
Stagnation Pressure P_0 [MPa]	1.151 ± 0.01	3.037 ± 0.01

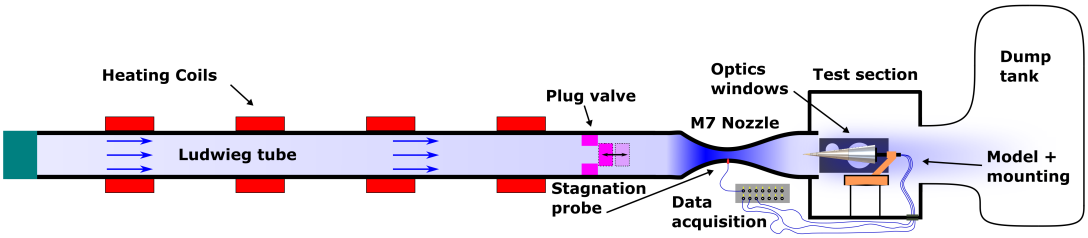


Figure 5.4: Oxford University High Density Tunnel schematic.

Wylie et al. [68, 225]. A simple schematic of its components is shown in Figure 5.4. For the given experimental conditions, the flow properties are listed in Table 5.1. The cone model is mounted at the nozzle exit to ensure exposure to the core flow delivering those conditions [68]. In addition, the test object is aligned parallel to the oncoming flow using a pitch and yaw step-motor traverse system.

5.9.2 Coolant Injection

The gas for the coolant injection flows from a reservoir tank through a flange into the test section and then towards the front injector plenum through a pipe inside the cone. The control sequence for the mass flow device FMA2611A is exactly as outlined in Chapter 4. In addition to the mass flow rate, the pressure in the pipe leading towards the injector is recorded. The blowing ratios are computed using calculated boundary layer edge properties via an approximated Taylor-Macoll solution [265, 266] assuming a perfect gas in the tunnel. The coolant mass flux is determined by converting the standard liters per minute value recorded from the mass flow controller into g/s using ideal gas relations. Due to the outflow profiles (see Section 5.10.3) the blowing ratio is given as an average over the entire porous surface. The given B_h values [154, 156] for the stagnation point are calculated by

employing the measured plenum pressure in a 1D-Darcy Fochheimer approach [174] with material coefficients for CE170 obtained from Naved et al. [159].

5.9.3 PCB Piezoelectric Sensors

To capture second mode oscillations at the surface, we employ PCB132A31 and PCB132B38 transducers manufactured by PCB Piezotronics Inc. [293]. We minimize any downstream effect of possible surface imperfections by flush mounting the gauges. The signal is amplified by an ICP Signal conditioner 483C15 series and then read at 2 MHz by a NI PXIe-6368 Multifunction I/O Module. Matlab's pwelch function delivers and estimate for the power spectral densities [274–277]. In addition, a continuous wavelet transform is calculated for the entire test time using a morse wavelet [294–296].

5.9.4 Kulite Piezoresistive Sensors

The pressure in the plenum of the nose tip injector is measured by a Kulite XCQ-062 17 bar range. The sensors' function is based on the piezoresistive effect of p-type silicon [297]. The Kulites are connected to a Fylde FE-H379-TA, data is then recorded with a 0.5 μs time base by a NI PXIe-6368 Multifunction I/O Module even though their response is only valid for frequencies below 20 kHz [8].

5.9.5 Thin Film Gauges

The thin film gauges in use were either manufactured in-house by the University of Oxford Instrumentation Workshop [298] or by the equivalent institution at the University of Queensland [299]. The high speed heat flux data is reconstructed by an impulse response based post-processing software [300]. The substrate material for the sensors in use is either Quartz [301] or Macor [302], wherein material properties were inferred from the given references. The cylindrical substrate body has a 2 mm diameter and a depth of 8 mm, sufficient to be assumed as semi-infinite [303]. Said substrate is inserted into a hollow cylinder of PEEK, doubling the gauges' total

diameter to 4 mm. The sensors' signal is recorded with a sampling frequency of 125 kHz. Shown Stanton numbers are computed using the following relationship:

$$St = \frac{\dot{q}}{\rho_e u_e c_p (T_r - T_w)} \tag{5.2}$$

Hereby, $\dot{q}$ is the heat flux, c_p is the heat capacity of dry air and T_w is the wall temperature. Herein, $\dot{q}$ and T_w are inferred from thin film gauge data and the recovery temperature T_r is calculated via

$$T_r = T_e(1 + r((\gamma - 1)/2)M_e^2) \tag{5.3}$$

Using a recovery factor of $r = Pr^{1/2}$ laminar flow $r = Pr^{1/3}$ for turbulent flow [18], where Pr is the Prandtl number. A feedback loop is applied in the analysis to determine the correct recovery factor for each gauge. Prior to the test campaign, gauges are calibrated in a MMM Medcenter Einrichtungen GmbH FC-B2V-M/Friocell 222 oven for the temperature range of $15 - 40°C$ [304] using the original cabling to ensure the same lead resistance. As the gauges were already installed in the steel or aluminium model parts the calibration oven maintains each of the 6 temperature steps for 160 minutes to allow the parts to come to equilibrium. This was confirmed by two K-type thermocouples connected with the model. Temperature response of each individual gauge was then obtained via a linear regression model. Reference curves for heat transfer on the cone are calculated using Eckert's [251, 267–269] reference enthalpy which includes transforming the respective solution for flat plates to a cone with the appropriate factors [270, 271]. The calibration procedure is completed by obtaining correction factors for two thin film gauges ($x = 426.7\,\text{mm}$ and $x = 140\,\text{mm}$), which deviated consistently from theoretical values by a constant. By comparing their measurement value in a laminar flow environment to the respectively Eckert correlation a factor was obtained to account for mounting imperfections. Said compensation is kept constant across all tests.

5.9.6 Z-type Schlieren

The schlieren system in use is assembled as a classical z-type schlieren layout with one additional flat mirror to match the spatial constraints of the experiment (see Figure 5.5). A razor blade is used as a knife edge to create a cutoff and image density gradients in vertical direction as intensity changes [228, 233, 235, 236]. The setup ensures that the plane of maximum focus lies central to the cone. Knife edge and camera are mechanically inclined by 7°. This enables recording density gradients normal to the model surface and allows to maximize field of view along the cone and frame rate simultaneously. A list of the optical components in use can be found below in Table 5.2 in combination with Figure 5.5. Frames are recorded using a Phantom TMX 7510 (Version 100002) at a frame rate of 700 kHz and an exposure of 1.161 μs. The total frame size is 1280 x 64 pixels. However, the field of view is limited by the tunnel windows and the mirrors. The location of the schlieren as well as the resolution are calibrated using a recognizable frame and a semitransparent checkerboard, respectively. Immediately before every shot, a no-flow background image is taken using the exact same settings as during the test. For Figure 5.3, frames were exported from the Phantom Camera Control Software 3.6 in .tif format with bit depth 8. Post-Processing the images encompasses the following steps: Using the checkerboard, an undistortion operation is performed for background and video frames respectively. This step is necessary due to the increased size of the field of view compared to Chapter 4, making the images more susceptible to fisheye effects. The mean background image (without flow) is subtracted from all schlieren frames. Subsequently, the cone edge is identified using a patial area effect based algorithm [283, 284] ensuring repeatability. This allows to rotate the image to a horizontal position. The same edge enables application of the previously obtained calibration and hence to locate the field of view on the cone within the general coordinate system. Dark corners caused by the edges of the mirrors are cropped away on both ends of the image strip and a gamma correction (Matlab's imadjust function) is applied to increase contrast. An average is calculated from 1000 schlieren images around the time of interest. This average is then subtracted from the shown single

Table 5.2: Optical components for z-type schlieren.

Part	Description	Manufacturer	Part Number	Details
A	High Power LED Box	Oxford University Instrumentation Workshop/Luminus	PT-120G-L11-MPN	Continuous high power LED chip with added focusing optics and interlock logic. Emitted wavelength: 480 – 580 nm, 525 nm dominant [305]
B	Parabolic Mirror	North Hants Eng.	3080/3077	12” diameter parabolic mirror, f=1600 mm
C	Flat Mirror	North Hants Eng.	T501 60386/69061	12” diameter flat mirror
D	Flat Mirror	OWL	-	4” diameter flat mirror
E	Knife Edge	-	-	Razor Blade
F1	Convex Focusing Lens	Thorlabs	AC508-075-A-ML mounted to LCP01/M	Convex Lens, f=75 mm
F2	Focusing Lens	Nikon	Nikkor 50 mm, 1:1.4 D	Camera lens used for additional focusing
F3	Camera Lens	Tamron	A001-C	AF70-200mm F\2.8
G	High Speed Camera	Phantom	TMX 7510 (Version 100002)	

images, which ensures an emphasis of time dependent instabilities. To reveal details such as turbulence and instability waves, we represent schlieren intensity via a colormap. The colorscale is then limited to 70% of the maximum pixel value, leading to saturation in more pixels, however highlighting instabilities better.

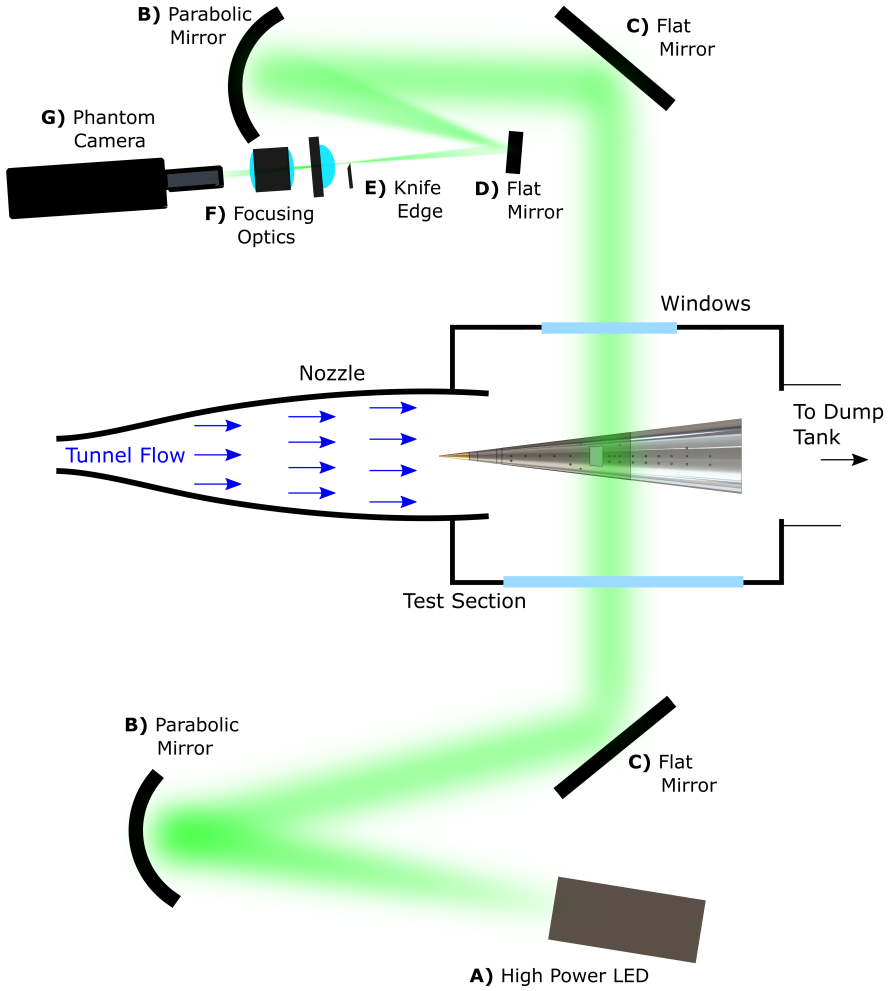


Figure 5.5: z-type schlieren system at HDT test section.

5.9.7 Uncertainty Analysis

Uncorrelated errors were propagated according to the standard uncertainty propagation procedures outlined in e.g. Morrison [252] for all analytical mathematical expressions. When an iterative algorithm was used, a Monte Carlo method is applied. By using the respective uncertainties of the input quantities as a standard deviation, normal distributions of 10,000 values are generated. Drawing inputs randomly from those distributions and feeding it into the iterative calculations yields a distribution of output values. One standard deviation of said result serves as the final uncertainty. This method is applied for the calculation of the Mach number from the pitot-to-stagnation pressure ratio, the Taylor-Macoll solutions [265, 266] for boundary

layer edge properties and the Eckert reference enthalpies [267]. The calculations and uncertainty propagations are conducted in this order, as each will rely on the inputs of the previous ones. Uncertainties for the bandpowers are calculated by using Matlabs' inbuilt pwelch function. The χ^2 – approach delivers upper and lower bounds given for the PSD for a 99% confidence interval [306]. Those bounds are then used to compute the upper and lower end of the error bars in the bandpower plots.

5.10 Extended Data

5.10.1 Experiment at low Reynolds Number

The stabilization effect of helium was furthermore confirmed at a different unit Reynolds number. Using the same experimental setup and running the tunnel with $Re_u = 12.8 \cdot 10^6\, m^{-1}$ a much more stable uncooled case was achieved. Natural transition does not start until the last third of the cone as seen in Figure 5.6 and the related injection tests re-iterate what has previously been shown. A larger blowing ratio of helium moves the transition location further back than a lower blowing ratio. Nitrogen advances transition, the direct comparison of the two coolants is however more difficult in this case due to a difference in relative injection rates. Similarly, the PCB results confirm the same trends initially revealed in Figure 5.2. Schlieren data can unfortunately not be provided for this condition.

5.10.2 Experiments with different Injector Material

Some nominal condition cases were repeated with a permeable tip made from BF100 Al porous aluminium [258], and alternative to CE170. This nose tip had the same external and internal geometry and the motivation was hence to examine sensitivity to outflow profiles, pore size and injector material. Results are depicted in Figure 5.7. No qualitative differences could be found and only very little quantitative disagreements, which are mostly within the given uncertainty. In conclusion, the stabilizing effect of helium could be confirmed across Reynolds numbers, injector materials and outflow profiles.

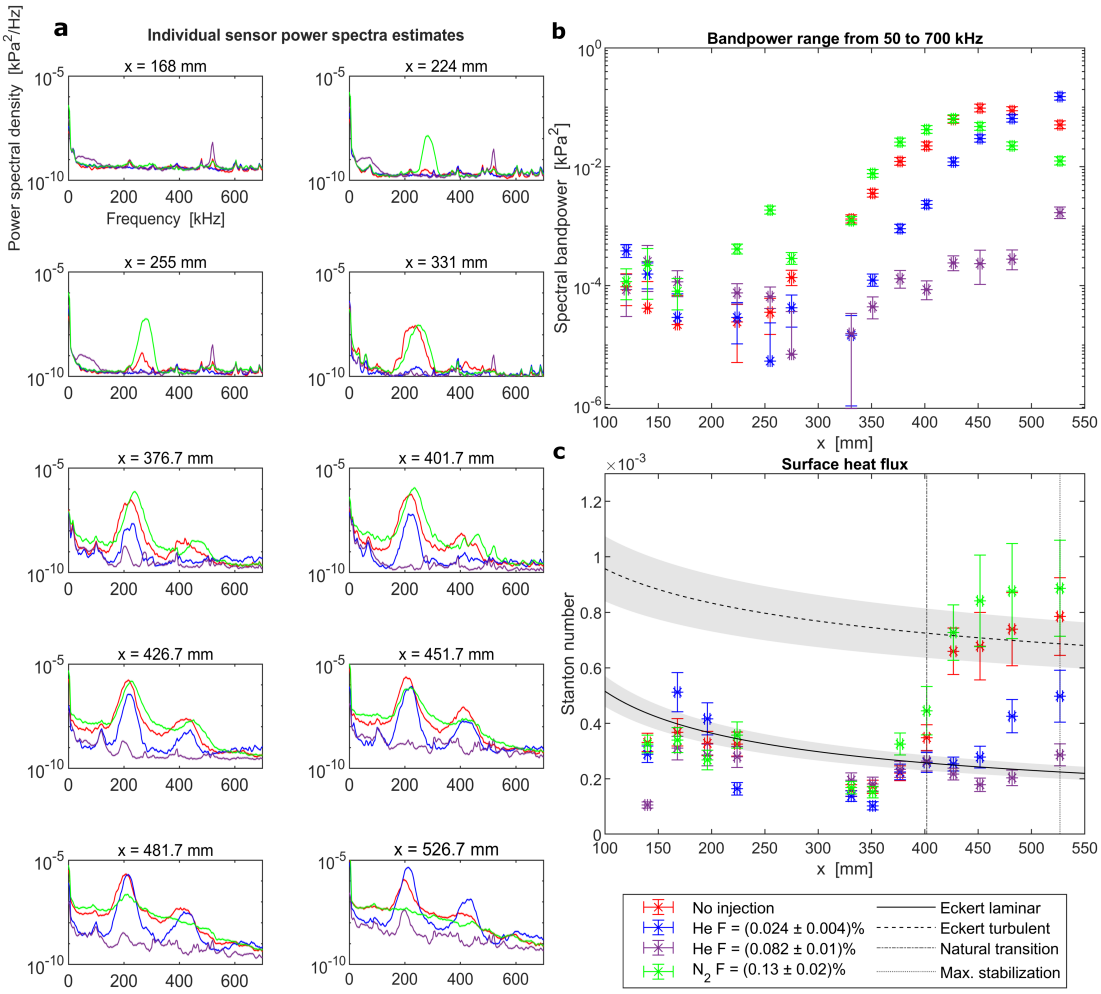


Figure 5.6: Results from surface instrumentation for lower unit Reynolds number. On the left-hand column, individual power spectral estimates are shown for several differential pressure sensors. The top right corner shows the integrated bandpower belonging to the power spectra. The bottom right plot indicates the heat flux measured by thin film gauges along the cone. The discrete points are compared to Eckert correlation [267]. Colours represent different injection rates and gases and are kept consistent across all plots within the figure. Error bars indicated 68% confidence intervals.

5.10.3 Nosetip Outflow Profiles

Two different nose tip materials were used. One was made from porous CE170 and the other one from porous aluminium BF100AL [258, 307]. BF100Al has a porosity of 17% and CE170 has a porosity of 19% [258, 307]. The internal plenum geometry of the porous nose cones can be seen in the respective technical drawing in Appendix A.1. It consists of three drilled holes with one-, two- and four-millimetre diameter.

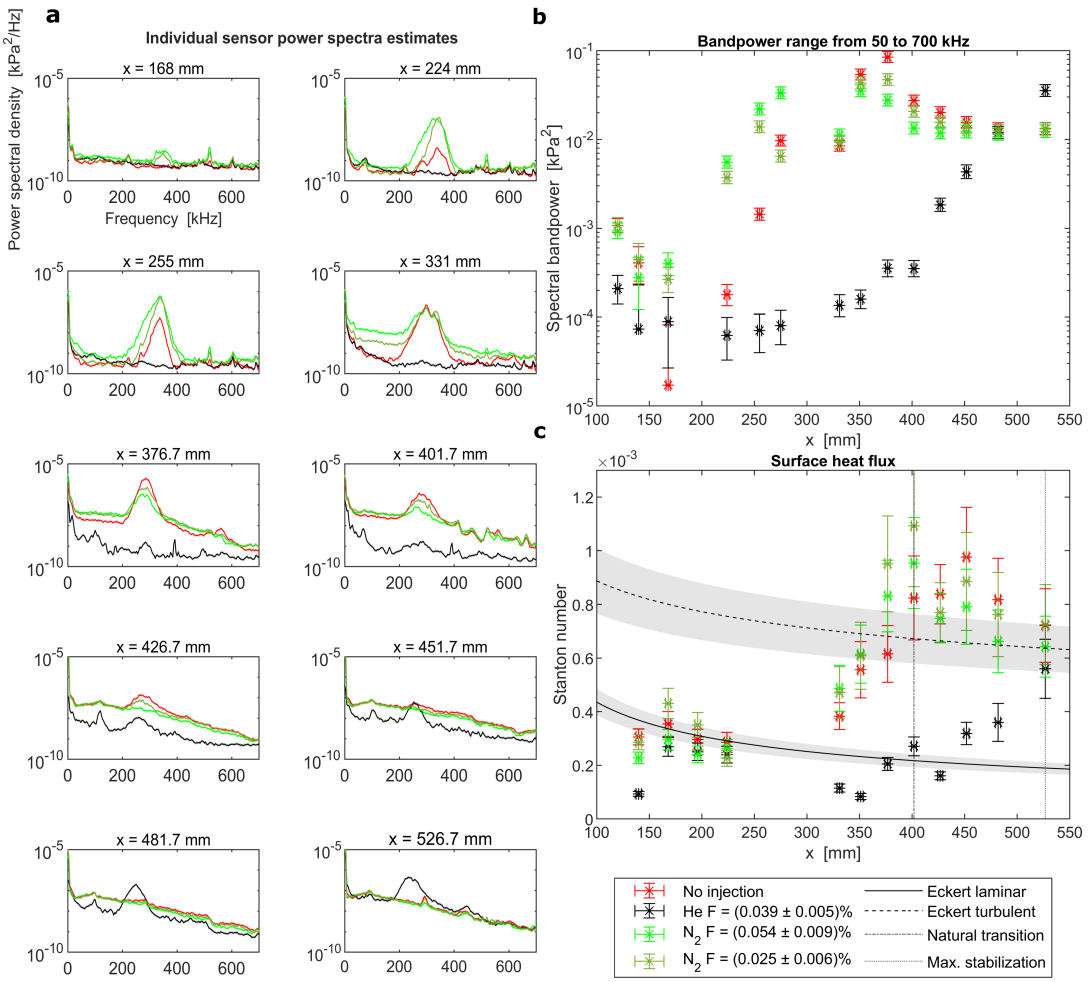


Figure 5.7: Results for surface instrumentation. The nose tip in use was made from BF100Al. All error bars indicated 68% confidence intervals.

Initially, the internal cavity was designed as a cone which followed the outer structure and would thus maintain a constant thickness throughout the injector. To reduce manufacturing cost and complexity, this was amended to the shown design, which allows using standard drill bits. Simulations were conducted with the porous flow solver of Comsol multiphysics 5.5. They confirmed a satisfactory outflow profile under the given external flowfield conditions. The internal steps only cause minimal deviations in outflow velocity which were deemed insignificant compared to usual inhomogeneities in porous materials [308].

Similarly to the procedures described in Chapter 4 and by Dittert et al. [184], the outflow profile of those conical injector segments was characterized using a Dantec

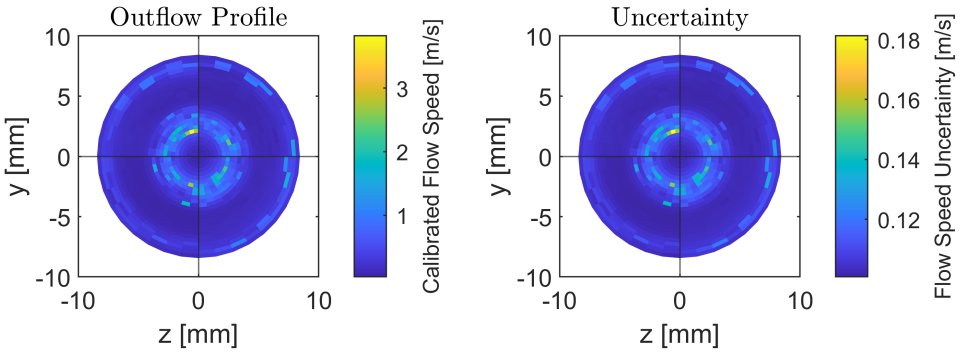
Dynamic 55P11 straight hotwire probe connected to a Dantec Dynamic Streamline Pro signal conditioner. Compared to the Chapter above, the probe arm now only needs three degrees of freedom to follow the geometry. Hence, a traverse assembly of two rotational and one translational step motors allows to automatically sample 900 flow velocity values along the segment shape at (1.5 ± 0.5) mm surface normal distance, while air is transpired through the samples at 5.0 slpm. The tests were conducted at atmospheric external pressure and can hence not replicate the true outflow profile inside the tunnel during a test with varying and inhomogeneous surface pressure distribution. This measurement does also not give information about outflow activity of individual pores in the μm range. It can however show that the interfaces of porous and impervious material seal appropriately. Additionally, the obtained outflow maps demonstrate a reasonably homogeneous effusion distribution on the large scale. Albeit structural differences in effusion uniformity are evident in Figure 5.8 - the BF100 Al sample seems to transpire more gas near the tip - Section 5.10.2 has already discussed how this barely lead to any noticeable difference.

5.10.4 Continuous Wavelet Transforms

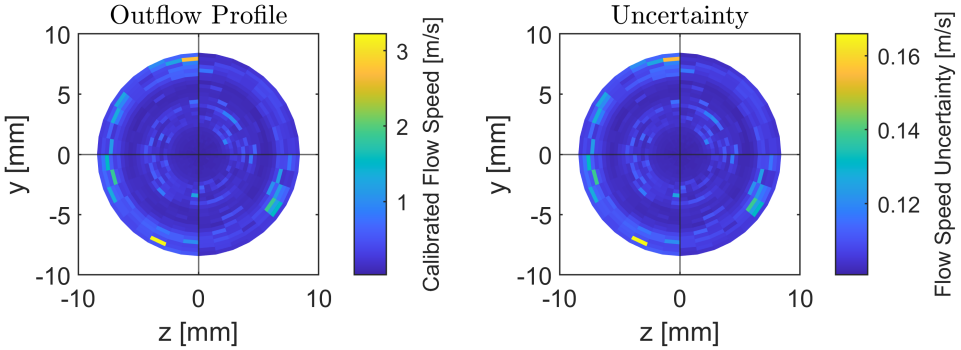
While the PSDs in Figure 5.2 show a time average across the test, using a continuous wavelet transform can resolve the spectral content over time. It is hence visible how the individual second mode wave packets travel across the high frequency pressure sensors. As indicated in Figure 5.9, Figure 5.10 and Figure 5.11 the magnitude of the individual packets is reduced by helium injection. In addition, the occurrence of second mode packets itself is also strongly reduced. Turbulence can again be inferred from the spread of the power spectrum into lower frequencies.

5.10.5 Average Schlieren Image

Subtracting a time averaged schlieren image from single frames highlights instabilities in Figure 5.3. Those time averages across 1000 consecutive frames are shown below. Mean turbulent structures are distinguishable from the laminar boundary layer by its reduction in intensity and a thickened, blurred appearance above the cone surface.



(a) BF100Al nose tip



(b) CE170 nose tip

Figure 5.8: 2D projection of Outflow profile, BF100Al nose tip. The uncertainty color map represents 68% confidence intervals.

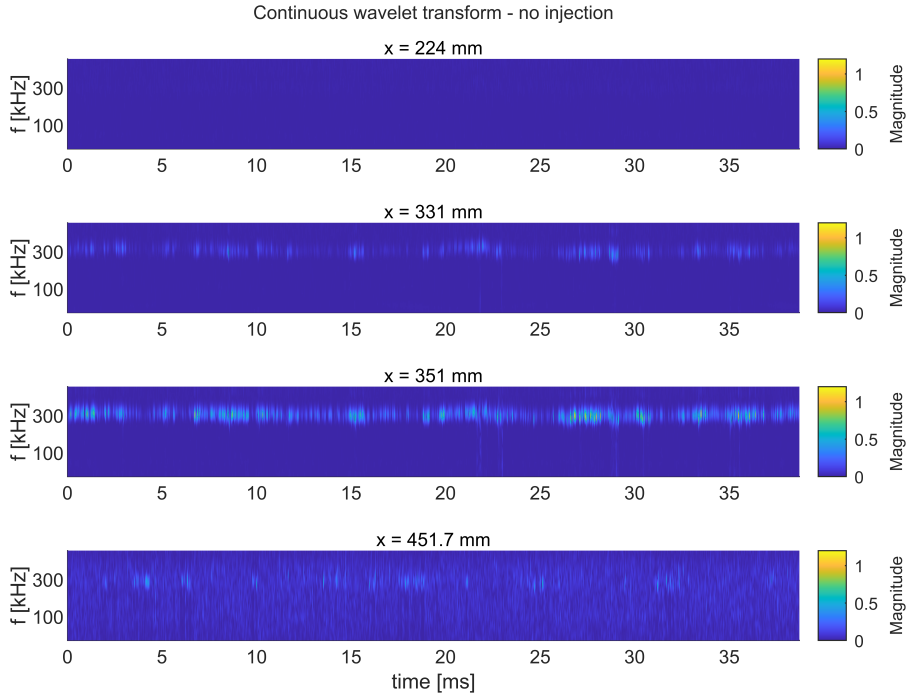


Figure 5.9: Continuous Wavelet Transform for natural transition case. All individual plots are shown with the same color scale. The CWT relate to the experimental cases shown in Figure 5.2

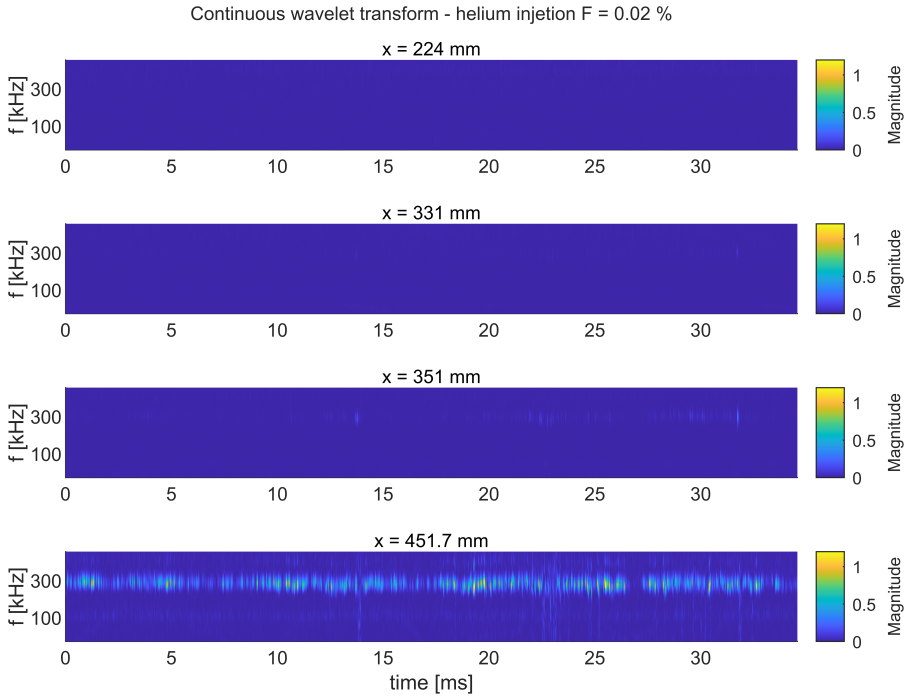


Figure 5.10: Continuous Wavelet Transform for low helium injection case. All individual plots are shown with the same color scale. The CWT relate to the experimental cases shown in Figure 5.2

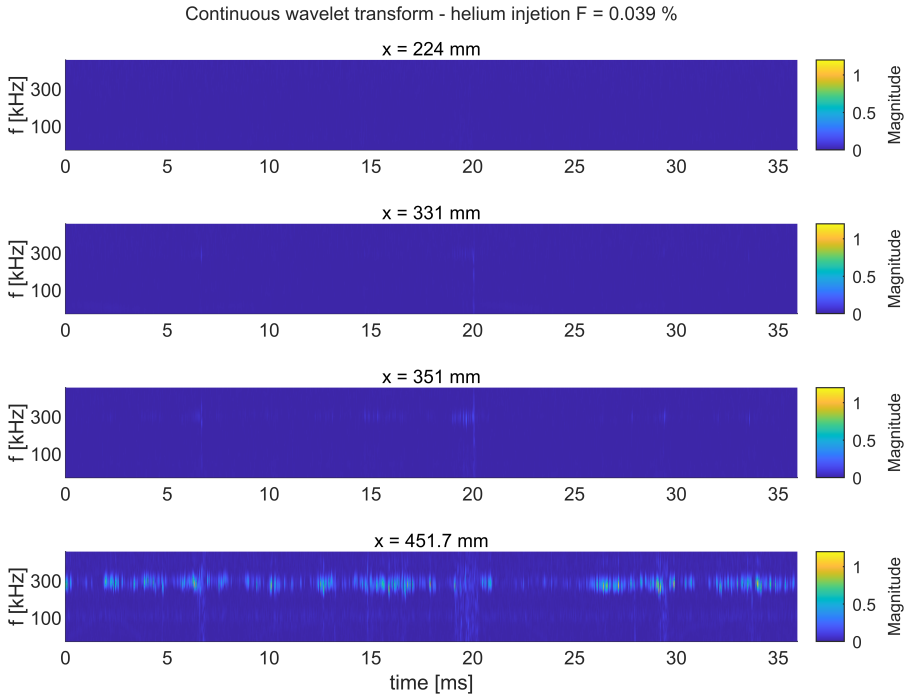


Figure 5.11: Continuous Wavelet Transform for moderate helium injection case. All individual plots are shown with the same color scale. The CWT relate to the experimental cases shown in Figure 5.2

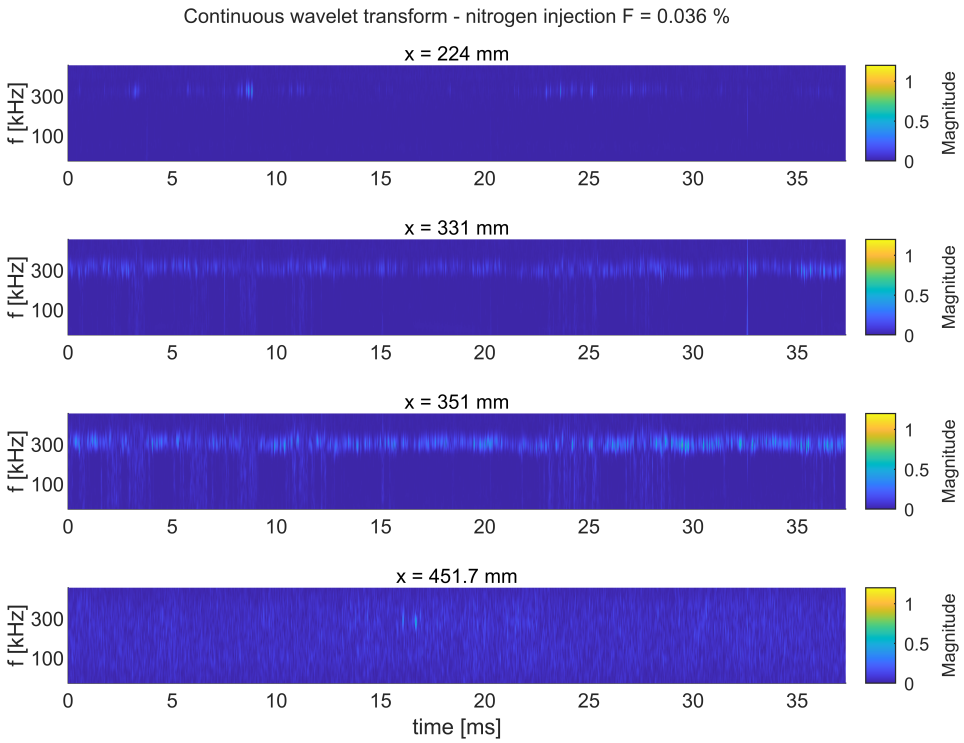


Figure 5.12: Continuous Wavelet Transform for moderate nitrogen injection case. All individual plots are shown with the same color scale. The CWT relate to the experimental cases shown in Figure 5.2

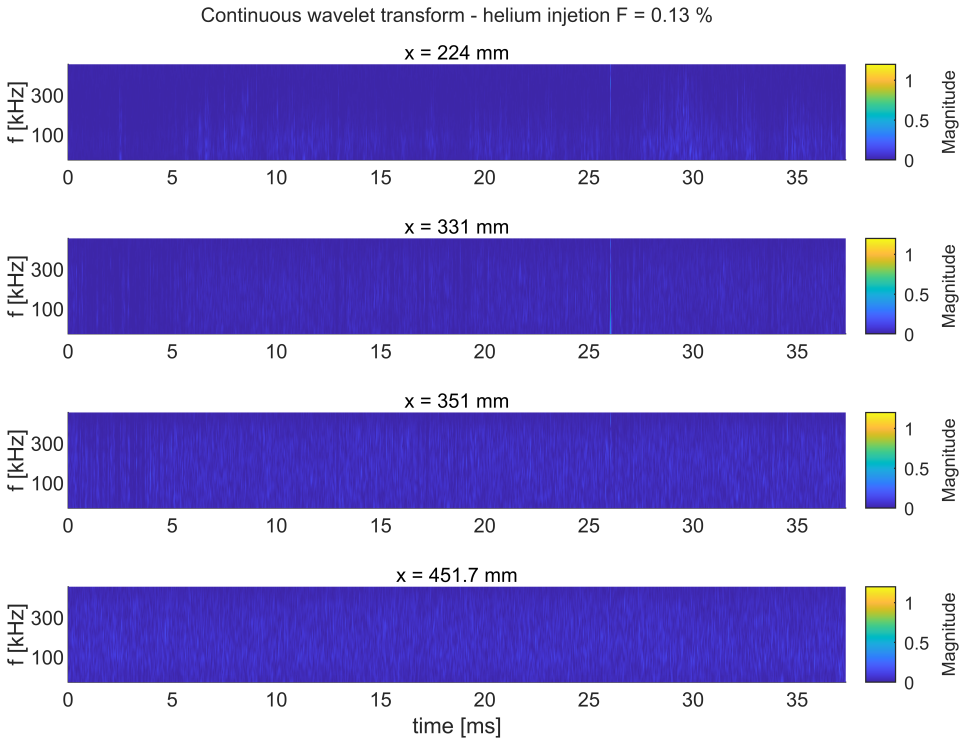


Figure 5.13: Continuous Wavelet Transform for high helium injection case. All individual plots are shown with the same color scale. The CWT relate to the experimental cases shown in Figure 5.2

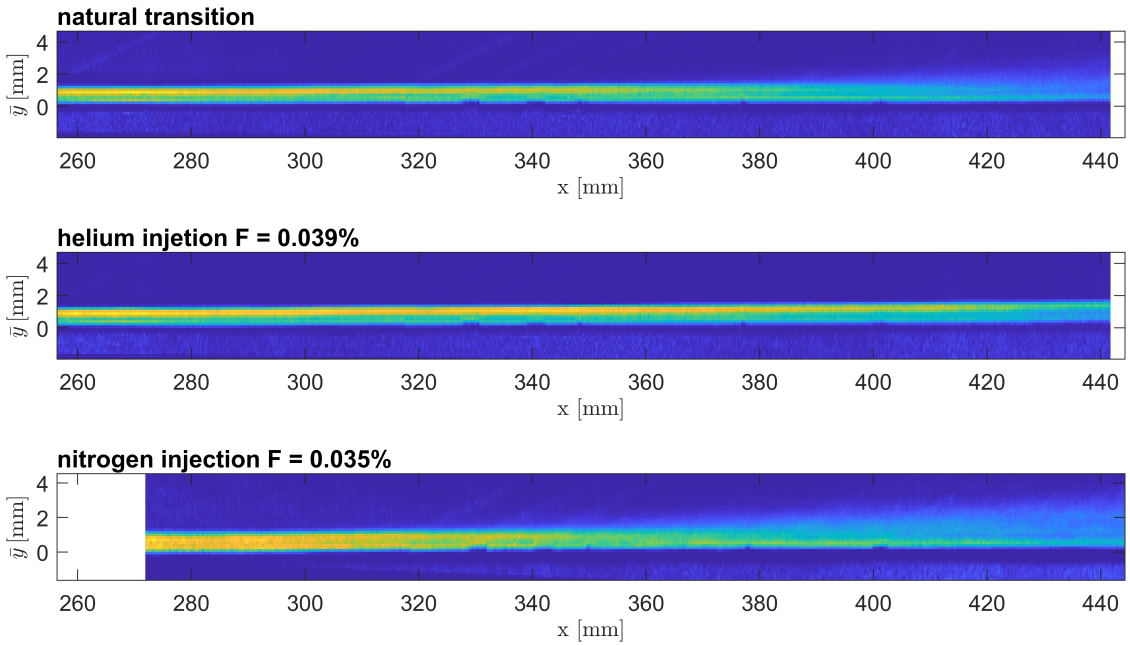


Figure 5.14: Average of 1000 schlieren frames around point of interest. Those images were subtracted from the single frames shown in Figure 5.3.

Statement of Authorship

Title: Hypersonic Boundary Layer Stabilization by Helium Injection

Status: Unpublished and unsubmitted work written in a manuscript style

Author Contributions:

- **Philipp Kerth** had the idea for the test cases, cone model and analysis performed. He designed the model, assembled it, instrumented it, ran all experiments, collected the data and analysed it. He wrote the manuscript with input from Matthew McGilvray.
- **Raghul Ravichandran** designed and commissioned the hot wire traverse system.
- **Andrew Pilkington and Hassan Saad Ifti** re-designed the porous nose tips and their internal geometry.
- **Sebastien Wylie** acted in a supervising role during model design, test case selection and data analysis.

- **Matthew McGilvray** supervised the project and organized and managed the funding.

Student Confirmation:



Date: 08/01/2023

Supervisor Confirmation:



Date: 10/01/2023

6

Decoupling Boundary Layer Transition and Heat Flux Reduction for Hypersonic Transpiration Cooling

Contents

6.1 Foreword 120
6.2 Introduction 120
6.3 Experimental Setup 123
6.3.1 Test Model with Gas Injection 123
6.3.2 Surface Instrumentation 126
6.3.3 Z-type Schlieren 126
6.3.4 Focused Laser Differential Interferometry (FLDI) 127
6.3.5 Flow Conditions 132
6.4 Experimental Results 133
6.4.1 Surface Heat Flux 133
6.4.2 Surface Pressure Fluctuations 133
6.4.3 Schlieren Images 136
6.4.4 Schlieren Power Spectra 137
6.4.5 Frequency Shift within Boundary Layer 141
6.4.6 Second Mode Power Distribution across the Boundary Layer Thickness 141
6.4.7 Experimental Definition of Transition 147
6.5 Discussion 152
6.6 Conclusions 153

6.1 Foreword

Chapter 5 leaves only little room for ambiguity - a transition delay was found - while Chapter 4 is harder to interpret. From only surface pressure and second mode data, it is not obviously deducible how turbulence develops with cooling. This last Chapter shall be dedicated to carefully and rigorously evaluating measurement techniques with respect to their reliability under given experimental situations. Could some techniques lead to misinterpretations or even contradict each other? Highlighting possible shortcomings for measurements of transition with cooling shall enhance not only the robustness of the previously presented findings, but also the right choice of metrology for future experiments. Only minor structural changes were made to the paper format. Items added to the paper appendix - they were deemed necessary for completeness albeit not essential for the arguments presented - are now added to the respective sections in the chapter to aid the written thesis format. Furthermore, references to other papers are replaced with links to the appropriate chapters. The statement of authorship can be found at the end of the chapter.

6.2 Introduction

While a re-entry vehicle descends through earth's atmosphere along its trajectory, boundary layer transition may not be present at high altitudes, but upon increasing density and Reynolds number turbulence will eventually move forward on the geometry with drastic aerothermodynamic consequences [39, 263]. Driven by the need of prediction methods and design tools [190] as well as scientific foundational research ambitions, more needs to be understood about the fluid physical mechanisms, causing said process [57].

Despite suffering from higher noise levels compared to free flight, wind tunnel measurements are still an integral component of this research [57, 60, 79]. In those facilities, researchers commonly utilize the connection of turbulence with aerodynamic friction and hence heat transfer [64] to determine the transition location

[8]. Techniques such as infrared thermography [52, 108], thermocouples [8, 109], thin film gauges [309, 310], atomic layer thermopiles (ALTP) [104, 259] and temperature sensitive paint [149] are commonly used in the field to infer instability data or laminar-turbulent transition from surface heat flux recordings. However, when a cooling technique is present, surface instruments might receive a superposition of competing effects and be unable to accurately resolve turbulent heating. Use of hotwires [311–313] may eliminate such ambiguities, but those probes have severe limitations in hypersonic flow environments due to their fragility and invasive nature [101].

The arbitrariness of determining the transition location experimentally has been extensively discussed in the literature [57]. Schneider highlights [57] that transition is a process along a certain region. He subsequently argues that describing transition as a precise line on a vehicle will thus strongly rely on the criterion chosen by the researcher [57]. Addressing said problem more than 40 years ago, Pate [314] concludes: "When conducting transition studies at least two methods should always be used. Optical methods (schlieren, shadowgraph) often provide a satisfactory second technique." [314]

Due to strong heating effects in the hypersonic speed regime [13], effusion cooling has been of interest for decades, which is evident when considering how References [36, 47, 56] discuss studies distributed across more than 60 years. If gas is transpired out of the wall, it will impact transition [36, 56, 109]. Moreover, the state of the boundary layer also influences the cooling quality [163]. Any type of active heat mitigation has been found to generally advance transition and can thus cause an increase in friction and heat transfer [56, 64] leading to excess heating rather than the desired cooling effect [47]. Experimental and theoretical studies into said dilemma are therefore necessary. Concerning the problematic of detecting transition accurately with injection, Schneider [56] particularly criticises a study Dunavant and Everhart [181] conducted, for not sufficiently incorporating the heat mitigation effect of injection into their analysis method. He therefore brands their results as "subject to interpretation" [56].

Two more recent studies conducted on cones with gas injection both experimentally inferred transition from surface thermocouple data [104, 203, 210]. For Jewell et al. [109, 210], injection happened close to the apex and transition was determined via an intermittency method [81, 210]. In contrast, Camillo et al. [104] had injection in the direct vicinity of transition on their cone model. They [104] acknowledge the problem of having cooling and transition present in the same area, while attempting to capture a heat transfer increase due to beginning turbulence. Their method to infer transition onset is based on comparing theoretically obtained laminar heat flux levels to averaged thermocouple data [104]. Schlieren images show damping of whole second mode wave packets, which strongly supports their argument about a discovered stabilization [104].

Work presented in Chapter 5 has dealt with a similar gas injection scenario, wherein transition was inferred from schlieren images and thin film gauges. Hereby, as opposed to Camillo et al. [104] and similarly to Jewell et al. [210], transition happened far away from the injection location. The porous nose injector segment ended at an axial distance of 58 mm, while transition occurred around 350 mm at $Re_u = 18 \cdot 10^6\, m^{-1}$. It was thus assumed that the cooling effect had largely subsided and observed heat flux reductions were predominantly due to a delay in transition. Upon designing the experiments and analysing the aforementioned data, we considered Pate's recommendation [314] and anticipated problems with determining transition advance or delay. Contrastingly, schlieren, surface pressure and heat flux measurements were all in good agreement with respect to boundary layer stability results. It is however assumed that the contrasting injector location in the work presented below - a porous segment within the cone frustum - may complicate stability measurements.

Stalmach et al. [190] discussed the problematic of measuring transition location with cooling in great detail. Among other aspects, they specifically highlight discrepancies in between optics (shadowgraph in their case) and surface heat transfer. While the former technique is usually triggered through completion of transition as indicated by optically recognizable full turbulence, the latter usually marks the very upstream

limit of a transition region [190]. Stalmach et al. [190] acknowledge how especially the former may be corrupted by injection of coolants. It needs to be mentioned here how the geometry of their injector deviates significantly from the presented example below. Their nearly entirely porous cone will have caused thin film gauges to always be influenced by gas injection from the nearest vicinity. This significant difference in coolant outflow physics paired with the advances in understanding of transition mechanisms motivates further research.

In this work, we extend parts of Camillo et al.'s [104] research with a different coolant, helium and at a low enthalpy environment, yet with a similar geometry and Mach number. Herein, we aim to discuss related aspects as Stalmach et al. [190] with respect to inferring transition location, albeit with a significantly different injector geometry and modern high frequency measurement techniques which enables to extend their argumentation to instability waves. Helium yields more effective cooling [36, 159] and a larger effect on the boundary layer thickness [49] than nitrogen at the same blowing rate which shall improve insight into intertwining of turbulence, injection and heat transfer reduction in the presented experiments. We specifically focus our investigation on this aspect to improve robustness of past and future studies. With foreign gas effusion, different methods such as non-intrusive optical techniques may be necessary to quantify boundary layer instability modes accurately and complement surface measurements. Herein, we aim to experimentally decouple the effect of boundary layer transition induced heating from the heat transfer reduction due to active transpiration cooling. An in-depth discussion and comparison of different metrological methods to infer transitions validates respective accuracies and is geared towards maintaining precision and clarity by highlighting potential ambiguities.

6.3 Experimental Setup

6.3.1 Test Model with Gas Injection

The 7° half-angle cone, shown in Figure 6.1, has been previously employed in the same configuration and injector in Chapter 4. Similarly to Chapter 4, the

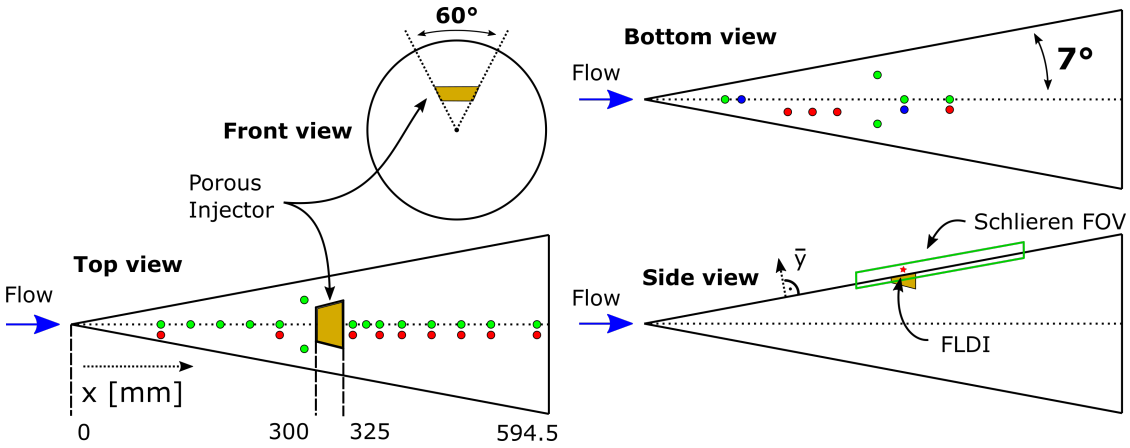


Figure 6.1: Test model geometry. Blue points represent absolute pressure gauges, red are thin film gauges and green PCB high frequency pressure transducers. The porous injector patch is marked in yellow, which spans a 60° azimuth. $\bar{y}$ is the wall normal coordinate.

model has a sharp nosetip, is instrumented with high frequency differential pressure sensors (PCB) and now additionally with thin film gauges (TFG). Model dimensions and instrumentation locations can be seen in Figure 6.1. 0° angle of attack and yaw is maintained for all tests with ±0.1° uncertainty. Microporous aluminium BF100Al [258] is used to transpire gas into the boundary layer. It has a mean pore diameter of $30 - 40\,\mu$m [307]. A plenum below the 10 mm thick porous patch allows measurement of the plenum pressure using a Kulite XT-190 SM. Gas flow through the porous injector is controlled using an Omega FMA2611A mass flow controller, like in all other chapters. Before the campaign, a curve of mass flow rate versus plenum pressure is recorded. Due to the radial 10 mm thickness the Darcy and Forchheimer coefficients of the porous material patch can be determined using a simplex search algorithm applied to the aforementioned curve [175, 272]. The Darcy-coefficient is $K_D = (8.26 \pm 0.04) \cdot 10^{-14}/m$ and the Forchheimer-coefficient is $K_F = (5.3 \pm 0.1) \cdot 10^{-10}/m^2$. The blowing ratio is then computed via:

$$F = \frac{\dot{m}_c}{\rho_e u_e A} \tag{6.1}$$

Herein, we employ the same method as in Chapter 4 to obtain the boundary layer edge properties via an approximation [265, 266] and the the coolant mass flux through the Darcy-Forchheimer equation.

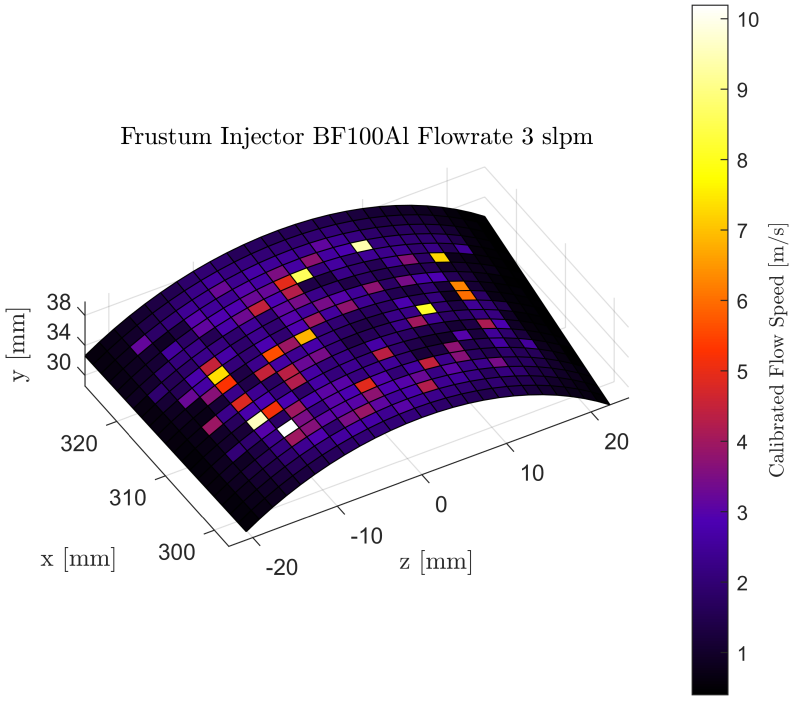


Figure 6.2: Injector effusion map.

Similarly to Ifti et al. [175], Miró Miró et al. [108], Dittert et al. [184] and with the exact same procedure as presented in Chapter 4 the effusion profile of the injector patch was measured using a hot wire again. After collecting the data presented in Chapter 4 the model had been disassembled and partially refurbished. In an attempt to investigate the reproducibility of said effusion characteristics we repeat the outflow measurement procedure from Chapter 4. Using the traverse arm, the porous 3D segment's outflow distribution was scanned at a distance of $(1.5 \pm 0.5\,\mathrm{mm})$. The result is plotted as a velocity map in Figure 6.2, showing no leaks at the interfaces of porous aluminium and impervious steel. The presented flow velocity measurement does not represent the actual outflow speed from microscopic pores. The hot-wire is too large and its distance from the porous material was too far in order to resolves such features. Macroscopic outflow hotspots or leaks could only be located with an accuracy in the $\sim$ 2mm range. Any pipework and fittings were rigorously checked for its sealing quality by using leak detector spray.

6.3.2 Surface Instrumentation

PCB 132A31 and 132B38 piezoelectric sensors are - like all other surface sensor types - flush mounted in the instrumentation hole locations shown in Figure 6.1 using RTV silicone. Using the manufacturer calibration, the signals are converted from voltage to pressure. A sampling rate of 2 MHz allows the calculation of Welch's power spectral density estimate at suitably high frequencies [274–277] for our current analysis aims.

We obtain surface heat flux values from the following equation 6.2, where $\dot{q}$ is the surface heat flux and c_p is the tunnel test gas heat capacity, T_r is the recovery and T_w the wall temperature.

$$St = \frac{\dot{q}}{\rho_e u_e c_p (T_r - T_w)} \tag{6.2}$$

Point measurements on the cone surface are obtained using thin film gauges [298, 299], distributed along the axial length of the cone as shown in Figure 6.1. Sensors, calibration and analysis method are equivalent to Section 5.9.5. Oldfield's [300] processing methods allows conversion of voltages sampled at 125 kHz into heat flux data.

The correction factors obtained for two gauges (at $x = 433.7\,\mathrm{mm}$ and $x = 147\,\mathrm{mm}$) are likewise carried over from Chapter 5. To unequivocally distinguish between laminar and turbulent levels of heat flux we compare measurements to respective Eckert correlations for conical flow [268, 271, 315].

6.3.3 Z-type Schlieren

The z-type schlieren system [233, 235, 236] employed to observe the boundary layer in this chapter is precisely the same as in Chapter 5 to capture cone-surface normal density gradients. The field of view is also alike, as visible in Figure 6.1. All data processing steps are equivalent up until generating colourmaps. Those steps shall only be very briefly be summarized here: Precautions were taken to remove distortions of the images and locate the field of view relative to the cone. Both are achieved by recording a chequerboard mounted to the cone prior to closing

the tunnel test section. Background subtraction and image enhancement ensure improvement of schlieren signal quality. In the results presented below we however add further processing steps to enable assessment of optically measured frequency content. For optimal comparability, PSDs are calculated with the same procedure as for PCB sensors directly for each pixel over a range of 2000 frames. Every pixel is herein treated as an independent time series of schlieren signal intensities $I(t)$, sampled at a 700 kHz frame rate. As the sampling frequency and number of data points is lower compared to the surface instrumentation, the Hann windows is adapted accordingly to 200 points in length.

6.3.4 Focused Laser Differential Interferometry (FLDI)

The idea for this "non-imaging common path interferometer" [316] is more than 50 years old [317] and the system has since proven its favourable characteristics to conduct measurements in a hypersonic flow fields and associated boundary layers [316, 318] (see also e.g. [70, 319]). The Oxford FLDI largely follows the setups described by Smeets [317], Schmidt et al. [318] or Fulghum [316] except with a few components added to match spatial constraints. It firstly consists of a Ventus 550 mW 671 nm continuous wave laser (**A**) (Figure 6.3) whose beam is divided into two of orthogonal polarization using a Wollaston prism (**G**) with 2 arc minute splitting angle, alike the original setup proposed by Smeets [317]. A biconvex lens **H** subsequently focuses the separated beams [318]. This generates what would be described as 'depth-of-field' in a camera [237] and hence concentrates the sensitivity of FLDI in a narrow field in beam wise direction [316, 317, 319]. Herein, focal lengths of the lenses were specifically selected to match the width of the HDT's test section. Two adjustable mirrors (**I**) turn the beam by 90° twice to save space next to the test section windows, giving the Oxford FLDI a z-shaped light path. Said mirrors are finely adjustable and allowed precise alignment of the beam to the model. Similarly, the optical rails on both sides of the tunnel were mounted on Thorlabs LJ750/M lab jacks enabling high precision vertical positioning of the interferometer's measurement point.

Component	Description
A	Laser Quantum Ventus 671
B	Iris aperture
C	Achromatic doublet lens
D	Pinhole + Achromatic doublet lens
E	Faraday isolator with linear polariser
F	Aspheric lens f = 10mm
G	Birefringent Wollaston prism
H	Biconvex lens f = 100 mm
I	Adjustable mirror
J	45° - Polariser
K	Polarizing beam splitter
L	Photodiode
M	Picoscope with differential port

Table 6.1: FLDI Components.

Alike schlieren systems, FLDI utilizes the Gladstone-Dale relation [234] which links gas density and refractive index [228, 316–318]. The optical principle of said interferometer allows metrological access to any refractive index fluctuations by comparing polarization states of the two independent paths within the test volume [316–318], which is achieved using two photodiodes (**L**) and a differential port connected to an oscilloscope (**M**) in our system. In good agreement with the values from e.g. Ceruzzi [319], the beam separation at the point of focus has been determined to be $(64 \pm 7)\,\mu$m using a Thorlabs BC106N-UV/M beam profiler. More information about the technique's general working principle can be found in the original publication from Smeets [317] or in theses from Fulghum [316], Parziale [70] or Ceruzzi [319, 320].

Recording and Alignment Procedure

FLDI data acquisition was run for 20 ms and sampled with an oscilloscope at 10 MHz, while the laser was run at full power during a tunnel shot. The trigger signal for the recording was set to match the start of the desired steady state conditions in the HDT.

Alignment of the system was conducted by shining the laser point onto a semi transparent chequerboard which was in a fixed position relative to the cone above

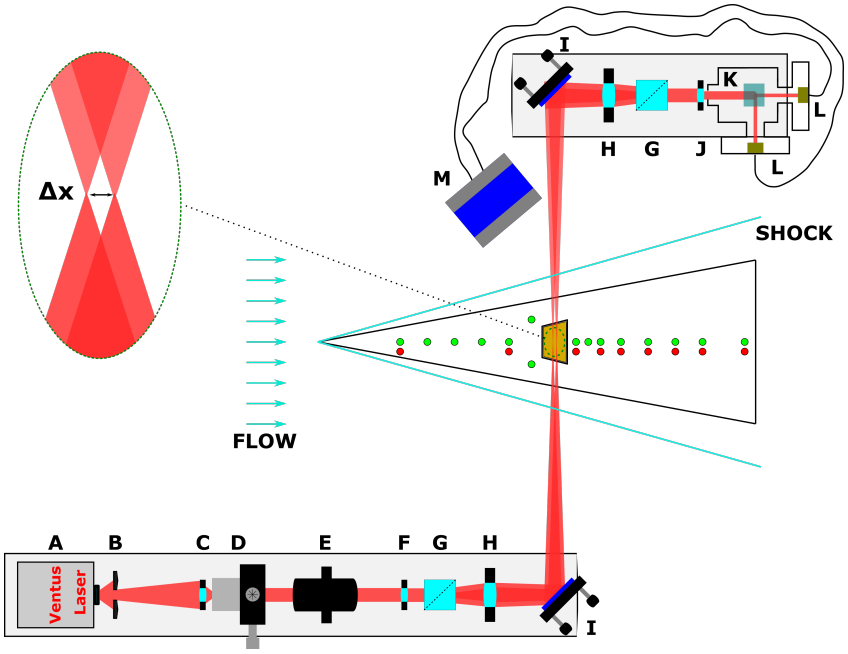


Figure 6.3: FLDI setup. The components can be found in Table 6.1.

the injector and orthogonal to the FLDI beam direction. A photo was then taken with a normal camera, imaging point, cone edge and chequerboard. Using matlab inbuilt functions [321], the chequerboard of 1 mm square size is used to relate pixel (px) coordinates to mm. Cone edge and known position of the chequerboard relative to the cone then allow the calculation of the laser point location in the coordinate system of x and $\bar{y}$ as defined in Figure 6.1.

Depth of Field of FLDI Setup

As described before, a particular asset of such laser interferometers is their narrow depth of field. Similarly to Ceruzzi et al. [320], we move a fluctuation source along the beam in order to characterize the system's response. Here, this is not a gaseous jet as in Ref. [320], but a Multicomp Pro 300 kHz sound transceiver, which was driven by a function generator. It is mechanically traversed along the FLDI light path around the sensitive region in a bench-top investigation at room temperature and atmospheric pressure. Using the same acquisition procedure and sampling as described in Section 6.3.4, voltages were acquired for 19 locations spaced evenly along the beam path. PSDs were calculated for each recording and the value at

300 kHz was then plotted against the coordinate along the beam z (see blue points in Figure 6.4 a)). A Gaussian fit provides an estimate for the Full Width at Half Max (FWHM) at around 43 mm or the standard deviation $\sigma \simeq 18\,\mathrm{mm}$. A simple geometric consideration already discussed similarly by Smeets [317] roughly outlines whether free stream fluctuations may lie within the sensitive region: The cone is approximately 76 mm in diameter at the location where FLDI is applied. The distance from one side of the conical shock to the other is 95 mm at $x = 312.5\,\mathrm{mm}$ at a height of 38 mm above the centreline of the cone. This is respectively the approximate height coordinate of the laser beam. 2σ of the sensitive region at the given frequency and wavelength lay therefore inside the shock layer. Several recent publications discussed the depth-of-field of FLDI in more detail with some particularly focusing on its ability to penetrate turbulent environments around the object of interest [70, 320, 322, 323]. All those sources reveal dependencies of the depth-of-field on the frequency, wavelength and amplitude of density disturbances within the probed flowfield. Therefore, the consideration above is too stronlgy simplified.

Frequency and wavelength of the second mode could not be matched simultaneously during the bench-top test at room temperature for Figure 6.4 a). 300 kHz frequency correspond to $\lambda \approx 1.1\,\mathrm{mm}$ sound wavelength, whereas the second mode wavelength is around 2.5 mm at the relevant tunnel conditions. Ceruzzi and Cadou [320] present an overview of a transfer function for FLDI systems, by reproducing and combining work from Parziale et al. [70] and Schmidt and Shepherd [318]. The proportionalities in the transfer function suggest that the sensitive field of the FLDI system is considerably larger and the maximum sensitivity substantially lower at $\lambda = 2.5\,\mathrm{mm}$ than at $\lambda = 1.1\,\mathrm{mm}$, where it was characterized.

Calculating the full transfer function requires knowledge of the beam diameter. This value has however not been obtained yet for the current system. Instead, we utilize the bench-top measurement to obtain this parameter by fitting the transfer function to the measured points. Transfer function and PSD values were normalized with their respective maximum. With this fitting procedure we obtain $r_b \approx 5.6\,\mu\mathrm{m}$.

Using this value, we calculate the transfer function and extrapolate the bench-top measurement to $\lambda = 2.5\,\text{mm}$. This roughly predicts the FLDI depth-of-field at the relevant second mode frequency. For completeness, we re-plot Fig. 4 from Ceruzzi and Cadou [320] in Figure 6.4 b), showing the full transfer function for the Oxford FLDI. Note that the curves for $\lambda = 2.5\,\text{mm}$ and $\lambda = 1.1\,\text{mm}$ are normalized slices through the contour plot parallel to the z-axis.

Section 3.3.4 discusses how the core flow of HDT's Mach 7 nozzle extends to around $r = 130\,\text{mm}$ from the centreline. Figure 6.4 predicts that the instrument's sensitivity will have decreased to less than 10 % of its nominal value at only $r = 100\text{mm}$. HDT's noise spectra exhibit a considerable drop in noise content with higher frequencies [68]. Hence, even if the sensitive region extends into the turbulent tunnel boundary layers, second mode signals at large enough amplitudes will still likely dominate. However, without further measurements about the system's sensitivity at $\lambda \approx 2.5\,\text{mm}$ one must conservatively assume that the signal contains some freestream fluctuations. Benitez et al. [322] used DNS to simulate such a signal of interest which was framed by turbulence. Their simulation of FLDI responses confirmed that relying on the axial diminution of its sensitivity was justified for high frequency measurements, but less acceptable for larger wavelengths and lower frequencies. Benitez et al.'s [322] simulated interferometer setup is similar to the version presented here, having the same Wollaston prisms. In contrast, the beam separation is considerably larger at $168\,\mu\text{m}$. Benitez et al. [323] warn how fluctuations with $\lambda > 1\,\text{mm}$ are "integrated across the length of the beam" [323], when analysing another set of simulation cases. They however also report that a smaller beam separation reduces the depth-of-field, albeit at the cost of total responsiveness [323]. With respect to line integration, the Oxford FLDI should exhibit more favourable characteristics than the setup simulated by Benitez et al. [322, 323]. Furthermore, the noise spectrum of HDT does not concentrate much power around 300 kHz. Should however high frequency content at millimetre scale wavelengths be present around the nozzle core-flow, it is likely recorded to some extent by our FLDI setup.

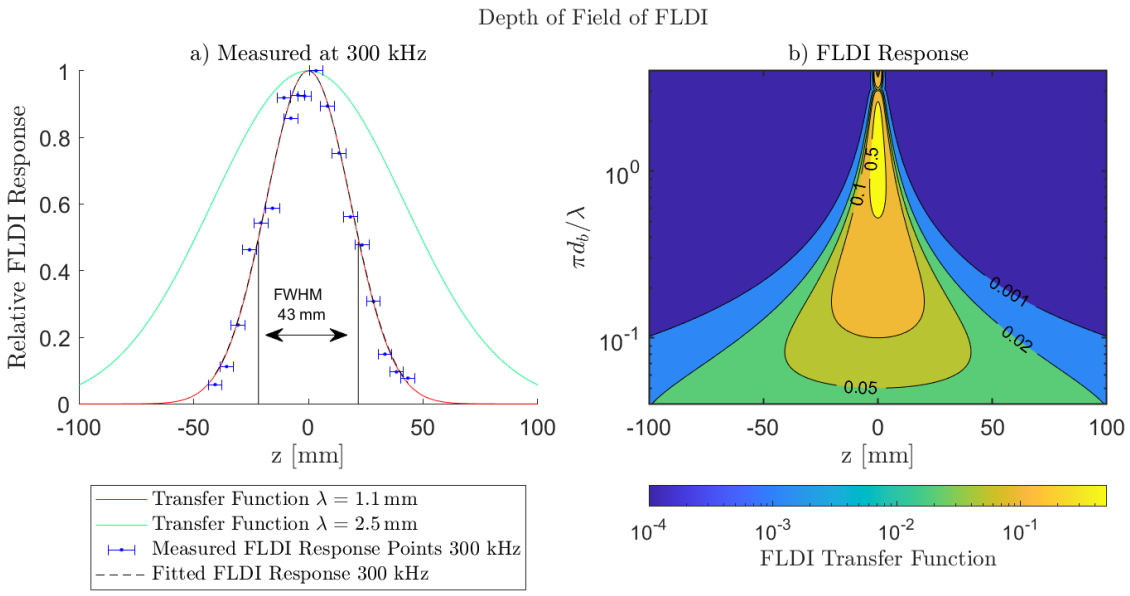


Figure 6.4: a) Depth of field of the FLDI setup. z is the coordinate parallel to the beam centred at the focal point of the system. Measured data for a single frequency near the expected instability is compared to the fitted transfer function and the extrapolated transfer function at the expected second mode frequency. Error bars indicate the diameter of the sound transceiver. b) Replots Fig. 4 from Ceruzzi and Cadou [320] and shows the full transfer function of the FLDI. $d_b = 2r_b$ is the beam diameter.

Property	Value	68 % Confidence
T_0 [K]	460	±15
M_∞	7.00	±0.03
T_∞ [K]	43	±1.5
Re_u [10^6/m]	12.8	±0.7
p_∞ [Pa]	520	±15
p_0 [kPa]	2160	±80
u_∞ [m/s]	915	±10
μ_∞ [10^{-6} Pa s]	3.0	±0.1

Table 6.2: HDT Condition.

6.3.5 Flow Conditions

The cone model was placed in the test section of a Ludwieg tube, namely the Oxford Thermofluid Institute's High Density Tunnel (HDT) [225, 243, 245]. More information about the facility, the working principle and previous experiments with similar models can be found in the references given above. The flow properties of the used flow condition can be found in Table 6.2.

6.4 Experimental Results

6.4.1 Surface Heat Flux

Figure 6.5 plots the heat flux as recorded by thin film gauges along the cone for various injection scenarios and an uncooled case. If transition is defined as the most upstream thin film gauge showing a heat flux significantly exceeding the laminar correlation (in agreement with Stalmach et al. [190]), then downstream nitrogen and helium injection both yield a transition delay. For those injection gases, Figure 6.5 shows a reduction of heat transfer downstream of the porous patch. For nitrogen as a coolant, a fast recovery of the heat flux profile is observed: A short term reduction below the uncooled baseline is directly followed by excess heating, which is the prime example of a known shortcoming of transpiration cooling. In contrast, helium injection seems to be largely beneficial for a flight vehicle, as the heat transfer profile rises above the laminar baseline further downstream compared to the uncooled case. In addition, overshooting of the turbulent heat flux correlation is reduced. During the suppression of Stanton number values below the laminar Eckert correlation, a stabilization in terms of heat flux could be observed. Qualitatively, the heat transfer results from Camillo et al. [104] could hence be verified for nitrogen and helium injection. An important difference hereby is the total temperature. While HEG reaches above 2800 K [104], HDT does not exceed 460 K.

It remains unclear where the boundary layer transitions to turbulence when exclusively analysing thin film gauge measurements. The separate effects of cooling and transition cannot be directly inferred from a surface heat flux gauge alone. The bandpower values shown in figure 6.5 were calculated as integrals over PSDs. These are provided in Figure 6.6.

6.4.2 Surface Pressure Fluctuations

Common knowledge in the field links hypersonic boundary layer transition on slender, 2D, axisymmetric geometries in low disturbance environments with growth and decay of second mode instabilities [90, 324]. As Figure 6.5 indicates for the

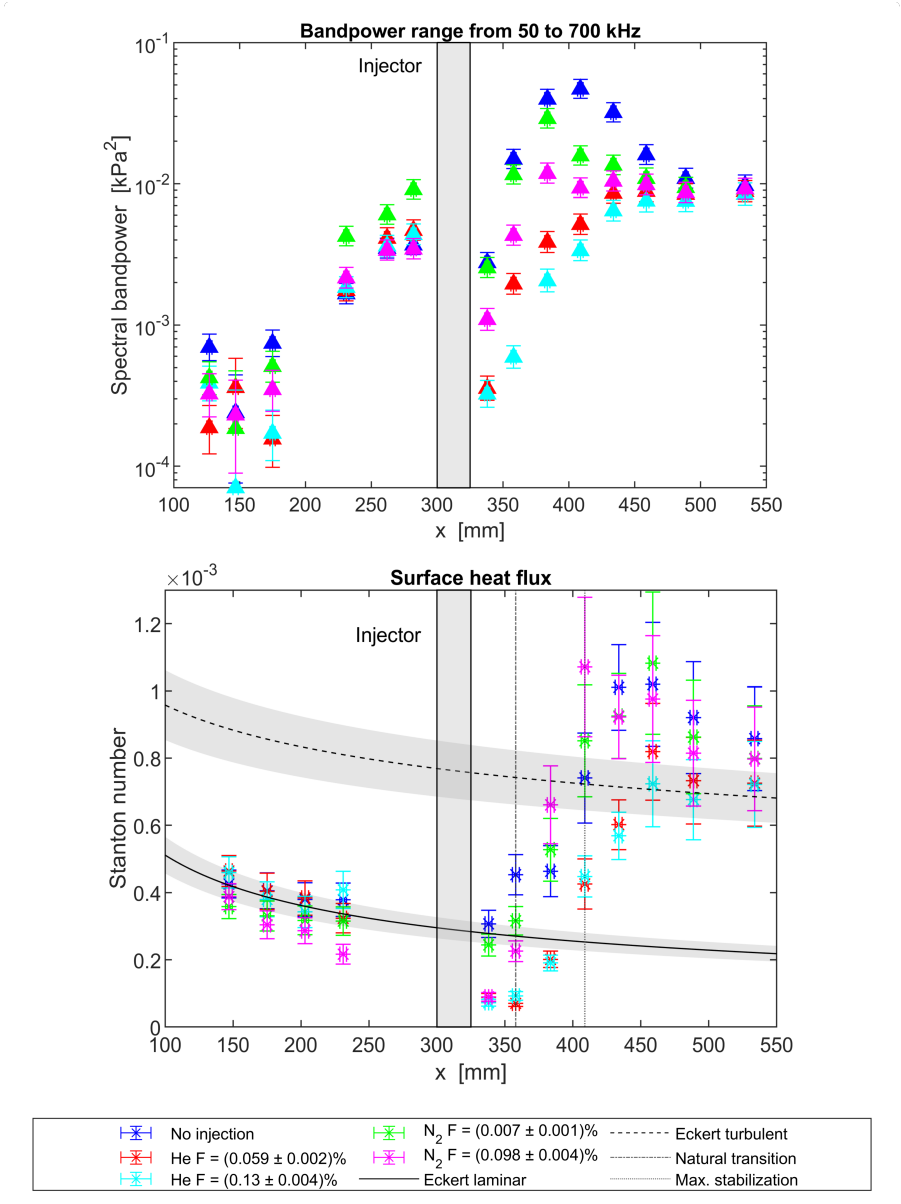


Figure 6.5: Results from surface instrumentation. (left) High frequency pressure. Only the cumulative bandpower is shown in the figure. Second mode frequency peaks lie in the 280 kHz region and hence the first and second harmonic are included in the integrated power. (right) Heat flux distribution across the cone. Colours represent gases and injection ratios and are kept coherent across figures.

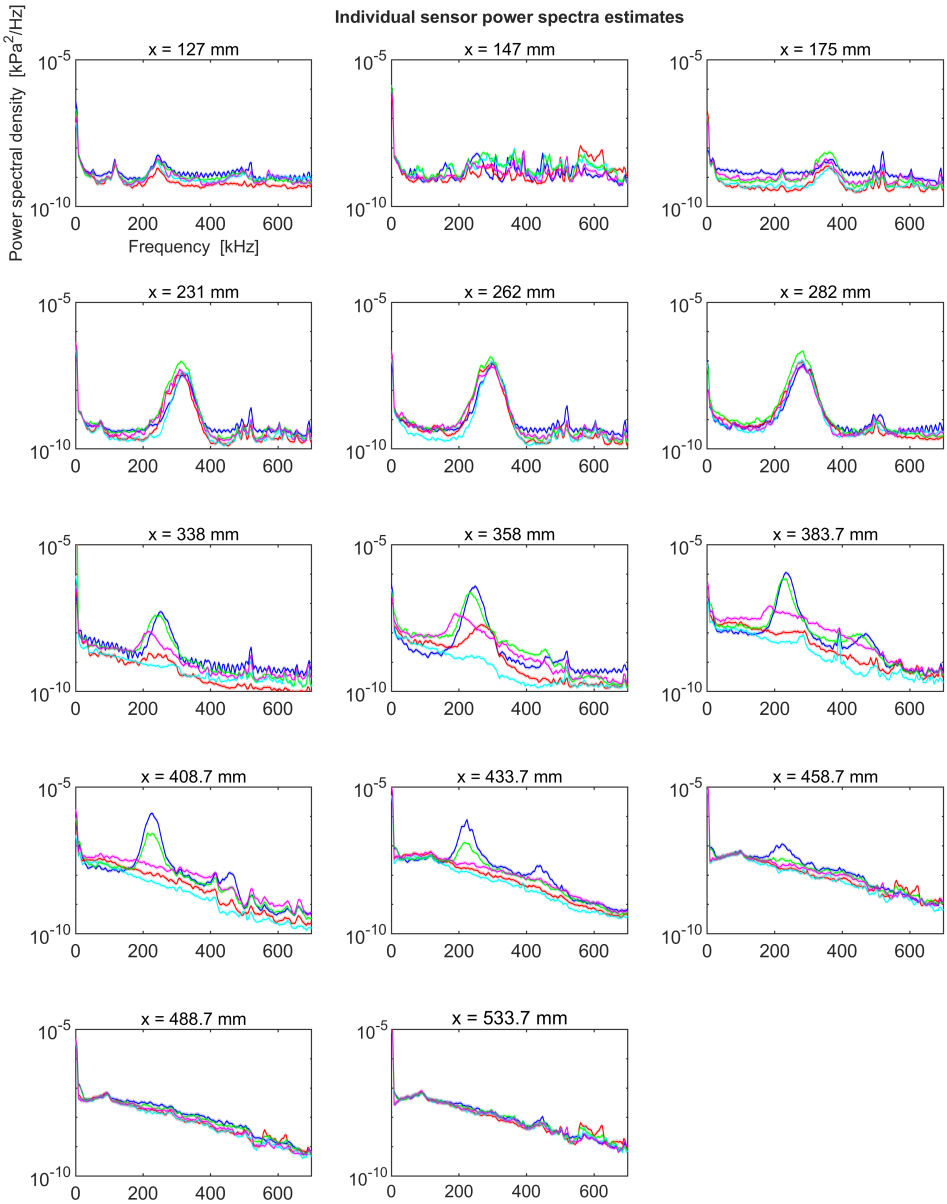


Figure 6.6: All power spectra used to calculate the bandpower shown in Figure 6.5. Color convention is the same as in Figure 6.5.

uncooled case, a specific region of frequencies is being amplified before the boundary layer decays to turbulence. Schlieren images in Figure 6.7 confirm a coincidence of the asymptotic behaviour downstream of $x = 450\,\text{mm}$ with onset of full turbulence. Landau and Lifshitz describe turbulence as "Irregular[ly] disordered" [74] velocity distributions. Such distributions do not show specific amplified frequencies and therefore exhibit lower total bandpower values. Cases with helium injection show a drop even below turbulent levels of bandpower downstream of the injector. A model and simulations presented in [49, 51, 285] suggest that for laminar boundary layers, the coolant of a downstream injection patch forms a "slab" [49] below the original free stream gas. As a result, the observed instability damping with helium injection could be for two reasons. Firstly, attenuation of the instability itself may take place. This would mean that power of the oscillation is reduced as for example shown by Leyva et al. [203] for carbon dioxide injection. Or secondly, surface instrumentation may only measure the helium coolant film which has not mixed and interacted enough with the established boundary layer and its instabilities to receive any second mode power.

For nitrogen cooling, an amplification above chaotic level is observed downstream of the injection. This indicates that at least some growth of second modes still contributes to transition onset. This is not the case for helium. Surface pressure spectra and bandpower values downstream of the injector show no sign of modal amplification an therefore indicate a bypass mechanism [83, 93, 94, 212] at the surface.

6.4.3 Schlieren Images

Surface instrumentation has shown reduced heating and second mode activity in the close vicinity of the model surface. Schlieren images now provide insight into whether those observations hold for the rest of the boundary layer thickness.

In Figure 6.7 second modes can be observed and transition completion can be seen in the most downstream fifth of the image for nitrogen injection $F(\text{N}_2) = 0.01\%$ and natural transition. Note that the PCB bandpower and the heat flux signals are

time averages, while those single schlieren frames are not. Despite showing laminar heating levels, schlieren indicate full turbulence for $F(\mathrm{He}) = 0.1\%$ downstream of $x = 350\,\mathrm{mm}$. For strong helium injection cases, surface pressure and heat transfer measurements can both not accurately resolve transition onset.

A blowing ratio of $F(\mathrm{He}) = 0.06\%$ yields less extreme results. Full turbulence does not seem to develop until around $x = 380\,\mathrm{mm}$ for the depicted frame. For this case, the schlieren in the video depict how the second mode oscillations seem to be displaced from the surface. Wave packets were observed to follow the thickening of the boundary layer and keep oscillating in the upper layer visible in fourth row of Figure 6.7. This suspicion will be confirmed through spectral analysis in the sections below.

Selecting one frame at random from a whole video does not appreciate the inherently unsteady nature of a transitioning boundary layer, but is nevertheless necessary to depict features that may remain concealed when only showing a time-averaged schlieren photograph. It is thus noted that those frames in Figure 6.7 are in contrast to all spectral analysis items shown in this Chapter, as those always represent mean flow conditions.

6.4.4 Schlieren Power Spectra

Second mode oscillations have a frequency below the Nyquist limit of the employed schlieren system and the 170 mm long field of view therefore allows tracking of their growth and decay across the injector. Ifti et al. [49, 285] model the laminar injection process as a layer of coolant displacing the original boundary layer gas. Those two entities are considered largely independent and only gradually mix through diffusion. Aspects of the model offer an explanation of the observed differences in optical and surface instrumentation.

Surface pressure spectra show how the second mode power is reduced at the surface for helium injection during coolant effusion, intuitively agreeing with said model and with Camillo et al.'s [104] findings. An independent coolant layer is now in contact with the sensor. Nonetheless, Figure 6.8 suggests that the second mode power is

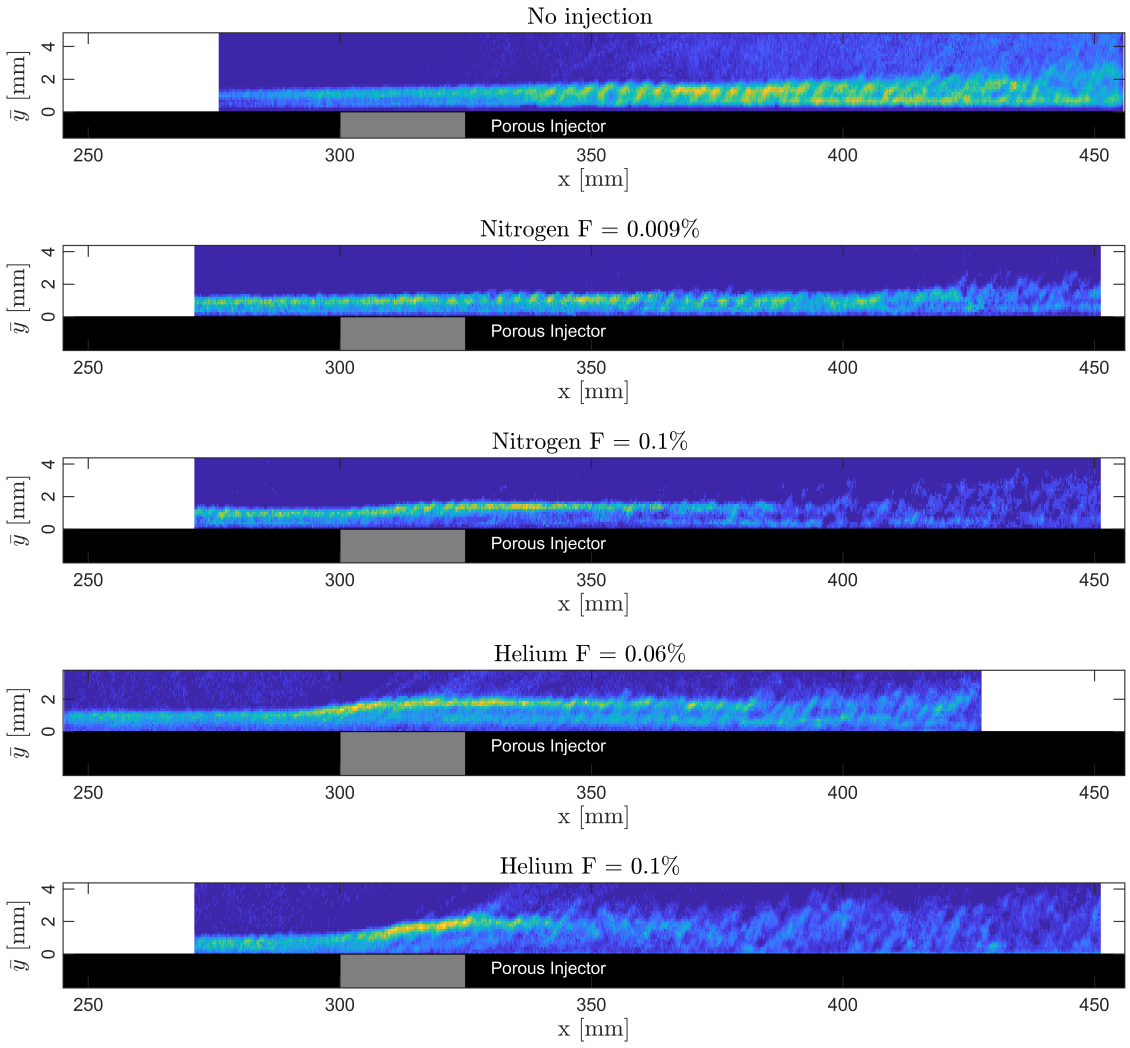


Figure 6.7: Single schlieren frames of shots with and without injection. The injector is marked in the images. Images are not to scale in width and height.

not reduced across the whole boundary layer thickness. Surprisingly, instead of an exclusive damping, the second mode oscillation does not attenuate and seems to simply be pushed above the surface by the coolant injection.

To illustrated the outlined discovery, two paths are selected for plotting the schlieren frequency spectra. Firstly, the straight yellow path (in Figure 6.8) follows the pixel line at the edge of the upstream uncooled boundary layer and maintains this height, slicing through the middle of the thickened boundary layer once in the area of helium injection. At this height, the strongest second mode wave crests were observed propagating undisturbed before interacting with the coolant. Secondly, 10 points

along the boundary layer edge profile were manually selected by the experimenter to form the red path (named special path in Figure 6.8). The continuous line is then calculated by linearly interpolating consecutive pairs of manually selected points. Finally, the lowest pixel at every x-location the path intersects with is selected, and its PSD included in the top plot of Figure 6.8.

Above the injector and downstream ($x \geq 300\,\text{mm}$), second mode power is found in the red path but no longer in the yellow as represented by the spectral power maps for each path in Figure 6.8. This is particularly around and downstream of $x = 320\text{mm}$, where more signal is present at the height of the red path in the region around 280 kHz than at the original boundary layer height. Furthermore, such analytical steps confirm a suspicion already visible in line five of Figure 6.7, where the coolant seems to displace an original band of compressed fluid along with wave packets travelling within. The model by Ifti [49] could be interpreted as a slab of coolant displacing air as well as instabilities. Thus, second modes do persist, however not predominantly at the surface or inside the original boundary layer geometry. Wall heat flux and pressure are hence suboptimal indicators for spatial progression of boundary layer instabilities with injection. They cannot measure the displaced air boundary layer.

Schlieren images alone cannot prove that the visible lower layer in Figure 6.7 (line five) is pure or predominantly helium. Nevertheless, research work on mixing of injection gases does suggest so. Ifti et al. [50] conducted experiments in HDT at the identical Re_u, Mach number and comparable blowing ratios, as part of an investigating into laminar coolant mixing on a flat plate model. Their work used pressure sensitive paint [325, 326] and demonstrated how helium injection at comparable blowing ratios ($F \approx 0.04\%$) was much more effective at displacing oxygen than nitrogen injection, a finding furthermore confirmed with IR thermography [159] in the same wind tunnel. Albeit both observations only hold at the surface, which stresses the discrepancy of surface and non-intrusive measurements again, numerical simulations can complement the picture. It is shown by Ifti et al. [51] how most of the injected helium is concentrated below approximately $60 - 70\%$ of the total boundary

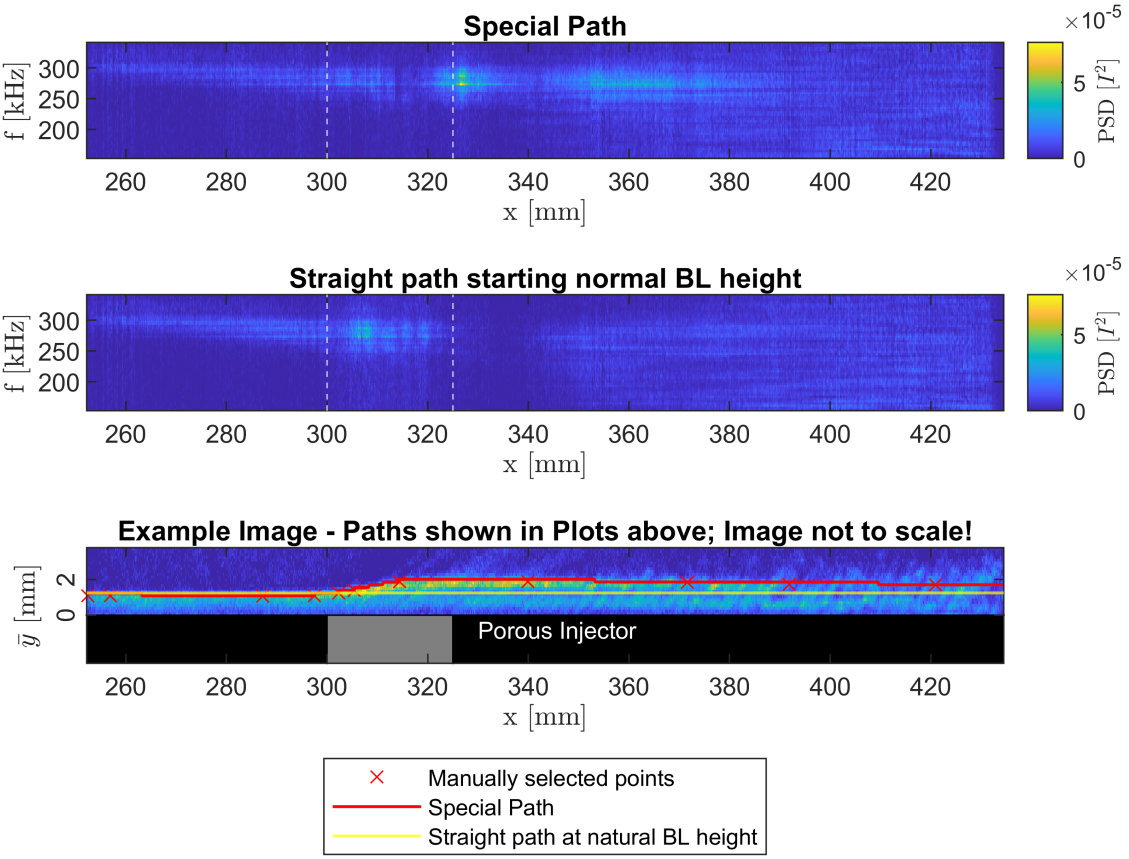


Figure 6.8: Power spectra maps of schlieren images. The PSD is calculated for every pixel along the shown paths. Power is represented in the colorscale. Both power spectra along the paths are calculated with the same procedure across the same images. The schlieren images correspond to the case $F = 0.06\%$ in Figure 6.7.

layer height [51]. While this might confirm the presence of a helium layer for about 30 mm downstream of the injector, no further conclusions can unfortunately be drawn. Ifti et al.'s [50] experiments did not involve transitioning flow, as their boundary layer remained laminar across the entire test object. The experiments here and those of Ifti et al. [50] deviate substantially when turbulent mixing occurs due to transition of the conical flow. For the close downstream vicinity of the injector boundary layer thickening observed in schlieren and analytical predictions in [49, 285] match reasonably. For $F(\mathrm{He}) = 0.06\%$ the height of the coolant slab is projected as $h(\mathrm{He}) \approx 0.76\,\mathrm{mm}$ and for $F(\mathrm{He}) = 0.1\%$ $h(\mathrm{He}) \approx 1.2\,\mathrm{mm}$. The aforementioned theoretical values were computed using Ifti et al.'s [49, 285] equation (see Equation 4.3) shown and explained in Chapter 4. In the shown schlieren images, the boundary layer thickens by approximately 0.85 mm and 1.16 mm respectively

across the 25 mm length of the injector. For the nitrogen case with $F = 0.01\%$ an increase in height was below the pixel resolution.

6.4.5 Frequency Shift within Boundary Layer

In Chapter 4, the frequency shift of second modes with injection of different gases was characterized similarly to Schmidt et al. [180]. While the latter authors investigated Mach 4 flow deducting the frequency shifts from schlieren measurements, this work has previously presented experiments at Mach 7 using high frequency surface pressure gauges in Chapter 4. It was found by both that higher injection rates lead to a stronger reduction in frequency.

As research by Wylie et al. [225] suggests that transition in the HDT is dominated by second modes for the given Mach number and model, the underlying stability physics might differ from Schmidt et al. [180]. Surface instruments have been found to be unreliable in measuring the second mode downstream of an injector in previous sections. It is thus critical to determine whether the frequency shift observed and discussed in Chapter 4 is only an effect of the coolant on the sensor or whether it holds for the entire boundary layer thickness. Figure 6.9 suggests the latter. Comparing power spectra maps of a cooled and uncooled case at 1.2 mm and 1.1 mm above the cone evidently shows an attenuation in spectral power and a reduction in central second mode frequency. Herein, the agreement of Mack mode frequencies from schlieren and PCB are it satisfactory agreement. Only the spectral broadening as e.g. observed by Camillo et al. [104] for nitrogen injection and predicted by Miró Miró et al. [169] for helium transpiration does not occur. This effect was not observed in surface pressure signals either (see Chapter 4).

6.4.6 Second Mode Power Distribution across the Boundary Layer Thickness

Investigating the dependency of second mode growth and decay reveals further details about the transition process with and without injection. For a natural transition case, most of the spectral power is found at or even above the laminar

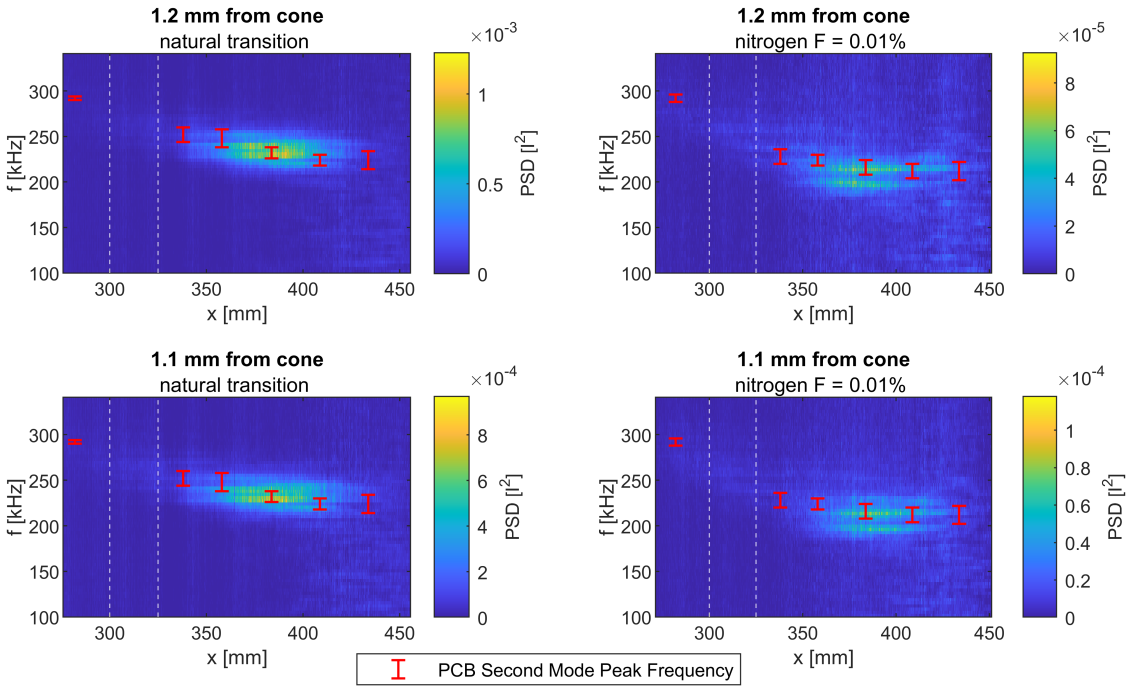


Figure 6.9: Power spectra maps of schlieren images. PSDs are calculated for each pixel along a path with the given distance from the detected cone edge. The error bars given for the central frequency of the second mode as measured by PCB at the surface represent the full width at half maximum of the fitted gaussian distribution. The injector location is marked as a white dashed in the colour maps.

boundary layer height in our experiments (see Figure 6.10). This is in good agreement with other spectral analysis results in the field [8, 99, 110, 112]. For nitrogen injection (Figure 6.11), only little change is found in that respect. The observable shift to lower frequencies and a faster decay to turbulence have been discussed in the previous sections.

For $F(\mathrm{He}) = 0.1\%$ an onset of full turbulence across the entire boundary layer thickness shifts far upstream as visualized in Figure 6.7. More accurate spectral analysis unambiguously confirms the finding, however the plot at $x \simeq 328\,\mathrm{mm}$ still indicates second mode activity, albeit displaced in wall normal direction. Chaotic oscillations exist from the cone edge up to 4 mm above, as shown by a broad spectrum of activated frequencies in Figure 6.12 downstream of $x \simeq 312.5\,\mathrm{mm}$ and they fully dominate the spectra at $x \simeq 420\,\mathrm{mm}$. For the helium injection case shown in Figure 6.8, $F(\mathrm{He}) = 0.06\%$, the existence of a stable film - likely pure coolant - can be measured. At x = 420 mm (bottom right in Figure 6.13) a turbulent

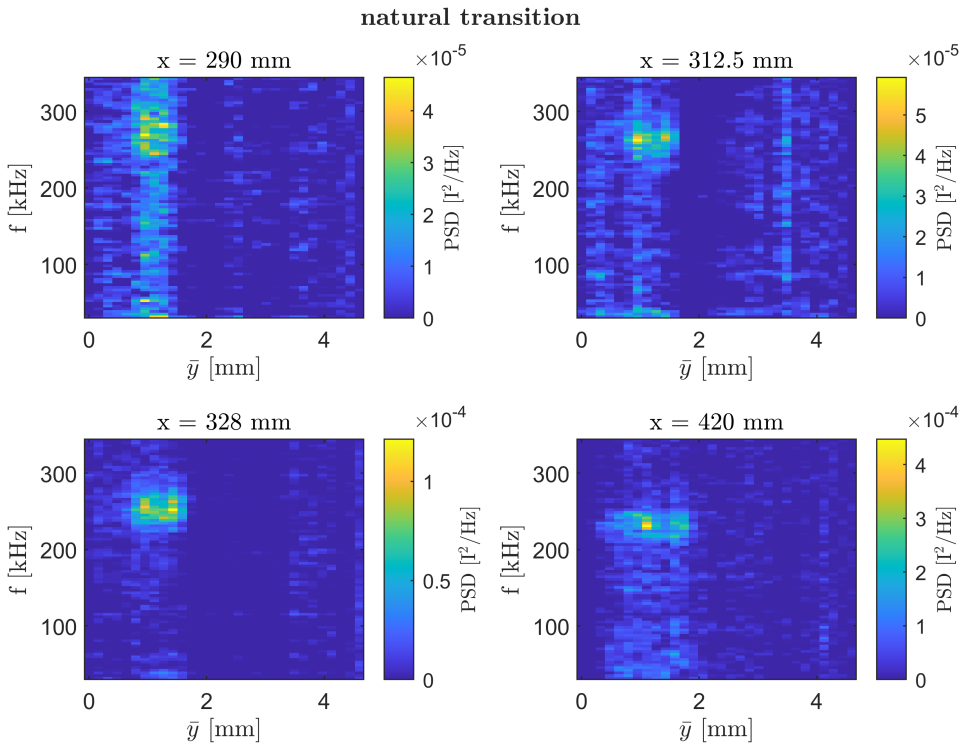


Figure 6.10: Wall-normal power spectra through boundary layer thickness without injection. The power spectra are plotted for four locations along the transition process. Because the schlieren system was not always aligned to the exact same position, $\bar{y}$ ranges change across the test cases. The same PSD calculations as for Figure 6.8 and 6.9 were used to generate the plots. The number of data points in $\bar{y}$-direction is limited by the schlieren optics and camera sensor. A resolution of approximately 6 pixels per mm.

spectrum can be found, however only above $\bar{y} \approx 0.8\,\text{mm}$. Hereby, as predicted by Ifti [49], the comparably voluminous thickening through helium injection, likely originating from its small molecular mass, has proven invaluable for unequivocal visualizations of said displacement. A transitioning boundary layer coexists on top of a laminar coolant film. Identifying transition through surface instrumentation may thus be significantly flawed and ambiguous in this case. Those sensors and any transition criteria would correctly detect laminar flow, which however does not represent the state across the hole boundary layer in $\bar{y}$ direction.

FLDI Measurements

Changes in wall normal second mode distribution due to injection are furthermore investigated by applying single-point FLDI at two locations above the injector $x = (312 \pm 1)\,\text{mm}$. FLDI location A is at $\bar{y}_A = (1.5 \pm 0.2)\,\text{mm}$ above the cone surface

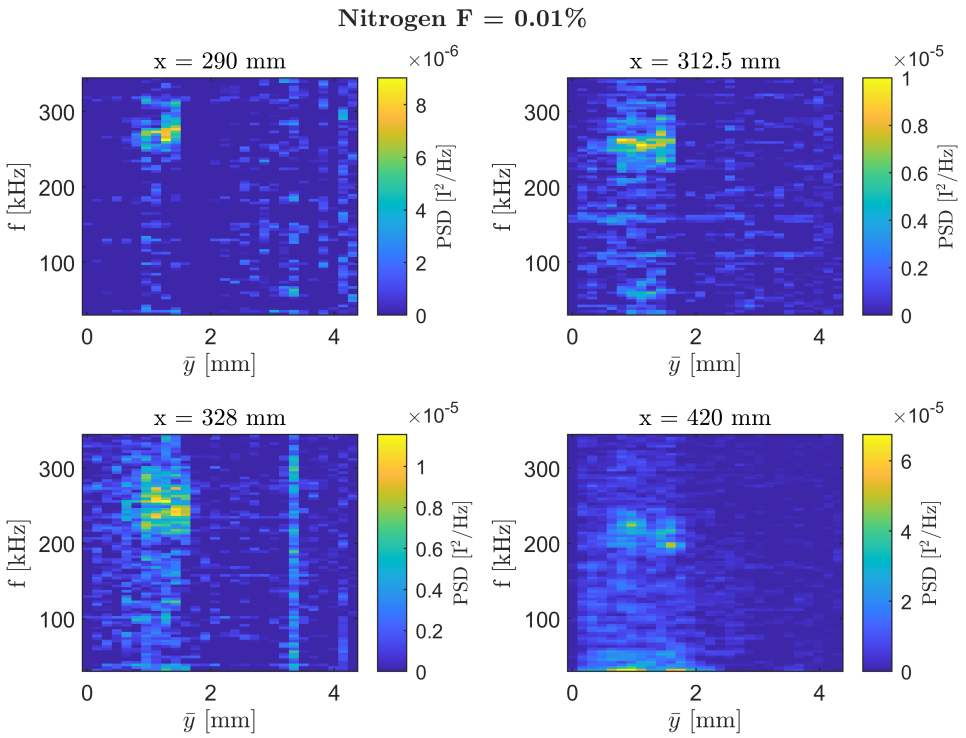


Figure 6.11: Wall-normal power spectra through boundary layer thickness with nitrogen injection. The power spectra are plotted for four locations along the transition process. Because the schlieren system was not always aligned to the exact same position, $\bar{y}$ ranges change across the test cases. The same PSD calculations as for Figure 6.8 and 6.9 were used to generate the plots. The number of data points in $\bar{y}$-direction is limited by the schlieren optics and camera sensor. A resolution of approximately 6 pixels per mm.

and lies just within the visible boundary layer, location B at $\bar{y}_B = (2.5 \pm 0.2)\,\mathrm{mm}$ lies within the post-shock flow outside of the natural boundary layer. Two tunnel runs are then performed while FLDI remains at a point, one without injection and one with helium cooling. The schlieren frames in the upper right corner of Figure 6.14 display all configurations.

In the left column of Figure 6.14, the respective spectra for the cases are shown. Due to the change of mechanical shape of the boundary layer, point B lies within a visible density gradient field for helium injection, but not for natural transition (see schlieren images in Figure 6.14). The FLDI power spectra demonstrate the according wall-normal rearrangement of the instability. Point A - at the very edge of the boundary layer - sees increased second mode activity through helium injection. Moreover, point B shows a noisy but distinct peak in the 300 kHz region with helium injection, but there is no sign of modal activity at location B during the

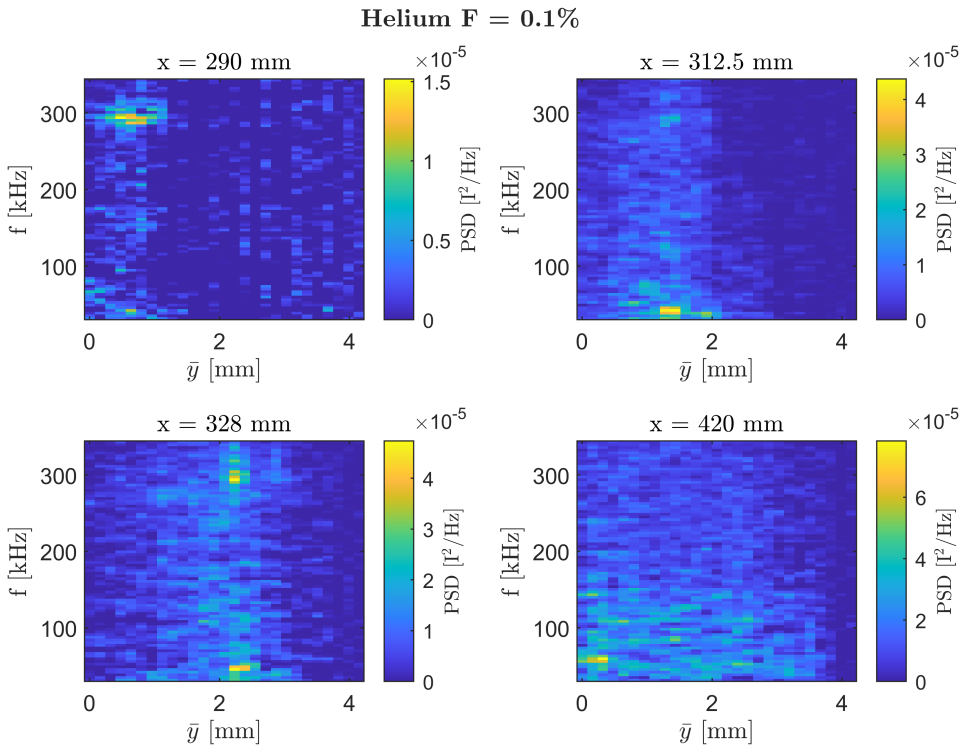


Figure 6.12: Wall-normal power spectra through boundary layer thickness with helium injection. The power spectra are plotted for four locations along the transition process. Because the schlieren system was not always aligned to the exact same position, $\bar{y}$ ranges change across the test cases. The same PSD calculations as for Figure 6.8 and 6.9 were used to generate the plots. The number of data points in $\bar{y}$-direction is limited by the schlieren optics and camera sensor. A resolution of approximately 6 pixels per mm.

corresponding measurement with natural transition. A reference case with nitrogen injection for FLDI point B delivers no beneficial data but was nevertheless included for completeness. With $F(\mathrm{N_2}) = 0.02\%$ the displacement was likely insufficient, the spectrum does exceed background level fluctuations.

Natural transition and helium injection were also recorded with schlieren. Hence, the two FLDI measurements can be qualitatively replicated by plotting the spectra of the corresponding pixels in the schlieren video. To increase accuracy, the uncertainty of the schlieren-vs-FLDI alignment will be expressed as an uncertainty in the relative position and compensated for by averaging the spectra of several pixels. As the adjustment in $\bar{y}$-direction was relatively precise due to the 10 μm steps of the lab jack, the alignment uncertainty is neglected in this coordinate. Nevertheless, an uncertainty of ± 1 pixels is assumed due to the diameter of the laser point. The

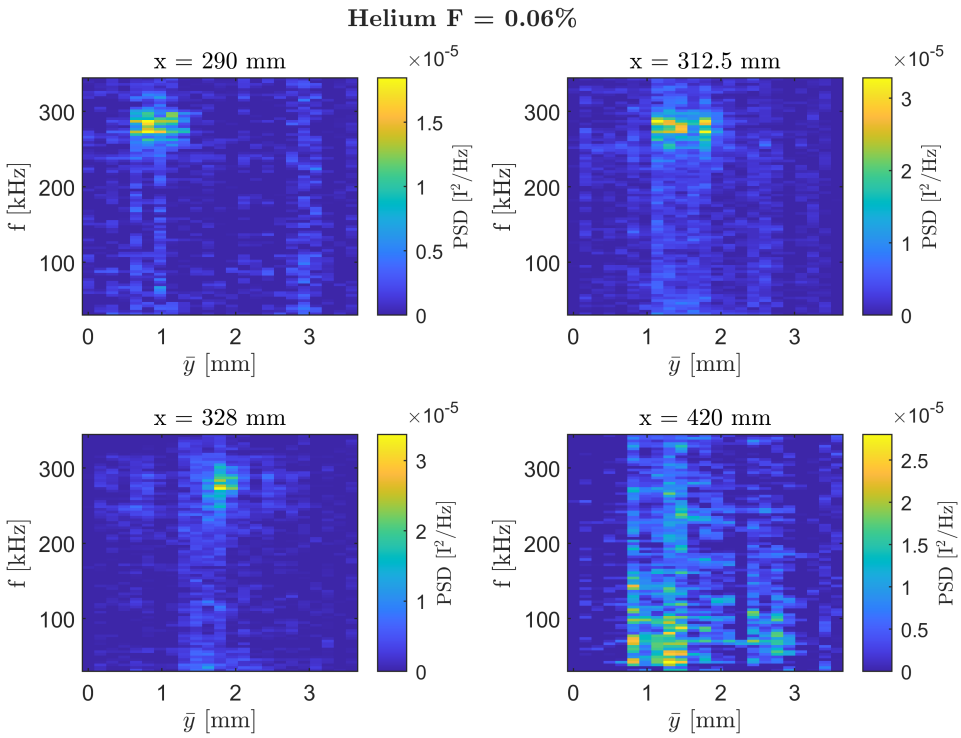


Figure 6.13: Wall-normal power spectra through boundary layer thickness with helium injection. The power spectra are plotted for four locations along the transition process. Because the schlieren system was not always aligned to the exact same position, $\bar{y}$ ranges change across the test cases. The same PSD calculations as for Figure 6.8 and 6.9 were used to generate the plots. The number of data points in $\bar{y}$-direction is limited by the schlieren optics and camera sensor. A resolution of approximately 6 pixels per mm.

manual alignment in x-direction is accounted for by an uncertainty of ± 5 pixels. Error bars in the schlieren spectra (Figure 6.14) are thus obtained by calculating the mean and standard error of PSDs within a rectangle of 33 pixels - 11 in $\bar{y}$-direction and 3 in x-direction - centred around the FLDI point. To exclude any possible contamination of the PSD through freestream content, the mean PSD of the top pixel row, high above the boundary layer is subtracted from all points, as indicated on the vertical axis of Figure 6.14. Negative values were set to 0 as they are unphysical.

Spectra directly taken for the corresponding pixels in schlieren qualitatively agree with FLDI. Frequency shift and increased bandpower can be observed for the comparison in Point A. For Point B, no sufficient signal was measured by schlieren. Its sensitivity cannot compete with a differential interferometer.

Both techniques complement surface instrumentation and FLDI confirms previous

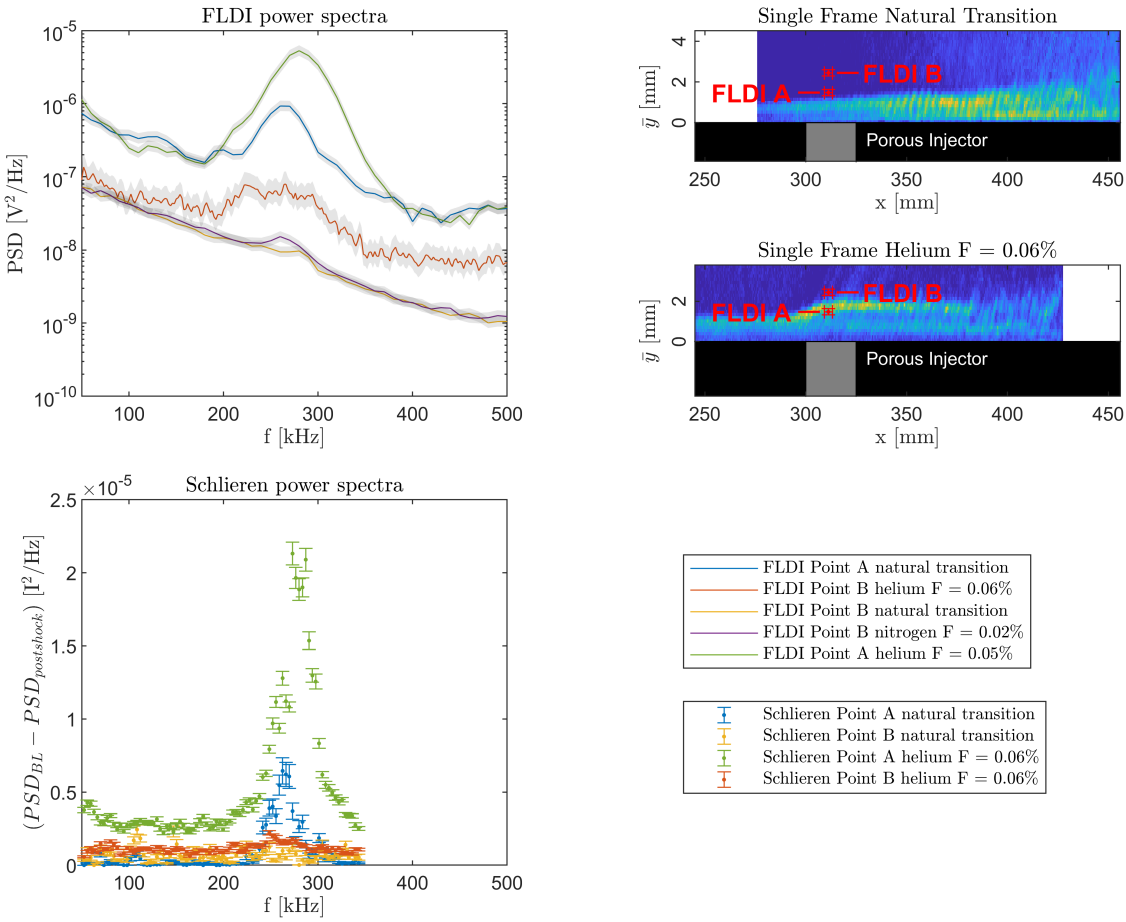


Figure 6.14: Both locations above the injector, where FLDI was applied are marked in a schlieren image. The errorbars do not indicate the size of the FLDI laser point but rather the goodness of reproducible realignment.

schlieren-based findings about second mode displacement. The bandpower decrease shown in Figure 6.5 obtained from pressure sensors seems to only hold for the close vicinity of the surface. Above the cone (in $\bar{y}$ direction), there is in fact a region where more oscillation activity is found with helium injection. Gas effusion into a developed and growing second mode instability at low enthalpy seems to have little damping or stabilizing effect. At least locally, injection pushes the second mode away from the surface and it can still be detected further away from the cone.

6.4.7 Experimental Definition of Transition

In the following section, several different techniques to infer transition onset will be presented and compared. Examples for each method are given in Figure 6.15.

First Thin Film Gauge: The most upstream heat flux gauge significantly above laminar level is selected as the transition onset point. Hereby, significant means the Stanton number exceeds the laminar Eckert correlation's 68 % confidence interval. As an example, $x_{tr} = 358\,\text{mm}$ for the natural transition case (Figure 6.5). This approach follows one of the three criteria used by Stalmach et al. [190].

Stanton Number Linear Fit: Similarly to Camillo et al. [104], a linear fit is calculated through the thin film gauge measurements post the local minimum. An example is shown in Figure 6.15. The intersection of the fit and the lower 68% confidence interval threshold of the laminar Eckert correlation is x_{tr} onset and the intersection of said fit with the lower bound of the turbulent theory is x_{tr} completion.

Schlieren Human Input: The schlieren videos from the tunnel tests showed a continuously moving transition front. All spectra and heat transfer values shown are time averages. In order to reproduce this, an experimenter is shown 100 randomly selected post-processed schlieren images like in Figure 6.7 from the steady flow test time. The start of full turbulence is manually selected by clicking on the transition point on every frame. Second modes are not counted as turbulence, only the presence of chaotically fluctuating eddies. The inputs from 100 frames are averaged and used as x_{tr}. This approach roughly follows the shadowgraph criteria used by Stalmach et al. [190].

Schlieren Low Frequency Power: As seen in previously shown spectra, the "[i]rregular disordered" [74] nature of turbulence causes a spread of fluctuations across a large frequency spectrum. The increasing presence of frequencies substantially lower than the second mode (i.e. f <100 kHz) is used as a transition criterion. A sum is calculated of all power in this range across the entire available $\bar{y}$ distance in the schlieren image. Defining x_{tr} is performed via *Matlab's* inbuilt change point detection. The number of change points

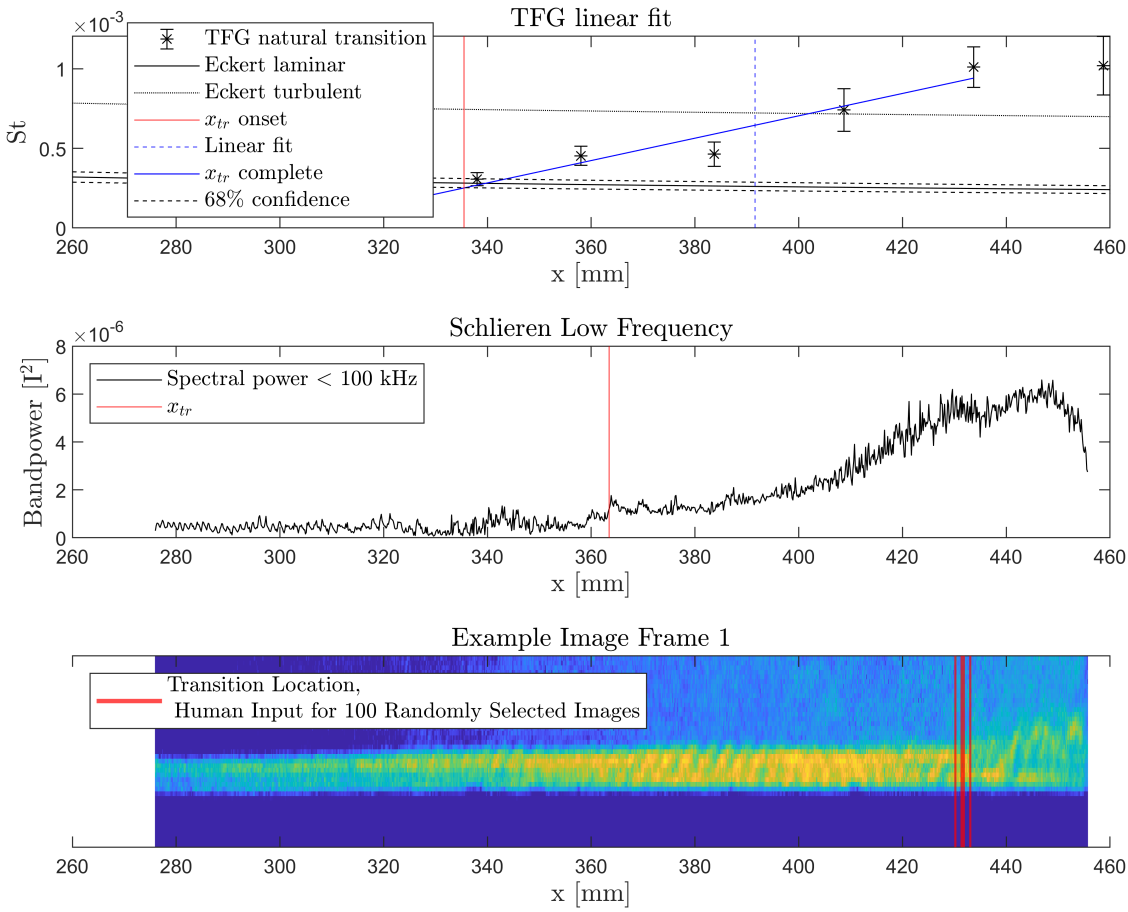


Figure 6.15: Summary of different transition location metrology for a case without injection.

is set to one, the used statistics is rms [327–329]. This method works very similarly to a criterion described by Shumway and Laurence [330].

Summary of Transition Locations

Table 6.3 summarizes the transition locations obtained from the methods described in Section 6.4.7. Even comparisons among those methods for a non-cooled case show a discrepancy of up to 90 mm. While the heat flux based methods are most likely triggered by amplified second modes, the schlieren based methods were not [190]. The latter techniques identify the completion of the transition process, while the former detect the onset [190]. Any investigated level of injection yields a transition delay when thin film gauges are used to infer transition onset. For schlieren based methods, the opposite is true. No schlieren criterion indicates a transition delay for

any injection case.

Further comparisons among the detection methods are shown in Figure 6.16, which closely follows the approach from Marvin and Akin [187] and Stalmach et al. [190]. Hereby, we introduce F_{MA}, the blowing parameter from Marvin and Akin [187]. Because their injection surface is large, they integrate the mass flux from the beginning of the porous section to x_{tr} and normalize it by the cone base surface, a method recently revitalized by Miró Miró et al. [108]. As all shown transition locations lie downstream of the injector, we always use the full supply mass flow and then normalize by 1/6 of the cone base surface at $x = 325\,\mathrm{mm}$, the axial end of the 60° injector segment. It is hereby noted that the introduction of F_{AK} against simply re-using F as above did not change any interpretation of Figure 6.16.

Figure 6.16 complements Table 6.3 and adds a comparison of the given transition values with a correlation from Marvin and Akin [187]. To accentuate differences in transition criteria, the ratio of cooled and uncooled x_{tr} is plotted on the vertical axis, wherein each of the points is normalized by the respective method's x_{tr} at $F = 0$. Colours denote each unique injection case and are consistent with previous figures from this chapter, different transition criteria are represented as symbols. Each symbols for one colour exhibit a substantial spread along the y-axis, underlining differences in sensitivity criteria of each method. Furthermore, it re-iterates the conclusion from Table 6.3: stabilization only occurs when referring to thin film gauge measurements. Our given data points for x_{tr} do not align well with Marvin and Akin's [187] correlation. Plausible reasons for this may be the substantial difference in injector geometry but also discrepancies in tunnel noise environment, flow temperature or model surface cannot be excluded. While Stalmach et al. [190] highlight discrepancies in between transition onset and completion methods, Figure 6.16 adds how trends from two completion criteria - schlieren and TFG fit (triangle symbol) - can still display significant disagreement, particularly with helium injection.

The compared methods are only a subset of those available in literature (see Pate [314] for a summary). Some of those mentioned, for example measurements

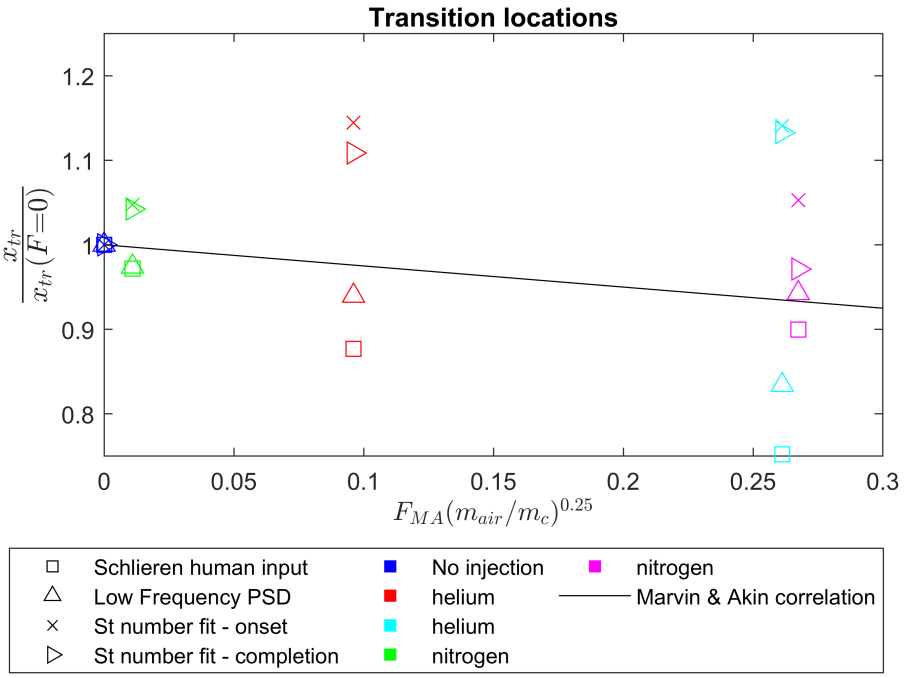


Figure 6.16: Comparison of transition locations. Figure plotted similar to [187, 190] with correlation from Marvin and Akin [187] included. In those calculations we followed Marvin and Akin [187] and used F in percent.

	Coolant				
	none	helium		nitrogen	
F [%]	0	0.04	0.1	0.01	0.17
Method	x_{tr} [mm]				
Schlieren human input	432	379	325	419	388
Schlieren low frequency power	364	342	303	354	343
TFG fit onset	340	387	382	355	356
TFG fit complete	392	434	443	408	380
First TFG	358	434	409	384	384

Table 6.3: Summary of transition locations rounded to the nearest mm value.

of increasing boundary layer thickness would not be applicably to gas injection cases. Others, like measurements of pitot pressure or examinations of surface oil patterns were not included into the discussion as they are profoundly different from methods applied here.

6.5 Discussion

Many of the key results from Camillo et al. [104] could be confirmed qualitatively with the present investigation. Nitrogen injection leads to a reduction in second mode power, which held across the entire boundary layer thickness and for surface pressure measurements. Heat flux could be kept at laminar level for an extended distance but then exceeded the uncooled baseline heating rate further downstream. Schlieren power spectra for those cases reached fully turbulent values earlier than without injection, indicating how only 'heat flux transition onset' but not 'transition completion' moves rearwards. From a heat transfer perspective, helium injection yields more effective results. This light gas kept the heat flux below the uncooled Stanton number profile for all measurement locations downstream of the porous segment.

When considering the instability mechanism, helium cooling shows different behaviour: Firstly, the 'mechanical' disruption to the boundary layer is visible in schlieren images. Its thickness grows by almost a factor of two and full turbulence can be observed in schlieren where neither of the surface instruments would suggest its presence. The boundary layer thickening can be ascribed to the low molecular mass [49] and high thermal diffusivity [169] of helium and has previously been reported [36]. Helium displaces boundary layer gas so effectively from the surface that neither skin friction, nor instability waves reach sensors. Upon turbulent mixing, this effect vanishes, but only slowly [50, 51]. Albeit difficult to quantify the uncertainty, inferring transition from heat flux or surface pressure is certainly incorrect in those cases.

It could now furthermore be shown how surface measurements with helium injection do not accurately depict the transition mechanism. Density fluctuation spectra derived from schlieren and FLDI showed how the second mode instability persisted above the surface. This could either lead to the interpretation that any instability damping only happens at the surface, or it means that the air boundary layer is pushed away from the sensors. An acoustic perturbation originating from a Mack mode oscillation would then have to penetrate a layer of helium, leading to the

observed reduction in band power in PCB measurements. Consequently, helium transpiration does not only displace boundary layer gas, but also the instability oscillations. In addition to the fluid mechanical disturbance introduced by gas injection, an instability mechanism could be detected, just not at the surface.

Returning to the contextualization with results from Camillo et al. [104] - they only used nitrogen in their study - it is currently unclear whether the discussed effect of helium on the second mode is unique to said gas or whether the dislocating behaviour is simply not as pronounced for nitrogen but qualitatively alike. Further research will be necessary to obtain clarity.

The assessment and comparison of different transition criteria delivered similar results as reported by Stalmach et al. [190]. As mentioned above, nitrogen and helium injection have proven capable of delaying a heat flux increase beyond laminar levels. Nevertheless, schlieren-based transition criteria indicated fully turbulent conditions further upstream than without injection for all those cases. Thus, we found gas effusion only moves 'heat flux transition onset' but not 'transition completion' rearwards.

6.6 Conclusions

By comparing analysis of different measurement techniques, the relationship of heat transfer increase, transition, instability and transpiration cooling was thoroughly investigated by utilizing a 7° half-angle cone model in a low enthalpy Mach 7 facility. With the presented results we extend the discussion about transition methods by Stalmach et al. [190] and deliver an extension to investigations about transpiration cooling and boundary layer stability from Camillo et al. [104].

Helium and nitrogen injection were performed using a small porous segment close to the natural transition onset location. At sufficiently low rates, injection of both gases was found to delay a rise of surface heat flux levels above a laminar correlation. Hereby, helium had a significantly stronger impact than nitrogen. Analysis of schlieren images showed and advance in transition for all those cases. In terms of second mode oscillations, surface pressure spectra also indicate instability damping

through foreign gas injection. Spectral analysis of schlieren data confirms this finding, as they also showed reduced frequency power. Damping further away from the wall was however not nearly as thorough as surface instruments indicated. Schlieren and FLDI measurements reveal that the instability fluctuations are mainly pushed away by the coolant injection, but keep existing. Specifically helium cooling is thus not found to achieve a transition delay when adhering to the definition as onset of fluid mechanical turbulence in contrast to heat transfer rise.

It can be concluded that foreign gas transpiration can damp or displace instabilities. Specifically minimal nitrogen injection lead to less oscillation activity at the surface and throughout the boundary layer. While the growth of second modes could be either reduced, interrupted or displaced from the surface for all those cases, turbulence still always occurred further upstream than without injection.

Surface pressure and heat transfer metrology has been shown to be insufficient in capturing the boundary layer stability state with downstream foreign gas injection. Information in the direct vicinity of the model surface is however still deemed invaluable and necessary for any investigation in hypersonic flow. Nevertheless, in this work we have shown that relying exclusively on such techniques would be inaccurate. Dependency on the distance from the model surface of several parameters necessitates the use of non-intrusive optical techniques such as schlieren to complement surface instruments. Applying four different methods showed that each one on their own would be unable to simultaneously capture the parameters heating and turbulence reliably. In agreement with Pate [314], high-speed schlieren images with a wide field of view have proven invaluable as a secondary metrology.

Statement of Authorship

Title: Decoupling Boundary Layer Transition and Heat Flux Reduction for Hypersonic Transpiration Cooling

Status: Unpublished and unsubmitted work written in a manuscript style

Author Contributions:

- **Philipp Kerth** had the idea for the test cases, cone model and analysis performed. He designed the model, assembled it, instrumented it, ran the experiments, collected the data and analysed it. He wrote the manuscript with input from Laurent M. Le Page and Matthew McGilvray.
- **Ben Williams and Laurent M. Le Page** assembled, improved and commissioned the FLDI system.
- **Laurent M. Le Page** set up FLDI for the tunnel tests, measured the depth of field of FLDI together with Philipp Kerth and ran FLDI during the tunnel test campaign.
- **Andrew Ceruzzi** helped during the analysis of the FLDI characteristics.
- **Sebastien Wylie** acted in a supervising role during model design, test case selection and data analysis
- **Matthew McGilvray** supervised the project and organized and managed the funding.

Student Confirmation:



Date: 08/01/2023

Supervisor Confirmation:



Date: 10/01/2023

7 Summary and Conclusion

Contents

7.1 Summary of Presented Work 157
7.2 Conclusion 158
7.3 Recommendations for Future Work 161

7.1 Summary of Presented Work

This thesis has investigated a transpiration cooled 7° half-angle cone in several different configurations at Mach 7 regarding boundary layer stability. Helium injection from a porous nose segment with a 1 mm nose radius caused a transition delay at low blowing ratios where immediate blow-off is self-evidently avoided. Thorough investigation of three independent probing methods yielded consistent findings regarding transition onset and completion, substantially enhancing confidence in the astonishing outcomes. Nitrogen injection did not show any benefits and only destabilized.

Gas injection into highly developed second mode instabilities close to the natural onset of transition on a cone with an impermeable, sharp nose tip caused a reduction in second mode frequency and power. Herein, frequency attenuation correlated with

the blowing ratio and the molecular mass of the coolant. Boundary layer thickening was observed across the injection length, which correlated with the same parameters. Gas injection into less developed instability due to a lower unit Reynolds number produced qualitatively equivalent results. Amongst all coolants, helium injection caused the strongest damping of the second mode.

Injection of nitrogen and helium from the downstream injector can suppress the increase of heat flux due to transition onset for an extended distance. In contrast, the completion of transition was found to always move upstream. Similarly, the damping of second mode oscillations indicated by surface pressure transducers with helium injection was seemingly due to a displacement of the disturbances by the coolant and not due to a reduction in fluctuation power. Schlieren images even revealed co-existence of laminar and turbulent flow, wherein the former was found at the surface and the latter above. Different experimental methods to determine the transition location yield significantly different results for an uncooled case. Foreign gas injection increases those discrepancies.

When comparing the outflow profiles of the frustum injector patch in Chapter 4 and 6 a difference is obvious with respect to mean outflow velocity, spatial distribution and uniformity. Those circumstances are believed to have been caused by previously applied glue migrating into the pores of said porous material after dismantling and before reassembly of the model in between test campaigns. The glue then blocked a certain percentage of pores. For both cases, outflow characterizations with the hot wire rig exist and can be adopted as reference values for the respective datasets if comparisons to other experiments are desired.

7.2 Conclusion

The following paragraph shall summarize and critically evaluate the contribution and progress of this research work with respect to the four outlined questions in Section 1.4.

Firstly, this thesis presents the first experimental demonstration of a boundary layer transition delay achieved by injecting a light gas in a hypersonic second mode

dominated boundary layer. It is furthermore the premier successful transition delay experiment in a low enthalpy flow with said characteristics. Albeit evidently initial and limited in many regards, the major contribution of this work may be the finding that effective leading edge cooling and stabilizing the boundary layer even far downstream may not be strictly mutually exclusive. It may be thought that this is in contrast to a consensus reached in the literature: light gases injected far upstream were thought to have the worst impact on stability. This has been found by several studies mentioned in Chapter 2 and revisited by authors of modern investigations (e.g. Jewell [109], Schmidt [180] or Camillo et al. [104]). When considering all experimental examples about stability and injection in Chapter 2, it is found that no directly comparable experiment or numerical investigation exists in the literature. Hence, interpretation of the presented results remains difficult. A possibility is that the observed stabilizing effect of helium is confined to a narrow subset of configurations. Only in this survey, helium injection has been performed from a small surface segment at the most upstream location, with a small nose bluntness, slender geometry, low enthalpy environment, uniform outflow, low enough blowing rates and distinctly hypersonic Mach number. To the knowledge of the author, no other study has ever tested a reasonably similar configuration. Missing one or two of the points mentioned could well mean that destabilizing effects prevail again and a transition delay cannot be observed. It is also currently unclear which physical effect caused the stabilization. A potential explanation is the disproportionate boundary layer thickening caused by helium injection which may increase the effective nose radius. However, this is drawn into question as only destabilization was observed with nitrogen injection, which should at least thicken the boundary layer as well to some extent. Other theories have been suggested, with most of them based on the simulation work from Miró Miró et al. [169]. Injection so far upstream may also hinder the noise receptivity process of a boundary layer.

Different coolant gases have a varying effect on developed instability oscillations. This was seen at surface instruments and with schlieren imaging. Depending on blowing ratio and molecular mass of the gas, the frequency of the second mode is

reduced. The work thus provides an experimental quantification and initial linear correlation of the second mode's "detuning" [104] behaviour for different gases and blowing ratios. While the data suggests how the thickening effect of injection must play a role, the involved fluid dynamics may be more complicated. Second modes may for example respond to injection by moving along the increased thickness. Such behaviour may be specific to small injection segments, but therefore be relevant for active cooling applications.

Comparing upstream and downstream injection remains problematic within the given dataset. For downstream effusion, the model had a sharp nose radius and the Reynolds number was lower than for the upstream cooling cases with a 1 mm nose radius. Nevertheless, the location is thought to have played a substantial role in determining stability characteristics, as schlieren never indicated any rearward movement of transition with downstream injection. Similarly, effusion from the nose segment did not alter second mode spectra in such a systematic way as blowing out of the frustum. Only a very careful inference shall be made herein: It seems likely that localized injection into a 'settled' boundary layer is fundamentally different with respect to fluid physics and instability than effusion at the leading edge. For the latter, any instability grows inside an already coolant-enriched boundary layer, while the former will inevitably displace oscillations and their established wave guide to some extent. The consequent destabilizing tendency may well be explained by the "shocklet" diagnosis from Miró Miró et al. [169].

Comparing measurement techniques has confirmed known contradictions in different definitions for transition locations with a downstream blowing effect. Expectedly, a coolant film originating from a nearby injector corrupts surface measurements when attempting to address instabilities. The research work may therefore provide fresh impetus to the scientific debate around experimentally detecting transition locations, especially with coolant effusion. It is found how transition onset and completion methods are both affected and can contradict each other. Only a synergy of optical methods and surface sensors and the critical analysis of several criterial enabled a comprehensive understanding of the contradicting phenomena. It could

be identified that in the conducted experiments downstream injection did not yield a transition delay in a fluid mechanical sense and only reduced heat transfer for either short or longer areas.

Furthermore, characterization of the injector effusion distributions disclosed inhomogeneites as well as changes in said outflow profile which motivates increased caution about a parameter so difficult to control, compare and quantify.

A contribution was made to the understanding of boundary layer stability and gas injection at hypersonic speeds. It has been shown experimentally that cooling at the most critical location can possibly be combined with a transition delay. This could significantly advance the applicability of transpiration cooling for sharp, slender geometries and their leading edges. Downstream injection with light gases potentially requires more careful consideration. Fluid turbulence and a local cooling effect may have to be balanced.

7.3 Recommendations for Future Work

A numerical re-investigation of the nosetip injection cases and helium stabilization could yield more insight into the transition delay mechanisms. It may also be of interest to investigate the difference of downstream and nose segment gas injection computationally. More analysis is needed on whether the small nose bluntness, the injection uniformity or the far upstream transpiration location could have been critical factors for observing transition delay. The speculations presented in 7.2 could hence be ruled out or verified.

Further experimental work could be conducted re-using the same cone model. Confirming the stabilization effect for other gases lighter than air such as neon, methane or even hydrogen may increase understanding of what physical gas property is responsible for the observations. For the likely case that tunnel noise receptivity played a role, it would be invaluable to repeat some experimental cases in a different facility, ideally a quiet tunnel.

It is currently unclear whether the stabilization effect is limited to second mode dominated transition processes. Performing nose tip helium injection at lower Mach

numbers could reveal further information which part of the transition mechanism was impacted and hindered by helium injection and variation of such parameters may prove invaluable for comparisons to simulation. Moving towards flight vehicle applicability, evaluating porous nose tip injection of light gases in a reflected shock tunnel with sufficient total temperature is the next step.

Nose tip and frustum injector materials exhibited significant non-uniformities. Improving the porous material with respect to pore size, homogeneity and surface quality may benefit experimental accuracy, reduce disturbances caused by injection and facilitate comparison to simulation.

Lastly, varying the injector geometry, such as position and surface area may help explore limits of applicability.

References

[1] RG Grant. *Flight: the complete history of aviation*. Dorling Kindersley Ltd, 2017.

[2] United Nations Office for Outer Space Affairs. *Online Index of Objects Launched into Outer Space*. Accessed Online: 07/12/2022. URL: `https://www.unoosa.org/oosa/osoindex/index.jspx?lf_id=`.

[3] Eugen Sänger. *Raketen-Flugtechnik*. Oldenbourg Wissenschaftsverlag, Berlin, 1933.

[4] Thomas A Heppenheimer. *Facing the heat barrier: a history of hypersonics*. Vol. 4232. U.S. Government Printing Office, Washington, DC, 2009.

[5] Hartmut E Sänger and Alexandre D Szames. "From the Silverbird to Interstellar Voyages". In: *54th International Astronautical Congress of the International Astronautical Federation, the International Academy of Astronautics, and the International Institute of Space Law* (Sept. 29–Oct. 3, 2003). IAC-03-IAA.2.4.a.07. Bremen, Germany, 2003.

[6] Peter P Wegener. *The Peenemünde wind tunnels: A memoir*. New Haven,CT: Yale University Press, 1996.

[7] Dietrich Eckardt. "The 1× 1 m hypersonic wind tunnel Kochel/Tullahoma 1940–1960". In: *CEAS Space Journal* 7.1 (2015), pp. 23–36.

[8] Guillaume Grossir. "Longshot hypersonic wind tunnel flow characterization and boundary layer stability investigations". PhD thesis. von Karman Institute for Fluid Dynamics - Université Libre de Bruxelles, 2015.

[9] Dennis R Jenkins. *Hypersonics before the shuttle: A concise history of the X-15 research airplane*. NASA Publication SP 2000-4518. National Aeronautics, Space Administration, NASA Office of Policy, and Plans, NASA History Office, 2000.

[10] R Chase and M Tang. "A history of the nasp program from the formation of the joint program office to the termination of the hystp scramjet performance demonstration program". In: *Sixth International Aerospace Planes and Hypersonic Technologies Conference* (Apr. 3–7, 1995). AIAA-95-6031. Chattanooga, TN: American Institute of Aeronautics and Astronautics, 1995.

[11] John J Bertin and Russell M Cummings. "Fifty years of hypersonics: where we've been, where we're going". In: *Progress in Aerospace Sciences* 39.6-7 (2003), pp. 511–536.

[12] Johnny G Armstrong. *Flight planning and conduct of the X-15A-2 envelope expansion program*. Tech. rep. FTC-TD-69-4. Air Force Flight Test Center, Edwards Air Force Base CA, 1969.

[13] John J Bertin and Russell M Cummings. "Critical hypersonic aerothermodynamic phenomena". In: *Annual Review of Fluid Mechanics* 38 (2006), p. 129.

[14] SD Williams, Donald M Curry, Dennis C Chao, and Vuong T Pham. "Ablation analysis of the Shuttle Orbiter oxidation protected reinforced carbon-carbon". In: *Journal of thermophysics and heat transfer* 9.3 (1995), pp. 478–485.

[15] Dorothy B Lee. *Apollo experience report: aerothermodynamics evaluation*. Tech. rep. TN D-6843. NASA, 1972.

[16] Eugene P Bartlett, Larry W Anderson, and Donald M Curry. "An evaluation of ablation mechanisms for the Apollo heat shield material". In: *Journal of Spacecraft and Rockets* 8.5 (1971), pp. 463–469.

[17] P Perrier. "Major lessons learned in hypersonic design of hermes". In: *Aerothermodynamics for space vehicles, Proceedings of the 2nd European Symposium held in ESTEC* (Nov. 21–25, 1994). Ed. by J. J. Hunt. Vol. 367. Noordwijk, The Netherlands: European Space Agency, 1995, p. 603.

[18] John J Bertin. *Hypersonic aerothermodynamics*. Washington, D.C.: AIAA, 1994.

[19] David Sziroczak and Howard Smith. "A review of design issues specific to hypersonic flight vehicles". In: *Progress in Aerospace Sciences* 84 (2016), pp. 1–28.

[20] Kingston Reif. "Hypersonic advances spark concern". In: *Arms Control Today* 48.1 (2018), pp. 29–30.

[21] Ernst Heinrich Hirschel and Claus Weiland. *Selected aerothermodynamic design problems of hypersonic flight vehicles*. Vol. 229. Springer Science & Business Media, 2009.

[22] EH Hirschel and C Weiland. "Design of hypersonic flight vehicles: some lessons from the past and future challenges". In: *CEAS Space Journal* 1.1 (2011), pp. 3–22.

[23] Ernst Heinrich Hirschel. *Basics of aerothermodynamics*. New York, US: Springer, 2005.

[24] John V Becker. "New approaches to hypersonic aircraft". In: *7th International Council of the Aeronautical Sciences Congress*. ICAS Paper 70-16. International Council of the Aeronautical Sciences. Rome, Italy, 1970.

[25] Donald M Curry. "Thermal protection systems manned spacecraft flight experience". In: *Current Technology for Thermal Protection Systems*. NASA, Conf. Publ. 3157. Langley Research Center, Washington DC: NASA, 1992.

[26] Dave R Moore, Charles J Stalmach, and Thomas C Pope. *Investigation of Ablation Effects on Hypersonic Dynamic Stability of a deg 10 Cone*. Tech. rep. AFFDL-TR-66-230. Wright-Patterson Air Force Base, Ohio: Air Force Flight Dynamics Laboratory, Research and Technology Division, 1967.

[27] M Holden. "Studies of transpiration cooling, surface roughness and entropy swallowing in transitional and turbulent boundary layers over nose tips". In: *30 th International Astronautical Federation Congress*. IAF-79-F-42. Munich, Germany: Pergamon Press for the International Astronautical Federation, 1979.

[28] Mark J Lewis. "Sharp leading edge hypersonic vehicles in the air and beyond". In: *SAE transactions* 1999-01-5514 (1999), pp. 841–851.

[29] Randall T Voland, Lawrence D Huebner, and Charles R McClinton. "X-43A hypersonic vehicle technology development". In: *Acta Astronautica* 59.1-5 (2006), pp. 181–191.

[30] Charles Leonard, Ruth Amundsen, and Walter Bruce. "Hyper-X hot structures design and comparison with flight data". In: *AIAA/CIRA 13th International Space Planes and Hypersonics Systems and Technologies Conference* (May 16–20, 2005). AIAA 2005-3438. Capua, Italy, 2005.

[31] Charles McClinton. "X-43-scramjet power breaks the hypersonic barrier: Dryden lectureship in research for 2006". In: *44th AIAA Aerospace Sciences Meeting and Exhibit* (Jan. 9–12, 2006). AIAA 2006-1. Reno, Nevada: American Institute of Aeronautics and Astronautics, 2006.

[32] Thomas Reimer, Markus Kuhn, Ali Gülhan, Burkhard Esser, Martin Sippel, and Arnold van Foreest. "Transpiration cooling tests of porous CMC in hypersonic flow". In: *17th AIAA International Space Planes and Hypersonic Systems and Technologies Conference* (Apr. 11–14, 2011). AIAA 2011-2251. San Francisco, CA, 2011.

[33] Kenneth Sutton and Randolph A Graves Jr. *A general stagnation-point convective heating equation for arbitrary gas mixtures*. Tech. rep. NASA-TR-R-376. 1971.

[34] James A Fay and Frederick R Riddell. "Theory of stagnation point heat transfer in dissociated air". In: *Journal of the Aerospace Sciences* 25.2 (1958), pp. 73–85.

[35] Scott D Kasen. "Thermal management at hypersonic leading edges". PhD thesis. University of Virginia, 2013.

[36] Ali Gülhan and S Braun. "An experimental study on the efficiency of transpiration cooling in laminar and turbulent hypersonic flows". In: *Experiments in fluids* 50 (3 2011), pp. 509–525.

[37] Christopher D Karlgaard, Paul V Tartabini, Robert C Blanchard, Michael Kirsch, and Matthew D Toniolo. "Hyper-X post-flight trajectory reconstruction". In: *Journal of Spacecraft and Rockets* 43.1 (2006), pp. 105–115.

[38] Christopher Karlgaard, John Martin, Paul Tartabini, and Mark Thornblom. "Hyper-X Mach 10 Trajectory Reconstruction". In: *AIAA Atmospheric Flight Mechanics Conference and Exhibit*. AIAA 2005-5920. San Francisco, CA: American Institute of Aeronautics and Astronautics, 2005.

[39] Charles B Johnson, P Calvin Stainback, Kathleen C Wicker, and Lillian R Boney. *Boundary-layer edge conditions and transition Reynolds number data for a flight test at Mach 20 (Reentry F)*. Tech. rep. NASA TM X-2584. 1972.

[40] Hicham Alkandry, Kyle Hanquist, and Iain D Boyd. "Conceptual analysis of electron transpiration cooling for the leading edges of hypersonic vehicles". In: *11th AIAA/ASME Joint Thermophysics and Heat Transfer Conference and AIAA Aviation Forum* (June 16–20, 2014). AIAA 6.2014-2674. Atlanta, GA, 2014.

[41] Mark M Opeka, Inna G Talmy, and JA Zaykoski. "Oxidation-based materials selection for 2000 C+ hypersonic aerosurfaces: Theoretical considerations and historical experience". In: *Journal of materials science* 39.19 (2004), pp. 5887–5904.

[42] Saeed Reza Ghadiani. "A multiphasic continuum mechanical model for design investigations of an effusion-cooled rocket thrust chamber". PhD thesis. University of Stuttgart, 2005.

[43] OJ Haidn, Jörg Riccius, Dmitry Suslov, S Beyer, and O Knab. "Development of technologies for a CMC-based combustion chamber". In: *Progress in Propulsion Physics* 1 (2009), pp. 645–658.

[44] James Michael Modlin. "Hypersonic aerospace vehicle leading edge cooling using heat pipe, transpiration and film cooling techniques". PhD thesis. Georgia Institute of Technology, 1991.

[45] H Neale Kelly and Max L Blosser. "Active cooling from the sixties to NASP". In: *Proceedings of a Workshop held at Langley Research Centre* (Feb. 11–12, 1992). NASA Conferecne Publication 3157. Hampton, Virginia: NASA, 1992, pp. 189–249.

[46] Ernst Rudolf Georg Eckert and John NB Livingood. *Comparison of effectiveness of convection-, transpiration-, and film-cooling methods with air as coolant.* Tech. rep. NACA-TN-3010. Lewis Flight Propulsion Laboratory, Cleveland, Ohio, 1953.

[47] Morris W Rubesin. *The influence of surface injection on heat-transfer and skin friction associated with the high-speed turbulent boundary layer.* Tech. rep. NACA-RM-A55L13. Moffett Field, CA: NASA Ames Aeronautical Lab, 1956.

[48] Arnold van Foreest, Martin Sippel, Ali Gülhan, Burkard Esser, BAC Ambrosius, and Kees Sudmeijer. "Transpiration cooling using liquid water". In: *Journal of Thermophysics and Heat Transfer* 23.4 (2009), pp. 693–702.

[49] Hassan Saad Ifti. "Transpiration Cooling of a Hypersonic Vehicle". PhD thesis. University of Oxford, 2022.

[50] Hassan Saad Ifti, Tobias Hermann, Marc Ewenz Rocher, Luke Doherty, Christopher Hambidge, Matthew McGilvray, and Luc Vandeperre. "Laminar transpiration cooling experiments in hypersonic flow". In: *Experiments in Fluids* 63.6 (2022), pp. 1–14.

[51] Hassan Saad Ifti, Tobias Hermann, Matthew McGilvray, and James Merrifield. "Numerical Simulation of Transpiration Cooling in a Laminar Hypersonic Boundary Layer". In: *Journal of Spacecraft and Rockets* 59.5 (2022), pp. 1726–1735.

[52] Imran Naved, Tobias Hermann, Matthew McGilvray, Marc Ewenz Rocher, Chris Hambidge, Luke Doherty, Laurent Le Page, Madeleine Grossman, and Luc Vandeperre. "Heat Transfer Measurements of a Transpiration-Cooled Stagnation Point in Transient Hypersonic Flow". In: *Journal of Thermophysics and Heat Transfer* 37.2 (2023), pp. 296–308.

[53] Marc Ewenz Rocher, Matthew McGilvray, Tobias A Hermann, Hassan S Ifti, Fabian Hufgard, Martin F Eberhart, Arne Meindl, Stefan Loehle, Tommaso Giovannini, and Luc J Vandeperre. "Testing a transpiration cooled zirconium-di-boride sample in the plasma tunnel at IRS". In: *AIAA SciTech Forum* (Jan. 7–11, 2019). AIAA 2019-1552. San Diego, California, 2019.

[54] Marc Ewenz Rocher, Tobias Hermann, Matthew McGilvray, Madeleine Grossman, and Luc Vandeperre. "Measuring the concentration of freestream species on a hypersonic transpiration-cooled stagnation point". In: *Journal of Spacecraft and Rockets* 59.4 (2022), pp. 1380–1387.

[55] Marc Ewenz Rocher, Tobias Hermann, and Matthew McGilvray. "Oxidation Response of Transpiration-Cooled ZrB 2 on a Hypersonic Stagnation Point". In: *Journal of Spacecraft and Rockets* 59.5 (2022), pp. 1486–1495.

[56] Steven P Schneider. "Hypersonic boundary-layer transition with ablation and blowing". In: *Journal of Spacecraft and Rockets* 47 (2 2010), pp. 225–237.

[57] Steven P Schneider. "Hypersonic laminar–turbulent transition on circular cones and scramjet forebodies". In: *Progress in Aerospace Sciences* 40.1-2 (2004), pp. 1–50.

[58] Kenneth Stetson and Roger Kimmel. "On hypersonic boundary-layer stability". In: *30th aerospace sciences meeting and exhibit*. 1992, p. 737.

[59] Roger Kimmel. "Aspects of hypersonic boundary layer transition control". In: *41st Aerospace Sciences Meeting and Exhibit* (Jan. 6–9, 2003). AIAA 2003-772. Reno, Nevada, 2003.

[60] Steven P Schneider. "Development of hypersonic quiet tunnels". In: *Journal of Spacecraft and Rockets* 45.4 (2008), pp. 641–664.

[61] Helen Reed, Roger Kimmel, Steven Schneider, Daniel Arnal, Helen Reed, Roger Kimmel, Steven Schneider, and Daniel Arnal. "Drag prediction and transition in hypersonic flow". In: *Sustained hypersonic flight, vol. 3. AGARD*. AIAA Paper 97-1818. 1997.

[62] Eric C Marineau. "Prediction methodology for second-mode-dominated boundary-layer transition in wind tunnels". In: *AIAA Journal* 55.2 (2017), pp. 484–499.

[63] Kei Y Lau. "Hypersonic boundary-layer transition: application to high-speed vehicle design". In: *Journal of Spacecraft and Rockets* 45.2 (2008), pp. 176–183.

[64] E Reginald Van Driest. "The problem of aerodynamic heating". In: *Aeronautical Engineering Review* 15 (1956), pp. 26–41.

[65] Charles L Fefferman. "Existence and smoothness of the Navier-Stokes equation". In: *The millennium prize problems*. Cambridge, MA: Clay Mathematics Institute, 2006, pp. 57–67.

[66] Allen Whitehead Jr. "NASP aerodynamics". In: *National Aerospace Plane Conference*. Paper 89-5013. AIAA, 1989.

[67] Steven P Schneider. "Effects of roughness on hypersonic boundary-layer transition". In: *Journal of Spacecraft and Rockets* 45.2 (2008), pp. 193–209.

[68] Sebastien Wylie. "Hypersonic boundary layer instability measurements at low and high angles of attack". PhD thesis. University of Oxford, 2020.

[69] William S Saric, Helen L Reed, and Edward J Kerschen. "Boundary-layer receptivity to freestream disturbances". In: *Annual review of fluid mechanics* 34 (2002), p. 291.

[70] NJ Parziale, JE Shepherd, and HG Hornung. "Differential interferometric measurement of instability in a hypervelocity boundary layer". In: *AIAA Journal* 51.3 (2013), pp. 750–754.

[71] Tobias Langener. "A contribution to transpiration cooling for aerospace applications using CMC walls". PhD thesis. University of Stuttgart, 2011.

[72] Pedro Paredes, Meelan M Choudhari, Fei Li, Joseph S Jewell, Roger L Kimmel, Eric C Marineau, and Guillaume Grossir. "Nose-tip bluntness effects on transition at hypersonic speeds". In: *Journal of Spacecraft and Rockets* 56.2 (2019), pp. 369–387.

[73] Pedro Paredes, Meelan M Choudhari, and Fei Li. "Mechanism for frustum transition over blunt cones at hypersonic speeds". In: *Journal of Fluid Mechanics* 894 (2020), A22.

[74] Lev Davidovich Landau and Evgenii Mikhailovich Lifshitz. *Fluid Mechanics: Landau and Lifshitz: Course of Theoretical Physics, Volume 6*. Vol. 6. Elsevier, 2013.

[75] Howard W Emmons. "The laminar-turbulent transition in a boundary layer-Part I". In: *Journal of the Aeronautical Sciences* 18.7 (1951), pp. 490–498.

[76] Bjorn Hof, Casimir WH Van Doorne, Jerry Westerweel, Frans TM Nieuwstadt, Holger Faisst, Bruno Eckhardt, Hakan Wedin, Richard R Kerswell, and Fabian Waleffe. "Experimental observation of nonlinear traveling waves in turbulent pipe flow". In: *Science* 305.5690 (2004), pp. 1594–1598.

[77] Osborne Reynolds. "XXIX. An experimental investigation of the circumstances which determine whether the motion of water shall be direct or sinuous, and of the law of resistance in parallel channels". In: *Philosophical Transactions of the Royal society of London* 174 (1883), pp. 935–982.

[78] Eli Reshotko. "Boundary-layer stability and transition". In: *Annual review of fluid mechanics* 8.1 (1976), pp. 311–349.

[79] Steven P Schneider. "Effects of high-speed tunnel noise on laminar-turbulent transition". In: *Journal of Spacecraft and Rockets* 38.3 (2001), pp. 323–333.

[80] Eli Reshotko. "Boundary layer instability, transition and control". In: *32nd Aerospace Sciences Meeting and Exhibit*. AIAA 1994-1. Reno, NV, U.S.A., 1994.

[81] R Narasimha. "The laminar-turbulent transition zone in the boundary layer". In: *Progress in Aerospace Sciences* 22.1 (1985), pp. 29–80.

[82] Itiro Tani. "Boundary-layer transition". In: *Annual Review of Fluid Mechanics* 1.1 (1969), pp. 169–196.

[83] Alexander Fedorov. "Transition and Stability of High-Speed Boundary Layers". In: *Annual Review of Fluid Mechanics* 43 (1 2011), pp. 79–95. URL: https://doi.org/10.1146/annurev-fluid-122109-160750.

[84] Hermann Schlichting and Joseph Kestin. *Boundary layer theory*. Vol. 121. Springer, 1961.

[85] Ludwig Prandtl. "Über Flussigkeitsbewegung bei sehr kleiner Reibung". In: *Verhandl. III, Internat. Math.-Kong., Heidelberg, Teubner, Leipzig* (1904), pp. 484–491.

[86] Michael Eckert. "Ludwig Prandtl and the growth of fluid mechanics in Germany". In: *Comptes Rendus Mécanique* 345.7 (2017), pp. 467–476.

[87] Itiro Tani. "History of boundary layer theory". In: *Annual review of fluid mechanics* 9.1 (1977), pp. 87–111.

[88] John David Anderson. *Hypersonic and high temperature gas dynamics 2nd Edition*. American Institute of Aeronautics and Astronautics, 2000.

[89] Mark V Morkovin. "On the many faces of transition". In: *Viscous drag reduction*. Ed. by C.S. Wells. Springer, 1969, pp. 1–31.

[90] Leslie M Mack. *Boundary-layer linear stability theory*. Tech. rep. AGARD Rep. No. 709, Special Course on Stability and Transition of Laminar Flow. California Inst of Tech Pasadena Jet Propulsion Lab, 1984.

[91] LM Mack. *Boundary layer stability theory*. Tech. rep. Doc. No. 900-277 Rev. A. Pasadena, CA: Jet Propulsion Laboratory California Institute of Technology, 1969.

[92] Eli Reshotko. "Transition issues at hypersonic speeds". In: *44th AIAA Aerospace Sciences Meeting and Exhibit* (Jan. 9–12, 2006). Reno, Nevada: AIAA, 2006, AIAA Paper 2006–707.

[93] Eli Reshotko. "Transient growth: a factor in bypass transition". In: *Physics of Fluids* 13.5 (2001), pp. 1067–1075.

[94] M V Morkovin. "Transition in open flow systems-a reassessment". In: *Bull. Am. Phys. Soc.* 39 (1994), p. 1882.

[95] Ludwig Prandtl. "Bemerkungen über die Entstehung der Turbulenz". In: *ZAMM-Journal of Applied Mathematics and Mechanics/Zeitschrift für Angewandte Mathematik und Mechanik* 1.6 (1921), pp. 431–436.

[96] Leslie M Mack. "Linear stability theory and the problem of supersonic boundary-layer transition". In: *AIAA Journal* 13.3 (1975), pp. 278–289.

[97] Galen B Schubauer and Harold K Skramstad. "Laminar Boundary-Layer Oscillations and Transition on". In: *Journal of research of the National Bureau of Standards* 38 (1947), p. 251.

[98] Jonathan Poggie, Roger Kimmel, Jonathan Poggie, and Roger Kimmel. "Disturbance evolution and breakdown to turbulence in a hypersonic boundary layer-Instantaneous structure". In: *35th Aerospace Sciences Meeting and Exhibit*. 1997, p. 556.

[99] SJ Laurence, Alexander Wagner, and Klaus Hannemann. "Experimental study of second-mode instability growth and breakdown in a hypersonic boundary layer using high-speed schlieren visualization". In: *Journal of Fluid Mechanics* 797 (2016), pp. 471–503.

[100] Malte Estorf, Rolf Radespiel, Steven Schneider, Heath Johnson, and Stefan Hein. "Surface-pressure measurements of second-mode instability in quiet hypersonic flow". In: *46th AIAA Aerospace Sciences Meeting and Exhibit* (Jan. 7–10, 2008). AIAA 2008-1153. Reno, Nevada, 2008.

[101] Dennis Berridge, Katya Casper, Shann Rufer, Christopher Alba, Daniel Lewis, Steven Beresh, and Steven Schneider. "Measurements and computations of second-mode instability waves in several hypersonic wind tunnels". In: *40th Fluid Dynamics Conference and Exhibit* (June 28–July 1, 2010). AIAA 2010-5002. Chicago, Illinois, 2010.

[102] Katya M Casper, Steven J Beresh, John F Henfling, Russell W Spillers, Brian OM Pruett, and Steven P Schneider. "Hypersonic wind-tunnel measurements of boundary-layer transition on a slender cone". In: *AIAA Journal* 54.4 (2016), pp. 1250–1263.

[103] Roger Kimmel. "Hypersonic boundary layer stability measurements using uncalibrated hot wires". In: *39th Aerospace Sciences Meeting and Exhibit* (Jan. 8–11, 2001). AIAA 2001-0275. Reno, Nevada, 2001.

[104] Giannino Ponchio Camillo, Alexander Wagner, Christian Dittert, Leroy Benjamin, Viola Wartemann, Jens Neumann, and Rüdiger Hink. "Experimental investigation of the effect of transpiration cooling on second mode instabilities in a hypersonic boundary layer". In: *Experiments in Fluids* 61.7 (2020), p. 162.

[105] JL Van Ingen. *A suggested semi-empirical method for the calculation of the boundary layer transition region.* Tech. rep. Rapport VTH-74. Delft University of Technology, Technische Hogeschool Delft, Vliegtuigbouwkunde, 1956.

[106] J Van Ingen. "The eN method for transition prediction. Historical review of work at TU Delft". In: *38th Fluid Dynamics Conference and Exhibit* (June 23–26, 2008). AIAA 2008-3830. Seattle, Washington, 2008.

[107] Apollo Milton Olin Smith and Nathalie Gamberoni. *Transition, pressure gradient and stability theory.* Tech. rep. Report ES26388. Douglas Aircraft Co., 1956.

[108] Fernando Miró Miró, Pieter Dehairs, Fabio Pinna, Maria Gkolia, Davide Masutti, Tamas Regert, and Olivier Chazot. "Effect of Wall Blowing on Hypersonic Boundary-Layer Transition". In: *AIAA Journal* 57 (4 2019), pp. 1567–1578.

[109] Joseph Stephen Jewell. "Boundary-layer transition on a slender cone in hypervelocity flow with real gas effects". PhD thesis. California Institute of Technology, 2014.

[110] Anthony Demetriades. *Hydrodynamic Stability and Transition to Turbulence in the Hypersonic Boundary Layer over a Sharp Cone.* Tech. rep. AFOSR TR-75-1435. Boiling AFB, DC: U.S. Air Force Office of Scientific Research, 1975.

[111] Ross M Wagnild. "High enthalpy effects on two boundary layer disturbances in supersonic and hypersonic flow". PhD thesis. Minnesota Univ Minneapolis, 2012.

[112] Anthony Demetriades. "Hypersonic viscous flow over a slender cone. III-Laminar instability and transition". In: *7th Fluid and Plasma Dynamics Conference* (June 17–19, 1974). AIAA Paper No. 75-535. Palo Alto, CA, 1974.

[113] Richard E Kennedy, Stuart J Laurence, Michael S Smith, and Eric C Marineau. "Hypersonic boundary-layer transition features from high-speed schlieren images". In: *55th AIAA Aerospace Sciences Meeting* (Jan. 9–13, 2017). AIAA 2017-1683. Grapevine, Texas, 2017.

[114] Guillaume Grossir, Fabio Pinna, Gabriele Bonucci, Tamas Regert, Patrick Rambaud, and Olivier Chazot. "Hypersonic boundary layer transition on a 7 degree half-angle cone at Mach 10". In: *7th AIAA Theoretical Fluid Mechanics Conference* (June 16–20, 2014). AIAA 2014-2779. Atlanta, GA, 2014.

[115] SJ Laurence, Alexander Wagner, and Klaus Hannemann. "Schlieren-based techniques for investigating instability development and transition in a hypersonic boundary layer". In: *Experiments in Fluids* 55.8 (2014), pp. 1–17.

[116] John Laufer. "Aerodynamic noise in supersonic wind tunnels". In: *Journal of the Aerospace Sciences* 28.9 (1961), pp. 685–692.

[117] SR Pate and CJ Schueler. *Effects of Radiated Aerodynamic Noise on Model Boundary-Layer Transition in Supersonic and Hypersonic Wind Tunnels.* Tech. rep. AEDC-TR-67-236 (AD666644). Arnold Engineering Development Center, Arnold Air Force Station, Tennessee, 1968.

[118] Samuel R Pate. "Effects of wind tunnel disturbances on boundary-layer transition with emphasis on radiated noise: a review". In: *11th Aerodynamic Testing Conference.* Colorado Springs, CO: AIAA Paper 1980-0431, 1980.

[119] Mark V Morkovin. "On transition experiments at moderate supersonic speeds". In: *Journal of the Aeronautical Sciences* 24.7 (1957), pp. 480–486.

[120] Lian Duan, Meelan M Choudhari, Amanda Chou, Federico Munoz, Rolf Radespiel, Thomas Schilden, Wolfgang Schröder, Eric C Marineau, Katya M Casper, Ross S Chaudhry, et al. "Characterization of freestream disturbances in conventional hypersonic wind tunnels". In: *Journal of spacecraft and rockets* 56.2 (2019), pp. 357–368.

[121] Leslie SG Kovasznay. "Turbulence in supersonic flow". In: *Journal of the Aeronautical Sciences* 20.10 (1953), pp. 657–674.

[122] Henry William Bennett. *An experimental study of boundary layer transition.* Tech. rep. Kimberly-Clark Corp, Neenah, WI, 1953.

[123] JG Spangler and CS Wells Jr. "Effects of freestream disturbances on boundary-layer transition." In: *AIAA Journal* 6.3 (1968), pp. 543–545.

[124] Kenneth F Stetson. "Hypersonic transition testing in wind tunnels". In: *Instability and transition.* Ed. by M. Y. Hussaini and R. G. Voight. Vol. 1. Berlin: Springer Verlag, 1990, pp. 91–100.

[125] P Calvin Stainback. "Hypersonic boundary-layer transition in the presence of wind-tunnel noise." In: *AIAA Journal* 9.12 (1971), pp. 2475–2476.

[126] Steven P Schneider and Christine E Haven. "Quiet-flow Ludwieg tube for high-speed transition research". In: *AIAA Journal* 33.4 (1995), pp. 688–693.

[127] Roger L Kimmel, David W Adamczak, Matthew P Borg, Joseph S Jewell, Thomas J Juliano, Scott A Stanfield, and Karen T Berger. "First and fifth hypersonic international flight research experimentation's flight and ground tests". In: *Journal of Spacecraft and Rockets* 56.2 (2019), pp. 421–431.

[128] Jason T Lachowicz, Ndaona Chokani, and Stephen P Wilkinson. "Boundary-layer stability measurements in a hypersonic quiet tunnel". In: *AIAA Journal* 34.12 (1996), pp. 2496–2500.

[129] Brandon C Chynoweth, Christopher Ward, and Steven P Schneider. "Measuring transition and instabilities in a Mach 6 hypersonic quiet wind tunnel". In: *44th AIAA Fluid Dynamics Conference* (June 16–20, 2014). AIAA 2014-2643. Atlanta, GA, 2014.

[130] Alex Bounitch, Daniel Lewis, and John Lafferty. “Improved measurements of" tunnel noise" pressure fluctuations in the AEDC hypervelocity wind tunnel No. 9”. In: *49th AIAA Aerospace Sciences Meeting including the New Horizons Forum and Aerospace Exposition* (Jan. 4–7, 2011). AIAA 2011-1200. Orlando, Florida, 2011.

[131] Scott A Berry, Thomas J Horvath, Brian R Hollis, Rick A Thompson, and H Harris Hamilton. “X-33 hypersonic boundary-layer transition”. In: *Journal of Spacecraft and Rockets* 38.5 (2001), pp. 646–657.

[132] Scott A Berry, Michael DiFulvio, and Matthew K Kowalkowski. *Forced boundary-layer transition on X-43 (Hyper-X) in NASA LaRC 31-inch Mach 10 air tunnel*. Tech. rep. NASA TM-2000-210315. 2000.

[133] K Stetson. “Nosetip bluntness effects on cone frustum boundary layer transition in hypersonic flow”. In: *16th Fluid and Plasmadynamics Conference* (July 12–14, 1983). AIAA 1983-1763. Danvers, MA, U.S.A, 1983.

[134] Eric J Softley. *Transition of the Hypersonic Boundary Layer on a Cone: Part II. Experiments at M= 10 and More on Blunt Cone Transition*. Tech. rep. TR-R68SD14. Philadelphia, PA: General Electric Co Missile and Space Division, 1968.

[135] C M Akin and J G Marvin. “Combined effects of mass addition and nose bluntness on boundary-layer transition”. In: *AIAA Journal* 8 (5 1970), pp. 857–863.

[136] Eric C Marineau, George C Moraru, Daniel R Lewis, Joseph D Norris, John F Lafferty, Ross M Wagnild, and Justin A Smith. “Mach 10 boundary layer transition experiments on sharp and blunted cones”. In: *19th AIAA International Space Planes and Hypersonic Systems and Technologies Conference* (June 16–20, 2014). AIAA 2014-3108. Atlanta, GA, 2014.

[137] George H Rushton and Kenneth F Stetson. “Shock tunnel investigation of boundary-layer transition at M equals 5.5.” In: *AIAA Journal* 5.5 (1967), pp. 899–906.

[138] J Muir and A Trujillo. “Experimental investigation of the effects of nose bluntness, free-stream unit Reynolds number, and angle of attack on cone boundary layer transition at a Mach number of 6”. In: *10th Aerospace Sciences Meeting* (Jan. 17–19, 1972). San Diego, CA, 1972, AIAA Paper No.72–216.

[139] Joseph S Jewell and Roger L Kimmel. “Boundary-layer stability analysis for Stetson’s Mach 6 blunt-cone experiments”. In: *Journal of Spacecraft and Rockets* 54.1 (2017), pp. 258–265.

[140] Antonio Ferri and Paul A Libby. “Note on an interaction between the boundary layer and the inviscid flow”. In: *Journal of the Aeronautical Sciences* 21.2 (1954), pp. 130–130.

[141] Egon Krause and Victor Zakkay. “Boundary conditions at the outer edge of the boundary layer on blunted conical bodies”. In: *AIAA Journal* 1.7 (1963), pp. 1671–1672.

[142] M Malik, R Spall, and C-L Chang. “Effect of nose bluntness on boundary layer stability and transition”. In: *28th Aerospace Sciences Meeting* (Jan. 8–11, 1990). AIAA 1990-112. Reno, NV, U.S.A., 1990.

[143] I Rosenboom, S Hein, and U Dallmann. "Influence of nose bluntness on boundary-layer instabilities in hypersonic cone flows". In: *30th AIAA Fluid Dynamics Conference* (June 28–July 1, 1999). AIAA 99-3591. Norfolk, VA, 1999.

[144] Kenneth F Stetson, Elton R Thompson, Joseph C Donaldson, and Leo G Siler. "Laminar boundary layer stability experiments on a cone at Mach 8. II- Blunt cone". In: *22nd Aerospace Sciences Meeting*. AIAA Paper 84-0006. Reno, NV: American Institute of Aeronautics and Astronautics, 1984.

[145] RJ Sanator, JP DeCarlo, and DT Torrillo. "Hypersonic boundary-layer transition data for a cold-wall slender cone". In: *AIAA Journal* 3.4 (1965), pp. 758–760.

[146] Eric J Softley, Bruce C Graber, and Robert E Zempel. "Experimental observation of transition of the hypersonic boundary layer." In: *AIAA Journal* 7.2 (1969), pp. 257–263.

[147] Travis S Kocian, Alexander J Moyes, Helen L Reed, Stuart A Craig, William S Saric, Steven P Schneider, and Joshua B Edelman. "Hypersonic crossflow instability". In: *Journal of Spacecraft and Rockets* 56.2 (2019), pp. 432–446.

[148] Joel Gronvall, Heath Johnson, and Graham Candler. "Hypersonic three-dimensional boundary layer transition on a cone at angle of attack". In: *42nd AIAA Fluid Dynamics Conference and Exhibit* (June 25–28, 2011). AIAA 2012-2822. New Orleans, Louisiana: American Institute of Aeronautics and Astronautics, 2011.

[149] Laura Paquin. "Effect of Cooling on Hypersonic Boundary-Layer Stability". PhD thesis. University of Maryland, College Park, 2022.

[150] CJ Scott. *Experimental Investigation of Laminar Heat Transfer and Transition with Foreign Gas Injection-A 16-Degree Porous Cone at Mach 5*. Tech. rep. AFOSR-TN-60-1370/UMRAL RR No. 174. Minneapolis, MN: University of Minnesota, Instiute of Technology, Rosemount Aeronautical Laboratories, 1960.

[151] Hirotaka Otsu, Kazuhisa Fujita, and Takeshi Ito. "Application of the transpiration cooling method for reentry vehicles". In: *45th AIAA Aerospace Sciences Meeting and Exhibit* (Jan. 8–11, 2007). AIAA 2007-1209. Reno, Nevada: American Institute of Aeronautics and Astronautics, 2007.

[152] H Bohrk, H Elsaber, and Hedrik Weihs. "The SHEFEX II thermal protection system". In: *7th European Symposium on Aerothermodynamics*. European Space Agency, 2011.

[153] CC Pappas and Arthur F Okuno. *Measurement of heat transfer and recovery factor of a compressible turbulent boundary layer on a sharp cone with foreign gas injection*. Tech. rep. NASA TN D-2230. 1964.

[154] Joseph G. Marvin and Ronald B. Pope. "Laminar convective heating and ablation in the Mars atmosphere". In: *AIAA Journal* 5 (2 1967), pp. 240–248.

[155] Robert T Swann and Claud M Pittman. *Numerical Analysis of the Transient Responce of Advanced Thermal Protection Systems for Atmosphereic Entry*. Tech. rep. TN D-1379. 1962.

[156] William Morrow Kays. "Heat transfer to the transpired turbulent boundary layer". In: *International Journal of Heat and Mass Transfer* 15.5 (1972), pp. 1023–1044.

[157] Lawrence W Woodruff and George C Lorenz. “Hypersonic turbulent transpiration cooling including downstream effects.” In: *AIAA Journal* 4.6 (1966), pp. 969–975.

[158] Hannah Böhrk, Henning Elsäßer, and Hendrik Weihs. “Flight Data from the Faceted TPS on SHEFEX II”. In: *8th European Symposium on Aerothermodynamics for Space Vehicles*. ESA Conference Bureau Noordwijk, The Netherlands. 2015.

[159] Imran Naved, Tobias Hermann, Chris Hambidge, Hassan Saad Ifti, Chiara Falsetti, Matthew McGilvray, Iullia S Tirichenko, and Luc Vandeperre. “Transpiration-Cooling Heat Transfer Experiments in Laminar and Turbulent Hypersonic Flows”. In: *Journal of Thermophysics and Heat Transfer* 37.2 (2023), pp. 281–295.

[160] Tobias Langener, Jens Von Wolfersdorf, and Johan Steelant. “Experimental investigations on transpiration cooling for scramjet applications using different coolants”. In: *AIAA Journal* 49.7 (2011), pp. 1409–1419.

[161] T Hermann, HS Ifti, M McGilvray, L Doherty, and RP Geraets. “Mixing characteristics in a hypersonic flow around a transpiration cooled flat plate model”. In: *HiSST: International Conference on High-Speed Vehicle Science Technology*. European Space Agency. Moscow, Russia, 2018.

[162] Hannah Böhrk, Olivier Piol, and Markus Kuhn. “Heat balance of a transpiration-cooled heat shield”. In: *Journal of Thermophysics and Heat Transfer* 24.3 (2010), pp. 581–588.

[163] Tobias Hermann, Matthew McGilvray, and Imran Naved. “Performance of transpiration-cooled heat shields for reentry vehicles”. In: *AIAA Journal* 58.2 (2020), pp. 830–841.

[164] Markus Kuhn, Hermann Hald, Ali Gülhan, Burkard Esser, and Herbert Olivier. “Experimental Investigations of Transpiration Cooled CMC’s in Supersonic Plasma Flows”. In: *Thermal Protection Systems and Hot Structures*. Vol. ESA Special Publcation 631. Noordwijk, The Netherlands: ESA Conference Bureau, 2006, pp. 1–9.

[165] Burkard Esser, Jorge Barcena, Markus Kuhn, Altug Okan, Lauren Haynes, Sandro Gianella, Alberto Ortona, Volker Liedtke, Daniele Francesconi, and Hideyuki Tanno. “Innovative thermal management concepts and material solutions for future space vehicles”. In: *Journal of Spacecraft and Rockets* 53.6 (2016), pp. 1051–1060.

[166] Hannah Boehrk, Viola Wartemann, Thino Eggers, Jan Martinez Schramm, Alexander Wagner, and Klaus Hannemann. “Shock tube testing of the transpiration-cooled heat shield experiment AKTiV”. In: *18th AIAA/3AF International Space Planes and Hypersonic Systems and Technologies Conference* (Sept. 24–28, 2012). AIAA 2012-5935. Tours, France: American Institute of Aeronautics and Astronautics, 2012.

[167] Morris W Rubesin. *An analytical estimation of the effect of transpiration cooling on the heat-transfer and skin-friction characteristics of a compressible, turbulent boundary layer*. Tech. rep. NACA-TN-3341. Ames Aeronautical Labs, 1954.

[168] Clifton H Mortensen and Xiaolin Zhong. "Real-gas and surface-ablation effects on hypersonic boundary-layer instability over a blunt cone". In: *AIAA Journal* 54.3 (2016), pp. 980–998.

[169] Fernando Miró Miró and Fabio Pinna. "Injection-gas-composition effects on hypersonic boundary-layer transition". In: *Journal of Fluid Mechanics* 890 (2020), R4.

[170] Michael Holden, Kathleen Rodriguez, and John Va. "An experimental study of transpiration cooling on the distribution of heat transfer and skin friction to a sharp slender cone at Mach 11 and 13". In: *28th AIAA Aerospace Sciences Meeting* (Jan. 8–11, 1990). AIAA-90-0308. Reno, NV, 1990.

[171] Michael Holden, Timothy Wadhams, and Erik Mundy. "A review of experimental studies of surface roughness and blowing on the heat transfer and skin friction to nosetips and slender cones in high mach numbers flows". In: *40th Thermophysics Conference* (June 23–26, 2008). AIAA 2008-3907. Seattle, Washington: American Institute of Aeronautics and Astronautics, 2008.

[172] Robert J Cresci and Paul A Libby. "The Downstream Influence of Mass Transfer at the Nost of a Slender Cone". In: *Journal of the Aerospace Sciences* 29.7 (1962), pp. 815–826.

[173] Luke Uribarri and Edward H Allen. "Electron transpiration cooling for hot aerospace surfaces". In: *20th AIAA International Space Planes and Hypersonic Systems and Technologies Conference* (July 6–9, 2015). AIAA 2015-3674. Glasgow, Scotland: American Institute of Aeronautics and Astronautics, 2015.

[174] Donald A Nield, Adrian Bejan, et al. *Convection in porous media*. Vol. 3. Springer, 2006.

[175] Hassan Saad Ifti, Tobias Hermann, and Matthew McGilvray. "Flow characterisation of transpiring porous media for hypersonic vehicles". In: *22nd AIAA international space planes and hypersonics systems and technologies conference* (Sept. 17–19, 2018). AIAA 2018-5167. Orlando, FL, 2018.

[176] Hannah Boehrk. "Transpiration cooling at hypersonic flight-AKTiV on SHEFEX II". In: *11th AIAA/ASME Joint Thermophysics and Heat Transfer Conference* (June 16–20, 2014). AIAA 2014-2676. Atlanta, GA, 2014.

[177] Hannah Böhrk and Ulrich Beyermann. "Secure tightening of a CMC fastener for the heat shield of re-entry vehicles". In: *Composite Structures* 92.1 (2010), pp. 107–112.

[178] MP Bacos. "Carbon-carbon composites: oxidation behavior and coatings protection". In: *Le Journal de Physique IV* 3.C7 (1993), pp. C7–1895.

[179] H Ifti, Tobias Hermann, and Matthew McGilvray. "Transpiration cooling at Mach 5 employing porous UHTC". In: *Conference on Flight vehicles, Aerothermodynamics and Re-entry Missions and Engineering (FAR)*. European Space Agency. Monopoli, Italy.

[180] Bryan Eric Schmidt. "On the stability of supersonic boundary layers with injection". PhD thesis. California Institute of Technology, 2016.

[181] James C Dunavant and Philip E Everhart. *Explorator heat-transfer measurements at Mach 10 on a 7.5 deg total-angle cone downstream of a region of air and helium transpiration cooling*. Tech. rep. NASA Technical Rept. TN-D-5554. 1969.

[182] Ivett Leyva, Joe Jewell, Stuart Laurence, Hans Hornung, and Joseph Shepherd. "On the impact of injection schemes on transition in hypersonic boundary layers". In: *16th AIAA/DLR/DGLR International Space Planes and Hypersonic Systems and Technologies Conference*. AIAA 2009-7204. 2009.

[183] Kevin Basore, Markus Selzer, Vincent Wheatley, Russell Boyce, David Mee, Bianca Capra, Markus Kuhn, and Stefan Brieschenk. "Performance comparison of distributed injection methods for hypersonic film-cooling". In: *Proceedings of the 20th Australasian Fluid Mechanics Conference (AFMC)*. Paper 487. Australasian Fluid Mechanics Society. Perth, WA, 2016.

[184] Christian Dittert, Markus Selzer, and Hannah Böhrk. "Flowfield and pressure decay analysis of porous cones". In: *AIAA Journal* 55.3 (2017), pp. 874–882.

[185] Christian Dittert, Markus Selzer, and Hannah Boehrk. "Characterization of the flow field of anisotropic porous cones with different wall thickness". In: *20th AIAA International Space Planes and Hypersonic Systems and Technologies Conference* (July 6–9, 2015). Glasgow, Scotland, 2015, AIAA 2015–3661.

[186] DR Moore, CJ Stalmach, TC Pope, and JE Jenkins. "Dynamic stability wind-tunnel tests of a 10 deg cone with simulated ablation at m equals 17." In: *AIAA Journal* 5.8 (1967), pp. 1377–1385.

[187] Joseph G Marvin and Clifford M Akin. "Combined effects of mass addition and nose bluntness on boundary-layer transition". In: *AIAA Journal* 8.5 (1970), pp. 857–863.

[188] V DiCristina. "Three-dimensional laminar boundary-layer transition on a sharp 8 degcone at Mach 10". In: *AIAA Journal* 8.5 (1970), pp. 852–856.

[189] George G Mateer and Howard K Larson. "Unusual boundary-layer transition results on cones in hypersonic flow." In: *AIAA Journal* 7.4 (1969), pp. 660–664.

[190] C J Stalmach Jr, J J Bertin, T C Pope, and M H McCloskey. *A study of boundary layer transition on outgassing cones in hypersonic flow*. Tech. rep. NASA-CR-1908, 1971.

[191] AL Laganelli and A Martellucci. "Downstream effects of gaseous injection through a porous nose". In: *10 th AIAA Aerospace Sciences Meeting* (Jan. 17–19, 1972). AIAA Paper No. 72-185. San Diego, CA, 1972.

[192] A L Laganelli, R P Fogaroli, and A Martellucci. *The effects of mass transfer and angle of attack on hypersonic turbulent boundary layer characteristics*. Tech. rep. TR-75-35. Air Force Flight Dynamics Lab, 1975.

[193] A Boudreau. "Transition measurements via heat-transfer instrumentation on a 0.5 bluntness 9.75-deg cone at Mach 7 with and without mass addition". In: *AIAA 20th Thermophysics Conference*. AIAA-85-1004. Williamsburg, Virginia, 1985.

[194] James C Dunavant and James C Mulligan. "Downstream cooling effectiveness of massive upstream transpiration from a slender cone." In: *AIAA Journal* 7.9 (1969), pp. 1796–1797.

[195] Anthony Martellucci. “Effects of mass transfer on hypersonic turbulent boundary-layer properties.” In: *AIAA Journal* 10.2 (1972), pp. 181–187.

[196] Marc Ewenz Rocher. “Application of transpiration cooling on hypersonic vehicles to mitigate material oxidation”. PhD thesis. University of Oxford, 2021.

[197] DR Kassoy. “On laminar boundary-layer blow-off. Part 2”. In: *Journal of Fluid Mechanics* 48.2 (1971), pp. 209–228.

[198] Robert J Moffat and William M Kays. “The turbulent boundary layer on a porous plate: experimental heat transfer with uniform blowing and suction”. In: *International Journal of Heat and Mass Transfer* 11.10 (1968), pp. 1547–1566.

[199] D. P. Georgiou and J. F. Louis. “The Transpired Turbulent Boundary Layer in Various Pressure Gradients and the Blow-Off Condition”. In: *Journal of Engineering for Gas Turbines and Power* 107.3 (July 1985), pp. 636–641. eprint: https://asmedigitalcollection.asme.org/gasturbinespower/article-pdf/107/3/636/5752369/636_1.pdf. URL: https://doi.org/10.1115/1.3239783.

[200] Kenneth K Yoshikawa. *Linearized theory of stagnation point heat and mass transfer at hypersonic speeds*. Tech. rep. NASA-TN-D-5246. 1969.

[201] Michael Holden. “An experimental study of massive blowing from a nosetip during Jovian entry”. In: *AIAA 16th Thermophysics Conference* (June 23–25, 1981). AIAA-981-1070. Palo Alto, CA, 1981.

[202] Dimitri Papamoschou. “Mach wave elimination in supersonic jets”. In: *AIAA Journal* 35.10 (1997), pp. 1604–1611.

[203] Ivett Leyva, Stuart Laurence, Amy Beierholm, Hans Hornung, Ross Wagnild, and Graham Candler. “Transition delay in hypervelocity boundary layers by means of CO2/acoustic instability interactions”. In: *47th AIAA Aerospace Sciences Meeting Including the New Horizons Forum and Aerospace Exposition* (Jan. 5–8, 2009). AIAA 2009-1287. Orlando, Florida, 2009.

[204] Keisuke Fujii and Hans G Hornung. “Experimental investigation of high-enthalpy effects on attachment-line boundary-layer transition”. In: *AIAA Journal* 41.7 (2003), pp. 1282–1291.

[205] Heath B Johnson, Trevor G Seipp, and Graham V Candler. “Numerical study of hypersonic reacting boundary layer transition on cones”. In: *Physics of Fluids* 10.10 (1998), pp. 2676–2685.

[206] Philippe H Adam and Hans G Hornung. “Enthalpy effects on hypervelocity boundary-layer transition: ground test and flight data”. In: *Journal of Spacecraft and Rockets* 34.5 (1997), pp. 614–619.

[207] Keisuke Fujii and Hans Hornung. “An experiment of high enthalpy effect on attachment line transition”. In: *15th AIAA Computational Fluid Dynamics Conference* (June 11–14, 2001). AIAA 2001-2779. Anaheim, California, 2001.

[208] Joseph Jewell, Ross Wagnild, Ivett Leyva, Graham Candler, and Joseph Shepherd. “Transition within a hypervelocity boundary layer on a 5-degree half-angle cone in air/CO2 mixtures”. In: *51st AIAA Aerospace Sciences Meeting Including the New Horizons Forum and Aerospace Exposition*. AIAA Paper 2013-0523. Grapevine (Dallas/Ft. Worth Region), Texas, 2013.

[209] Ross Wagnild, Graham Candler, Ivett Leyva, Joseph Jewell, and Hans Hornung. "Carbon dioxide injection for hypervelocity boundary layer stability". In: *48th AIAA Aerospace Sciences Meeting Including the New Horizons Forum and Aerospace Exposition* (Jan. 4–7, 2010). AIAA 2010-1244. Orlando, Florida, 2010.

[210] JS Jewell, IA Leyva, Nicholaus J Parziale, and Joseph E Shepherd. "Effect of gas injection on transition in hypervelocity boundary layers". In: *Proceedings of the 28th International Symposium on Shock Waves*. Springer. Manchester, UK, 2012, pp. 735–740.

[211] Viola Wartemann, Giannino Ponchio Camillo, Philipp Reiter, Jens Neumann, and Alexander Wagner. "Influence of transpiration cooling on second-mode instabilities investigated on hypersonic, conical flows". In: *CEAS Space Journal* 11.3 (2019), pp. 341–350.

[212] Alexander V Fedorov, Vitaly Soudakov, and Ivett A Leyva. "Stability analysis of high-speed boundary-layer flow with gas injection". In: *7th AIAA Theoretical Fluid Mechanics Conference*. AIAA 2014-2498. Atlanta, GA, 2014.

[213] Bryan E Schmidt, Neal Bitter, Hans Hornung, and Joseph Shepherd. "Experimental investigation of gas injection into the boundary layer on a slender body in supersonic flow". In: *7th AIAA Theoretical Fluid Mechanics Conference*. Atlanta, GA, 2014, AIAA 2014–2496.

[214] BE Schmidt, NP Bitter, HG Hornung, and JE Shepherd. "Injection into supersonic boundary layers". In: *AIAA Journal* 54.1 (2016), pp. 161–173.

[215] Bryan E Schmidt and Joseph Shepherd. "Measurements of instability in supersonic flow with injection by time-resolved flow visualization". In: *54th AIAA Aerospace Sciences Meeting*. AIAA 2016-059. San Diego, California, USA, 2016.

[216] Fei Li, Meelan Choudhari, Chau-Lyan Chang, and Jeffery White. "Boundary layer transition over blunt hypersonic vehicles including effects of ablation-induced out-gassing". In: *6th AIAA Theoretical Fluid Mechanics Conference* (June 27–30, 2011). AIAA 2011-3303. Honolulu, Hawai, 2011.

[217] Fei Li, Meelan Choudhari, Chau-Lyan Chang, and Jeffery White. "Effects of injection on the instability of boundary layers over hypersonic configurations". In: *Physics of Fluids* 25.10 (2013), p. 104107.

[218] Lianjin Zhao, Jianhua Wang, Jie Ma, Jia Lin, Jinlong Peng, Dejun Qu, and Lianzhong Chen. "An experimental investigation on transpiration cooling under supersonic condition using a nose cone model". In: *International Journal of Thermal sciences* 84 (2014), pp. 207–213.

[219] Nan Wu, Jianhua Wang, Fei He, Guangqi Dong, and Longsheng Tang. "An experimental investigation on transpiration cooling of a nose cone model with a gradient porosity layout". In: *Experimental Thermal and Fluid Science* 106 (2019), pp. 194–201.

[220] Yuan-Qing Liu, Pei-Xue Jiang, Shao-Shan Jin, and Ji-Guo Sun. "Transpiration cooling of a nose cone by various foreign gases". In: *International journal of heat and mass transfer* 53.23-24 (2010), pp. 5364–5372.

[221] VI Lysenko, SA Gaponov, BV Smorodsky, Yu G Yermolaev, and AD Kosinov. "Influence of distributed heavy-gas injection on stability and transition of supersonic boundary-layer flow". In: *Physics of Fluids* 31.10 (2019), p. 104103.

[222] Steven P Schneider. "Flight data for boundary-layer transition at hypersonic and supersonic speeds". In: *Journal of Spacecraft and Rockets* 36.1 (1999), pp. 8–20.

[223] H Julian Allen and Alfred J Eggers Jr. *A study of the motion and aerodynamic heating of missiles entering the earth's atmosphere at high supersonic speeds*. Tech. rep. NACA TN 4047. 1953.

[224] Sebastien Wylie and Matthew McGilvray. "HIFiRE-1 Post-Flight Experiments in the University of Oxford's High Density Tunnel". In: *AIAA Scitech 2019 Forum* (Jan. 7–11, 2019). AIAA 2019-1940. San Diego, California, 2019.

[225] Sebastien Wylie, Luke Doherty, and Matthew McGilvray. "Commissioning of the Oxford high density tunnel (HDT) for boundary layer instability measurements at Mach 7". In: *AIAA Aviation Forum 2018 Fluid Dynamics Conference*. AIAA 2018-3074. Atlanta, Georgia, 2018.

[226] Suria Devi Subiah. "Boundary Layer Instabilities in High and Low Enthalpy Hypersonic Facilities using High Speed Schlieren". PhD thesis. University of Oxford, 2022.

[227] Richard E Kennedy, Joseph S Jewell, Pedro Paredes, and Stuart J Laurence. "Characterization of instability mechanisms on sharp and blunt slender cones at Mach 6". In: *Journal of Fluid Mechanics* 936 (2022), A39.

[228] Gary S Settles. *Schlieren and shadowgraph techniques: visualizing phenomena in transparent media*. Springer Science & Business Media, 2001.

[229] Robert Hooke. *Micrographia: or some physiological descriptions of minute bodies made by magnifying glasses, with observations and inquiries thereupon*. Courier Corporation, 2003.

[230] J Rienitz. "Schlieren experiment 300 years ago". In: *Nature* 254.5498 (1975), pp. 293–295.

[231] Léon Foucault. "Mémoire sur la construction des télescopes en verre argenté". In: *Annales de l'observatoire de Paris*. Vol. 5. 1859, pp. 197–237.

[232] Léon Foucault et al. *Recueil des travaux scientifiques de Léon Foucault*. Vol. 1. Gauthier-villars, 1878.

[233] August Joseph Ignaz Toepler. *Beobachtungen nach einer neuen optischen Methode: Ein Beitrag Experimentalphysik*. 157. W. Engelmann, 1906.

[234] John Hall Gladstone and Thomas P Dale. "XIV. Researches on the refraction, dispersion, and sensitiveness of liquids". In: *Philosophical Transactions of the Royal Society of London* 153 (1863), pp. 317–343.

[235] Hubert Schardin. "Das toeplersche Schlierenverfahren: Grundlagen für seine Anwendung und quantitative Auswertung". In: *VDI Forschungsheft* 367.5 (1934), pp. 1–32.

[236] Hubert Schardin. "Die Schlierenverfahren und ihre Anwendungen". In: *Ergebnisse der exakten Naturwissenschaften* (1942), pp. 303–439.

[237] Haiyin Sun. *Basic optical engineering for engineers and scientists*. eng. SPIE monograph ; PM294. Bellingham, Washington: SPIE Press, 2018.

[238] SJ Laurence, Alexander Wagner, Klaus Hannemann, Viola Wartemann, Heinrich Lüdeke, Hideyuki Tanno, and Katsuhiro Itoh. "Time-resolved visualization of instability waves in a hypersonic boundary layer". In: *AIAA Journal* 50.1 (2012), pp. 243–246.

[239] Peter Collen, Luke J Doherty, Suria D Subiah, Tamara Sopek, Ingo Jahn, David Gildfind, Rowland Penty Geraets, Rowan Gollan, Christopher Hambidge, Richard Morgan, et al. "Development and commissioning of the T6 Stalker Tunnel". In: *Experiments in Fluids* 62.11 (2021), pp. 1–24.

[240] Arthur Kantrowitz and Robert L Trimpi. "A sharp-focusing schlieren system". In: *Journal of the Aeronautical Sciences* 17.5 (1950), pp. 311–314.

[241] Andrew Hyslop, Luke J Doherty, Matthew McGilvray, Andrew Neely, Liam P McQuellin, James Barth, and Gerrie Mullen. "Free-Flight Aerodynamic Testing of the Skylon Space Plane". In: *Journal of Spacecraft and Rockets* 58.5 (2021), pp. 1487–1497.

[242] Matthew McGilvray, Andrew J Neely, Christopher Hambidge, William Ivison, Tobias A Hermann, and Luke Doherty. "Fundamental Experiments of Fluidic Thrust Vectoring for a Hypersonic Vehicle". In: *AIAA Scitech 2019 Forum*. AIAA 2019-1680. San Diego, California, 2019.

[243] Matthew McGilvray, Luke J Doherty, Andrew J Neely, Robert Pearce, and Peter Ireland. "The oxford high density tunnel". In: *20th AIAA international space planes and hypersonic systems and technologies conference* (July 6–9, 2015). AIAA 2015-3548. Glasgow, Scotland, 2015.

[244] TV Jones, DL Schultz, and AD Hendley. *On the flow in an isentropic light piston tunnel*. Tech. rep. MoD (Proc Exec) Aeronautical Research Council R & M No 3731, 1973.

[245] Hubert Ludwieg. "Der Rohrwindkanal". In: *Zeitschrift für Flugwissenschaften* 3.7 (1955), pp. 206–216.

[246] Ferry FJ Schrijer and Willem J Bannink. "Description and flow assessment of the delft hypersonic Ludwieg tube". In: *Journal of Spacecraft and Rockets* 47.1 (2010), pp. 125–133.

[247] Malte Estorf, Torsten Wolf, and Rolf Radespiel. "Experimental and numerical investigations on the operation of the Hypersonic Ludwieg Tube Braunschweig". In: *Fifth European Symposium on Aerothermodynamics for Space Vehicles (ESA SP-563)* (Nov. 8–11, 2005). Ed. by D. Danesy. Cologne, Germany, 2005.

[248] TV Jones, P Street, and M Westby. "Recent enhancements to the DRA shock tunnel". In: *The European Forum on Wind Tunnels. Wind tunnels and wind tunnel test techniques* (Sept. 14–17, 1992). Southampton, 1992.

[249] Tobias Hermann, Matthew McGilvray, Chris Hambidge, Luke Doherty, and David Buttsworth. "Total temperature measurements in the oxford high density tunnel". In: *International conference on flight vehicles, aerothermodynamics and re-entry missions and engineering (FAR)*. European Space Agency. Monopoli, Italy, 2019.

[250] FG Keyes. "A summary of viscosity and heat-conduction data for He, A, H2, O2, N2, CO, CO2, H2O, and air". In: *Transactions of the American Society of Mechanical Engineers* 73.5 (1951), pp. 589–595.

[251] Frederick G Keyes. *The Heat Conductivity, Viscosity, Specific Heat and Prandtl Numbers for Thirteen Gases*. Tech. rep. No. 37. Massechusets Institute of Technology, Cambridge, 1952.

[252] Faith A Morrison. *Uncertainty Analysis for Engineers and Scientists: A Practical Guide*. Cambridge University Press, 2021.

[253] S Schneider, Craig Skoch, Shann Rufer, Shin Matsumura, and Erick Swanson. "Transition research in the Boeing/AFOSR Mach-6 quiet tunnel". In: *40th AIAA Aerospace Sciences Meeting & Exhibit* (Jan. 14–17, 2002). AIAA 2002-302. Reno, NV, U.S.A, 2002.

[254] Dan Marren and John Lafferty. "The AEDC hypervelocity wind tunnel 9". In: *Progress in Astronautics and Aeronautics* 198 (2002), pp. 467–478.

[255] Brian R Hollis and Salvatore Borrelli. "Aerothermodynamics of blunt body entry vehicles". In: *Progress in Aerospace Sciences* 48 (2012), pp. 42–56.

[256] Ross S Chaudhry, Graham V Candler, Kathryn A Gray, and Steven P Schneider. "Computations of Measured Pitot-Probe Spectra using Angled Freestream Disturbances and Comparisons to Experiments". In: *AIAA Scitech 2019 Forum* (Jan. 7–11, 2019). AIAA 2019-2149. San Diego, California, 2019.

[257] Omega Engineering Inc. *Mass Flow Controllers with 20+ Gas Select Functions*. Accessed: 02/05/2022. 2022. URL: https://www.omega.co.uk/pptst/FMA2600_FVL2600.html.

[258] Portec. *Metapore Porous Materials*. Accessed Online: 16/11/2022. 2022. URL: https://www.portec.ch/products/metapor-block-material.

[259] Michael A Kegerise and Shann J Rufer. "Unsteady heat-flux measurements of second-mode instability waves in a hypersonic flat-plate boundary layer". In: *Experiments in fluids* 57.8 (2016), pp. 1–15.

[260] Ryan Oddo, Jonathan L Hill, Mark F Reeder, Daniel Chin, Joshua Embrador, Jeffrey Komives, Matthew Tufts, Matthew Borg, and Joseph S Jewell. "Effect of surface cooling on second-mode dominated hypersonic boundary layer transition". In: *Experiments in Fluids* 62.7 (2021), p. 144.

[261] Philip Kerth, Sebastien Wylie, Raghul Ravichandran, and Matthew McGilvray. "Gas Injection into Second Mode Instability on a 7 degree Cone at Mach 7". In: *AIAA Aviation 2022 Forum* (June 27–July 1, 2022). AIAA 2022-3856. Chicago,IL and Virtual, 2022.

[262] Richard F. Ambrose and Scott Greene. *Four Challanges to Hypersonics*. Accessed: 02/05/2022. 2022. URL: https://www.lockheedmartin.com/en-us/capabilities/space/executive-blog-rick-ambrose-scott-greene-lmiq.html.

[263] Eli Reshotko. "Transition issues for atmospheric entry". In: *Journal of Spacecraft and Rockets* 45.2 (2008), pp. 161–164.

[264] Katya Casper, Steven Beresh, John Henfling, Russell Spillers, Brian Pruett, and Steven Schneider. "Hypersonic wind-tunnel measurements of boundary-layer pressure fluctuations". In: *39th AIAA Fluid Dynamics Conference* (June 22–25, 2009). AIAA 2009-4054. San Antonio, Texas.

[265] Geoffrey Ingram Taylor and J W Maccoll. “The air pressure on a cone moving at high speeds.—II”. In: *Proceedings of the Royal Society of London. Series A, Containing Papers of a Mathematical and Physical Character* 139 (838 1933), pp. 298–311.

[266] Takuto Ishimatsu and Etsuo Morishita. “Taylor-Maccoll Hypervelocity Analytical Solutions”. In: *Transactions of The Japan Society for Aeronautical and Space Sciences* 48 (May 2005), pp. 46–48.

[267] Ernst Rudolf Georg Eckert. *Survey of boundary layer heat transfer at high velocities and high temperatures*. Tech. rep. WADC TR 59-624. Wright Air Development Center (WADC), Air Research and Development Command, 1960.

[268] Thomas H Chilton and Allan Philip Colburn. “Mass transfer (absorption) coefficients prediction from data on heat transfer and fluid friction”. In: *Industrial and engineering chemistry* 26 (11 1934), pp. 1183–1187.

[269] William Sutherland. “LII. The viscosity of gases and molecular force”. In: *The London, Edinburgh, and Dublin Philosophical Magazine and Journal of Science* 36.223 (1893), pp. 507–531.

[270] W Mangler. “Zusammenhang zwischen ebenen und rotationssymmetrischen Grenzschichten in kompressiblen Flüssigkeiten”. In: *ZAMM-Journal of Applied Mathematics and Mechanics/Zeitschrift für Angewandte Mathematik und Mechanik* 28.4 (1948), pp. 97–103.

[271] L F Crabtree, R L Dommett, and J G Woodley. *Estimation of heat transfer to flat plates, cones and blunt bodies*. Tech. rep. R & M 3637. Ministry of Technology, Aeronautical Research Council, 1965.

[272] John A Nelder and Roger Mead. “A simplex method for function minimization”. In: *The computer journal* 7.4 (1965), pp. 308–313.

[273] Jeffrey C Lagarias, James A Reeds, Margaret H Wright, and Paul E Wright. “Convergence properties of the Nelder–Mead simplex method in low dimensions”. In: *SIAM Journal on optimization* 9.1 (1998), pp. 112–147.

[274] Peter Welch. “The use of fast Fourier transform for the estimation of power spectra: a method based on time averaging over short, modified periodograms”. In: *IEEE Transactions on audio and electroacoustics* 15 (2 1967), pp. 70–73.

[275] Petre Stoica, Randolph L Moses, et al. *Spectral analysis of signals*. Vol. 452. Pearson Prentice Hall Upper Saddle River, NJ, 2005.

[276] Julius Von Hann. *Handbook of climatology*. MacMillan, 1903.

[277] Alan V Oppenheim. *Discrete-time signal processing*. Pearson Education India, 1999.

[278] Andrew Morris. “Charaterisation of a novel field asymmetric ion mobility spectrometer and its evaluation for non-traditional applications”. PhD thesis. The Open University, 2011.

[279] Robert R Lindner, Carlos Vera-Ciro, Claire E Murray, Snežana Stanimirović, Brian Babler, Carl Heiles, Patrick Hennebelle, WM Goss, and John Dickey. “Autonomous gaussian decomposition”. In: *The Astronomical Journal* 149.4 (2015), p. 138.

[280] Keaton Bell. *Fitting features in a power spectrum with least squares and MLE.* Accessed: 2022-05-01. 2018. URL: http://keatonb.github.io/archivers/powerspectrumfits.

[281] Eric Jones, Travis Oliphant, Pearu Peterson, et al. *SciPy: Open source scientific tools for Python.* 2001. URL: http://www.scipy.org/.

[282] Roland Span. "D2. 2 Properties of Dry Air". In: *VDI-GVC, Ed. VDI Heat Atlas. 2nd Ed.* Springer Berlin Heidelberg, 2010, pp. 172–191.

[283] Agustín Trujillo-Pino, Karl Krissian, Miguel Alemán-Flores, and Daniel Santana-Cedrés. "Accurate subpixel edge location based on partial area effect". In: *Image and Vision Computing* 31 (1 2013), pp. 72–90. URL: https://www.sciencedirect.com/science/article/pii/S0262885612001850.

[284] Agustin Trujillo-Pino. *Accurate subpixel edge location.* Matlab Central File Exchange. Retrieved November 11, 2022. 2022. URL: https://www.mathworks.com/matlabcentral/fileexchange/48908-accurate-subpixel-edge-location.

[285] Hassan Saad Ifti, Tobias Hermann, and Matthew McGilvray. "Analytical Model of Wall Coolant Concentration Downstream of a Transpiring Injector in a Laminar Flow". In: *AIAA Journal* (2023). in press.

[286] Kenneth F Stetson. *Hypersonic boundary layer transition experiments.* Tech. rep. AFWAL-TR-80-3062. Air Force Wright Aeronautical Labs Wright-Patterson Air Force Base OH, 1980.

[287] Richard Thompson, Harris Hamilton II, Scott Berry, Thomas Horvath, and Robert Nowak. "Hypersonic boundary layer transition for X-33 phase II vehicle". In: *36th AIAA Aerospace Sciences Meeting and Exhibit.* AIAA Paper 98-0867. 1998.

[288] Alexander V Fedorov and Andrew P Khokhlov. "Prehistory of instability in a hypersonic boundary layer". In: *Theoretical and Computational Fluid Dynamics* 14.6 (2001), pp. 359–375.

[289] James M Kendall. "Wind tunnel experiments relating to supersonic and hypersonic boundary-layer transition". In: *AIAA Journal* 13.3 (1975), pp. 290–299.

[290] Leslie M Mack. "Linear stability theory and the problem of supersonic boundary-layer transition". In: *AIAA Journal* 13.3 (1975), pp. 278–289.

[291] Arthur F Okuno and CC Pappas. *Heat-transfer measurement for binary gas laminar boundary layers with high rates of injection.* Tech. rep. NASA TN-D-2473. 1964.

[292] Joseph G Marvin and Ronald B Pope. "Laminar convective heating and ablation in the Mars atmosphere." In: *AIAA Journal* 5.2 (1967), pp. 240–248.

[293] PCB Piezotronics Inc. *Micro ICP pressure sensor 140 mV/psi, pigtail conn. (for high frequency Installation and Operating Manual).* Accessed Online: 24/11/2022. URL: http://pcbpiezotronics.co.uk/contentstore/docs/PCB_Corporate/Pressure/Products/Manuals/132A31.pdf.

[294] Sofia C Olhede and Andrew T Walden. "Generalized morse wavelets". In: *IEEE Transactions on Signal Processing* 50.11 (2002), pp. 2661–2670.

[295] Jonathan M Lilly and Sofia C Olhede. "On the analytic wavelet transform". In: *IEEE transactions on information theory* 56.8 (2010), pp. 4135–4156.

[296] Jonathan M Lilly and Sofia C Olhede. "Generalized Morse wavelets as a superfamily of analytic wavelets". In: *IEEE Transactions on Signal Processing* 60.11 (2012), pp. 6036–6041.

[297] Kulite Semiconductor Products Inc. *Section 2 - Kulite Sensing Technology*. Accessed Online: 24/11/2022. URL: https://kulite.com//assets/media/2018/01/section2.pdf.

[298] Matthew Collins, Kam Chana, and Thomas Povey. "New technique for the fabrication of miniature thin film heat flux gauges". In: *Measurement science and technology* 26.2 (2015), p. 025303.

[299] M Hayne. *The Manufacture and Mounting of Thin Film Gauges for Heat Transfer*. SID-61-275. St. Lucia, Australia: Univ. of Queensland, Dept. of Mechanical Engineering, 2003.

[300] M. L. G. Oldfield. "Impulse Response Processing of Transient Heat Transfer Gauge Signals". In: *Journal of Turbomachinery* 130.2 (Mar. 2008). 021023. eprint: https://asmedigitalcollection.asme.org/turbomachinery/article-pdf/130/2/021023/5680943/021023_1.pdf. URL: https://doi.org/10.1115/1.2752188.

[301] *Quartz – Density – Heat Capacity – Thermal Conductivity*. Accessed Online: 24/11/2022. URL: https://material-properties.org/quartz-density-heat-capacity-thermal-conductivity/.

[302] Inc. Goodfellows. *MACOR Machinable Glass Ceramic - Bar*. Accessed Online: 24/11/2022. URL: https://www.goodfellow.com/uk/en-gb/displayitemdetails/p/ma80-br-000110/macor-machinable-glass-ceramic-bar.

[303] Donald Lorimer Schultz and TV Jones. *Heat-transfer measurements in short-duration hypersonic facilities*. Tech. rep. AGARDograph No. 165, 1973.

[304] Charles G Miller III. *Comparison of thin-film resistance heat-transfer gages with thin-skin transient calorimeter gages in conventional hypersonic wind tunnels*. Tech. rep. NASA TR 83197. 1981.

[305] Luminus Devices Inc. *PT-120-TE Product Datasheet*. Accessed Online: 04/01/2023. 2019. URL: https://www.mouser.co.uk/datasheet/2/245Luminus_PT-120_Datasheet-1511584.pdf.

[306] MathWorks. *pwelch - Welch's power spectral density estimat*. Accessed Online: 04/01/2023. 2022. URL: https://uk.mathworks.com/help/signal/ref/pwelch.html.

[307] Tooling LLC. *Metapor BF100 Al - Air permeable material*. Accessed Online: 10/11/2022. URL: https://toolingtechgroup.com/wp-content/uploads/2018/12/1-metapor-BF100-Data-Sheet.pdf.

[308] Andrew Pilkington. private communication. 2022.

[309] FK Owen and CC Horstman. "Hypersonic transitional boundary layers". In: *AIAA Journal* 10.6 (1972), pp. 769–775.

[310] Dylan J Wise and Michael K Smart. "Roughness-induced transition of hypervelocity boundary layers". In: *Journal of Spacecraft and Rockets* 51.3 (2014), pp. 847–854.

[311] Kenneth Stetson, Roger Kimmel, Joseph Donaldson, and Leo Siler. "A comparison of planar and conical boundary layer stability and transition at a Mach number of 8". In: *AIAA 22nd Fluid Dynamics, Plasma Dynamics and Lasers Conference* (June 24–26, 1991). AIAA Paper 1991-1639. Honolulu, Hawaii, 1991.

[312] Kenneth F Stetson and Roger L Kimmel. "Example of second-mode instability dominance at a Mach number of 5.2". In: *AIAA Journal* 30.12 (1992), pp. 2974–2976.

[313] John E LaGraff. "Observations of hypersonic boundary-layer transition using hot wire anemometry". In: *AIAA Journal* 10.6 (1972), pp. 762–769.

[314] Samuel R Pate. *Dominance of Radiated Aerodynamic Noise on Boundary-Layer Transition in Supersonic-Hypersonic Wind Tunnels. Theory and Application.* Tech. rep. AEDC-TR-77-107. Arnold Engineering Development Center, Arnold Air Force Station, Tennessee, 1978.

[315] Ernst Rudolf Georg Eckert and John NB Livingood. *Comparison of effectiveness of convection-, transpiration-, and film-cooling methods with air as coolant.* Tech. rep. NACA-TN-3010. Lewis Flight Propulsion Laboratory, Cleveland, Ohio, 1954.

[316] Matthew R Fulghum. "Turbulence measurements in high-speed wind tunnels using focusing laser differential interferometry". PhD thesis. The Pennsylvania State University, 2014.

[317] G Smeets. "Laser interferometer for high sensitivity measurements on transient phase objects". In: *IEEE transactions on Aerospace and Electronic Systems* 2 (1972), pp. 186–190.

[318] Bryan E Schmidt and JE Shepherd. "Analysis of focused laser differential interferometry". In: *Applied optics* 54.28 (2015), pp. 8459–8472.

[319] Andrew Ceruzzi. "Development of two-point focused laser differential interferometry for applications in high-speed wind tunnels". PhD thesis. University of Maryland, 2022.

[320] Andrew P Ceruzzi and Christopher P Cadou. "Interpreting single-point and two-point focused laser differential interferometry in a turbulent jet". In: *Experiments in Fluids* 63.7 (2022), pp. 1–25.

[321] MathWorks. *checkerboard - Create checkerboard image.* Accessed Online: 04/01/2023. 2022. URL: `https://uk.mathworks.com/help/images/ref/checkerboard.html`.

[322] Elizabeth K Benitez, Matthew P Borg, J Luke Hill, Matthew T Aultman, Lian Duan, Carson L Running, and Joseph S Jewell. "Quantitative focused laser differential interferometry with hypersonic turbulent boundary layers". In: *Applied Optics* 61.31 (2022), pp. 9203–9216.

[323] Elizabeth K Benitez, Matthew P Borg, Colin Rhodes, and Joseph S Jewell. "Optical-axis spatial sensitivity of a simulated focused laser differential interferometer". In: *AIAA Journal* 61.5 (2023), pp. 1925–1938.

[324] Alexander Fedorov. “Transition and Stability of High-Speed Boundary Layers”. In: *Annual Review of Fluid Mechanics* 43 (1 2011), pp. 79–95. URL: https://doi.org/10.1146/annurev-fluid-122109-160750.

[325] Marc Ewenz Rocher, Tobias Hermann, Matthew McGilvray, Hassan Saad Ifti, Joao Vieira, Chris Hambidge, Mark Kenneth Quinn, Madeleine Grossman, and Luc Vandeperre. “Pressure-sensitive paint diagnostic to measure species concentration on transpiration-cooled walls”. In: *Experiments in Fluids* 63.1 (2022), pp. 1–11.

[326] M Ewenz Rocher, Tobias Hermann, Matthew McGilvray, HS Ifti, and Mark Quinn. “Studying the Film Effectiveness of Transpiration Cooled Walls Using Pressure Sensitive Paint”. In: *International Conference on Flight vehicles, Aerothermodynamics and Re-entry Missions and Engineering (FAR)* (Sept. 30–Oct. 3, 2019). European Space Agency. Monopoli, Italy, 2019.

[327] MathWorks. *findchangepts - Find abrupt changes in signals*. Accessed Online: 17/11/21. 2022. URL: https://uk.mathworks.com/help/signal/ref/findchangepts.html.

[328] Rebecca Killick, Paul Fearnhead, and Idris A Eckley. “Optimal detection of changepoints with a linear computational cost”. In: *Journal of the American Statistical Association* 107.500 (2012), pp. 1590–1598.

[329] Marc Lavielle. “Using penalized contrasts for the change-point problem”. In: *Signal processing* 85.8 (2005), pp. 1501–1510.

[330] Nathan Shumway and Stuart J Laurence. “Methods for identifying key features in schlieren images from hypersonic boundary-layer instability experiments”. In: *53rd AIAA Aerospace Sciences Meeting* (Jan. 5–9, 2015). AIAA 2015-1787. Kissimmee, Florida, 2015.

[331] ES Gadelmawla, Monir M Koura, Talal MA Maksoud, Ibrahiem M Elewa, and HH Soliman. “Roughness parameters”. In: *Journal of Materials Processing Technology* 123.1 (2002), pp. 133–145.

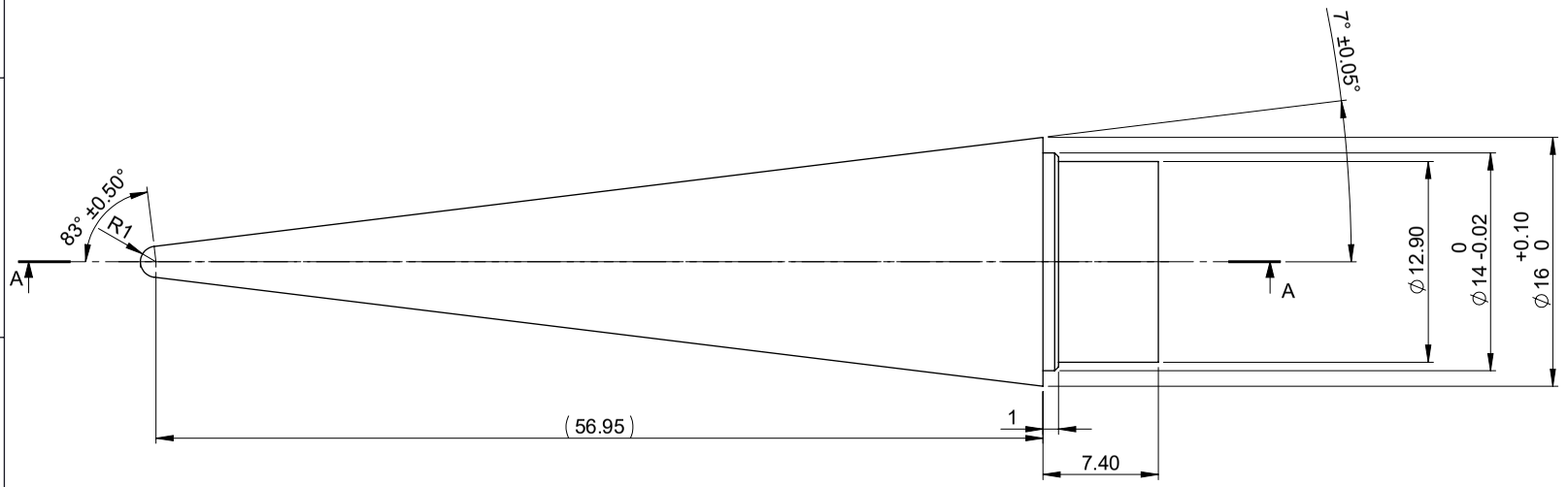
Appendices

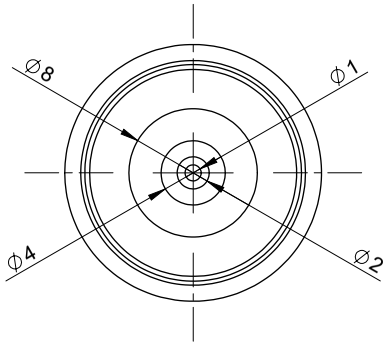
A
Appendix

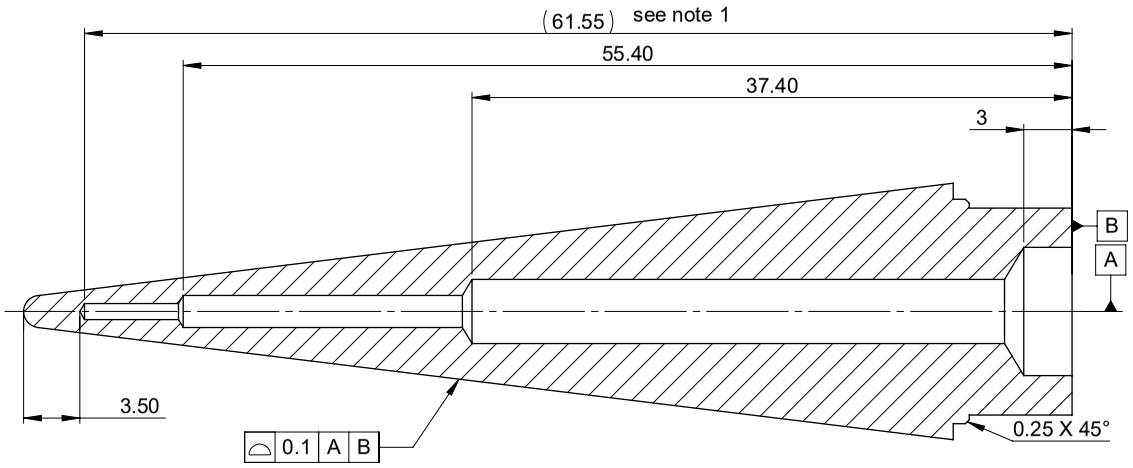
A.1 Technical Drawings for Cone Model

REV.	MODIFICATION	BY	DATE
0	NEW		

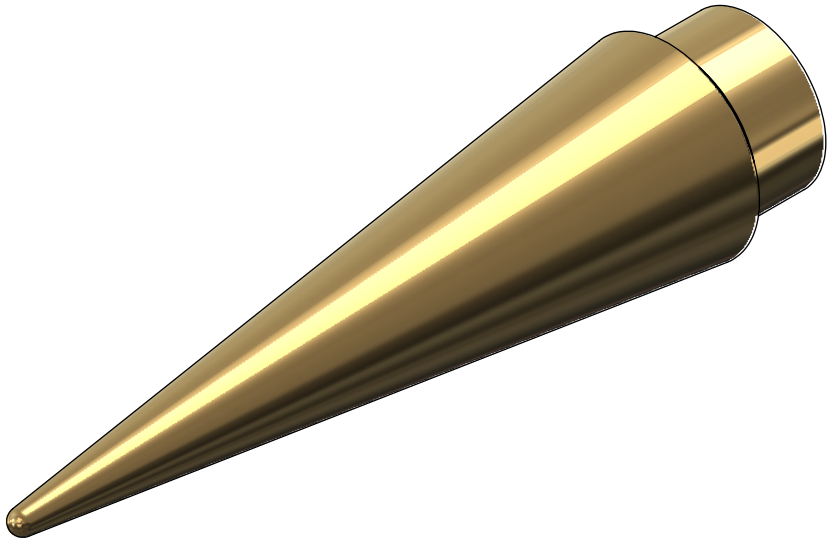
NOTES:
1) For standard drill head of 118°







SECTION A-A



This is a CAD produced drawing - no manual modifications are to be made.
This drawing is the property of the University of Oxford. It must not be copied, or the contents thereof or any information received in conjunction therewith be imparted to any third party. It must not be used for any other contract and the receipt of this drawing implies that these conditions as stated are accepted.

TOLERANCES UNLESS OTHERWISE STATED			
—	≤ 100 mm	= ± 0.1 mm	
> 100 mm	≤ 1000 mm	= ± 0.2 mm	
> 1000 mm	—	= ± 0.5 mm	
	Angular	= ± 1.0 °	

DESIGNED BY	HI	SCALE	3:1
DRAWN BY	HI	DATE	16/2/22
APPROVED BY	AP	DATE	14/3/22

MATERIAL: BF100Al or CE170

DO NOT SCALE - IF IN DOUBT ASK
DIMENSIONS IN mm
REMOVE ALL BURRS AND SHARP EDGES

Oxford Hypersonics
Oxford Thermofluids Insititute
Southwell Building
Osney Mead
Oxford OX2 0ES
Tel: 01865 288723

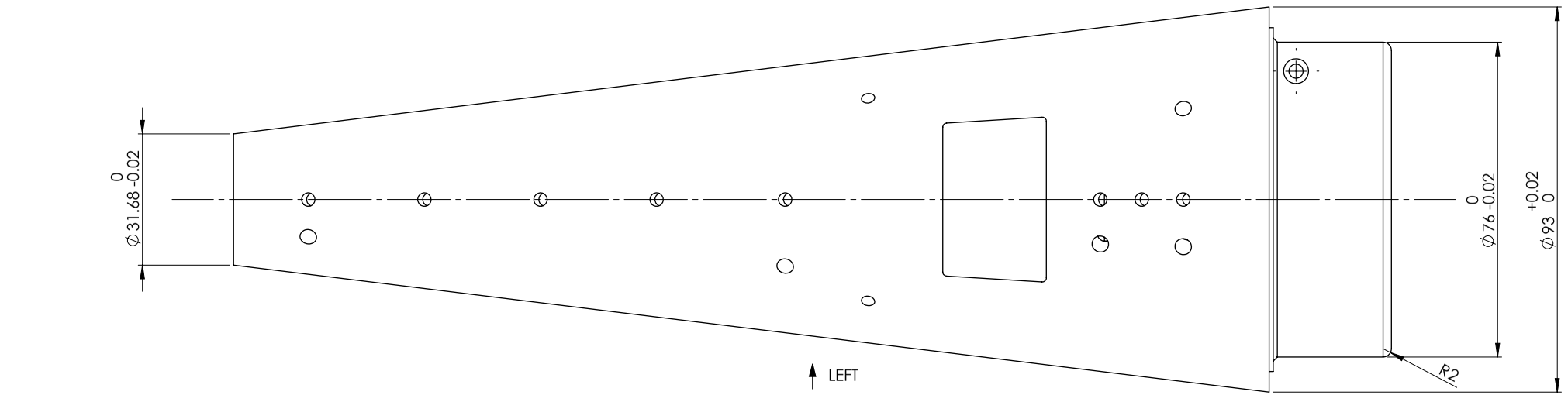
DESCRIPTION: Porous Injector Nose Tip R1

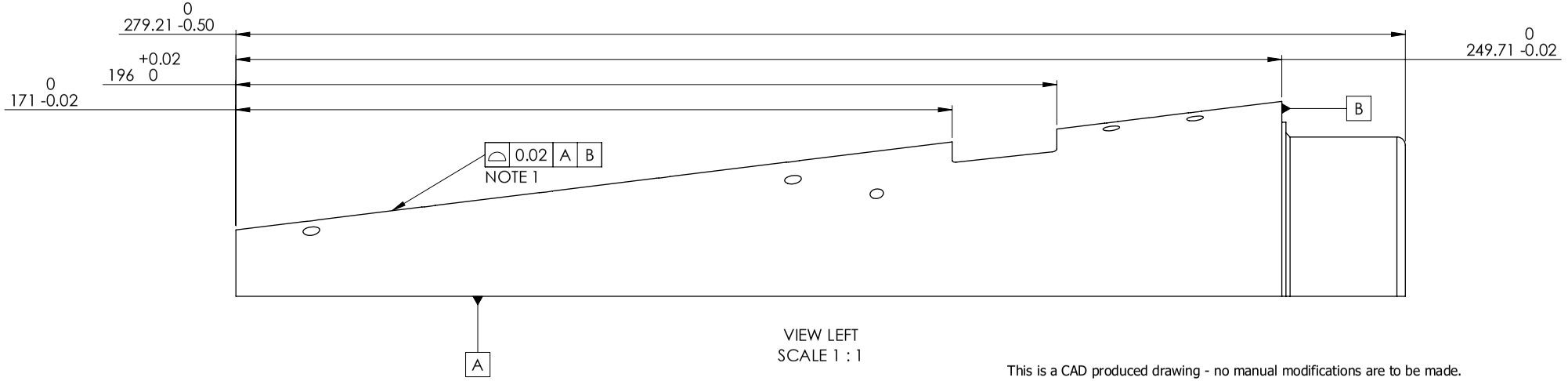
PART NUMBER	SHEET	ISSUE	
HYP-MACHC-001-03	1/1	0.1	A3

SOLIDWORKS Educational Product. For Instructional Use Only.

REV.	MODIFICATION	BY	DATE
0	NEW		
1	MATERIAL, SENSOR HOLES, FILLETS	PK	24/09/20

NOTES
1) FINAL SKIMMING OF SURFACES WITH WHOLE ASSEMBLY
2) FOR ASSEMBLY SEE ASSEMBLY DRAWING





VIEW LEFT
SCALE 1 : 1

This is a CAD produced drawing - no manual modifications are to be made.
This drawing is the property of the University of Oxford. It must not be copied, or the contents thereof or any information received in conjunction therewith be imparted to any third party. It must not be used for any other contract and the receipt of this drawing implies that these conditions as stated are accepted.

TOLERANCES UNLESS OTHERWISE STATED
— ≤ 100 mm = ± 0.1 mm
> 100 mm ≤ 1000 mm = ± 0.2 mm
> 1000 mm — = ± 0.5 mm
Angular = ± 1.0 °

DESIGNED BY	PK	SCALE	1:2
DRAWN BY	PK	DATE	21/08/20
APPROVED BY	TH	DATE	25/08/20

MATERIAL: Stainless Steel 303

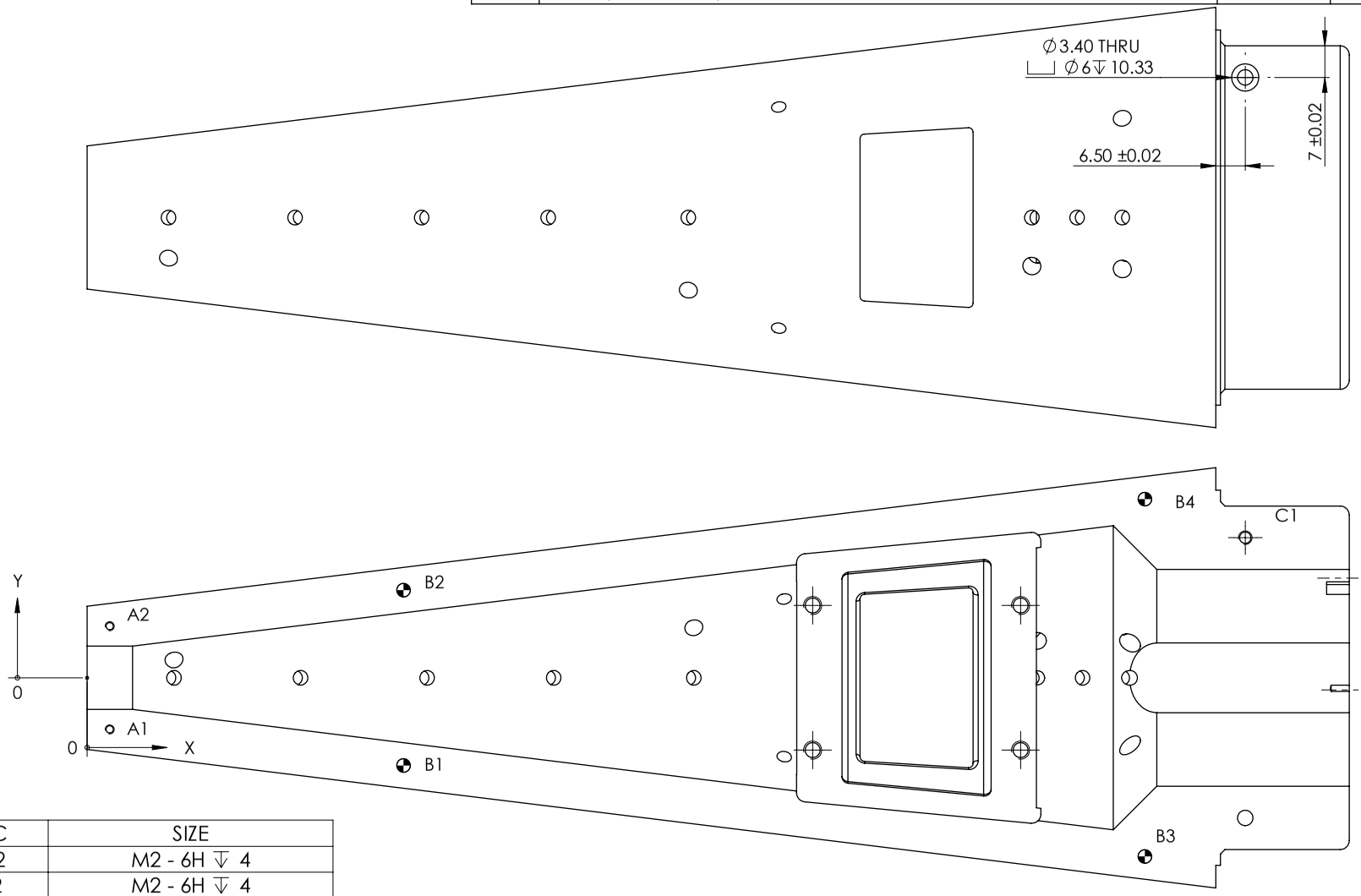
DO NOT SCALE - IF IN DOUBT ASK
DIMENSIONS IN mm
REMOVE ALL BURRS AND SHARP EDGES

Oxford Hypersonics
Oxford Thermofluids Insititute
Southwell Building
Osney Mead
Oxford OX2 0ES
Tel: 01865 288723

DESCRIPTION: SOUTH HALF OF MID SEGMENT

PART NUMBER	SHEET	ISSUE	
HYP-TCC-003-01	1/10	1.1	A3

REV.	MODIFICATION	BY	DATE
0	NEW		
1	MATERIAL, SENSOR HOLES, FILLETS	PK	24/09/20



TAG	X LOC	Y LOC	SIZE
A1	5	-11.42	M2 - 6H ↧ 4
A2	5	11.42	M2 - 6H ↧ 4
B1	70	-19.40	⌀ 3 H7 +0.01 0 ↧ 4
B2	70	19.40	⌀ 3 H7 +0.01 0 ↧ 4
B3	234	-39.53	⌀ 3 H7 +0.01 0 ↧ 4
B4	234	39.53	⌀ 3 H7 +0.01 0 ↧ 4
C1	256.21	31	⌀ 2.50 ↧ 5 M3 - 6H ↧ 6

This is a CAD produced drawing - no manual modifications are to be made.
This drawing is the property of the University of Oxford. It must not be copied, or the contents thereof or any information received in conjunction therewith be imparted to any third party. It must not be used for any other contract and the receipt of this drawing implies that these conditions as stated are accepted.

TOLERANCES UNLESS OTHERWISE STATED
— ≤ 100 mm = ± 0.1 mm
> 100 mm ≤ 1000 mm = ± 0.2 mm
> 1000 mm — = ± 0.5 mm
Angular = ± 1.0 °

DESIGNED BY	PK	SCALE	1:2
DRAWN BY	PK	DATE	21/08/20
APPROVED BY	TH	DATE	25/08/20

MATERIAL: Stainless Steel 303

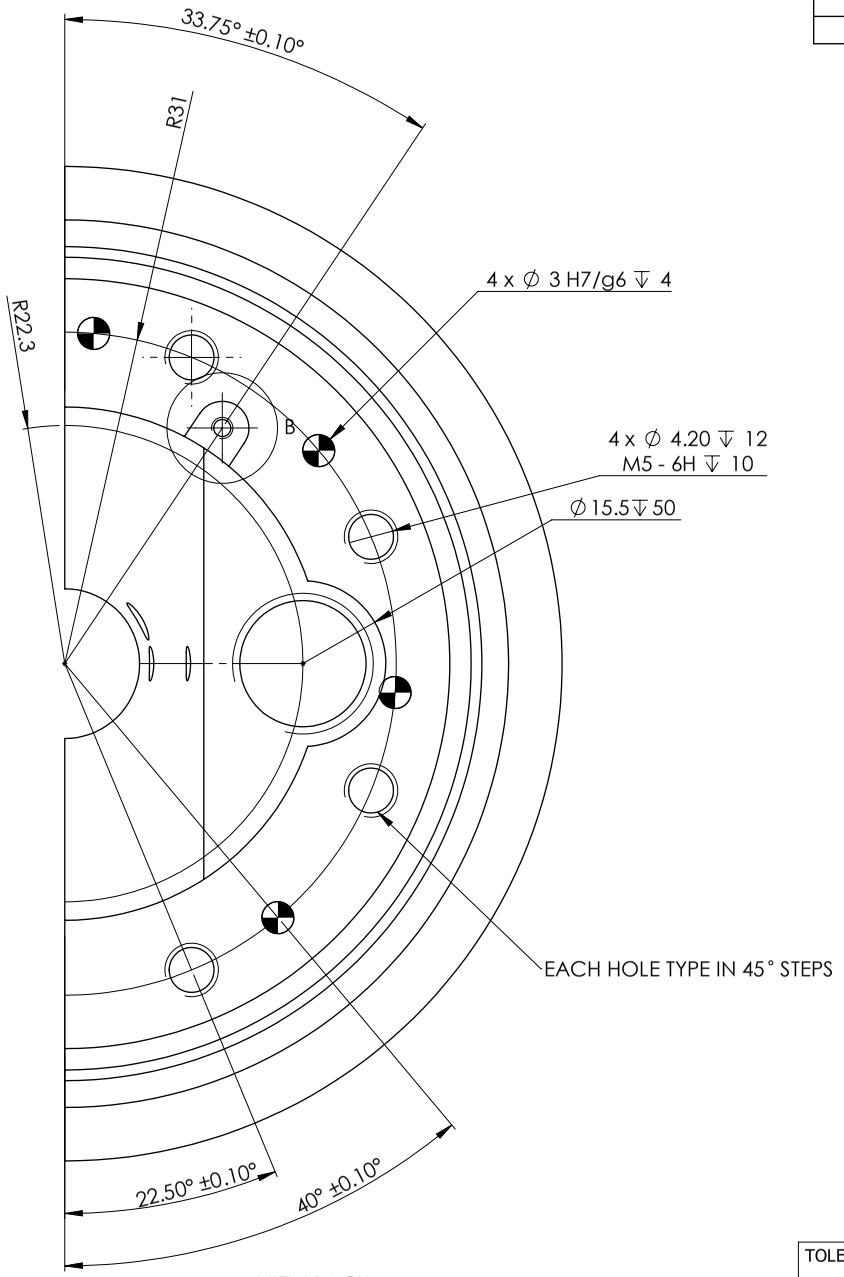
DO NOT SCALE - IF IN DOUBT ASK
DIMENSIONS IN mm
REMOVE ALL BURRS AND SHARP EDGES

Oxford Hypersonics
Oxford Thermofluids Insititute
Southwell Building
Osney Mead
Oxford OX2 0ES
Tel: 01865 288723

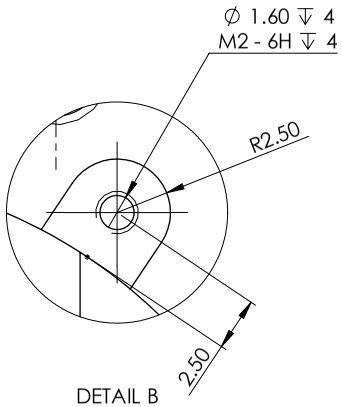
DESCRIPTION: SOUTH HALF OF MID SEGMENT

PART NUMBER	SHEET	ISSUE	
HYP-TCC-003-01	2/10	1.1	A3

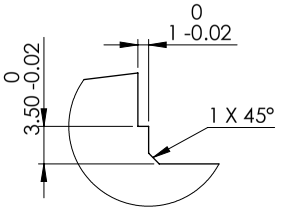
REV.	MODIFICATION	BY	DATE
0	NEW		
1	MATERIAL, SENSOR HOLES, FILLETS	PK	24/09/20



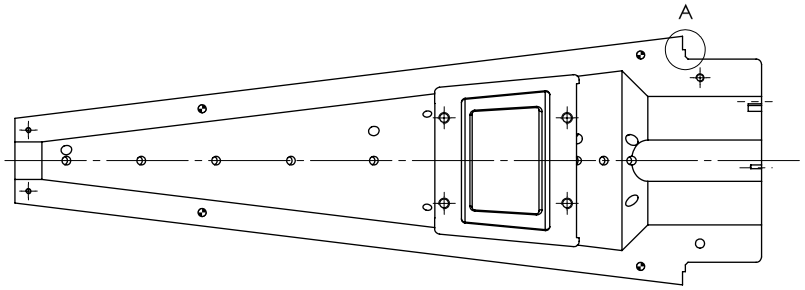
VIEW BACK
SCALE 2 : 1



DETAIL B
SCALE 4 : 1



DETAIL A
SCALE 2 : 1



This is a CAD produced drawing - no manual modifications are to be made.
This drawing is the property of the University of Oxford. It must not be copied, or the contents thereof or any information received in conjunction therewith be imparted to any third party. It must not be used for any other contract and the receipt of this drawing implies that these conditions as stated are accepted.

TOLERANCES UNLESS OTHERWISE STATED			
—	≤ 100 mm	= ± 0.1 mm	
> 100 mm	≤ 1000 mm	= ± 0.2 mm	
> 1000 mm	—	= ± 0.5 mm	
	Angular	= ± 1.0 °	
DESIGNED BY	PK	SCALE	1:2
DRAWN BY	PK	DATE	21/08/20
APPROVED BY	TH	DATE	25/08/20

MATERIAL: Stainless Steel 303

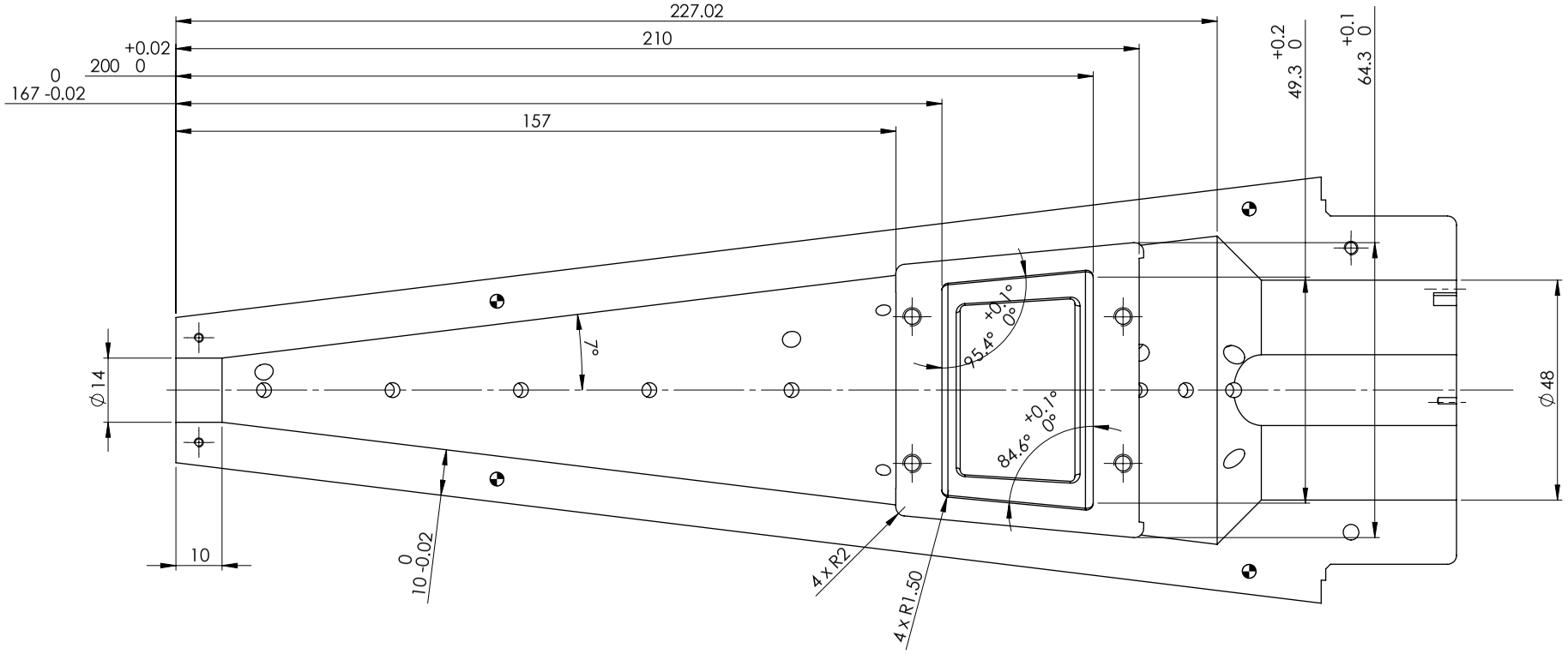
DO NOT SCALE - IF IN DOUBT ASK
DIMENSIONS IN mm
REMOVE ALL BURRS AND SHARP EDGES

Oxford Hypersonics
Oxford Thermofluids Insititute
Southwell Building
Osney Mead
Oxford OX2 0ES
Tel: 01865 288723

DESCRIPTION: SOUTH HALF OF MID SEGMENT

PART NUMBER	SHEET	ISSUE	
HYP-TCC-003-01	3/10	1.1	A3

REV.	MODIFICATION	BY	DATE
0	NEW		
1	MATERIAL, SENSOR HOLES, FILLETS	PK	24/09/20



This is a CAD produced drawing - no manual modifications are to be made.
This drawing is the property of the University of Oxford. It must not be copied, or the contents thereof or any information received in conjunction therewith be imparted to any third party. It must not be used for any other contract and the receipt of this drawing implies that these conditions as stated are accepted.

TOLERANCES UNLESS OTHERWISE STATED			
—	≤ 100 mm	= ± 0.1 mm	
> 100 mm	≤ 1000 mm	= ± 0.2 mm	
> 1000 mm	—	= ± 0.5 mm	
	Angular	= ± 1.0 °	
DESIGNED BY	PK	SCALE	1:2
DRAWN BY	PK	DATE	21/08/20
APPROVED BY	TH	DATE	25/08/20

MATERIAL: Stainless Steel 303

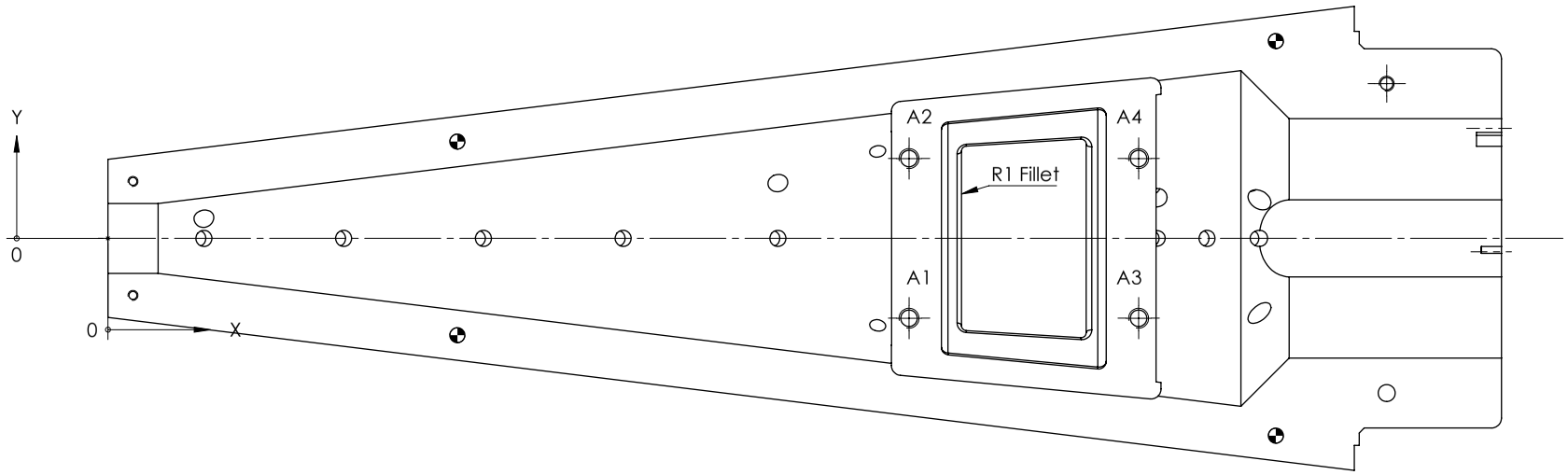
DO NOT SCALE - IF IN DOUBT ASK
DIMENSIONS IN mm
REMOVE ALL BURRS AND SHARP EDGES

Oxford Hypersonics
Oxford Thermofluids Insititute
Southwell Building
Osney Mead
Oxford OX2 0ES
Tel: 01865 288723

DESCRIPTION: SOUTH HALF OF MID SEGMENT

PART NUMBER	SHEET	ISSUE	
HYP-TCC-003-01	4/10	1.1	A3

REV.	MODIFICATION	BY	DATE
0	NEW		
1	MATERIAL, SENSOR HOLES, FILLETS	PK	24/09/20



TAG	X LOC	Y LOC	SIZE
A1	160.50	-16	M4 - 6H ↧ 10
A2	160.50	16	M4 - 6H ↧ 10
A3	206.50	-16	M4 - 6H ↧ 10
A4	206.50	16	M4 - 6H ↧ 10

This is a CAD produced drawing - no manual modifications are to be made.
This drawing is the property of the University of Oxford. It must not be copied, or the contents thereof or any information received in conjunction therewith be imparted to any third party. It must not be used for any other contract and the receipt of this drawing implies that these conditions as stated are accepted.

TOLERANCES UNLESS OTHERWISE STATED
— ≤ 100 mm = ± 0.1 mm
> 100 mm ≤ 1000 mm = ± 0.2 mm
> 1000 mm — = ± 0.5 mm
Angular = ± 1.0 °

DESIGNED BY	PK	SCALE	1:2
DRAWN BY	PK	DATE	21/08/20
APPROVED BY	TH	DATE	25/08/20

MATERIAL: Stainless Steel 303

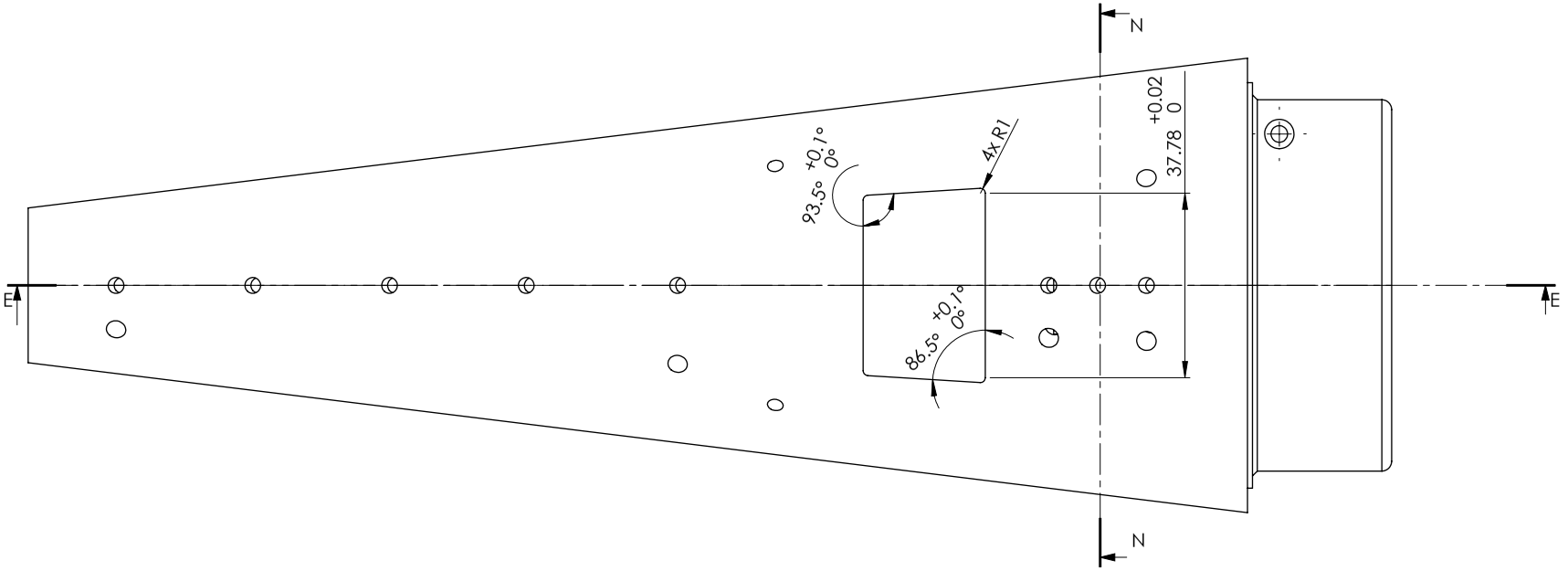
DO NOT SCALE - IF IN DOUBT ASK
DIMENSIONS IN mm
REMOVE ALL BURRS AND SHARP EDGES

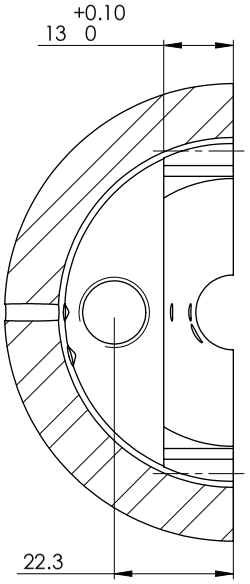
UNIVERSITY OF OXFORD
Oxford Hypersonics
Oxford Thermofluids Insititute
Southwell Building
Osney Mead
Oxford OX2 0ES
Tel: 01865 288723

DESCRIPTION: SOUTH HALF OF MID SEGMENT

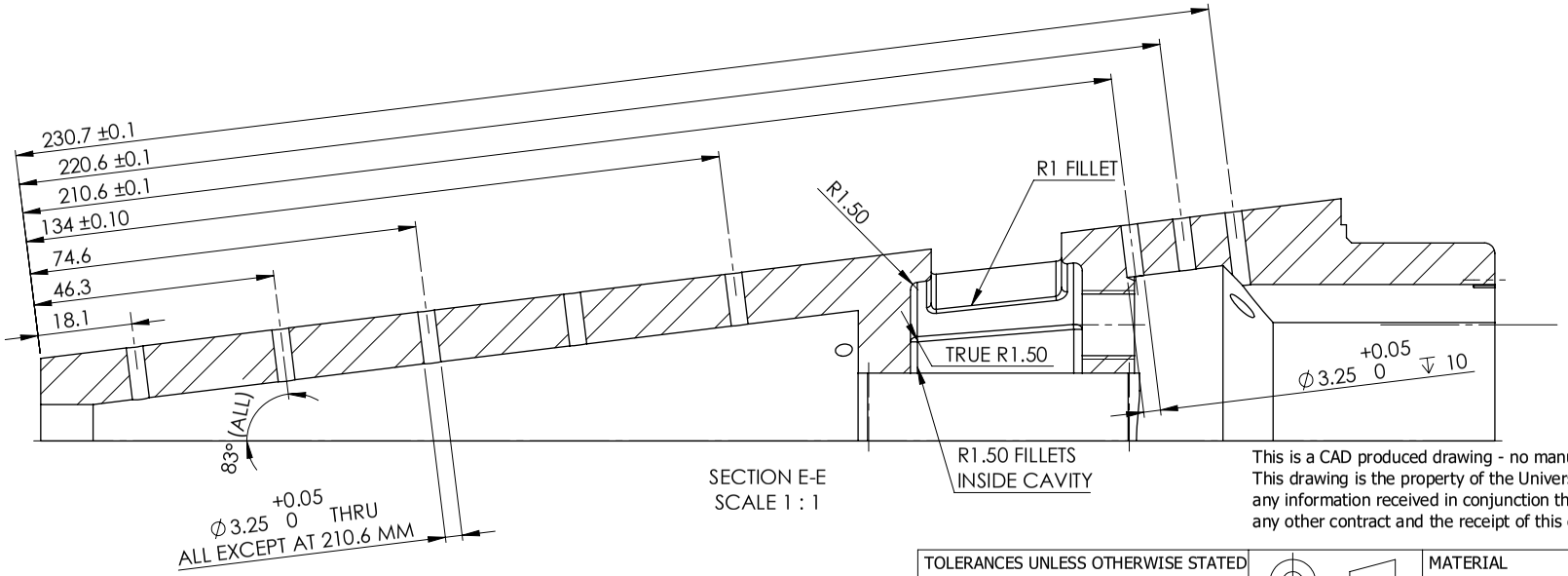
PART NUMBER	SHEET	ISSUE	
HYP-TCC-003-01	5/10	1.1	A3

REV.	MODIFICATION	BY	DATE
0	NEW		
1	MATERIAL, SENSOR HOLES, FILLETS	PK	24/09/20





SECTION N-N
SCALE 1 : 1



SECTION E-E
SCALE 1 : 1

This is a CAD produced drawing - no manual modifications are to be made.
This drawing is the property of the University of Oxford. It must not be copied, or the contents thereof or any information received in conjunction therewith be imparted to any third party. It must not be used for any other contract and the receipt of this drawing implies that these conditions as stated are accepted.

TOLERANCES UNLESS OTHERWISE STATED			
—	≤ 100 mm	= ± 0.1 mm	
> 100 mm	≤ 1000 mm	= ± 0.2 mm	
> 1000 mm	—	= ± 0.5 mm	
	Angular	= ± 1.0 °	

DESIGNED BY	PK	SCALE	1:2
DRAWN BY	PK	DATE	21/08/20
APPROVED BY	TH	DATE	25/08/20

MATERIAL: Stainless Steel 303

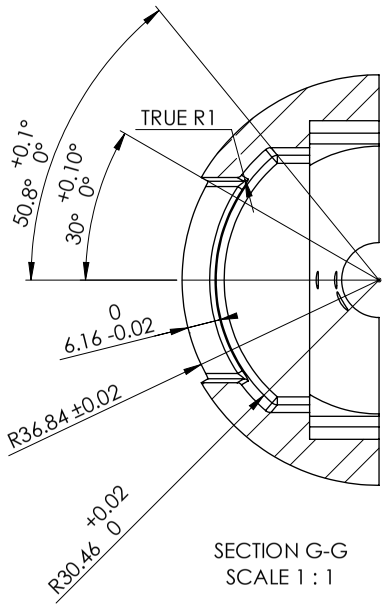
DO NOT SCALE - IF IN DOUBT ASK
DIMENSIONS IN mm
REMOVE ALL BURRS AND SHARP EDGES

Oxford Hypersonics
Oxford Thermofluids Insititute
Southwell Building
Osney Mead
Oxford OX2 0ES
Tel: 01865 288723

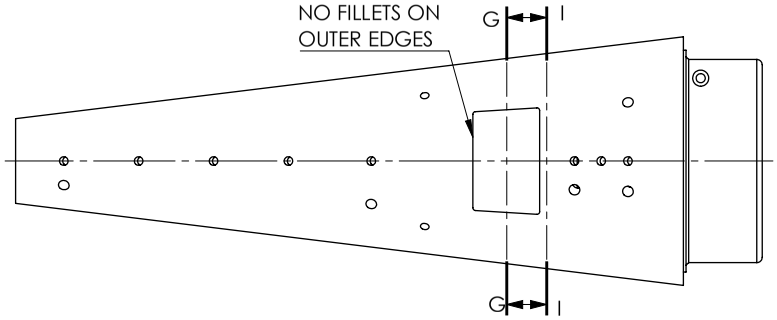
DESCRIPTION: SOUTH HALF OF MID SEGMENT

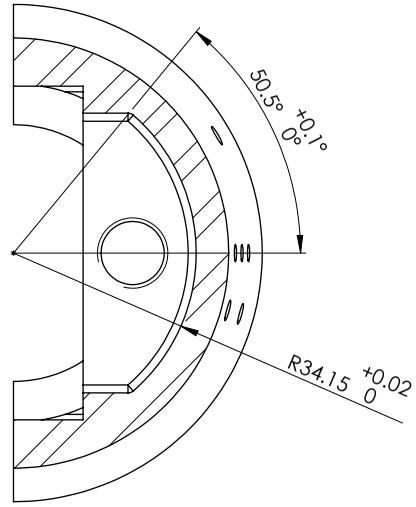
PART NUMBER	SHEET	ISSUE	
HYP-TCC-003-01	6/10	1.1	A3

REV.	MODIFICATION	BY	DATE
0	NEW		
1	MATERIAL, SENSOR HOLES, FILLETS	PK	24/09/20



SECTION G-G
SCALE 1 : 1





SECTION I-I
SCALE 1 : 1

This is a CAD produced drawing - no manual modifications are to be made.
This drawing is the property of the University of Oxford. It must not be copied, or the contents thereof or any information received in conjunction therewith be imparted to any third party. It must not be used for any other contract and the receipt of this drawing implies that these conditions as stated are accepted.

TOLERANCES UNLESS OTHERWISE STATED
— ≤ 100 mm = ± 0.1 mm
> 100 mm ≤ 1000 mm = ± 0.2 mm
> 1000 mm — = ± 0.5 mm
Angular = ± 1.0 °

DESIGNED BY	PK	SCALE	1:2
DRAWN BY	PK	DATE	21/08/20
APPROVED BY	TH	DATE	25/08/20

MATERIAL
Stainless Steel 303

DO NOT SCALE - IF IN DOUBT ASK
DIMENSIONS IN mm
REMOVE ALL BURRS AND SHARP EDGES

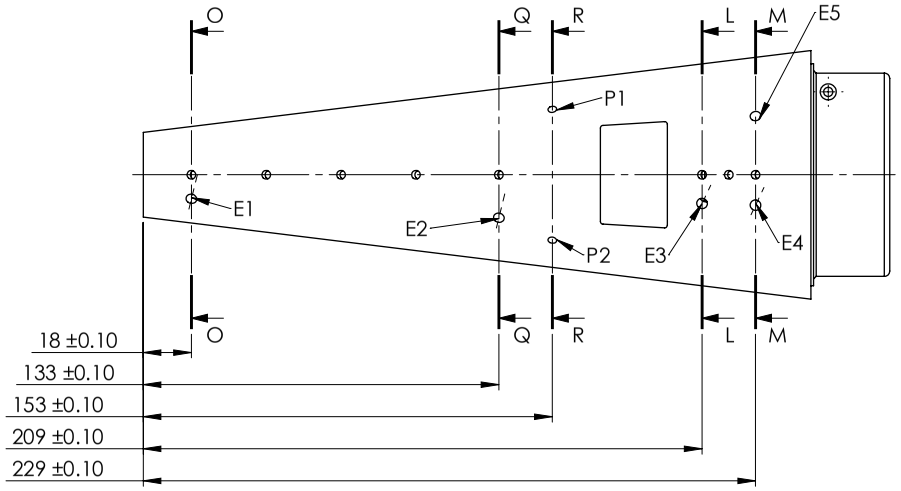
Oxford Hypersonics
Oxford Thermofluids Insititute
Southwell Building
Osney Mead
Oxford OX2 0ES
Tel: 01865 288723

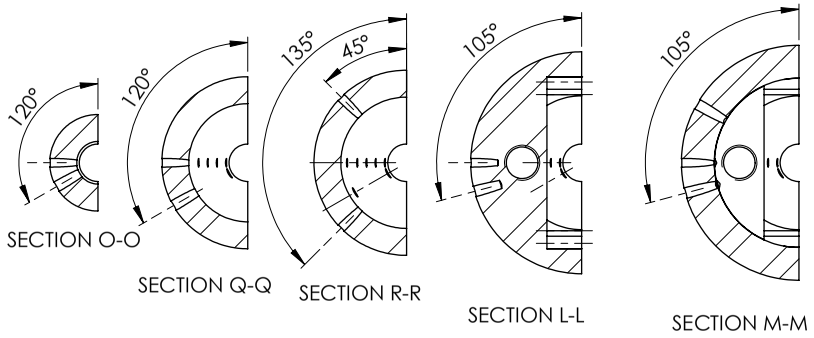
DESCRIPTION
SOUTH HALF OF MID SEGMENT

PART NUMBER	SHEET	ISSUE	
HYP-TCC-003-01	7/10	1.1	A3

REV.	MODIFICATION	BY	DATE
0	NEW		
1	MATERIAL, SENSOR HOLES, FILLETS	PK	24/09/20

SECTION VIEWS NOT PARRALEL TO HOLES. HOLES ARE THRU AS SPECIFIED IN TABLE





NAME	TYPE	DIMENSIONS
E1	HTG	∅ 4 THRU
E2	HTG	∅ 4 THRU
E3	HTG	∅ 4 THRU
E4	HTG	∅ 4 THRU
E5	HTG	∅ 4 THRU
P1	PCB	∅ 3.25 THRU
P2	PCB	∅ 3.25 THRU

ALL SURFACE HOLES ARE SURFACE NORMAL
TOLERANCES:
+ 0.05
-0.00

This is a CAD produced drawing - no manual modifications are to be made.
This drawing is the property of the University of Oxford. It must not be copied, or the contents thereof or any information received in conjunction therewith be imparted to any third party. It must not be used for any other contract and the receipt of this drawing implies that these conditions as stated are accepted.

TOLERANCES UNLESS OTHERWISE STATED
— ≤ 100 mm = ± 0.1 mm
> 100 mm ≤ 1000 mm = ± 0.2 mm
> 1000 mm — = ± 0.5 mm
Angular = ± 1.0 °

DESIGNED BY	PK	SCALE	1:2
DRAWN BY	PK	DATE	21/08/20
APPROVED BY	TH	DATE	25/08/20

MATERIAL: Stainless Steel 303

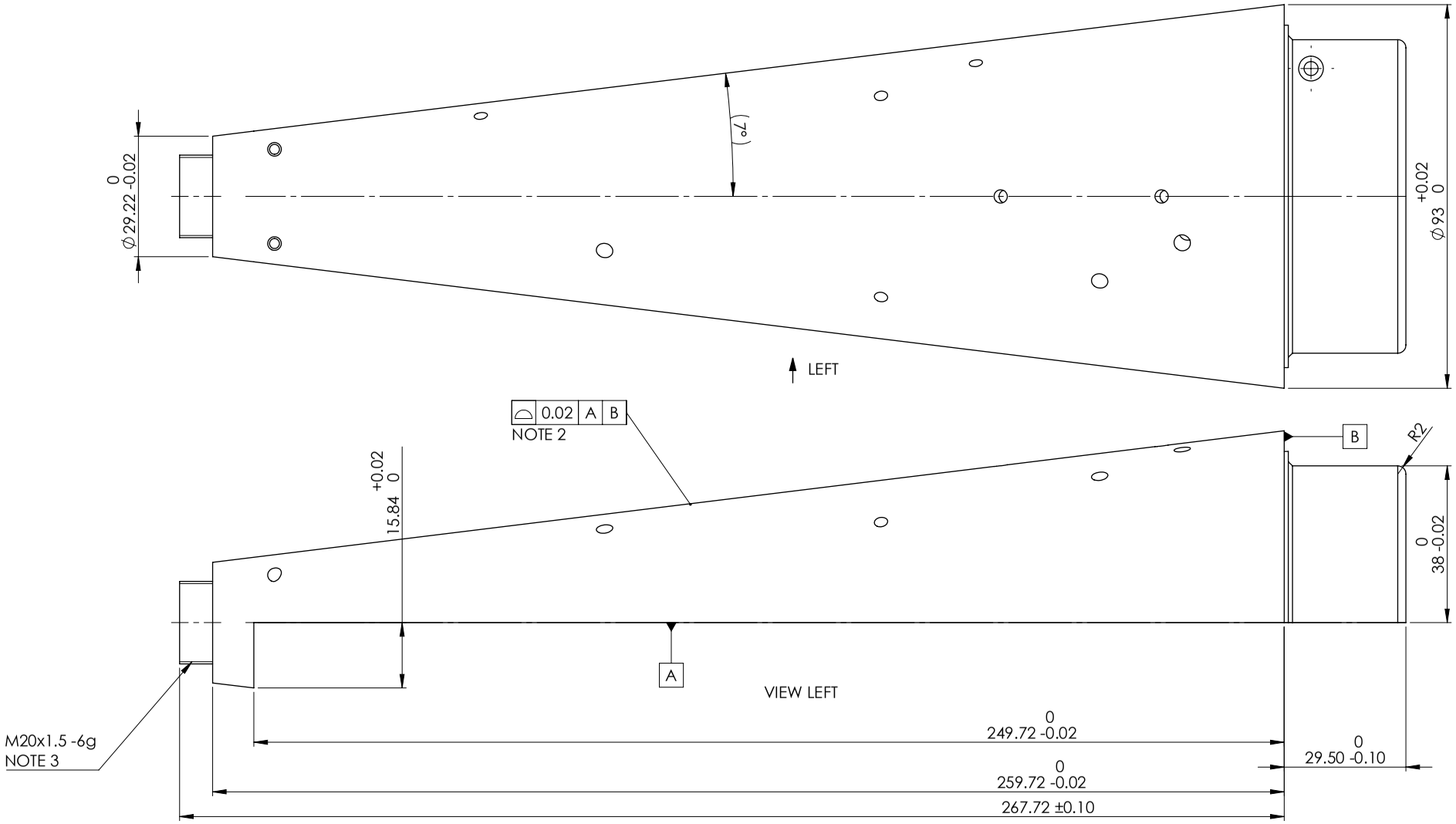
DO NOT SCALE - IF IN DOUBT ASK
DIMENSIONS IN mm
REMOVE ALL BURRS AND SHARP EDGES

Oxford Hypersonics
Oxford Thermofluids Insititute
Southwell Building
Osney Mead
Oxford OX2 0ES
Tel: 01865 288723

DESCRIPTION: SOUTH HALF OF MID SEGMENT

PART NUMBER	SHEET	ISSUE	
HYP-TCC-003-01	8/10	1.1	A3

REV.	MODIFICATION	BY	DATE
0	NEW		



This is a CAD produced drawing - no manual modifications are to be made.
This drawing is the property of the University of Oxford. It must not be copied, or the contents thereof or any information received in conjunction therewith be imparted to any third party. It must not be used for any other contract and the receipt of this drawing implies that these conditions as stated are accepted.

NOTES:
1) TO BE ASSEMBLED WITH TCC-003-01, TCC-004, TCC-005 AND TCC-001-15
2) FINAL SKIMMING OF SURFACE WITH WHOLE ASSEMBLY
3) UNDERCUT THREAD AS NECESSARY

TOLERANCES UNLESS OTHERWISE STATED			
—	≤ 100 mm	= ± 0.1 mm	
> 100 mm	≤ 1000 mm	= ± 0.2 mm	
> 1000 mm	—	= ± 0.5 mm	
	Angular	= ± 1.0 °	

DESIGNED BY	PK	SCALE	1:1
DRAWN BY	PK	DATE	20/08/20
APPROVED BY	TH	DATE	25/08/20

MATERIAL: Stainless Steel 316L

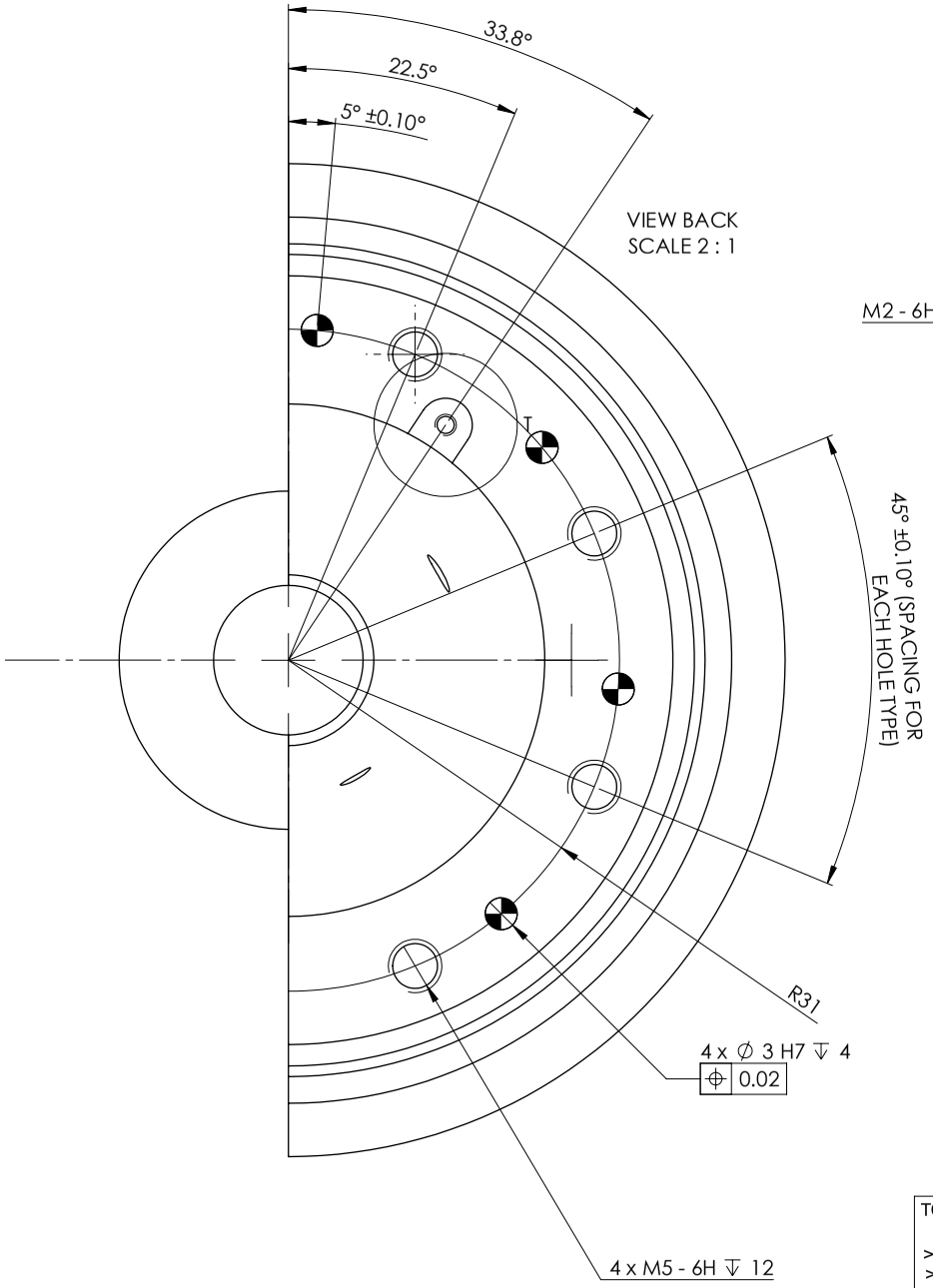
DO NOT SCALE - IF IN DOUBT ASK
DIMENSIONS IN mm
REMOVE ALL BURRS AND SHARP EDGES

Oxford Hypersonics
Oxford Thermofluids Insititute
Southwell Building
Osney Mead
Oxford OX2 0ES
Tel: 01865 288723

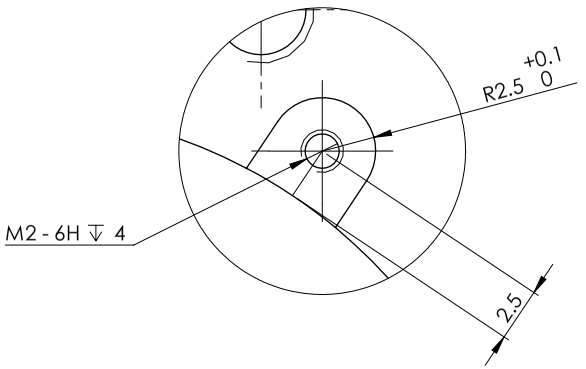
DESCRIPTION: NORTH HALF OF MID SEGMENT

PART NUMBER	SHEET	ISSUE	
HYP-TCC-002	1/6	0.1	A3

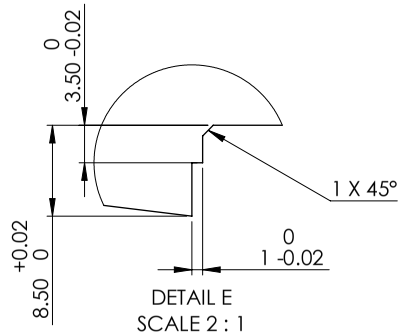
REV.	MODIFICATION	BY	DATE
0	NEW		



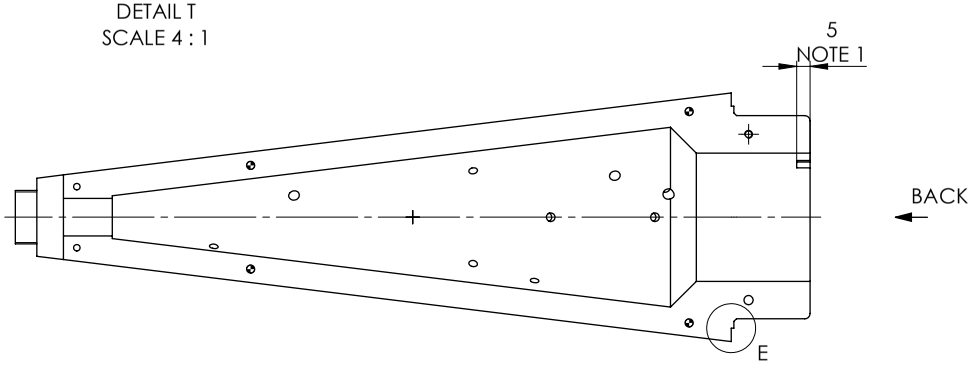
VIEW BACK
SCALE 2 : 1



DETAIL T
SCALE 4 : 1



DETAIL E
SCALE 2 : 1



NOTES:
1) DEPTH FOR DETAIL T

This is a CAD produced drawing - no manual modifications are to be made.
This drawing is the property of the University of Oxford. It must not be copied, or the contents thereof or any information received in conjunction therewith be imparted to any third party. It must not be used for any other contract and the receipt of this drawing implies that these conditions as stated are accepted.

TOLERANCES UNLESS OTHERWISE STATED			
—	≤ 100 mm	= ± 0.1 mm	
> 100 mm	≤ 1000 mm	= ± 0.2 mm	
> 1000 mm	—	= ± 0.5 mm	
	Angular	= ± 1.0 °	

DESIGNED BY	PK	SCALE	1:2
DRAWN BY	PK	DATE	20/08/20
APPROVED BY	TH	DATE	25/08/20

MATERIAL: Stainless Steel 316L

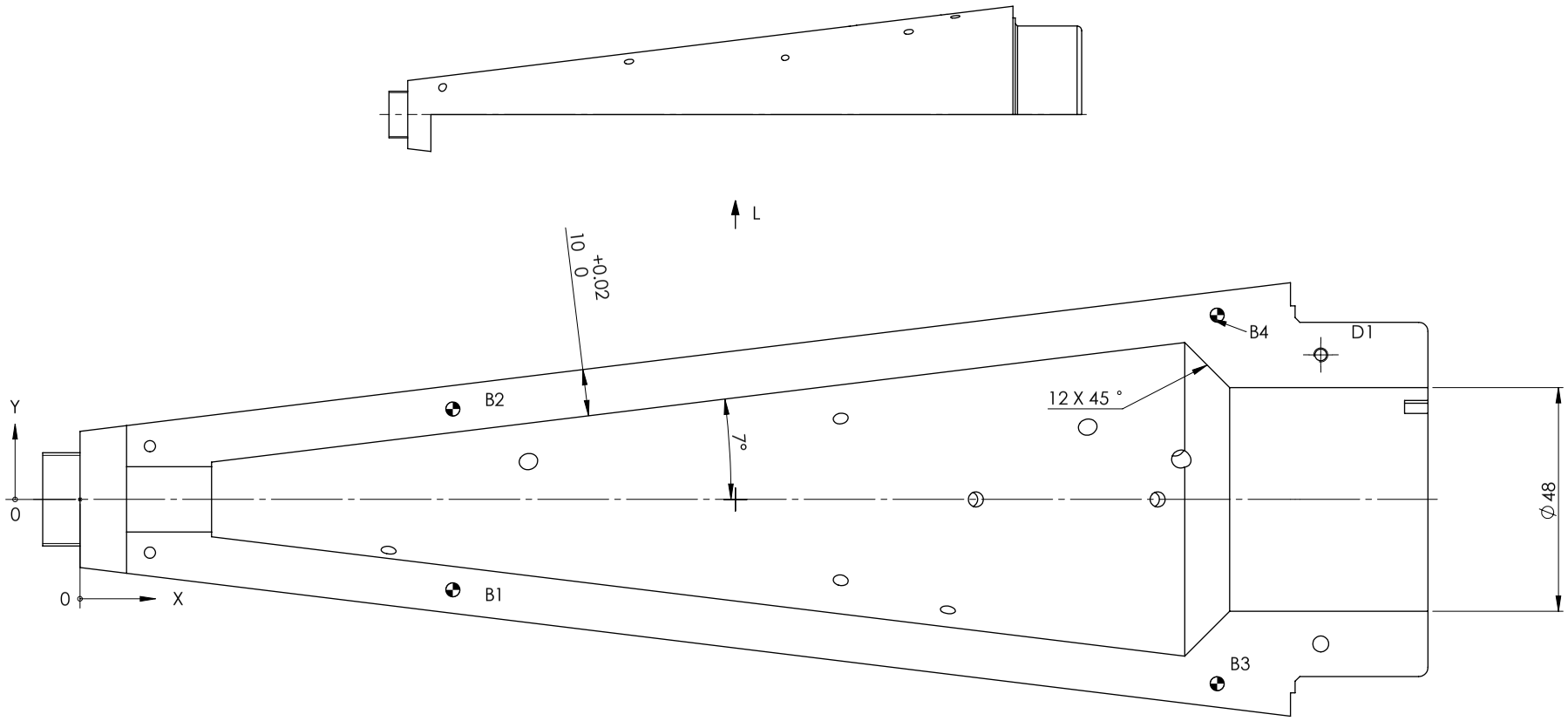
DO NOT SCALE - IF IN DOUBT ASK
DIMENSIONS IN mm
REMOVE ALL BURRS AND SHARP EDGES

Oxford Hypersonics
Oxford Thermofluids Insititute
Southwell Building
Osney Mead
Oxford OX2 0ES
Tel: 01865 288723

DESCRIPTION: NORTH HALF OF MID SEGMENT

PART NUMBER	SHEET	ISSUE	
HYP-TCC-002	2/6	0.1	A3

REV.	MODIFICATION	BY	DATE
0	NEW		



TAG	X LOC	Y LOC	SIZE
B1	80	-19.40	∅ 3 - H7 ↧ 4
B2	80	19.40	∅ 3 - H7 ↧ 4
B3	244	-39.53	∅ 3 - H7 ↧ 4
B4	244	39.53	∅ 3 - H7 ↧ 4
D1	266.22	31	M3 - 6H ↧ 6

VIEW L
SCALE 1 : 1

This is a CAD produced drawing - no manual modifications are to be made.
This drawing is the property of the University of Oxford. It must not be copied, or the contents thereof or any information received in conjunction therewith be imparted to any third party. It must not be used for any other contract and the receipt of this drawing implies that these conditions as stated are accepted.

TOLERANCES UNLESS OTHERWISE STATED
— ≤ 100 mm = ± 0.1 mm
> 100 mm ≤ 1000 mm = ± 0.2 mm
> 1000 mm — = ± 0.5 mm
Angular = ± 1.0 °

DESIGNED BY	PK	SCALE	1:2
DRAWN BY	PK	DATE	20/08/20
APPROVED BY	TH	DATE	25/08/20

MATERIAL
Stainless Steel 316L

DO NOT SCALE - IF IN DOUBT ASK
DIMENSIONS IN mm
REMOVE ALL BURRS AND SHARP EDGES

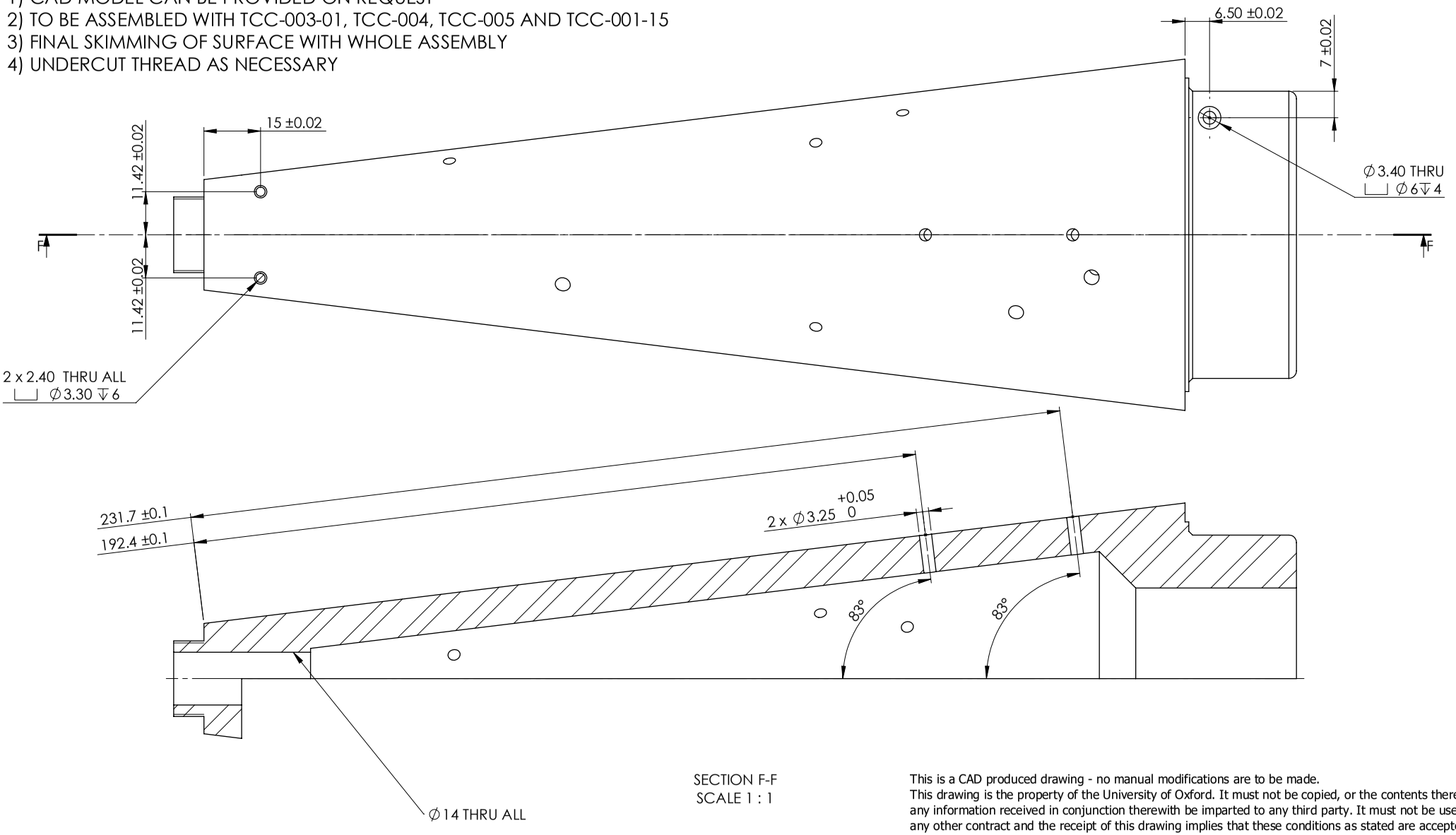
Oxford Hypersonics
Oxford Thermofluids Insititute
Southwell Building
Osney Mead
Oxford OX2 0ES
Tel: 01865 288723

DESCRIPTION
NORTH HALF OF MID SEGMENT

PART NUMBER	SHEET	ISSUE	
HYP-TCC-002	3/6	0.1	A3

REV.	MODIFICATION	BY	DATE
0	NEW		

NOTES:
1) CAD MODEL CAN BE PROVIDED ON REQUEST
2) TO BE ASSEMBLED WITH TCC-003-01, TCC-004, TCC-005 AND TCC-001-15
3) FINAL SKIMMING OF SURFACE WITH WHOLE ASSEMBLY
4) UNDERCUT THREAD AS NECESSARY



SECTION F-F
SCALE 1 : 1

This is a CAD produced drawing - no manual modifications are to be made.
This drawing is the property of the University of Oxford. It must not be copied, or the contents thereof or any information received in conjunction therewith be imparted to any third party. It must not be used for any other contract and the receipt of this drawing implies that these conditions as stated are accepted.

TOLERANCES UNLESS OTHERWISE STATED			
—	≤ 100 mm	= ± 0.1 mm	
> 100 mm	≤ 1000 mm	= ± 0.2 mm	
> 1000 mm	—	= ± 0.5 mm	
	Angular	= ± 1.0 °	
DESIGNED BY	PK	SCALE	1:2
DRAWN BY	PK	DATE	20/08/20
APPROVED BY	TH	DATE	25/08/20

MATERIAL: Stainless Steel 316L

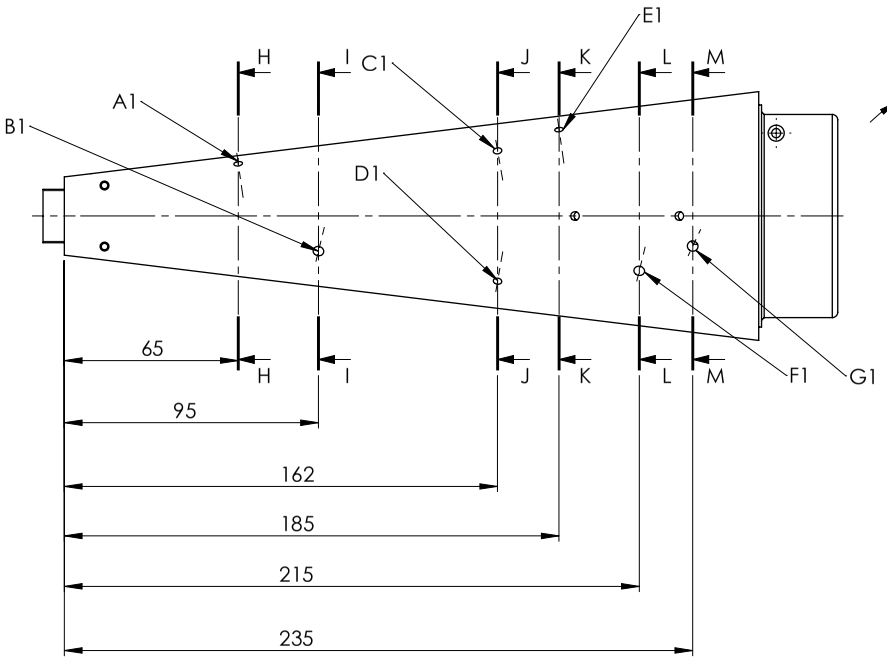
DO NOT SCALE - IF IN DOUBT ASK
DIMENSIONS IN mm
REMOVE ALL BURRS AND SHARP EDGES

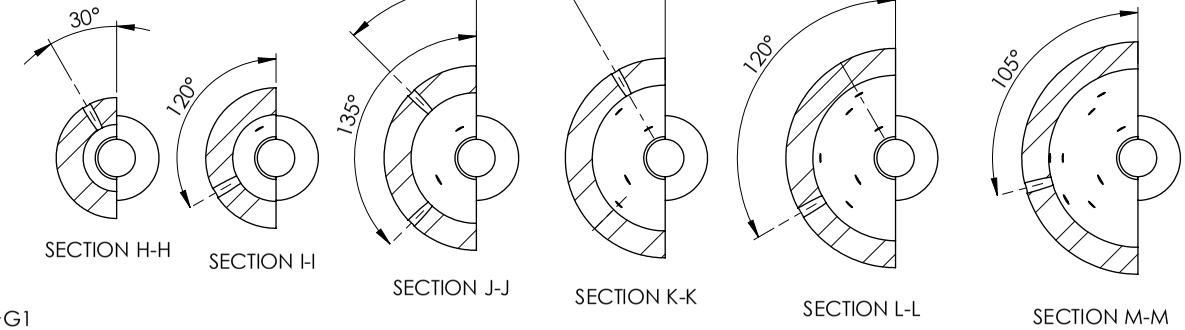
Oxford Hypersonics
Oxford Thermofluids Insititute
Southwell Building
Osney Mead
Oxford OX2 0ES
Tel: 01865 288723

DESCRIPTION: NORTH HALF OF MID SEGMENT

PART NUMBER	SHEET	ISSUE	
HYP-TCC-002	4/6	0.1	A3

REV.	MODIFICATION	BY	DATE
0	NEW		





HOLE NUMBER	SIZE
A1	∅4 THRU
B1	∅4 THRU
C1	∅3.25 THRU
D1	∅3.25 THRU
E1	∅4 THRU
F1	∅4 THRU
G1	∅4 THRU

PRECISION FOR ALL SURFACE HOLE DIAMETERS
+0.05
-0.00

ALL HOLES ARE SURFACE NORMAL

This is a CAD produced drawing - no manual modifications are to be made.
This drawing is the property of the University of Oxford. It must not be copied, or the contents thereof or any information received in conjunction therewith be imparted to any third party. It must not be used for any other contract and the receipt of this drawing implies that these conditions as stated are accepted.

TOLERANCES UNLESS OTHERWISE STATED
— ≤ 100 mm = ± 0.1 mm
> 100 mm ≤ 1000 mm = ± 0.2 mm
> 1000 mm — = ± 0.5 mm
Angular = ± 1.0 °

DESIGNED BY	PK	SCALE	1:2
DRAWN BY	PK	DATE	20/08/20
APPROVED BY	TH	DATE	25/08/20

MATERIAL
Stainless Steel 316L

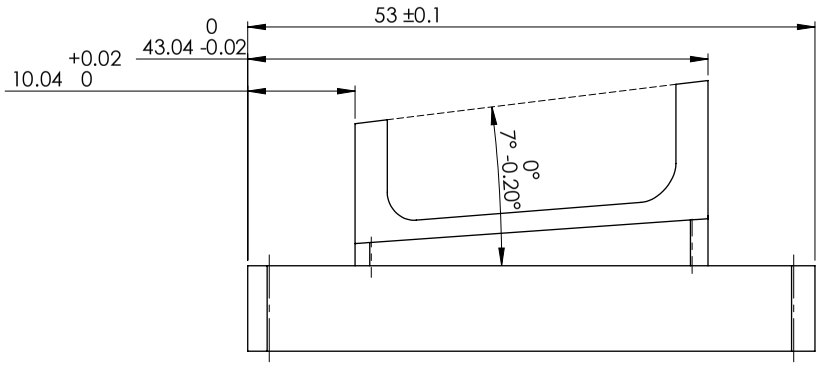
DO NOT SCALE - IF IN DOUBT ASK
DIMENSIONS IN mm
REMOVE ALL BURRS AND SHARP EDGES

Oxford Hypersonics
Oxford Thermofluids Insititute
Southwell Building
Osney Mead
Oxford OX2 0ES
Tel: 01865 288723

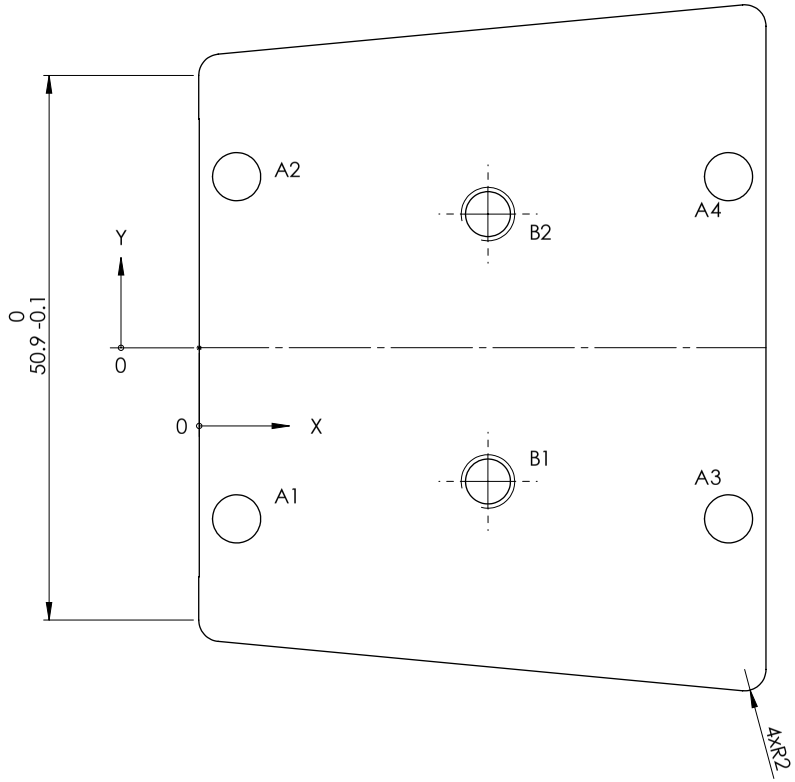
DESCRIPTION
NORTH HALF OF MID SEGMENT

PART NUMBER	SHEET	ISSUE	
HYP-TCC-002	5/6	0.1	A3

REV.	MODIFICATION	BY	DATE
0	NEW		
1	FILLET RADII, ANGLES	PK	21/10/20



TAG	X LOC	Y LOC	SIZE
A1	3.50	-16	∅ 4.50 THRU ALL
A2	3.50	16	∅ 4.50 THRU ALL
A3	49.50	-16	∅ 4.50 THRU ALL
A4	49.50	16	∅ 4.50 THRU ALL
B1	27	-12.50	∅ 4.20 THRU ALL M5 - 6H THRU ALL
B2	27	12.50	∅ 4.20 THRU ALL M5 - 6H THRU ALL



VIEW BACK
SCALE 2 : 1

NOTES:
1) THIS PART IS TO FIT THE CAVITY IN HYP-TCC-003-01 WITH HYP-TCC-003-03 INSERTED

This is a CAD produced drawing - no manual modifications are to be made.
This drawing is the property of the University of Oxford. It must not be copied, or the contents thereof or any information received in conjunction therewith be imparted to any third party. It must not be used for any other contract and the receipt of this drawing implies that these conditions as stated are accepted.

TOLERANCES UNLESS OTHERWISE STATED
— ≤ 100 mm = ± 0.1 mm
> 100 mm ≤ 1000 mm = ± 0.2 mm
> 1000 mm — = ± 0.5 mm
Angular = ± 1.0 °

DESIGNED BY	PK	SCALE	1:1
DRAWN BY	PK	DATE	20/08/20
APPROVED BY	TH	DATE	25/08/20

MATERIAL
STAINLESS STEEL 303

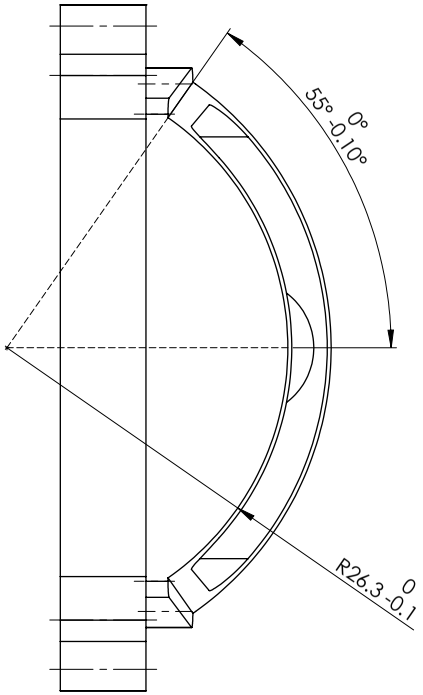
DO NOT SCALE - IF IN DOUBT ASK
DIMENSIONS IN mm
REMOVE ALL BURRS AND SHARP EDGES

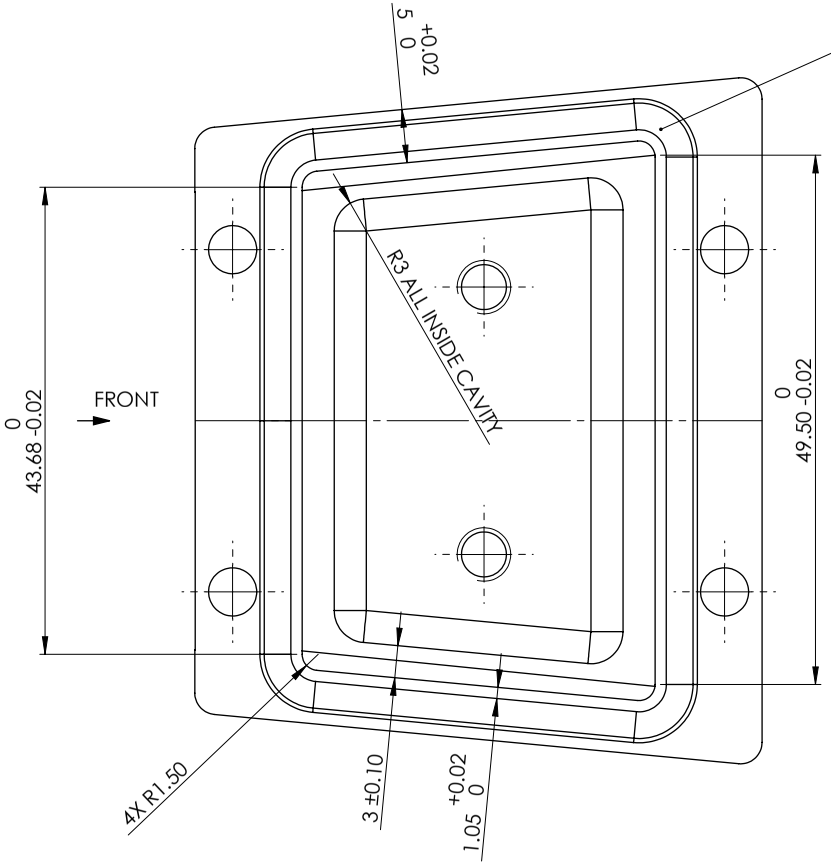
Oxford Hypersonics
Oxford Thermofluids Insititute
Southwell Building
Osney Mead
Oxford OX2 0ES
Tel: 01865 288723

DESCRIPTION
LID FOR SOUTH HALF OF MID SEGMENT

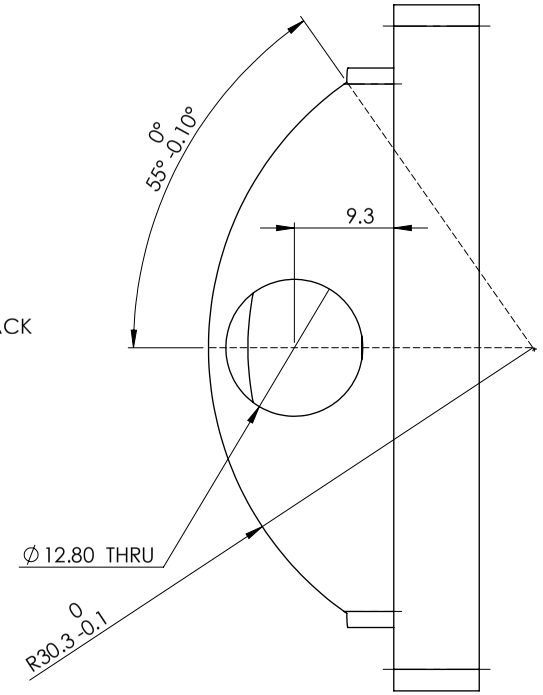
PART NUMBER	SHEET	ISSUE	
HYP-TCC-003-02	1/4	1.1	A3

REV.	MODIFICATION	BY	DATE
0	NEW		
1	FILLET RADII, ANGLES	PK	21/10/20





VIEW FRONT
SCALE 2 : 1



VIEW BACK
SCALE 2 : 1

This is a CAD produced drawing - no manual modifications are to be made.
This drawing is the property of the University of Oxford. It must not be copied, or the contents thereof or any information received in conjunction therewith be imparted to any third party. It must not be used for any other contract and the receipt of this drawing implies that these conditions as stated are accepted.

TOLERANCES UNLESS OTHERWISE STATED			
—	≤ 100 mm	= ± 0.1 mm	
> 100 mm	≤ 1000 mm	= ± 0.2 mm	
> 1000 mm	—	= ± 0.5 mm	
	Angular	= ± 1.0 °	
DESIGNED BY	PK	SCALE	1:1
DRAWN BY	PK	DATE	20/08/20
APPROVED BY	TH	DATE	25/08/20

MATERIAL
STAINLESS STEEL 303

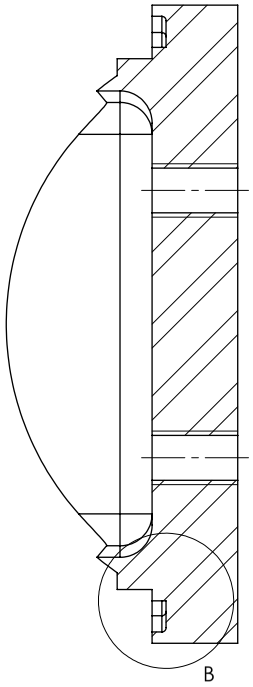
DO NOT SCALE - IF IN DOUBT ASK
DIMENSIONS IN mm
REMOVE ALL BURRS AND SHARP EDGES

Oxford Hypersonics
Oxford Thermofluids Insititute
Southwell Building
Osney Mead
Oxford OX2 0ES
Tel: 01865 288723

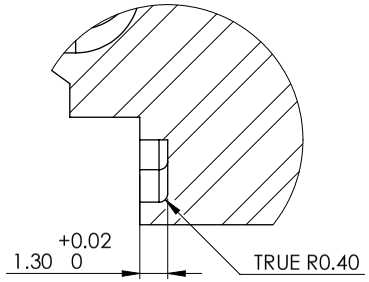
DESCRIPTION
LID FOR SOUTH HALF OF MID SEGMENT

PART NUMBER	SHEET	ISSUE	
HYP-TCC-003-02	2/4	1.1	A3

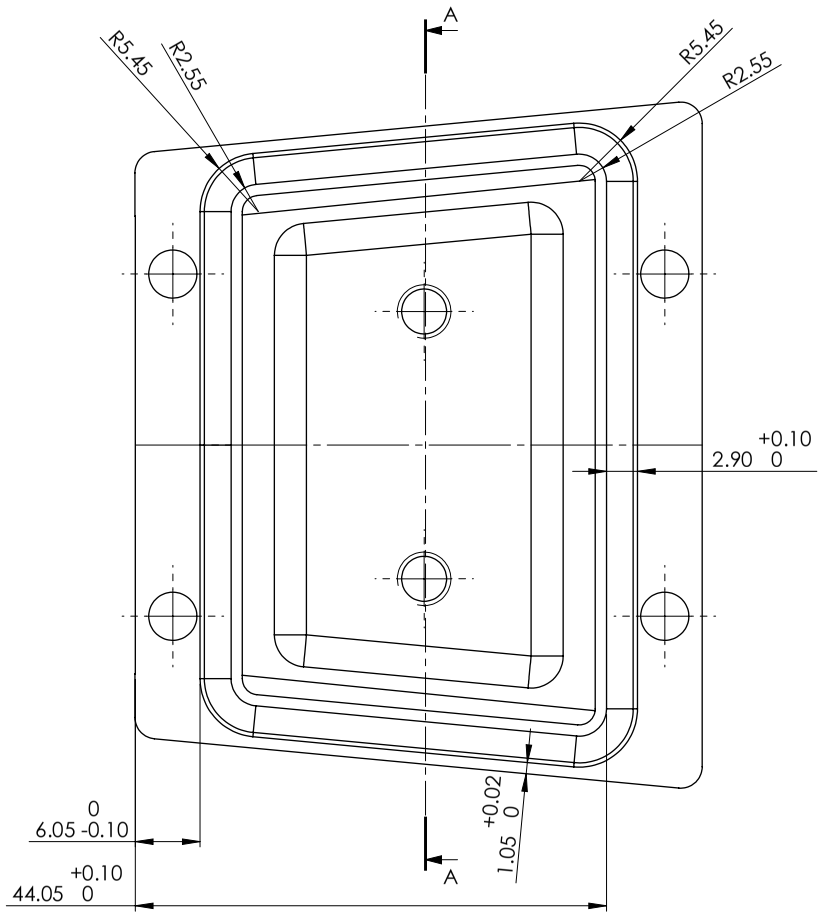
REV.	MODIFICATION	BY	DATE
0	NEW		
1	FILLET RADII, ANGLES	PK	21/10/20



SECTION A-A
SCALE 2 : 1



DETAIL B
SCALE 4 : 1



NOTE:
O-RING GROOVE IN DETAIL B ACCORDINT TO
BS ISO 3601-2:2016 FOR O-RING WITH NOMINAL DIAMETER
1.78 MM

This is a CAD produced drawing - no manual modifications are to be made.
This drawing is the property of the University of Oxford. It must not be copied, or the contents thereof or any information received in conjunction therewith be imparted to any third party. It must not be used for any other contract and the receipt of this drawing implies that these conditions as stated are accepted.

TOLERANCES UNLESS OTHERWISE STATED
— ≤ 100 mm = ± 0.1 mm
> 100 mm ≤ 1000 mm = ± 0.2 mm
> 1000 mm — = ± 0.5 mm
Angular = ± 1.0 °

DESIGNED BY	PK	SCALE	1:1
DRAWN BY	PK	DATE	20/08/20
APPROVED BY	TH	DATE	25/08/20

MATERIAL
STAINLESS STEEL 303

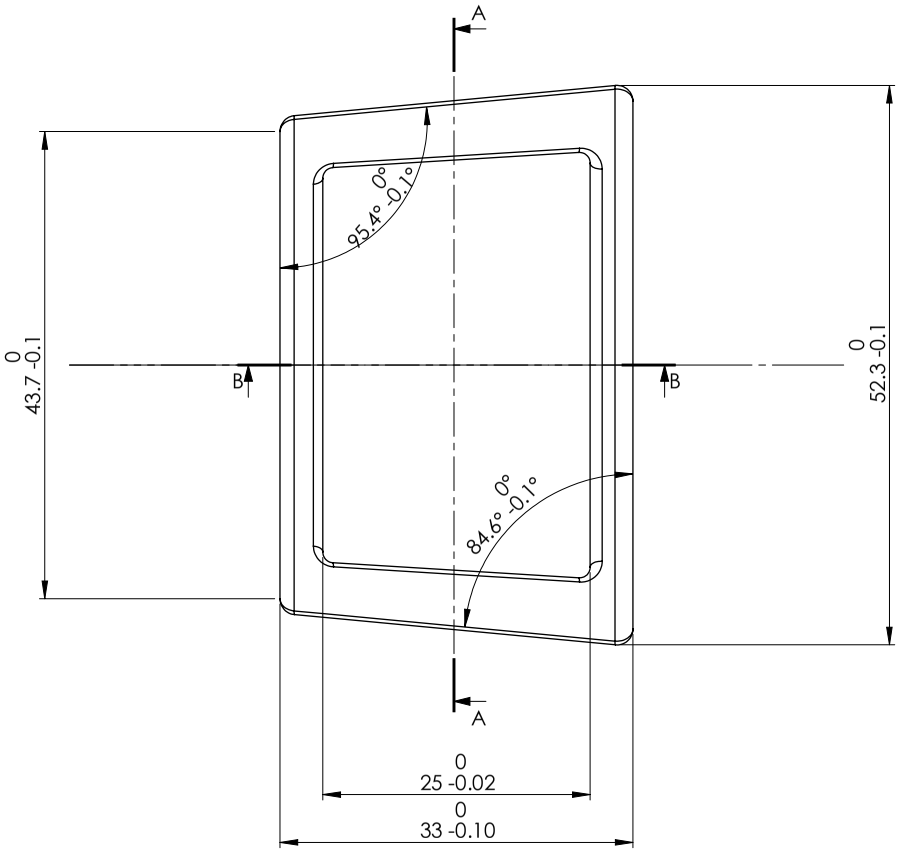
DO NOT SCALE - IF IN DOUBT ASK
DIMENSIONS IN mm
REMOVE ALL BURRS AND SHARP EDGES

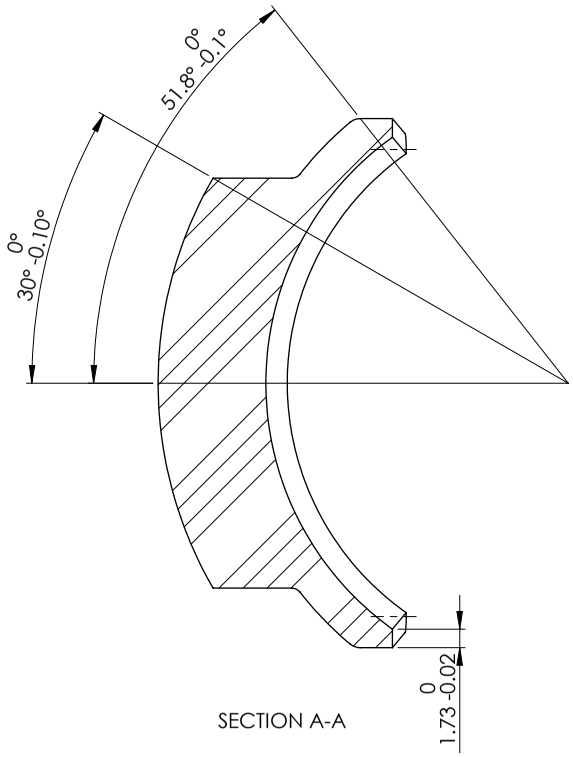
UNIVERSITY OF OXFORD
Oxford Hypersonics
Oxford Thermofluids Insititute
Southwell Building
Osney Mead
Oxford OX2 0ES
Tel: 01865 288723

DESCRIPTION
LID FOR SOUTH HALF OF MID SEGMENT

PART NUMBER	SHEET	ISSUE	
HYP-TCC-003-02	3/4	1.1	A3

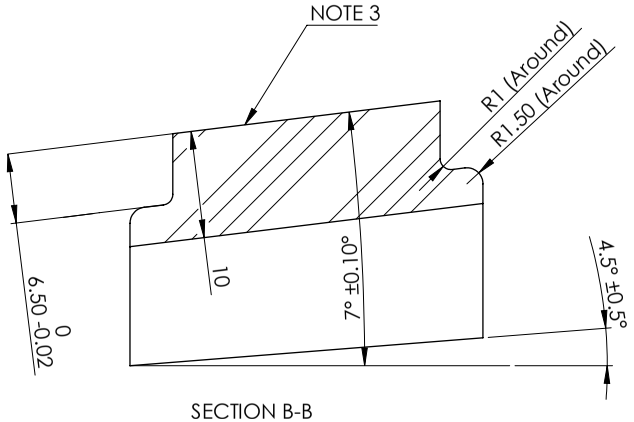
REV.	MODIFICATION	BY	DATE
0	NEW		





SECTION A-A

NOTES:
1) THIS PART IS TO BE INSERTE INTO THE CAVITY OF TCC-003-01
2) FINAL SKIMMING OF SURFACE IS DONE AT THE IN HOUSE WORKSHOP OF THE UNIVERSITY OF OXOFRD WITH THE WHOLE ASSEMBLY
3) LEAVE 0.5 MM OF MATERIAL ON SURFACE FOR FINAL SKIMMING



SECTION B-B

This is a CAD produced drawing - no manual modifications are to be made.
This drawing is the property of the University of Oxford. It must not be copied, or the contents thereof or any information received in conjunction therewith be imparted to any third party. It must not be used for any other contract and the receipt of this drawing implies that these conditions as stated are accepted.

TOLERANCES UNLESS OTHERWISE STATED			
—	≤ 100 mm	= ± 0.1 mm	
> 100 mm	≤ 1000 mm	= ± 0.2 mm	
> 1000 mm	—	= ± 0.5 mm	
	Angular	= ± 1.0 °	

DESIGNED BY	PK	SCALE	2:1
DRAWN BY	PK	DATE	20/08/20
APPROVED BY	TH	DATE	25/08/20

MATERIAL: BF100AL

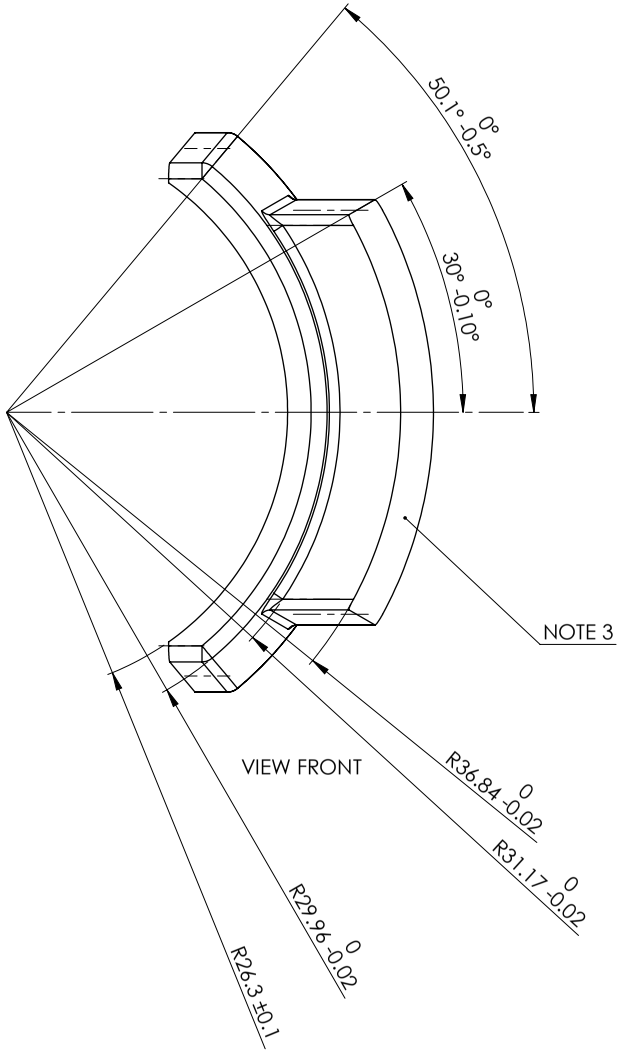
DO NOT SCALE - IF IN DOUBT ASK
DIMENSIONS IN mm
REMOVE ALL BURRS AND SHARP EDGES

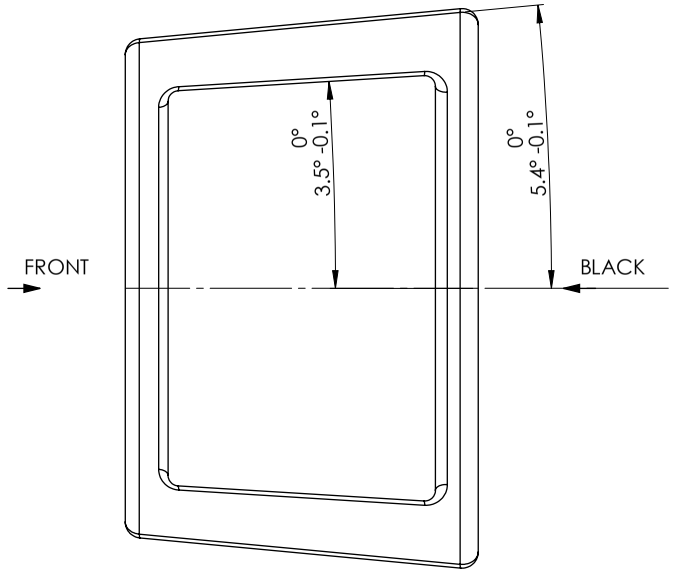
Oxford Hypersonics
Oxford Thermofluids Insititute
Southwell Building
Osney Mead
Oxford OX2 0ES
Tel: 01865 288723

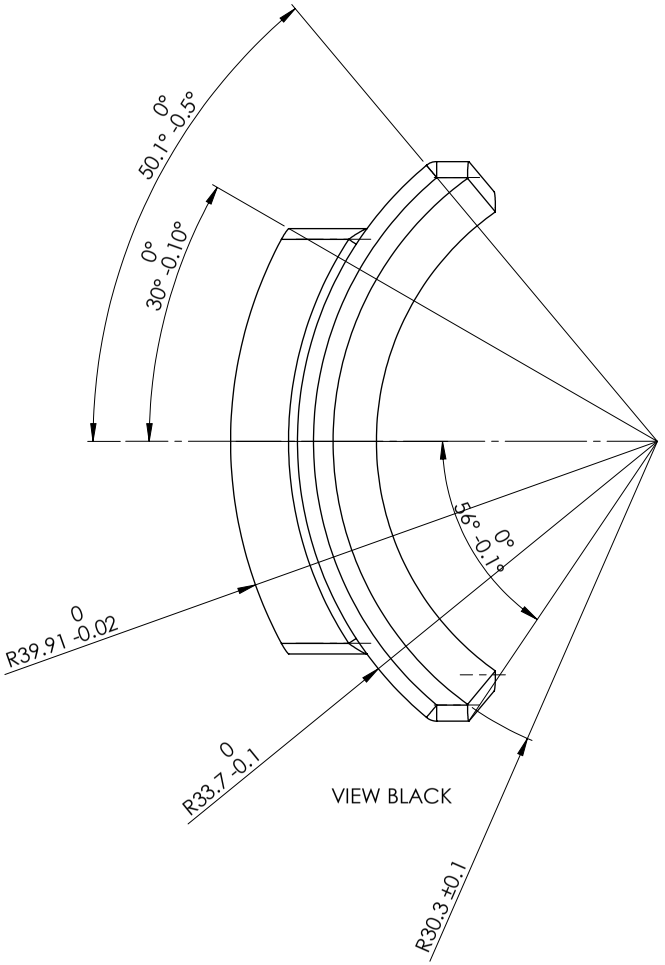
DESCRIPTION: POROUS INSERT INTO TCC-003-01

PART NUMBER	SHEET	ISSUE	
HYP-TCC-003-03	1/4	1.1	A3

REV.	MODIFICATION	BY	DATE
0	NEW		







This is a CAD produced drawing - no manual modifications are to be made.
This drawing is the property of the University of Oxford. It must not be copied, or the contents thereof or any information received in conjunction therewith be imparted to any third party. It must not be used for any other contract and the receipt of this drawing implies that these conditions as stated are accepted.

TOLERANCES UNLESS OTHERWISE STATED			
—	≤ 100 mm	= ± 0.1 mm	
> 100 mm	≤ 1000 mm	= ± 0.2 mm	
> 1000 mm	—	= ± 0.5 mm	
	Angular	= ± 1.0 °	
DESIGNED BY	PK	SCALE	2:1
DRAWN BY	PK	DATE	20/08/20
APPROVED BY	TH	DATE	25/08/20

MATERIAL: BF100AL

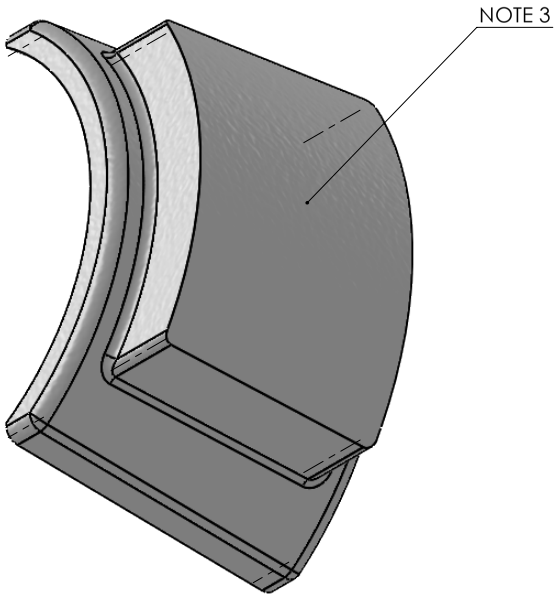
DO NOT SCALE - IF IN DOUBT ASK
DIMENSIONS IN mm
REMOVE ALL BURRS AND SHARP EDGES

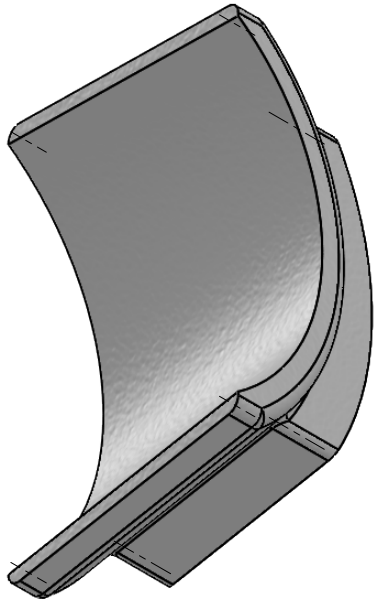
Oxford Hypersonics
Oxford Thermofluids Insititute
Southwell Building
Osney Mead
Oxford OX2 0ES
Tel: 01865 288723

DESCRIPTION: POROUS INSERT INTO TCC-003-01

PART NUMBER	SHEET	ISSUE	
HYP-TCC-003-03	2/4	1.1	A3

REV.	MODIFICATION	BY	DATE
0	NEW		





This is a CAD produced drawing - no manual modifications are to be made.
This drawing is the property of the University of Oxford. It must not be copied, or the contents thereof or any information received in conjunction therewith be imparted to any third party. It must not be used for any other contract and the receipt of this drawing implies that these conditions as stated are accepted.

TOLERANCES UNLESS OTHERWISE STATED			
—	≤ 100 mm	= ± 0.1 mm	
> 100 mm	≤ 1000 mm	= ± 0.2 mm	
> 1000 mm	—	= ± 0.5 mm	
	Angular	= ± 1.0 °	
DESIGNED BY	PK	SCALE	2:1
DRAWN BY	PK	DATE	20/08/20
APPROVED BY	TH	DATE	25/08/20

MATERIAL: BF100AL

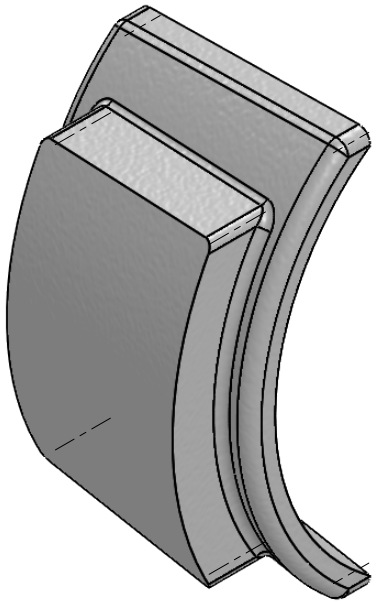
DO NOT SCALE - IF IN DOUBT ASK
DIMENSIONS IN mm
REMOVE ALL BURRS AND SHARP EDGES

Oxford Hypersonics
Oxford Thermofluids Insititute
Southwell Building
Osney Mead
Oxford OX2 0ES
Tel: 01865 288723

DESCRIPTION: POROUS INSERT INTO TCC-003-01

PART NUMBER	SHEET	ISSUE	
HYP-TCC-003-03	3/4	1.1	A3

REV.	MODIFICATION	BY	DATE
0	NEW		



This is a CAD produced drawing - no manual modifications are to be made.
This drawing is the property of the University of Oxford. It must not be copied, or the contents thereof or any information received in conjunction therewith be imparted to any third party. It must not be used for any other contract and the receipt of this drawing implies that these conditions as stated are accepted.

TOLERANCES UNLESS OTHERWISE STATED			
—	≤ 100 mm	= ± 0.1 mm	
> 100 mm	≤ 1000 mm	= ± 0.2 mm	
> 1000 mm	—	= ± 0.5 mm	
	Angular	= ± 1.0 °	
DESIGNED BY	PK	SCALE	2:1
DRAWN BY	PK	DATE	20/08/20
APPROVED BY	TH	DATE	25/08/20

MATERIAL: BF100AL

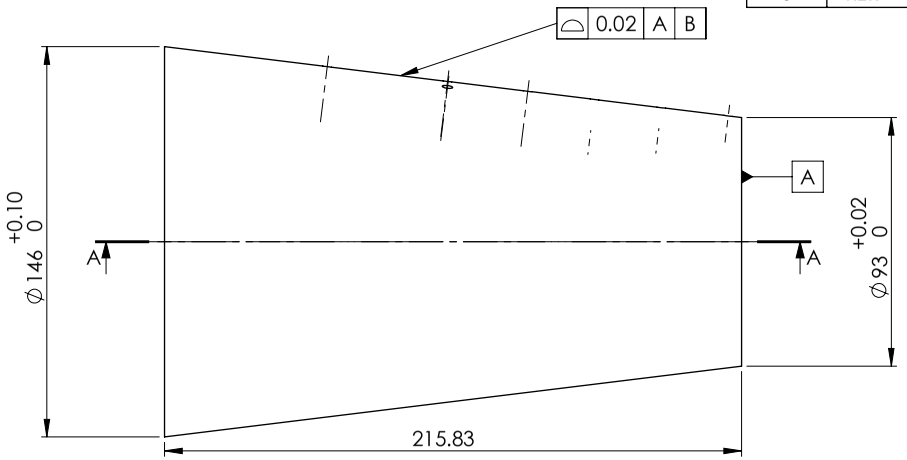
DO NOT SCALE - IF IN DOUBT ASK
DIMENSIONS IN mm
REMOVE ALL BURRS AND SHARP EDGES

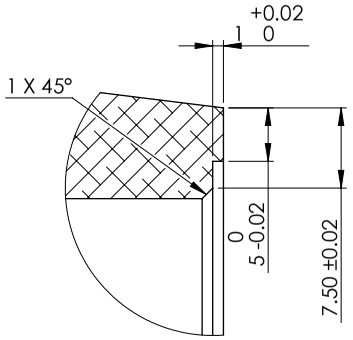
Oxford Hypersonics
Oxford Thermofluids Insititute
Southwell Building
Osney Mead
Oxford OX2 0ES
Tel: 01865 288723

DESCRIPTION: POROUS INSERT INTO TCC-003-01

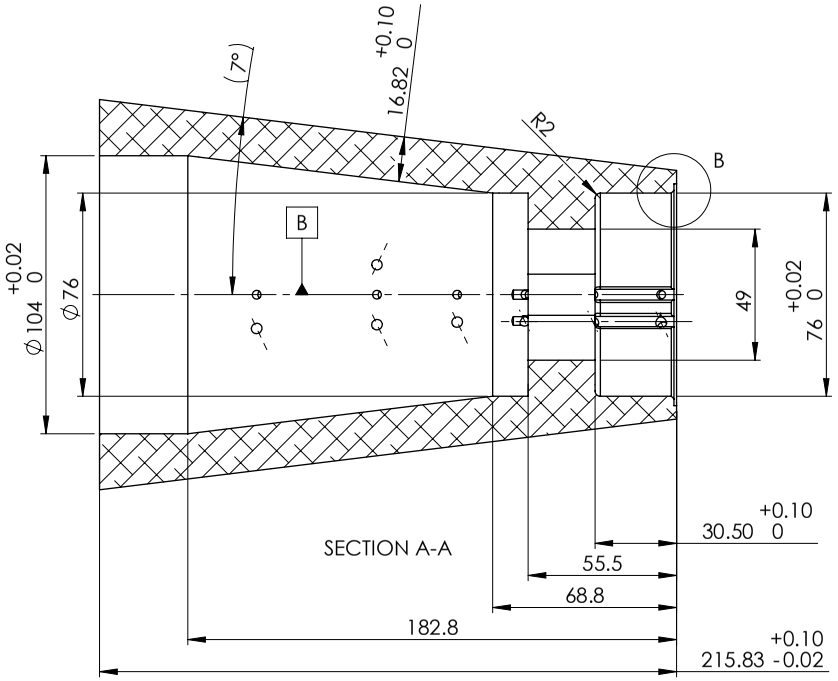
PART NUMBER	SHEET	ISSUE	
HYP-TCC-003-03	4/4	1.1	A3

REV.	MODIFICATION	BY	DATE
0	NEW		





DETAIL B
SCALE 2 : 1



SECTION A-A

This is a CAD produced drawing - no manual modifications are to be made.
This drawing is the property of the University of Oxford. It must not be copied, or the contents thereof or any information received in conjunction therewith be imparted to any third party. It must not be used for any other contract and the receipt of this drawing implies that these conditions as stated are accepted.

TOLERANCES UNLESS OTHERWISE STATED
— ≤ 100 mm = ± 0.1 mm
> 100 mm ≤ 1000 mm = ± 0.2 mm
> 1000 mm — = ± 0.5 mm
Angular = ± 1.0 °

DESIGNED BY	PK	SCALE	1:2
DRAWN BY	PK	DATE	26/02/21
APPROVED BY		DATE	

MATERIAL
7075 - T6 ALUMINIUM

DO NOT SCALE - IF IN DOUBT ASK
DIMENSIONS IN mm
REMOVE ALL BURRS AND SHARP EDGES

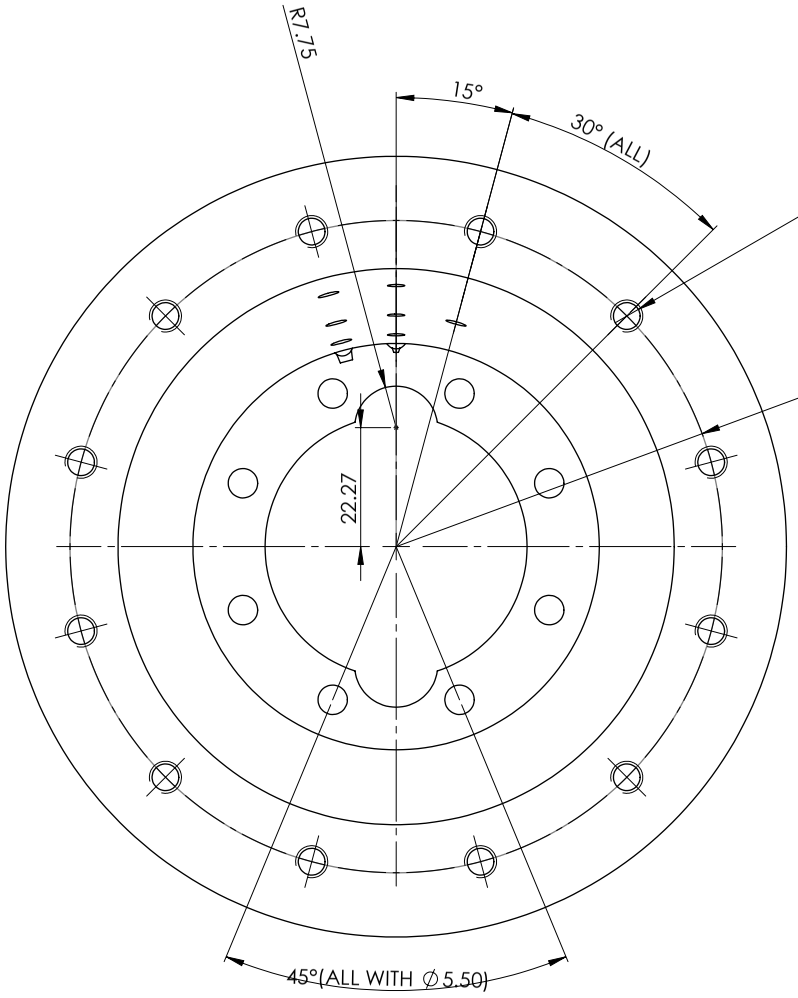
UNIVERSITY OF OXFORD
Oxford Hypersonics
Oxford Thermofluids Insititute
Southwell Building
Osney Mead
Oxford OX2 0ES
Tel: 01865 288723

DESCRIPTION
FULL REARSEGMENT OF TCC

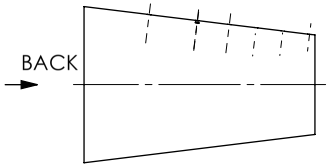
PART NUMBER	SHEET	ISSUE	
TCC-006	1/4	0.1	A3

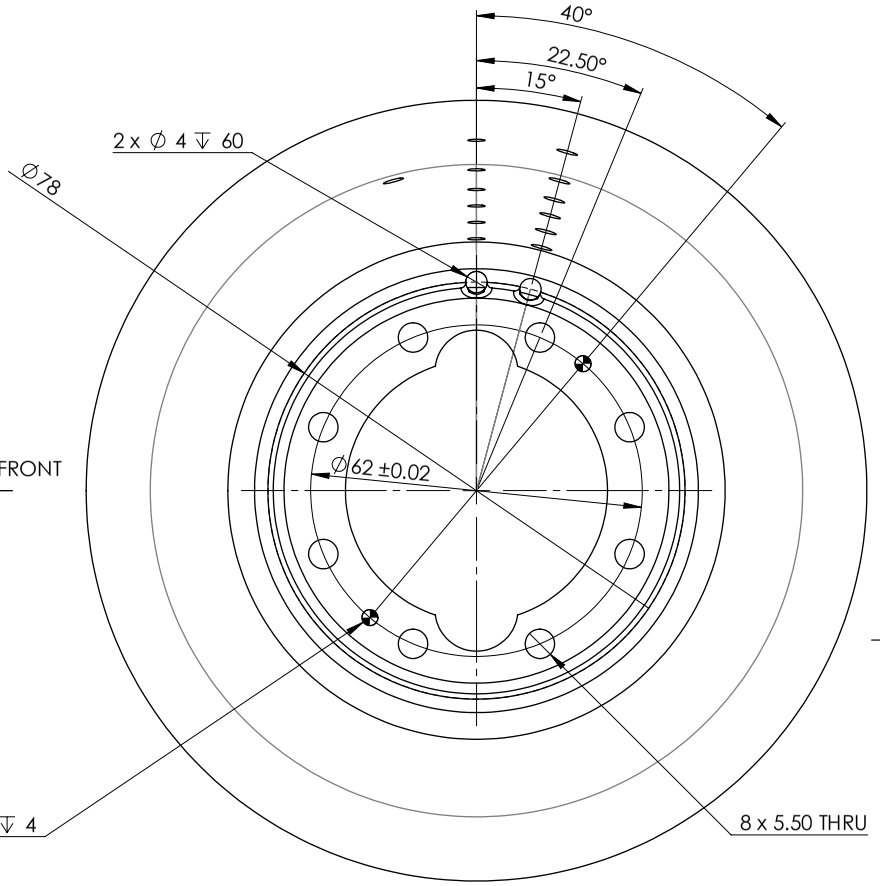
SOLIDWORKS Educational Product. For Instructional Use Only.

REV.	MODIFICATION	BY	DATE
0	NEW		



VIEW BACK
SCALE 1 : 1





VIEW FRONT
SCALE 1 : 1

This is a CAD produced drawing - no manual modifications are to be made.
This drawing is the property of the University of Oxford. It must not be copied, or the contents thereof or any information received in conjunction therewith be imparted to any third party. It must not be used for any other contract and the receipt of this drawing implies that these conditions as stated are accepted.

TOLERANCES UNLESS OTHERWISE STATED			
—	≤ 100 mm	= ± 0.1 mm	
> 100 mm	≤ 1000 mm	= ± 0.2 mm	
> 1000 mm	—	= ± 0.5 mm	
	Angular	= ± 1.0 °	
DESIGNED BY	PK	SCALE	1:2
DRAWN BY	PK	DATE	26/02/21
APPROVED BY		DATE	

MATERIAL: 7075 - T6 ALUMINIUM

DO NOT SCALE - IF IN DOUBT ASK
DIMENSIONS IN mm
REMOVE ALL BURRS AND SHARP EDGES

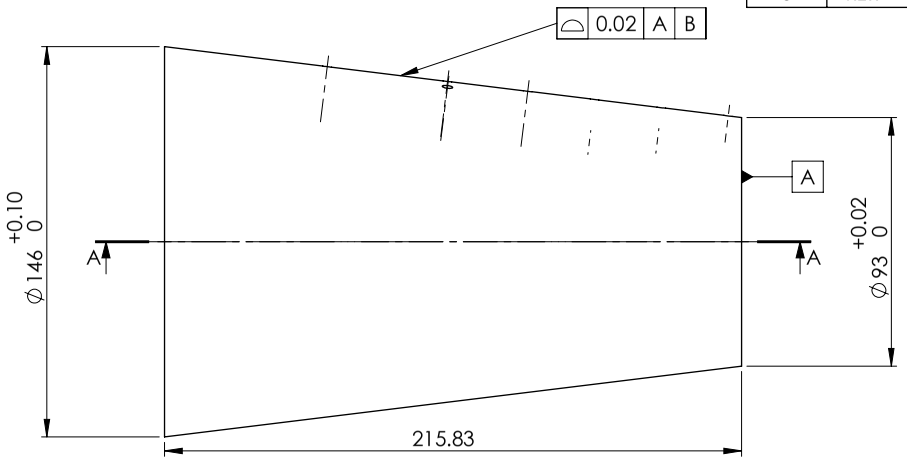
Oxford Hypersonics
Oxford Thermofluids Insititute
Southwell Building
Osney Mead
Oxford OX2 0ES
Tel: 01865 288723

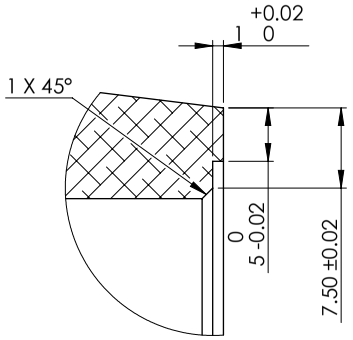
DESCRIPTION: FULL REARSEGMENT OF TCC

PART NUMBER	SHEET	ISSUE	
TCC-006	2/4	0.1	A3

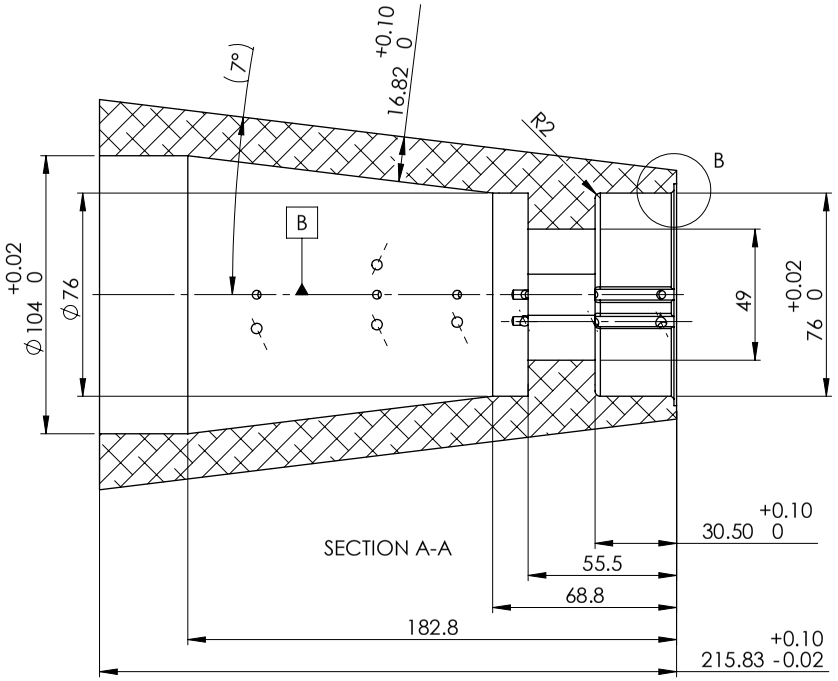
SOLIDWORKS Educational Product. For Instructional Use Only.

REV.	MODIFICATION	BY	DATE
0	NEW		





DETAIL B
SCALE 2 : 1



SECTION A-A

This is a CAD produced drawing - no manual modifications are to be made.
This drawing is the property of the University of Oxford. It must not be copied, or the contents thereof or any information received in conjunction therewith be imparted to any third party. It must not be used for any other contract and the receipt of this drawing implies that these conditions as stated are accepted.

TOLERANCES UNLESS OTHERWISE STATED
— ≤ 100 mm = ± 0.1 mm
> 100 mm ≤ 1000 mm = ± 0.2 mm
> 1000 mm — = ± 0.5 mm
Angular = ± 1.0 °

DESIGNED BY	PK	SCALE	1:2
DRAWN BY	PK	DATE	26/02/21
APPROVED BY		DATE	

MATERIAL
7075 - T6 ALUMINIUM

DO NOT SCALE - IF IN DOUBT ASK
DIMENSIONS IN mm
REMOVE ALL BURRS AND SHARP EDGES

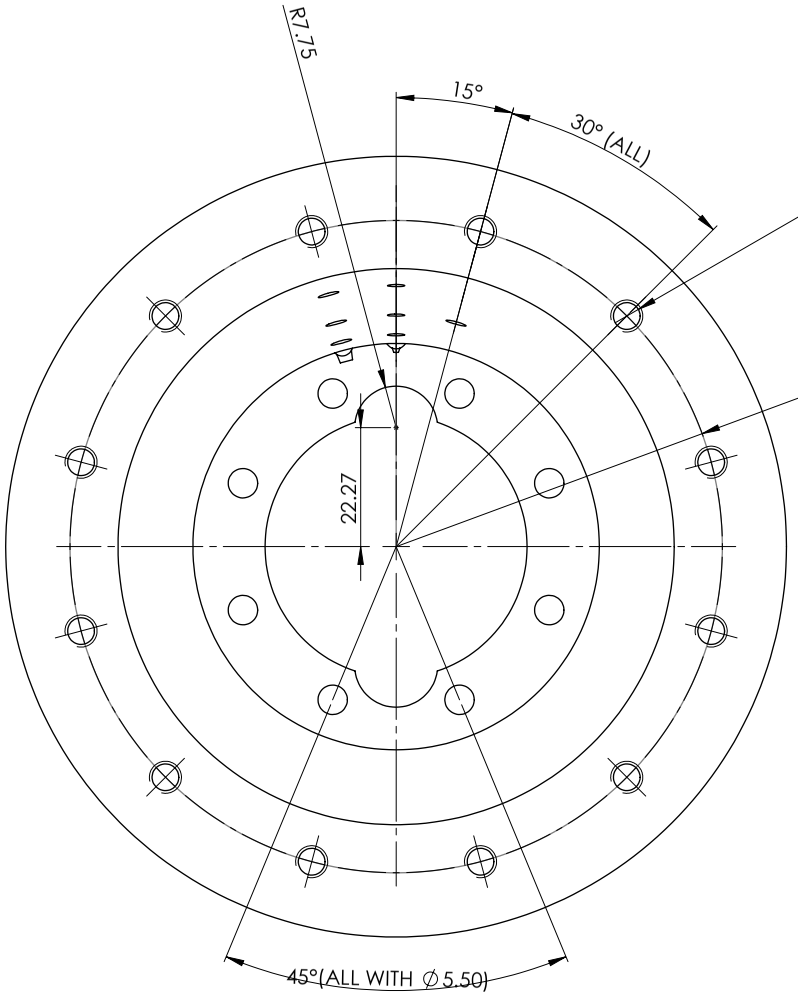
UNIVERSITY OF OXFORD
Oxford Hypersonics
Oxford Thermofluids Insititute
Southwell Building
Osney Mead
Oxford OX2 0ES
Tel: 01865 288723

DESCRIPTION
FULL REARSEGMENT OF TCC

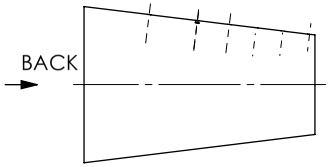
PART NUMBER	SHEET	ISSUE	
TCC-006	1/4	0.1	A3

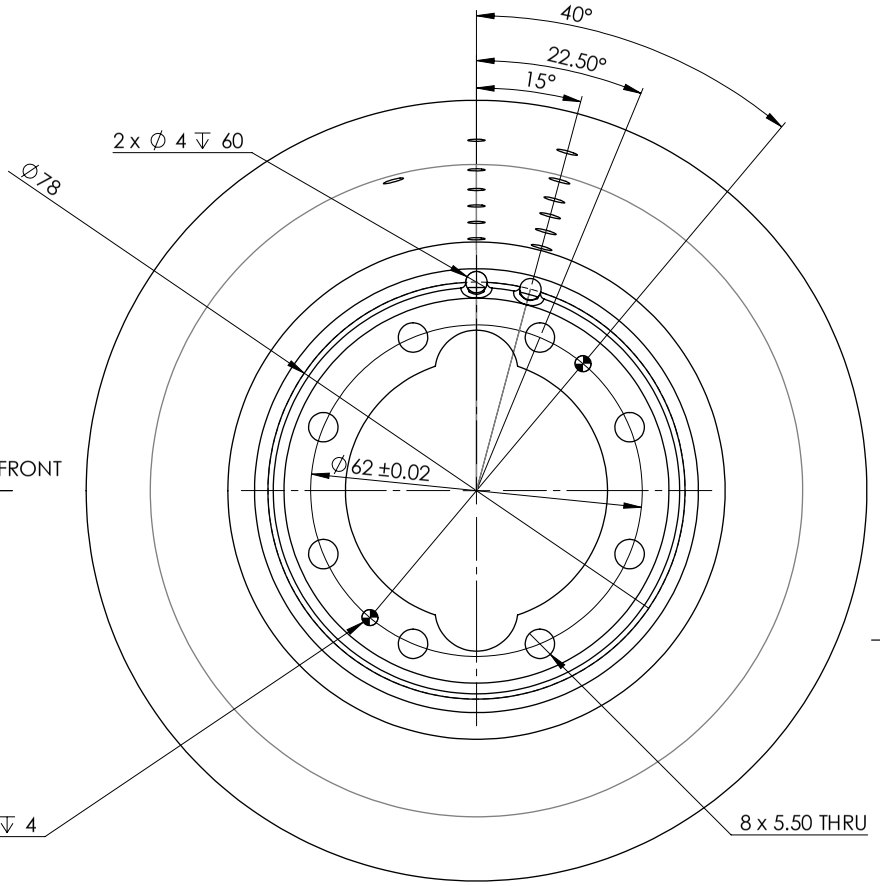
SOLIDWORKS Educational Product. For Instructional Use Only.

REV.	MODIFICATION	BY	DATE
0	NEW		



VIEW BACK
SCALE 1 : 1





VIEW FRONT
SCALE 1 : 1

This is a CAD produced drawing - no manual modifications are to be made.
This drawing is the property of the University of Oxford. It must not be copied, or the contents thereof or any information received in conjunction therewith be imparted to any third party. It must not be used for any other contract and the receipt of this drawing implies that these conditions as stated are accepted.

TOLERANCES UNLESS OTHERWISE STATED			
—	≤ 100 mm	= ± 0.1 mm	
> 100 mm	≤ 1000 mm	= ± 0.2 mm	
> 1000 mm	—	= ± 0.5 mm	
	Angular	= ± 1.0 °	
DESIGNED BY	PK	SCALE	1:2
DRAWN BY	PK	DATE	26/02/21
APPROVED BY		DATE	

MATERIAL: 7075 - T6 ALUMINIUM

DO NOT SCALE - IF IN DOUBT ASK
DIMENSIONS IN mm
REMOVE ALL BURRS AND SHARP EDGES

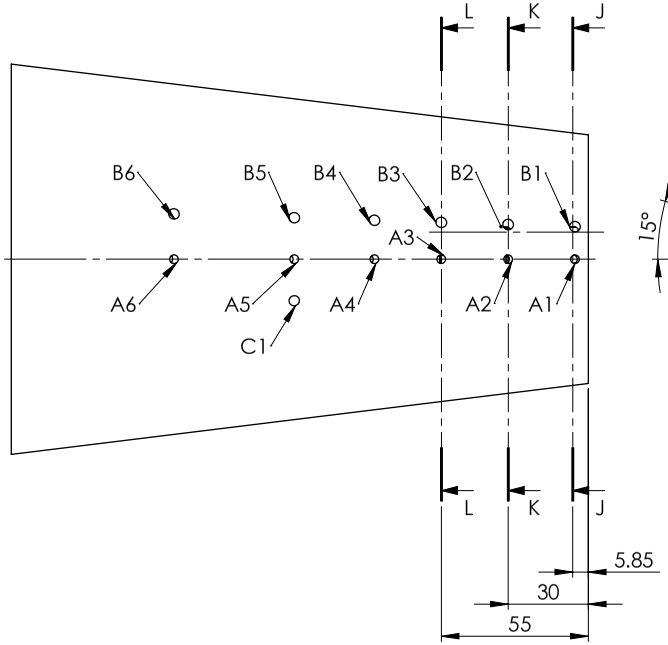
Oxford Hypersonics
Oxford Thermofluids Insititute
Southwell Building
Osney Mead
Oxford OX2 0ES
Tel: 01865 288723

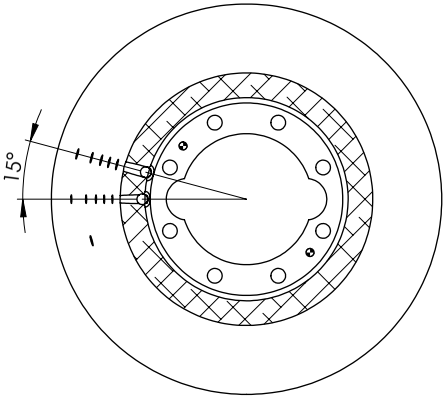
DESCRIPTION: FULL REARSEGMENT OF TCC

PART NUMBER	SHEET	ISSUE	
TCC-006	2/4	0.1	A3

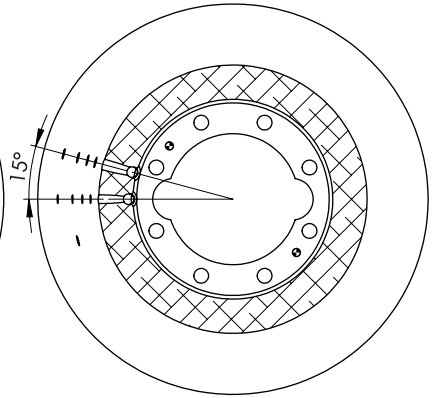
SOLIDWORKS Educational Product. For Instructional Use Only.

REV.	MODIFICATION	BY	DATE
0	NEW		

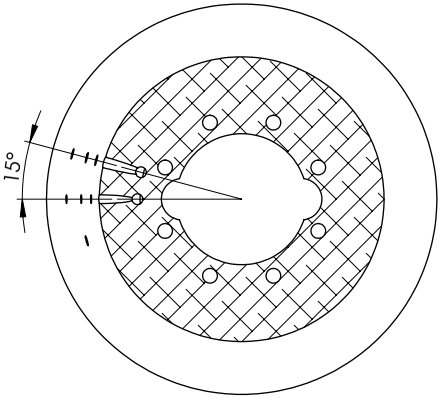




SECTION J-J



SECTION K-K



SECTION L-L

ALL HOLES NORMAL TO THE CONE SURFACE

HOLE TYPE	SIZE	TOLERANCE
A	∅3.25	+0.05 -0
B	∅ 4.0	+0.05 -0
C	∅3.9	+0.05 -0

This is a CAD produced drawing - no manual modifications are to be made.
This drawing is the property of the University of Oxford. It must not be copied, or the contents thereof or any information received in conjunction therewith be imparted to any third party. It must not be used for any other contract and the receipt of this drawing implies that these conditions as stated are accepted.

TOLERANCES UNLESS OTHERWISE STATED
— ≤ 100 mm = ± 0.1 mm
> 100 mm ≤ 1000 mm = ± 0.2 mm
> 1000 mm — = ± 0.5 mm
Angular = ± 1.0 °

DESIGNED BY	PK	SCALE	1:2
DRAWN BY	PK	DATE	26/02/21
APPROVED BY		DATE	

MATERIAL: 7075 - T6 ALUMINIUM

DO NOT SCALE - IF IN DOUBT ASK
DIMENSIONS IN mm
REMOVE ALL BURRS AND SHARP EDGES

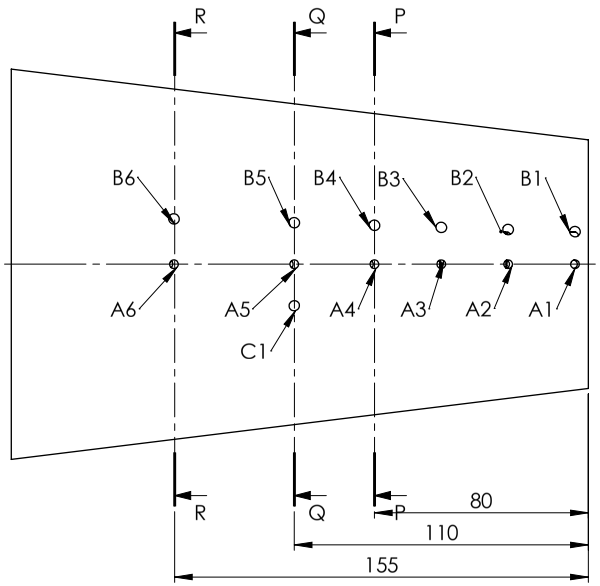
Oxford Hypersonics
Oxford Thermofluids Insititute
Southwell Building
Osney Mead
Oxford OX2 0ES
Tel: 01865 288723

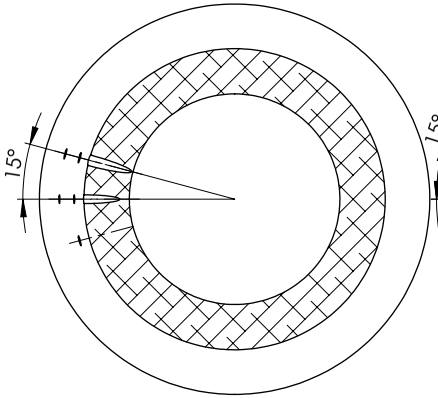
DESCRIPTION: FULL REARSEGMENT OF TCC

PART NUMBER	SHEET	ISSUE	
TCC-006	3/4	0.1	A3

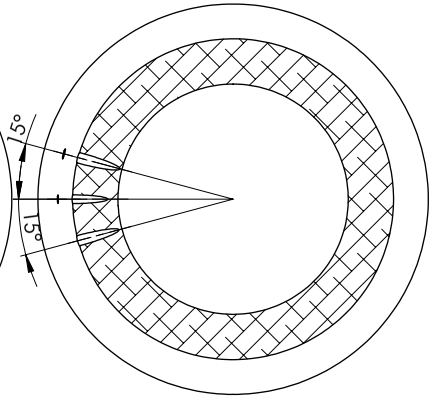
SOLIDWORKS Educational Product. For Instructional Use Only.

REV.	MODIFICATION	BY	DATE
0	NEW		

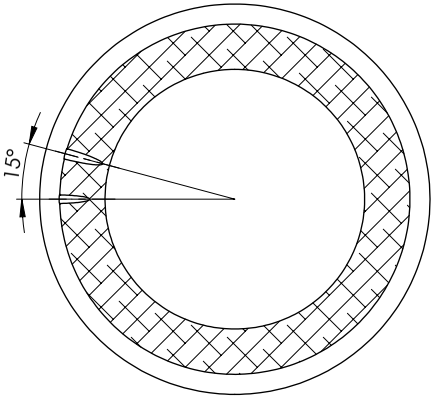




SECTION P-P



SECTION Q-Q



SECTION R-R

ALL HOLES NORMAL TO THE CONE SURFACE

HOLE TYPE	SIZE	TOLERANCE
A	∅3.25	+0.05 -0
B	∅ 4.0	+0.05 -0
C	∅3.9	+0.05 -0

This is a CAD produced drawing - no manual modifications are to be made.
This drawing is the property of the University of Oxford. It must not be copied, or the contents thereof or any information received in conjunction therewith be imparted to any third party. It must not be used for any other contract and the receipt of this drawing implies that these conditions as stated are accepted.

TOLERANCES UNLESS OTHERWISE STATED
— ≤ 100 mm = ± 0.1 mm
> 100 mm ≤ 1000 mm = ± 0.2 mm
> 1000 mm — = ± 0.5 mm
Angular = ± 1.0 °

DESIGNED BY	PK	SCALE	1:2
DRAWN BY	PK	DATE	26/02/21
APPROVED BY		DATE	

MATERIAL: 7075 - T6 ALUMINIUM

DO NOT SCALE - IF IN DOUBT ASK
DIMENSIONS IN mm
REMOVE ALL BURRS AND SHARP EDGES

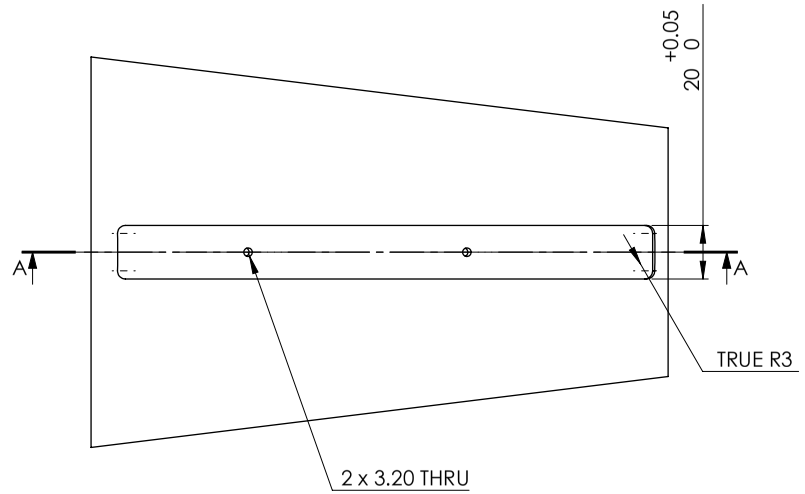
Oxford Hypersonics
Oxford Thermofluids Insititute
Southwell Building
Osney Mead
Oxford OX2 0ES
Tel: 01865 288723

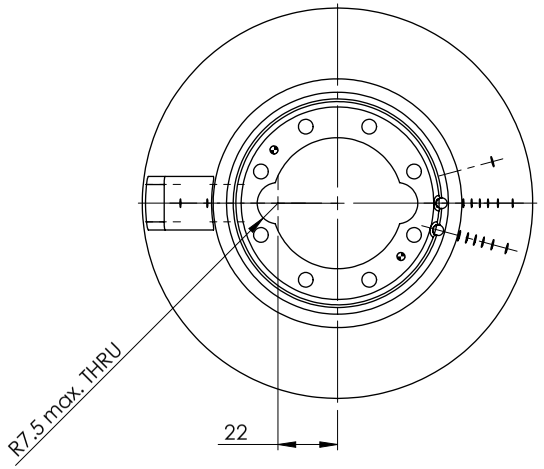
DESCRIPTION: FULL REARSEGMENT OF TCC

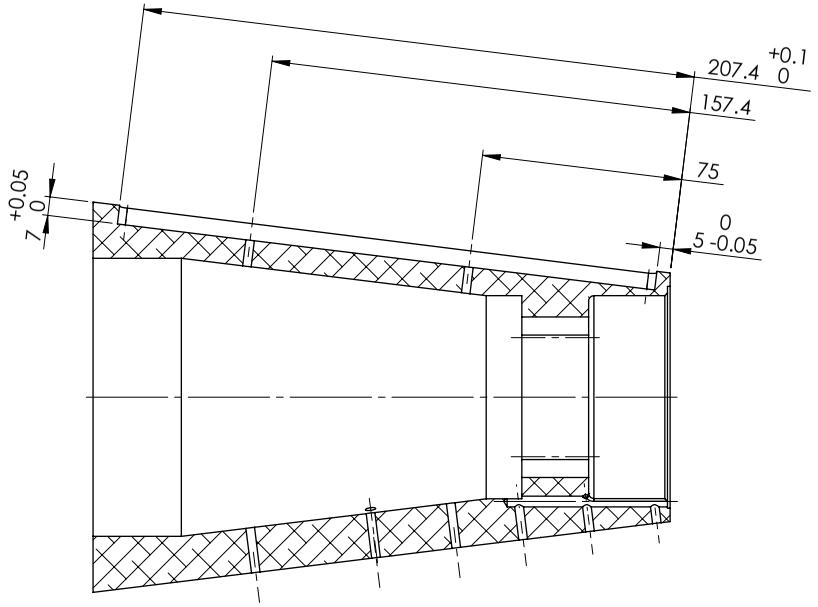
PART NUMBER	SHEET	ISSUE	
TCC-006	4/4	0.1	A3

SOLIDWORKS Educational Product. For Instructional Use Only.

REV.	MODIFICATION	BY	DATE
0	NEW		







SECTION A-A

This is a CAD produced drawing - no manual modifications are to be made.
This drawing is the property of the University of Oxford. It must not be copied, or the contents thereof or any information received in conjunction therewith be imparted to any third party. It must not be used for any other contract and the receipt of this drawing implies that these conditions as stated are accepted.

TOLERANCES UNLESS OTHERWISE STATED			
—	≤ 100 mm	= ± 0.1 mm	
> 100 mm	≤ 1000 mm	= ± 0.2 mm	
> 1000 mm	—	= ± 0.5 mm	
	Angular	= ± 1.0 °	
DESIGNED BY	PK	SCALE	1:2
DRAWN BY	PK	DATE	13/06/22
APPROVED BY		DATE	

MATERIAL: 7075 - T6 ALUMINIUM

DO NOT SCALE - IF IN DOUBT ASK
DIMENSIONS IN mm
REMOVE ALL BURRS AND SHARP EDGES

Oxford Hypersonics
Oxford Thermofluids Insititute
Southwell Building
Osney Mead
Oxford OX2 0ES
Tel: 01865 288723

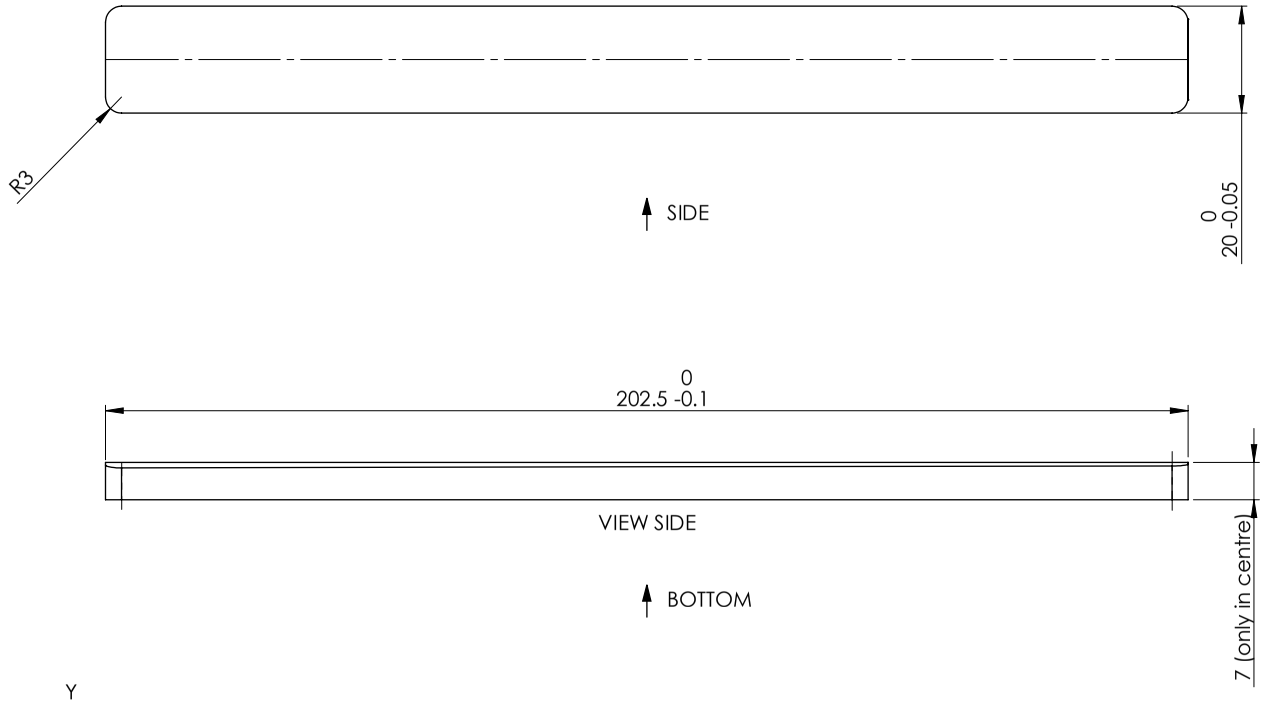
DESCRIPTION: FULL REARSEGMENT OF TCC

PART NUMBER	SHEET	ISSUE	
TCC-006-01	1/1	3.1	A3

SOLIDWORKS Educational Product. For Instructional Use Only.

REV.	MODIFICATION	BY	DATE
0	NEW		

NOTES:
1) INSERT INTO CONE HALF AND BLEND SURFACE TO BEST POSSIBLE SURFACE FINISH



TAG	X LOC	Y LOC	SIZE
A1	50	0	⌀ 2.50 ↧ 3.50 M3 - 6H ↧ 2
A2	132.5	0	

This is a CAD produced drawing - no manual modifications are to be made.
This drawing is the property of the University of Oxford. It must not be copied, or the contents thereof or any information received in conjunction therewith be imparted to any third party. It must not be used for any other contract and the receipt of this drawing implies that these conditions as stated are accepted.

TOLERANCES UNLESS OTHERWISE STATED
— ≤ 100 mm = ± 0.1 mm
> 100 mm ≤ 1000 mm = ± 0.2 mm
> 1000 mm — = ± 0.5 mm
Angular = ± 1.0 °

DESIGNED BY	PK	SCALE	1:1
DRAWN BY	PK	DATE	13/06/22
APPROVED BY		DATE	

MATERIAL: PEEK

DO NOT SCALE - IF IN DOUBT ASK
DIMENSIONS IN mm
REMOVE ALL BURRS AND SHARP EDGES

Oxford Hypersonics
Oxford Thermofluids Insititute
Southwell Building
Osney Mead
Oxford OX2 0ES
Tel: 01865 288723

DESCRIPTION: PEEK INSERT INTO CONE

PART NUMBER	SHEET	ISSUE	
TCC-005-01	1/1	3.1	A3

SOLIDWORKS Educational Product. For Instructional Use Only.

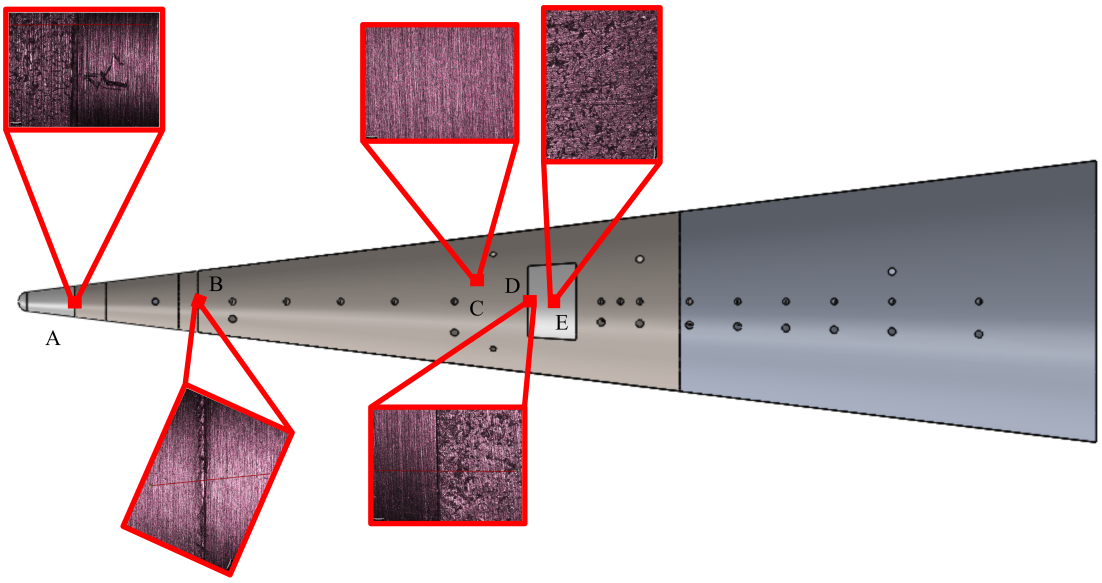


Figure A.1: Cone model with porous nose tip $R_N = 5\,\text{mm}$ configuration. The examined locations for surface roughness are indicated.

A.2 Surface Quality of Cone Model

During the machining and instrumentation process care has been taken to keep the surface as smooth as possible. In addition, the result has then been characterized using an Alicona Focus 3D measurement instrument to analyse roughness, step heights and gap widths on different segments of the model with five-fold magnification image scans. The examined locations can be found in Figure A.1 and the roughness values are summarized in Table A.1. To compare such quantities, Ra was calculated for each patch along three manually chosen straight paths. Hereby, Ra is defined as commonly found in the literature (see e.g. [331])

$$R_a = \frac{1}{l}\int_0^l |z(x)|\mathrm{d}x \tag{A.1}$$

The mean of the three paths is then used as the final result. If a model step is present, then the length and width are provided. It can be seen that the average surface roughness of the porous injector material is only marginally larger than the Ra of the steel part. It is hence assumed that the porosity and roughness of the porous aluminium injectors has no influence on the boundary layer.

Table A.1: Cone model roughness values

Location	Ra [μm]	Step width [μm]	Step height [μm]
A	-	100 ± 20	61 ± 9
B	-	120 ± 20	27 ± 5
C	2.5 ± 0.2	-	-
D	-	80 ± 16	45 ± 4
E	2.9 ± 0.2	-	-